To the Graduate Council:

I am submitting herewith a dissertation written by Robert Daniel Murphy entitled "Core Collapse Supernova Gravitational Waves: Theory, Detection, and Parameter Estimation." I have examined the final paper copy of this dissertation for form and content and recommend that it be accepted in partial fulfillment of the requirements for the degree of Doctor of Philosophy, with a major in Physics.

Anthony Mezzacappa, Major Professor

We have read this dissertation
and recommend its acceptance:

Anthony Mezzacappa

Mike Guidry

Ioannis Sgouralis

Eric Lentz

Vassilios Mewes

Accepted for the Council:

Marieke Van Puymbroeck

Vice Provost and Dean of the Graduate School

To the Graduate Council:
I am submitting herewith a dissertation written by Robert Daniel Murphy entitled "Core Collapse Supernova Gravitational Waves: Theory, Detection, and Parameter Estimation." I have examined the final electronic copy of this dissertation for form and content and recommend that it be accepted in partial fulfillment of the requirements for the degree of Doctor of Philosophy, with a major in Physics.

Anthony Mezzacappa, Major Professor

We have read this dissertation
and recommend its acceptance:

Anthony Mezzacappa

Mike Guidry

Ioannis Sgouralis

Eric Lentz

Vassilios Mewes

Accepted for the Council:

Marieke Van Puymbroeck

Vice Provost and Dean of the Graduate School

(Original signatures are on file with official student records.)

Core Collapse Supernova Gravitational Waves: Theory, Detection, and Parameter Estimation

A Dissertation Presented for the

Doctor of Philosophy

Degree

The University of Tennessee, Knoxville

Robert Daniel Murphy

August 2025

copyright © by Robert Daniel Murphy, 2025
All Rights Reserved.

Acknowledgments

Thank you to the UTK Physics Department for their commitment to my future and affording me opportunities for boundless learning and growth during the past eleven years.

More specifically, I would like to thank my major advisor Tony Mezzacappa for his patient guidance throughout my graduate career and enthusiastic commitment to my growth as a supernova scientist. I also thank him for allowing me the time I needed to rediscover the joy in physics. I also thank the UT-ORNL theoretical astrophysics research group for making this dissertation possible through the countless hours of work and computation it took to develop the state-of-the-art core collapse supernova simulation code that generated the high-fidelity data I utilized in my investigations. Thank you to Eric Lentz in particular for always being willing to discuss the eccentricities of Chimera, and all the other conversations spawned along the way. I am grateful to my committee members for lending their time and expertise to serve on my committee, review my work, and provide their invaluable insight.

A significant portion of my development as a graduate student occurred outside of academic research, and for that I thank Sean Lindsay. He taught me that the process of becoming an educator is never really complete and that it never has to stop being fun to be effective. I also thank Paul Lewis for making telescope observations possible in the middle of downtown Knoxville, and for always keeping the Nielsen Physics building rooftop a welcoming and entertaining learning environment for all ages.

I would not be where I am today without my parents, Brian and Annette. Thank you for all the Saturdays at Taekwondo tournaments, band competitions, and Science Olympiad. I sincerely appreciate the immense effort it took to corral three children to all their extracurricular activities while working a full-time job. Thank you for allowing and encouraging me to be myself.

Most of all, I would like to thank my partner Katherine who truly changed my life. I cannot imagine reaching this milestone without her immeasurable support and encouragement. Thank you for pushing me when I needed it. Thank you for picking me up when I fall, metaphorically and literally. Thank you for your love. I am endlessly grateful that we get to experience life together.

Disclosure and Contributions

This dissertation contains edited text and results from published journal articles Mezzacappa et al. (2023); Murphy et al. (2024, 2025b) and a soon to be published article Murphy et al. (2025a), reproduced with permission from the publisher.

Statement of Disclosure

With the exception of Mezzacappa et al. (2023), from which only my direct contributions are included here, I am the primary author of all the other articles. Section 2.2 in Chapter 2 derives the bases for modal analysis I conduct, and is reproduced from Murphy et al. (2025a). Results and edited text from Mezzacappa et al. (2023); Murphy et al. (2025b) are contained mainly in Chapter 4, and results and edited text from Murphy et al. (2024, 2025a) are mainly contained in Chapter 5. I include no text from these articles of which I am not the author. Text is edited to reference material contained within this dissertation as well as publications, and citations have been edited to match the style of this dissertation. Figures 5.4 and 5.7 are reproductions from Murphy et al. (2024), edited to better fit the style of this dissertation.

Personal Contributions

While each of these papers represent a collaborative effort with all the coauthors, I personally performed a substantial part of the analysis for each study. I list below these contributions:

1. I developed and implemented the modal analysis presented in Murphy et al. (2025b), Section 2.2, and Chapter 3

2. I modified the method of regional decomposition used in Mezzacappa et al. (2023) to perform the analysis in Murphy et al. (2025b) and Chapter 4

3. I led the interpretation of the joint regional decomposition and modal analysis study in Murphy et al. (2025b) and Chapter 4

4. I implemented the code for producing the spectrograms from gravitational wave strains, as outlined in Section 2.1.6 and used in Murphy et al. (2024, 2025b,a)

5. I developed and performed all analysis of the high frequency component of gravitational wave emission in the absence of noise in Murphy et al. (2024) and Section 5.1

6. Using the detection statistics produced by collaborators, I quantified the detectability of differences due to the nuclear equation of state in Murphy et al. (2024) and Section 5.1

7. I refined and specified the connections present between the gravitational wave signals and hydrodynamic data for the models presented in Murphy et al. (2025a)

There, peeping among the cloud-wrack above a dark tor high up in the mountains, Sam saw a white star twinkle for a while. The beauty of it smote his heart, as he looked up out of the forsaken land, and hope returned to him. For like a shaft, clear and cold, the thought pierced him that in the end the Shadow was only a small and passing thing: there was light and high beauty for ever beyond its reach.

— J. R. R. Tolkien

The Return of the King

Abstract

This dissertation aims to advance the understanding of gravitational wave (GW) production in neutrino-driven core collapse supernovae (CCSNe) by providing a comprehensive analysis of the GW signals from state-of-the-art CCSN simulations. It further advances our understanding of GW production in CCSNe by investigating the effects of differing nuclear equations of state (EOS) and stellar structures on GW signals. CCSNe are explosions of massive stars initiated by gravitational collapse of their inner cores. This explosion is generated by the release of gravitational binding energy as the core transitions to a proto-neutron star (PNS) that evolves into either a neutron star or black hole over the course of tens of seconds. The PNS evolution produces the dominant contribution to the high frequency GW signal emitted by CCSNe. Thus, GWs provide a unique window directly into the deepest regions of the CCSN, otherwise opaque to electromagnetic emissions. The analysis conducted in this dissertation utilizes three-dimensional CCSN simulations from the state-of-the-art Chimera code and combines a regional decomposition of GW emission with a modal analysis of the PNS. The regional decomposition provides insight into source of GW emission, and the modal analysis connects that insight to the quasi-normal oscillation modes of the PNS that produce those GWs. Both analyses show that the gravitational wave emission begins near the surface of the PNS but is eventually dominated by emission deep within the PNS. The regional decomposition indicates that the initial PNS surface dominated GW emission is excited from matter accretion onto the PNS, and the later deep interior PNS dominated GW emission is excited by

Ledoux convection and convective overshoot. The modal analysis confirms that the character of quasi-normal modes of oscillation of the PNS changes precisely at the time the source of emission changes, initially described by buoyancy-driven oscillations and later by pressure-driven oscillations. Using two-dimensional CHIMERA simulations, this dissertation demonstrates that the high frequency component of CCSNe GW signals is sensitive to the nuclear EOS, and, in principle, these EOS effects are detectable in current-generation GW detectors. Finally, this dissertation shows the effects of progenitor stellar structure on CCSN GW emission.

Table of Contents

1 Introduction **1**

1.1 Historic Foundations . . . 2

1.2 Stellar Collapse and Bounce . . . 3

1.3 Shock Stagnation . . . 5

1.4 Multi-dimensional Effects and Shock Revival . . . 6

1.5 Modern Simulations . . . 8

1.5.1 CHIMERA . . . 12

1.6 CCSNe Gravitational Wave Predictions . . . 14

2 Methods **20**

2.1 Gravitational Wave Extraction . . . 20

2.1.1 Gravitational Waves in the Weak Field Limit . . . 22

2.1.2 Transverse-Traceless Gauge . . . 26

2.1.3 Gravitational Waves with Sources . . . 30

2.1.4 Gravitational Wave Polarization . . . 35

2.1.5 Gravitational Waves in CCSN . . . 39

2.1.6 Gravitational Wave Spectrograms . . . 45

2.2 Perturbative Analysis . . . 46

2.2.1 Linearized Equations . . . 48

2.2.2 Assumption of Hydrostatic Equilibrium . . . 52

2.2.3 Linearized System Solutions . . . 53

2.2.4 Boundary Conditions 60

3 Computational Development **62**

3.1 Numerical Scheme 63

3.2 Testing Modal Analysis 64

4 Gravitational Wave Analysis for 3D CCSN Simulations **71**

4.1 Models 71

4.2 Regional Decomposition 72

4.3 Models D15 and D25 73

4.3.1 Regional Decomposition of the Strains 73

4.3.2 Fractional Luminosity as a Function of Radius 78

4.3.3 Modal Analysis 80

4.4 Model D9.6 91

4.5 Perturbative Analysis with a Different Boundary 100

4.6 Summary 103

4.7 Comparison to Other Work 107

5 Gravitational Wave Analysis of Two-Dimensional CCSN Simulations **110**

5.1 Dependence of the Reconstructed Core Collapse Supernova Gravitational Wave High-Frequency Feature on the Nuclear Equation of State in Real Interferometric Data 111

5.1.1 Introduction 111

5.1.2 Chimera E-series Simulations 118

5.1.3 Included Equations of State 118

5.1.4 Slope Estimation Without Noise 120

5.1.5 Fit to HFF 123

5.1.6 Dimensionality Comparison 126

5.1.7 Curvature of the HFF 129

5.1.8 Discussion . . . 131
5.1.9 Conclusion . . . 137
5.2 Gravitational Waves as a Probe of Core Collapse Supernova Progenitor Structure . . . 138
5.2.1 Introduction . . . 139
5.2.2 Core-Collapse Supernova Models . . . 141
5.2.3 Gravitational Wave Extraction . . . 143
5.2.4 Total Gravitational Wave Strain . . . 144
5.2.5 Regional Decomposition . . . 151
5.2.6 Prompt Convection . . . 155
5.2.7 Neutrino-Driven Convection and the SASI . . . 159
5.2.8 Linear Memory . . . 163
5.2.9 Summary, Discussion, and Conclusion . . . 167

6 Conclusions and Outlook **170**
6.1 Future Modal Analyses . . . 171
6.2 Discussion and Future Outlook . . . 172

Bibliography **176**

Vita **204**

List of Tables

3.1 Dimensionless structure variables for a Newtonian, self-gravitating star with polytropic index $n = 1.5$. 66

3.2 Quasi-normal oscillation mode frequencies for $n = 1.5$ polytropic star as determined numerically in Horedt (2004). 67

5.1 HFF first-order polynomial approximation coefficients: $f(t) = \alpha t + \beta$. 124

5.2 Coefficients for the second-order approximation in time of the HFF below 1 kHz and below 2 kHz. 131

5.3 HFF slope estimation results in real interferometric noise for distances of 1 kpc, 5 kpc, and 10 kpc. 132

5.4 HFF starting frequency estimation results, in real interferometric noise, for distances of 1 kpc, 5 kpc, and 10 kpc. 133

5.5 F-series linear approximation coefficients for the HFF. 149

List of Figures

2.1 Hydrostatic equilibrium deviation for D15 (top) and D25 (bottom). . 54

3.1 Eigenfrequencies and percent residuals for $n = 1.5$ polytropic star. . . 68

3.2 L_2-norm as a function of number of radial cells. 69

4.1 Simplified schematic showing regional boundaries, with region 5 extending outside the figure and arrows approximating convective motion. 74

4.2 Gravitational wave strains by region for D15 with updated boundaries. 75

4.3 Gravitational wave strains by region for D25 with updated boundaries. 77

4.4 Fractional gravitational wave luminosity with respect to time and radius. 79

4.5 Spectrograms and eigenfrequency evolution for model D15. 83

4.6 Spectrograms and eigenfrequency evolution for model D25. 84

4.7 Eigenfunction amplitudes around avoided crossing times for D15. . . 85

4.8 PNS oscillation mode gravitational wave production efficiency. 88

4.9 PNS oscillation mode power emitted as gravitational waves. 90

4.10 Spectrograms by region and overlaid eigenfrequency evolution for D15. 92

4.11 Spectrograms by region and overlaid eigenfrequency evolution for D25. 93

4.12 Hydrostatic equilibrium deviation for model D9.6. 94

4.13 Spectrogram for D9.6 with early eigenfrequency evolution overlaid. . . 96

4.14 Regional strains for D9.6 from 0–100 ms after bounce. 97

4.15 Regional strain breakdown for model D9.6. 98

4.16 Fractional gravitational wave luminosity with respect to time and radius for D9.6. 99
4.17 Spectrograms and eigenfrequency evolution for model D9.6. 101
4.18 Gravitational wave emission efficiency and power output for D9.6. . . 102
4.19 Eigenfrequency evolution with the 10^{10} g cm^{-3} density contour as the outer boundary in our modal analysis overlaid on the $h_{+/\times}$-polarized spectrograms for D15. 104

5.1 Strains for each E-series model computed along the z-axis at the source. 121
5.2 Spectrograms for each E-series model, with the color axis showing the logarithm of the power spectrum, $\log_{10}(P)$. 122
5.3 Linear-best-fit lines for maximum power spectral density output. . . . 125
5.4 First-order HFF approximations without noise, across E-series models. 127
5.5 Spectrograms for two-dimensional (top) and three-dimensional (bottom) CCSN simulations using the LSBCK EOS with first-order HFF approximation. 128
5.6 Quadratic-best-fit lines for maximum power spectral density output. . 130
5.7 HFF slopes estimated by our DNN model including the range of variability of the HFF starting frequency across E-series models for detection distances of 1 kpc, 5 kpc, and 10 kpc. 135
5.8 Depiction of new regions I–III for two-dimensional CCSN models. . . 145
5.9 h_+-polarized strains multiplied by a distance of 10 kpc for F15.78 (purple) and F15.79 (teal). 147
5.10 Spectrograms for F15.78 and F15.79. 148
5.11 F-series spectrograms overlaid with the linear approximation of the HFF. The gray dashed line denotes the start time of the HFF. 150
5.12 Gravitational wave luminosity for F15.78 (purple) and F15.79 (teal). . 152
5.13 Total gravitational wave energy for F15.78 (purple) and F15.79 (teal). 153

5.14 Gravitational wave strains produced in regions I, II, and III, for F15.78 (purple) and F15.79 (teal). 154
5.15 Electron fraction and Ledoux criterion for F15.78 shortly after bounce. 156
5.16 Electron fraction and Ledoux criterion for F15.79 shortly after bounce. 157
5.17 Gravitational wave strains produced in region I, multiplied by a distance of 10 kpc, during the first 150 ms after core bounce for F15.78 (purple) and F15.79 (teal). 158
5.18 Specific entropy within the inner 200 km of the F15.78 model at 190 ms (top), 398 ms (middle), and 756 ms (bottom) postbounce. 160
5.19 Specific entropy within the inner 200 km of the F15.79 model at 244 ms (top), 446 ms (middle), and 664 ms (bottom) postbounce. 161
5.20 Gravitational wave strains produced in regions I and II, multiplied by a distance of 10 kpc, starting at 600 ms postbounce for F15.78 (purple) and F15.79 (teal). 162
5.21 F15.78 specific entropy at 442 ms and 1258 ms for $r <= 10{,}000$ km. . 164
5.22 F15.79 specific entropy at 500, 734, and 1636 ms for $r <= 10{,}000$ km. 165
5.23 Gravitational wave strain from the anisotropic emission of neutrinos. 166
5.24 Total h_+-polarized gravitational wave strain from both the anisotropic emission of neutrinos and matter motion, multiplied by a distance of 10 kpc for F15.78 (purple) and F15.79 (teal). The observer of the explosion is aligned along the z-axis of the simulation. 168

Chapter 1

Introduction

Core collapse supernovae (CCSNe, singular CCSN) refer to the explosions of massive stars as the result of collapse of their inner-core. Supernovae are broadly characterized based on the absence or presence of hydrogen in their spectral lines as type I or type II supernovae, respectively. CCSNe fall into the category of type II, with additional spectral differences allowing for further subdivisions within this category. Regardless of the subdivision, all Type II supernovae result from the collapse of their inner-core to densities at which the strong nuclear force becomes repulsive and halts collapse, generating a shockwave that eventually rips the star apart. As some of the most energetic events in the Universe, CCSNe embody the unique physics at extreme densities and temperatures unattainable in terrestrial laboratories. The resulting explosion will not only be visible across the electromagnetic spectrum, but it will also generate neutrinos and gravitational waves carrying information from the deepest regions of the CCSNe that, if the events are close enough, can be detected on Earth. As such, CCSNe are exciting sources for the emerging field of multimessenger astronomy and have the potential to test physics at otherwise inaccessible limits.

The focus of this dissertation is broadly on analyzing the gravitational waves produced from CCSNe modeled using the massively parallel CHIMERA (Bruenn et al., 2020) CCSN simulation code. In particular, it investigates the physical processes

connected with gravitational wave generation in CCSNe to ascertain more precisely the information that is contained within the gravitational wave signal, and presents two studies as examples of using gravitational wave detections to investigate CCSNe. The rest of this chapter is dedicated to a broad overview of CCSNe theory and simulation, as well as their connections to gravitational wave generation. Chapter 2 will derive the methods used to extract gravitational waves from CCSNe simulations, and the methods for a perturbative analysis of the proto-neutron star (PNS) that evolves behind the shockwave of a CCSN. Chapter 3 outlines the computational development of this perturbative analysis. Using these methods, Chapter 4 sources and characterizes the gravitational wave emission from three-dimensional CHIMERA simulations. Chapter 5 presents two, two-dimensional CCSNe simulation studies that demonstrate the use of gravitational wave analysis to investigate CCSNe. Finally, Chapter 6 summarizes my findings and provides a brief discussion on the future outlook for gravitational wave analysis from CCSNe.

1.1 Historic Foundations

Supernovae have likely been observed throughout human history by the sudden appearance of "new" (Latin "nova") stars that stayed in the sky for months at a time. Reliable recorded events span the last two millennia, with modern observations across the electromagnetic spectrum connecting the location and age of supernova remnants to historical accounts (Clark and Stephenson, 1977; Green, 2002; Stephenson and Green, 2009; Murphey et al., 2021). Such connections are not merely academic in nature, as precise information on the age of these remnants allows more accurate predictions of the conditions that gave rise to these extreme events (e.g., Díaz-Rodríguez et al. (2021); Ritter et al. (2021); Coffin et al. (2022); Omand et al. (2025)).

Despite observations made by some of the foremost scientist of the sixteenth and seventeenth centuries (e.g., Tycho Brahe and Johannes Kepler), the provenance of these supernovae was not identified until the twentieth century. In 1934, two years

after the discovery of the neutron, a theory was proposed that supernovae are the result of mass "annihilation" in a star as it transitions from "an ordinary star into a *neutron* star," releasing massive amounts of kinetic and electromagnetic energy in the process (Baade and Zwicky, 1934a,b,c). The gravitational binding energy freed from such a transition to a neutron star would be on the order of 10^{53} erg, enough energy to expel the remaining matter in an explosion. This hypothesis was proposed not only to explain the origin of supernovae, but also to connect supernovae with the production of cosmic rays, i.e., high-energy, charged particles of non-terrestrial origin. Thus, from the inception of supernova theory, supernovae have been suggested sources of multimessenger signals.

1.2 Stellar Collapse and Bounce

As our understanding of stellar evolution and nuclear theory continued to develop, supernova theory began to mature. All stars, by definition, come into existence when nuclear fusion of hydrogen into helium begins in their cores. This nuclear fusion provides thermal pressure that stabilizes the star against the force of gravity. If a star is massive enough, $M_{\rm ZAMS} \gtrsim 8$–$10\ M_\odot$ (n.b., $M_{\rm ZAMS}$ is the "zero-age main sequence" mass and $M_\odot$ is the mass of the Sun), throughout the star's lifetime its core will contract and enable the fusing of heavier elements. At the transition between each stage of burning, as the current fuel runs out the thermodynamic pressure supplied by the nuclear reactions decreases to the point where gravity causes the core to contract. As the core contracts, its temperature increases, and it eventually will be able to start nuclear reactions with the next fuel source (e.g., from hydrogen fusion to helium fusion, helium fusion to α-chain reactions, etc.) (Burbidge et al., 1957). For massive stars, this process proceeds until an iron-group element core (i.e., elements with $\gtrsim 56$ nucleons) is produced. The fusion of these elements in the inner-core will result in a net energy loss, and so fusion can no longer provide the support needed to prevent gravitational collapse.

While collapse is imminent, electron degeneracy pressure, i.e., the inability of electrons to occupy the same quantum state, is able to support the inner-core temporarily. However, as matter accumulates on the inner-core, the mass approaches the limit of stability between electron degeneracy pressure and gravity, the Chandrasekhar mass of M ∼1.2–1.4 $M_\odot$ for pure iron or pure helium, respectively. In tandem, electron capture on nuclei and free protons, generated as thermal reactions cause nuclei to dissociate, begins to decrease the number of free electrons, and so too the electron degeneracy pressure. With decreased degeneracy support, gravity becomes dominant and collapse begins.

Throughout collapse, nuclei in the inner-core disassociate into free neutrons and protons that interact with free positrons and electrons to create a neutron rich environment. These nucleons collapse to densities beyond nuclear saturation density, $\sim 10^{14}$ g cm^{-3}, where nucleon–nucleon repulsion due the strong nuclear force, in addition to neutron degeneracy pressure, abruptly halts collapse and causes pressure waves to propagate outward from the core (Colgate et al., 1961). This sudden halt of collapse is termed core "bounce." These pressure waves and infalling matter from the outer core meet at the sonic point, where infalling matter exceeds the local speed of sound. This creates a discontinuity in pressure, density, and velocity, which forms a shock that propagates outward from the inner-core.

The first simulation modeling the gravitational collapse and bounce of a 10 $M_\odot$ star was performed in 1966 by Colgate and White (1966). Already, this CCSN simulation involved numerical implementations to model radiation-hydrodynamics that coupled with both nuclear physics through an equation of state and weak interaction physics through neutrino emission and absorption through pair annihilation, beta-decay, and the inverse reactions. This effectively showed the basic theory of stellar collapse was feasible, and the production of the shockwave after bounce was a strong indicator that this "prompt" mechanism was how stars exploded as supernovae. This first simulation only tracked the shockwave for ∼0.2 s after core bounce, but,

unfortunately, over the next decades longer simulations failed to show this shockwave moving far beyond the outer-core of the star.

1.3 Shock Stagnation

These later simulations observed that the shockwave tends to lose energy as it moves outward. Part of the energy losses may be attributed to the dissociation of nuclear matter passing through the shock. Additionally, once the shock passes through lower density regions of the star, the diffusion speed of neutrinos overtakes the speed of the shock, whhich results in a neutrino burst that carries away significant amounts of energy. This loss of energy causes the shock to stall at a radius of ∼100–200 km before ultimately falling back into the inner-core for one-dimensional CCSN simulations Mezzacappa (2005).

In contrast to the "prompt" explosion mechanism, Bethe and Wilson (1985) proposed a delayed explosion mechanism facilitated through neutrino heating. Their detailed analysis showed that the absorption of electron- and antielectron-neutrinos by matter behind the shock deposited $\sim 4 \cdot 10^{50}$ erg of energy into the stalled shockwave, which is enough to account for weak supernovae. This energy was deposited on the order of a few hundreds of milliseconds after bounce, so that if the shock did not fall back to the inner-core before then, neutrinos would be capable of depositing a significant fraction of the energy needed for the full explosion.

While promising, this mechanism fails to produce supernovae in one-dimensional simulations in most cases, with the only exceptions being low mass progenitor stars with steep density profiles (Müller, 2016). Due to the complicated nature of neutrino transport, approximate transport schemes were the only practical computational methods for over a decade. However, even with the advent of numerical implementations of ab initio, general relativistic Boltzmann neutrino transport schemes, one-dimensional simulations failed to produce supernova explosions (Liebendörfer

et al., 2001). This failure to explode in one-dimensional simulations highlights the fundamental multi-dimensional nature of CCSN.

1.4 Multi-dimensional Effects and Shock Revival

Before introducing multi-dimensional effects in CCSN simulations, it is necessary to delineate the structure behind the shock further. The deepest region of the supernova, the inner-core that bounced to create the shock wave, will eventually evolve into either a black hole or a neutron star. During its evolution to that ultimate state, it is referred to as a proto-neutron star (PNS). For this dissertation, the surface of the PNS is defined by the spherically averaged 10^{11} g cm^{-3} density contour. This radius agrees with the radius of the flavor-, and energy-averaged neutrino sphere (i.e., the average radius at which neutrinos transport can no longer be described purely through diffusion). Just outside of the PNS, neutrino–matter interactions, on average, remove energy from the region. However, there exits a radius at which net-energy loss from neutrino emission is balanced by net-energy gain from neutrino absorption. This defines the gain radius, and the region of net neutrino heating between the gain radius and the shock is called the gain region. Outside the shock, matter is falling radially inward, causing an accretion flow through the shock.

In the general case for CCSN, multi-dimensional effects from hydrodynamic instabilities are necessary to enhance neutrino heating behind the shock. Within the PNS, entropy and lepton gradients, sustained through the continual emission of neutrinos of all flavors, cause Ledoux convection that can boost the neutrino luminosity, i.e., the power radiated from the PNS as neutrinos (Epstein, 1979; Wilson and Mayle, 1988; Burrows and Lattimer, 1988). In the gain region, neutrino heating generates a negative entropy gradient that leads to so-called neutrino-driven convection. In both cases, this convection can fundamentally alter the heating of matter behind the shock such that regions of shockwave expansion can arise while significant accretion onto the PNS is still occurring (Herant et al., 1994; Burrows

et al., 1995; Janka and Müller, 1995). This accretion onto the PNS further boosts the production of neutrinos, which, in turn, continue to add energy behind the shock.

Moreover, multi-dimensional simulations showed that nonspherical perturbations to the shock can develop into a stationary accretion shock instability (SASI) (Blondin et al., 2003; Janka et al., 2005; Blondin and Mezzacappa, 2006). This SASI is a global and non-radial oscillation, dominated by dipole and quadrupolar oscillation modes, with a characteristic frequency. The instability can grow stronger by an advective-acoustic cycle (Foglizzo et al., 2007). Similar to convection, SASI can bring matter into the gain region to increase the effect of neutrino heating, as well as push the shock radius to radii with lower ram pressure (i.e., the pressure due to infalling matter) where radiation pressure can cause the shock radius to continue growing.

While seemingly necessary for successful CCSN explosions, increased dimensionality in simulations is not sufficient to ensure explosion (Janka and Mueller, 1996). In particular, Mezzacappa et al. (1998) showed that improved realism in neutrino transport methods led to lower neutrino luminosities and decreased neutrino heating when compared to two-dimensional simulations using more approximate neutrino transport. Additionally, increasing from two- to three-dimensional CCSN simulations results in yet more changes in CCSN evolution. As two-dimensional simulations enforce a rotational symmetry, nonphysical artifacts can develop that are not present in three-dimensional simulations, and these artifacts have significant effects on CCSN evolution. In general, two-dimensional CCSN models explode more rapidly than their three-dimensional counterparts due to varying contributions from: (1) the turbulent energy cascade moving energy from small to large scales in two-dimensions and in the reverse direction in three-dimensions (Hanke et al., 2012), (2) the creation of larger neutrino-driven buoyancy plumes in two-dimensions than three-dimensions that result in more rapid expansion of the shock (Couch, 2013), (3) artificially increased neutrino luminosities in two-dimensional neutrino transport schemes (Dolence et al., 2015; Skinner et al., 2016) that are not present in equivalent three-dimensional neutrino transport schemes (Glas et al., 2019). Despite the earlier shock revival

for two-dimensional simulations, three-dimensional effects play a beneficial role for strengthening the CCSN explosion after shock revival (Müller, 2015).

1.5 Modern Simulations

The past six decades of CCSN research have yielded significant lessons that shape the current state-of-the-art CCSN simulations. Namely, that accuracy of neutrino-transport and neutrino interactions is paramount to realistically account for energy transfer from neutrinos to matter in the shock. Additionally, CCSNe are inherently multi-dimensional phenomena, and are sensitive to differences in two- and three-dimensional simulations. Even so, with the limitations of two-dimensional simulations well quantified, ab initio simulations with sophisticated neutrino-transport are capable of making useful qualitative predictions.

Throughout this overview, I have focused on the broad advancements in CCSN theory that brought the field to its current understanding of CCSNe evolution. Essential to each of these advancements was the fundamental physics known to be important from the onset. All CCSN simulation codes rely on accurately solving hydrodynamic equations to achieve the multi-dimensional fluid instabilities (PNS convection, SASI, neutrino-driven convection) that boost neutrino heating. Coupled to the hydrodynamics is the treatment of gravity, in a Newtonian, general relativistic (GR), or pseudo-Newtonian (i.e., Newtonian with GR corrections) framework. The inclusion of GR effects, for both the pseudo-Newtonian and full GR treatments, results in a more compact PNS and greater neutrino heating (Müller et al., 2012; O'Connor and Couch, 2015). A nuclear equation of state (EOS) is necessary to connect the thermodynamic and hydrodynamic variables at extreme temperatures and densities in the inner core before bounce, and in and around the PNS after bounce. One of the most important observables from CCSNe are the elements present in supernova remnants. Thus, realistic nuclear reaction networks make the most direct connections to astronomical observations of supernova remnants. With the need for

each aspect of the problem to couple with all the others, CCSNe are among the most comprehensive examples of a multi-physics problem. Each aspect of CCSN simulation has experienced its own share of advances in accuracy and efficiency of computation, and, broadly speaking, the advancements in the last two decades have advanced in tandem with advancements in high-performance computing (HPC) as computational speeds approached, and eventually reached, the exaflop scale, i.e., 10^{18} floating-point operations per second.

At this time, for non- and slowly-rotating progenitors, sophisticated three-dimensional CCSN simulations have reached consensus on the neutrino driven explosion mechanism (Burrows and Vartanyan, 2021; Yamada et al., 2024; Janka, 2025). In the case of rapidly rotating progenitors, less common than slowly-rotating progenitors, similar consensus has been reached for the magnetorotational mechanism in those CCSNe explosions (Woosley and Bloom, 2006; Bugli et al., 2021; Obergaulinger and Aloy, 2022; Powell et al., 2023). These sophisticated codes include Chimera, CoCoNuT-FMT, Prometheus-Vertex, Fornax, 3DnSNe, the Einstein-Toolkit based `Zelmani` code, and combinations of other codes with FLASH and ZEUS-MP. I will briefly overview, without comparison of the accuracy between each code, the other simulation codes and their successful three-dimensional CCSNe simulations. The Chimera simulation code will be discussed in detail in Section 1.5.1.

The CoCoNuT-FMT code combines the Core Collapse with Nu Technology (CoCoNuT) GR hydrodynamics code, developed initially by Dimmelmeier et al. (2002), with the fast multigroup neutrino transport (FMT) code of Müller and Janka (2015). It solves the 3+1 dimensional Einstein equations in spherical polar coordinates in the conformal flatness conditions (CFC) approximation, and uses Godunov-type, approximate Riemann solvers to solve the relativistic hydrodynamics equations. The FMT scheme produces an approximate solution to the neutrino energy equation (i.e., the transport equation for the zeroth angular moment of the neutrino distribution function) by applying a closure relation from a two-stream approximate solution to

the Boltzmann equation. The FMT neutrino transport scheme is applied in the "ray-by-ray" approximation. With the CoCoNuT-FMT code, many CCSNe simulations initiated with various progenitors successfully revive the shock and explode: 11.2 $M_\odot$ (Müller, 2015), 18 $M_\odot$ (Müller et al., 2017), 15 $M_\odot$ rotating progenitor that explodes only when assisted by magnetohydrodynamics (Müller and Varma, 2020), 15 $M_\odot$ rotating progenitor simulated with various nuclear EOS and rotation rates (Powell and Müller, 2024), rapidly rotating 39 $M_\odot$ and non-rotating 20 $M_\odot$ Wolf-Rayet stars (Powell and Müller, 2020), electron capture supernova of an 8.8 $M_\odot$ progenitor, and CCSNe of 9.0 $M_\odot$ and 9.6 $M_\odot$ progenitors (Stockinger et al., 2020), and 16.9 $M_\odot$ progenitor with both strong and weak magnetic fields, where the strong magnetic fields result in an earlier and stronger explosion (Varma et al., 2023). There are also several successful explosions for ultra-stripped (i.e., initially massive stars that have shed their outer layers through stellar evolution) progenitors: 2.5 $M_\odot$ helium core (Müller et al., 2018), 3.5 $M_\odot$ helium core (Powell and Müller, 2019), and 9.6–12.5$M_\odot$ helium cores (Müller et al., 2019).

The Prometheus-Vertex code combines the Prometheus piece-wise parabolic hydrodynamics solver of Fryxell et al. (1989) with the Vertex neutrino transport code of Rampp and Janka (2002), which solves both the neutrino energy and momentum density equations (i.e., the transport equation for the zeroth and first angular moments of the neutrino distribution function) in spherical symmetry. The neutrino transport is performed in the "ray-by-ray-plus" approximation (Buras et al., 2006), and closure is achieved with a variable Eddington factor based on a solution to the Boltzmann equation. Gravity is treated in a psuedo-Newtonian context, where a spherically symmetric potential is modified with GR corrections (Marek et al., 2006). To avoid time step restrictions due to the convergence of grid lines at the poles of the grid, three-dimensional simulations with this code utilize an axis-free Yin-Yang grid (Wongwathanarat et al., 2010). With iterations of Prometheus-Vertex throughout its development, many CCSNe simulations initiated with various progenitors successfully revive the shock and explode: 27 $M_\odot$ (Hanke et al., 2013),

9.6 $M_\odot$ (Melson et al., 2015b), 20 $M_\odot$ with strange quark contributions to neutrino–nucleon interactions (Melson et al., 2015a), rapidly rotating 15 $M_\odot$ (Summa et al., 2018), and 18.88 $M_\odot$ (Bollig et al., 2021). For the 18.88 $M_\odot$ progenitor, previous simulations with Prometheus-Vertex did not result in explosion (Müller et al., 2016). However, by evolving the progenitor in three-dimensions for seven minutes pre-collapse (Yadav et al., 2020), asymmetric perturbations developed which enabled the successful explosion of Bollig et al. (2021).

The Fornax code (Skinner et al., 2019) solves Newtonian hydrodynamic equations in a covariant way to enable any coordinate system to be used, and evolves the zeroth and first moments of the neutrino transport equations. The gravitational potential is solved using a multipole expansion with the monopole term corrected to include GR effects. Static mesh refinement is used to solve time step restrictions near the poles of simulations in spherical coordinates. With Fornax, many CCSNe simulations initiated with various progenitors successfully explode and evolve for several seconds after bounce: 9–12 $M_\odot$, 16–20 $M_\odot$, 25 $M_\odot$, and 60 $M_\odot$ progenitors (Burrows et al., 2019; Radice et al., 2019; Vartanyan et al., 2019c; Burrows et al., 2020), 12.5 $M_\odot$ and 15 $M_\odot$ progenitors with the last few seconds pre-collapse evolved in three-dimensions (Vartanyan et al., 2022), 8.1 $M_\odot$ and 9.0–9.6 $M_\odot$ progenitors that explode in one-dimension, but have more accurate observable characteristics in three-dimensions (Wang and Burrows, 2024).

The 3DnSNe code, originally based on the hydrodynamics solver of ZEUS-MP (Hayes et al., 2006), was developed (Takiwaki et al., 2012, 2014, 2016) to include neutrino transport through the isotropic diffusion source approximation (IDSA) of Liebendörfer et al. (2009). In the IDSA scheme, each species of neutrino has a distribution function decomposed into an isotropic and streaming component that are evolved separately. The gravitational potential is solved in a multipole expansion with GR corrections on the monopole term. Using the 3DnSNe code, throughout its evolution, CCSNe simulations initiated with various progenitors successful revive the shock and explode: 11.2 $M_\odot$ progenitor (Takiwaki et al., 2012; Nakamura et al., 2019)

with various resolutions and seed perturbations (Takiwaki et al., 2014), 27 $M_\odot$ rapidly rotating progenitor (Takiwaki et al., 2016), 18.3 $M_\odot$ progenitor evolved through binary evolution to match observational criteria of the 1987a CCSN progenitor (Nakamura et al., 2022), and 16 progenitors from 9–24$M_\odot$ (Nakamura et al., 2025)

The final set of simulations have fewer three-dimensional results, but are at least as sophisticated as the previous entries. Kuroda et al. (2020) implemented a fully relativistic magnetohydrodynamics solver with energy dependent evolutions of the zeroth and first moments of the neutrino transport equations with an analytic closure developed by Kuroda et al. (2012, 2016b). They successfully modeled the explosion of a 20 $M_\odot$ progenitor, but only when the model is rotating and magnetic fields are evolved. Using the `Zelmani` GR neutrino-hydrodynamics code (Ott et al., 2012, 2013), which implements energy dependent evolution of the zeroth and first moment neutrino transport equations, CCSNe simulations of 12–40 $M_\odot$ progenitors exploded (Roberts et al., 2016; Ott et al., 2018). Pan et al. (2021) used FLASH (Fryxell et al., 2000; Dubey et al., 2008) with IDSA neutrino transport and multipole gravity with GR corrections on the monopole term to simulate CCSNe for non-, slowly-, and rapidly-rotating 40 $M_\odot$ progenitors and found that the rotating models explode.

1.5.1 CHIMERA

Chimera (Bruenn et al., 2020) is a massively parallel code developed for the explicit purpose of modeling CCSNe. Its name is derived from the mythical chimera, with three distinct heads that unite to make a creature that is greater than the sum of its parts. The computational grid in Chimera uses spherical polar coordinates (r, θ, ϕ). The radial grid is not uniform and can change at each time step to better capture convective events or the movement of the shock.

The first "head" of Chimerais a radiation-hydrodynamic solver utilizing a modified version of the split, Lagrangian-plus-remap scheme with piecewise parabolic reconstruction (Colella and Woodward, 1984). It has been extended to incorporate

a range of interconnected physics: advection of multiple species, absorption and emission of energy from compositional changes within the fluid, nuclei coming into or out of nuclear statistical equilibrium (NSE), multipole Newtonian self gravity with GR corrections on the monopole term, and momentum and energy exchange with neutrinos. The hydrodynamic variables are coupled to the thermodynamic variables through a tabulated EOS, with several possible nuclear EOS that can be applied at high densities. The innermost core of the radial grid is evolved in spherically symmetry. This region is defined so that it remains sufficiently below any regions of convection of the PNS. The radius of this spherically symmetric region changes with time, but is typically $\lesssim$6–8 km.

The second "head" of CHIMERA is the multigroup, flux-limited diffusion neutrino transport solver based on Bruenn (1985). This solves the zeroth moment neutrino transport equation for the neutrino energy density for electron neutrinos, heavy neutrinos (i.e., muon- and tau-neutrinos), and their anti-neutrino counterparts. Flux-limiting is used to close the system with the first moment equation in the limit of both diffusion and free-streaming. This evolution is split into a transport term, accounting for changes to the energy density from sources and transport, and an advection term, accounting for changes due to energy advection. These terms are evolved in the "ray-by-ray-plus" (RbR+) approximation (Buras et al., 2006), where multi-energy neutrino transport is performed in spherical symmetry for a number of radial rays and neutrinos advect laterally with matter in optically thick regions. Neutrino–matter interactions in CHIMERA are based on those in Bruenn (1985) and include electron capture on protons and various nuclei, electron–positron annihilation, and nucleon–nucleon bremsstrahlung, along with their inverse weak reactions. Neutrino scattering processes included are isoenergetic scattering on nuclei, neutrino–electron scattering, and neutrino–nucleon scattering.

The final "head" of CHIMERA is the evolution of nuclear composition, where it is not in NSE, by the thermonuclear reaction network xNET developed by Hix and Meyer (2006) and Travaglio and Hix (2013). The simplest reaction network included is

the 14 species α-network that models nuclear reactions as interactions with α-particles (i.e., He nuclei) and those nuclei composed of integer multiples of α-particles, up to ^{60}Zn. This network can be enhanced to also evolve inert, free proton, neutrons, and ^{56}Fe. Beyond these, 150 and 160 species reaction networks are also implemented in CHIMERA, including multiple isotopes of all elements with atomic number, Z, from 1–30 (He to Zn).

While there are many CHIMERA simulations conducted in two-dimensions, including the two sets of simulations discussed in Chapter 5, three-dimensional simulations have successfully modeled the explosion of 9.6 $M_\odot$, 15 $M_\odot$, and 25 $M_\odot$ progenitors (Lentz et al., 2015; Mezzacappa et al., 2023). The simulations in Mezzacappa et al. (2023) utilized a Yin-Yang grid to achieve angular resolution of 1 degree in both θ and ϕ. These models were non-rotating, with the 9.6 $M_\odot$ model having zero metallicity and the 15 $M_\odot$ and 25 $M_\odot$ models having solar metallicities. The 9.6 $M_\odot$ model was evolved with the 160 species nuclear reaction network and 540 radial cells, and the larger progenitors were evolved with the α nuclear reaction network and 720 radial cells.

1.6 CCSNe Gravitational Wave Predictions

Since the inception of CCSNe theory, observation of events outside our Galaxy have confirmed that CCSNe are associated with gravitational collapse and compact remnants (Smartt, 2009). In our own Milky Way Galaxy, current observational evidence suggests that ∼2–4 CCSNe occur per century (Li et al., 2011; Adams et al., 2013). This is a more optimistic view than that provided by historical records, which only account for eight CCSNe over the last two millennia (Clark and Stephenson, 1977; Green, 2002), corresponding to ∼0.5 CCSNe per century. Likely, some CCSNe are occluded by interstellar material, which may have artificially lowered the naked eye observation rate (Murphey et al., 2021). However, as neutrino driven events, we expect neutrinos to be detectable from a Galactic CCSN within ∼10 kpc. Indeed,

roughly a dozen neutrinos were detected from CCSNe 1987a in the Large Magellanic Cloud, around ∼50 kpc away (Bionta et al., 1987; Hirata et al., 1987). Moreover, since the first gravitational wave detection from a binary black hole merger (Abbott et al., 2016), a new window to CCSNe observation has opened. As I will demonstrate in Chapter 2, CCSN are excellent generators of gravitational waves, which will not only be unimpeded by matter between the Galactic CCSN and our gravitational wave detectors, but they will also be unimpeded by the matter in the outer regions of the star itself. Beyond the benefit of providing a window into the most dense and energetic regions of the CCSNe, this also means that CCSNe simulations making predictions on observable gravitational wave signals need only simulate a few seconds after core bounce. For electromagnetic observables, the most accurate predictions need to simulate hours after core bounce to properly model shock breakout to the interstellar medium as done in Sandoval et al. (2021). Studies using three-dimensional CCSN simulations have already found favorable detection statistics for current and next generation gravitational wave detectors (e.g., Srivastava et al. (2019)). Thus, the multimessenger signals of the next Galactic CCSN are unlikely to be missed, and they will contain unprecedented insights deep into the most extreme regions of the event.

This section provides a brief overview of the connections between the dynamics of three-dimensional CCSN simulations and the predicted gravitational wave signals they generate. Chapter 5 presents relevant references to two-dimensional studies. Abdikamalov et al. (2022) and Mezzacappa and Zanolin (2024) present a more comprehensive overview of these connections.

Gravitational waves will be generated for the duration of CCSNe events, from the moment of core bounce onward. Most current CCSN simulations begin with progenitors produced from spherically symmetric stellar evolution simulations, and, as such, have no time-varying mass quadrupole moment as they proceed towards collapse (see Chapter 2 for the connection between gravitational waves and quadrupole mass moment). Even for realistic progenitors, the mass quadrupole moment for the star

during collapse will be small. However, when the core bounces, any rotation will develop a significant time-dependent mass quadrupole moment, causing a sharp spike in gravitational wave emission that rings down over the next ∼5 ms (Dimmelmeier et al., 2008; Richers et al., 2017; Andresen et al., 2019; Powell and Müller, 2020; Pajkos et al., 2021; Takiwaki et al., 2021). As the shock wave moves through the inner-core, it generates a negative entropy gradient giving rise to so-called "prompt" convection that generates high frequency (i.e., $\gtrsim$500 Hz) gravitational waves for a few tens of ms (seen in all CCSNe simulations referenced in this section). After prompt convection, there is a gravitational wave quiescent period until ∼100 ms after bounce, when convection develops and grows within the PNS and behind the shock wave. In progenitors that have large perturbations from spherical symmetry, either artificially imposed or caused by late stage nuclear burning pre-collapse, this quiescent period is shorter, or altogether absent as seen in the 9.6 $M_\odot$ progenitor of Mezzacappa et al. (2023). Thus, for real CCSN this quiescent period may not be present if significant asymmetries already exist within the star from stellar evolution. Nonetheless, ∼100 ms after bounce, the PNS has developed a significant lepton gradient from the emission of neutrinos of all flavors. This gives rise to Ledoux convection, and it is sustained for several seconds as the PNS continual emits neutrinos so that the lepton gradient does not dissipate. This PNS convection, and the convective overshoot into the layers stable to convection, can excite oscillations of the PNS that generate high frequency gravitational waves (Andresen et al., 2017; Mezzacappa et al., 2020, 2023). Beginning roughly at the same time, convection in the gain region behind the shock begins due to neutrino heating. This can cause stochastic, large scale matter motions that generate low frequency (i.e., $\lesssim$250 Hz) gravitational waves. Similarly, the large scale matter motions from SASI can cause gravitational waves with characteristic frequencies ∼50–150 Hz (e.g., Kuroda et al. (2016a, 2017); Powell et al. (2021); Mezzacappa et al. (2023)). Both of these phenomena can move matter from near the shock to the surface of the PNS, where they can excite oscilaltions of the PNS to create high frequency gravitational waves (Radice et al., 2019; Powell and Müller,

2019; Vartanyan et al., 2023). Thus, the PNS can be excited to oscillate from below by Ledoux convection, and from above through accretion of matter onto the surface of the PNS. Different conditions may make one excitation method more dominant than the other (Powell and Müller, 2019). At the onset of explosion, there will be some large asymmetry that develops and increases as the explosion proceeds outwards. This gives rise to a high amplitude, low frequency (i.e., $\lesssim$50 Hz) gravitational wave, eventually leading to a permanent deformation of spacetime known as gravitational wave "memory". The anisotropic emission of neutrinos, which are approximately free-streaming once they reach the less dense regions of the star after shock revival, also contributes to low frequency gravitational waves that effect the memory (Vartanyan and Burrows, 2020; Richardson et al., 2022, 2024). With the exception of those components of the gravitational wave signal arising from explosion, Pan et al. (2021) showed that failed explosions resulting in black hole formation also demonstrate many of these same characteristics.

This thesis focuses on analyzing the gravitational wave signals from non-rotating progenitors in the absence of magnetic fields. Powell and Müller (2024) showed that for weak magnetic field strengths (i.e., $\leq 10^8$ G) there was no discernible difference in the gravitational wave signals for progenitors with no magnetic fields. Andresen et al. (2021) demonstrated that there is also no discernible difference between the gravitational wave signals produced from CCSN simulations using the RbR+ approximation and signals produced from simulations using fully multi-dimensional neutrino transport schemes with the same neutrino interactions. Therefore, conclusions from the CHIMERA code are relevant even as neutrino transport methods continue to advance.

In Chapters 4 and 5, the analysis of CCSNe generated gravitational wave signals is restricted to the high frequency component of the signal. This is the signal generated by the oscillation of the PNS, whose contraction throughout the CCSN leads to a high-frequency component of the gravitational wave signal (i.e., high-frequency feature, or HFF) that increases with time. Ultimately, connecting the features of this part of the

signal with PNS will allow for parameter estimation, i.e., the mass and radius of the PNS, using a gravitational wave detection (Bizouard et al., 2021; Bruel et al., 2023; Powell and Müller, 2022).

Chapter 4 investigates the gravitational wave signals from three-dimensional CCSNe simulations in order to characterize and source its high frequency component. This extends and enhances studies that computed the regional contribution of the gravitational wave signal (Andresen et al., 2017; Mezzacappa et al., 2020, 2023). This regional decomposition based analysis is combined with a modal analysis of the PNS. This modal analysis is conducted with the perturbative analysis method derived in Chapter 2, which determines the eigenfrequencies and eigenfunctions of the quasi-normal, quadrupolar, non-radial modes of oscillation of the PNS. Previous three-dimensional studies find this high frequency component of the gravitational wave signal is described by low order ${}^2g$-modes at early times and later by the ${}^2f$-mode (Radice et al., 2019; Nakamura et al., 2022). Descriptions of these modes are discussed in detail in Chapter 4. One goal of this dissertation is to demonstrate that combining these analysis methods (i.e., regional decomposition and modal decomposition) allows for a more complete and accurate understanding of the generation of gravitational waves in CCSNe.

Chapter 5 investigates what other parameters affect this high frequency signal in the context of two-dimensional simulations. O'Connor and Couch (2018) compared the gravitational wave signals between two-dimensional and three-dimensional models and found that they do differ, with two-dimensional models having gravitational wave amplitudes almost an order of magnitude larger. This is due to the forced axisymmetry of the models that encourage the development of large accretion plumes along the axis of symmetry. In three-dimensional models, many smaller accretion plumes develop instead. With this in mind, a comparison of the high frequency component of the gravitational wave signal from two-and three-dimensional simulations that are otherwise identical is presented in Chapter 5.1.6. It is important

to note that the PNS excitation mechanism is inherently different in two-dimensions due to these accretion plumes, as discussed in Mezzacappa et al. (2020).

Chapter 2

Methods

This section serves as a pedagogical review of the key methods employed throughout this dissertation. Specific computational methods will be the subject of Chapter 3. As the focus of this dissertation is on gravitational waves, Section 2.1 is devoted to the derivation of the fundamental quadrupole formula for gravitational wave generation in the slow-motion, weak field limit of the linearized theory of gravity. Section 2.2, likewise, provides a pedagogical derivation of the equations of motion associated with the quasi-normal, non-radial oscillation modes of the proto-neutron star, and is a reproduction of the text, authored by me, in Murphy et al. (2025b).

2.1 Gravitational Wave Extraction

Here I work towards the ultimate expressions that will be used to extract gravitational waves from CCSN simulation data following the derivation in Kotake et al. (2006), beginning with the foundations of Einstein's theory of gravity. Throughout this dissertation, Greek indices will run from 0 to 3 where 0 is the time component of a four-vector. Latin indices will denote the spatial extent of a vector or tensor and run from 1 to 3. Partial derivatives of any general tensor $U^{\alpha_1\alpha_2\ldots\alpha_n}{}_{\beta_1\beta_2\ldots\beta_n}$ with respect to the component x^μ will be denoted with a subscript "$,\mu$", *e.g.* $U^{\alpha_1\alpha_2\ldots\alpha_n}{}_{\beta_1\beta_2\ldots\beta_n,\mu}$. We

also adopt the Einstein summation convention where repeated indices are summed over.

We will work in a general, four-dimensional differential spacetime manifold $\mathcal{M}$ in which exists the metric tensor $\mathbf{g}$ with signature $(-,+,+,+)$. We require the metric tensor to be torsion free and conserved under parallel transport and thus choose the Levi-Civita connection such that

$$\nabla \mathbf{g} = 0. \tag{2.1}$$

Adopting a general coordinate basis $\frac{\partial}{\partial x^\mu}$, the definition of covariant differentiation yields

$$\nabla_a U^\mu{}_\nu \equiv U^\mu{}_{\nu;\alpha} = \frac{\partial U^\mu{}_\nu}{\partial x^\alpha} + \Gamma^\mu{}_{\alpha\beta} U^\beta{}_\nu - \Gamma^\beta{}_{\alpha\nu} U^\mu{}_\beta, \tag{2.2}$$

and Equation (2.1) determines the connection coefficients $\Gamma^\alpha{}_{\mu\nu}$ through the metric function as

$$\Gamma^\alpha{}_{\mu\nu} = \frac{1}{2} g^{\alpha\beta} \left[\frac{\partial g_{\mu\beta}}{\partial x^\nu} + \frac{\partial g_{\nu\beta}}{\partial x^\mu} - \frac{\partial g_{\mu\nu}}{\partial x^\beta} \right]. \tag{2.3}$$

We can then define the Riemann curvature tensor as

$$R^\alpha{}_{\mu\beta\nu} \equiv \Gamma^\alpha{}_{\mu\nu,\beta} - \Gamma^\alpha{}_{\mu\beta,\nu} + \Gamma^\alpha{}_{\sigma\beta}\Gamma^\sigma{}_{\mu\nu} - \Gamma^\alpha{}_{\sigma\nu}\Gamma^\sigma{}_{\mu\beta}, \tag{2.4}$$

and the Ricci tensor and scalars as

$$R_{\mu\nu} = R^\alpha{}_{\mu\alpha\nu} \tag{2.5}$$

$$R = R^\alpha{}_\alpha. \tag{2.6}$$

The relationship between the curvature of spacetime and the matter distribution within that spacetime is described by the Einstein field equations given in geometrized units ($c = G = 1$) as

$$R_{\mu\nu} - \frac{1}{2} g_{\mu\nu} R = 8\pi T_{\mu\nu}, \tag{2.7}$$

where $T_{\mu\nu}$ is the matter stress-energy tensor. The Einstein tensor is defined in terms of the the Ricci tensor and scalars such that

$$G_{\mu\nu} \equiv R_{\mu\nu} - \frac{1}{2} g_{\mu\nu} R, \tag{2.8}$$

and the Einstein field equations become

$$G_{\mu\nu} = 8\pi T_{\mu\nu}. \tag{2.9}$$

2.1.1 Gravitational Waves in the Weak Field Limit

The gravitational waves generated from a CCSN will be produced far away from the location of their detection here on Earth. In this limit, we can approximate gravitational waves as a linear metric perturbation propagating on a locally flat background. We can thus approximate the metric $g_{\mu\nu}$ as the flat Minkowski metric $\eta_{\mu\nu}$ plus some small perturbation $h_{\mu\nu}$

$$g_{\mu\nu} = \eta_{\mu\nu} + h_{\mu\nu}, \tag{2.10}$$

where we require that

$$|h_{\mu\nu}| \ll 1. \tag{2.11}$$

As we proceed, we will linearize Equation (2.9) to first order in $\mathbf{h}$. Note that

$$\begin{aligned} g^{\alpha\beta} &= g^{\alpha\mu} g^{\beta\nu} g_{\mu\nu} \\ &= g^{\alpha\mu} g^{\beta\nu} \left(\eta_{\mu\nu} + h_{\mu\nu}\right) \\ &= \eta^{\alpha\beta} + h^{\alpha\beta}. \end{aligned} \tag{2.12}$$

Moving forward, all raising and lowering operations will be performed using the Minkowski tensor $\boldsymbol{\eta}$ since the full metric tensor $\mathbf{g}$ will introduce non-factors of $\mathbf{h}$.

Additionally, note that since the metric tensor is symmetric, the perturbation is also symmetric, $h_{\mu\nu} = h_{\nu\mu}$.

We first determine the connection coefficients in this perturbative scheme by noting

$$\begin{aligned} g_{\mu\nu,\alpha} &= \eta_{\mu\nu,\alpha} + h_{\mu\nu,\alpha} \\ &= h_{\mu\nu,\alpha}. \end{aligned} \tag{2.13}$$

This means, the connection coefficients in Equation (2.3) to first order in h become

$$\begin{aligned} \Gamma^{\alpha}{}_{\mu\nu} &= \frac{1}{2}\left(\eta^{\alpha\beta} + h^{\alpha\beta}\right)\left(h_{\mu\beta,\nu} + h_{\nu\beta,\mu} - h_{\mu\nu,\beta}\right) \\ &\approx \frac{1}{2}\eta^{\alpha\beta}\left(h_{\mu\beta,\nu} + h_{\nu\beta,\mu} - h_{\mu\nu,\beta}\right) \\ &= \frac{1}{2}\left(h^{\alpha}{}_{\mu,\nu} + h^{\alpha}{}_{\nu,\mu} - h_{\mu\nu}{}^{,\alpha}\right) \end{aligned} \tag{2.14}$$

This means contractions of connection coefficients with other contraction coefficients will introduce nonlinear terms in $\mathbf{h}$

$$\Gamma^{\alpha}{}_{\sigma\beta}\Gamma^{\sigma}{}_{\mu\nu} \sim \mathcal{O}(h^2). \tag{2.15}$$

The Riemann tensor then becomes

$$\begin{aligned} R^{\alpha}{}_{\mu\beta\nu} &= \Gamma^{\alpha}{}_{\mu\nu,\beta} - \Gamma^{\alpha}{}_{\mu\beta,\nu} + \mathcal{O}(h^2) \\ &\approx \frac{1}{2}\left(h^{\alpha}{}_{\mu,\nu\beta} + h^{\alpha}{}_{\nu,\mu\beta} - h^{,\alpha}{}_{\mu\nu,\beta}\right) - \frac{1}{2}\left(h^{\alpha}{}_{\mu,\beta\nu} + h^{\alpha}{}_{\beta,\mu\nu} - h^{,\alpha}{}_{\mu\beta,\nu}\right) \\ &= \frac{1}{2}\left(h^{\alpha}{}_{\nu,\mu\beta} - h^{\alpha}{}_{\beta,\mu\nu} + h^{,\alpha}{}_{\mu\beta,\nu} - h^{,\alpha}{}_{\mu\nu,\beta}\right). \end{aligned} \tag{2.16}$$

As before, contracting the Riemann tensor yields the Ricci tensor

$$\begin{aligned} R_{\mu\nu} = R^{\alpha}{}_{\mu\alpha\nu} &\approx \frac{1}{2}\left(h^{\alpha}{}_{\nu,\mu\alpha} - h^{\alpha}{}_{\alpha,\mu\nu} + h^{,\alpha}{}_{\mu\alpha,\nu} - h^{,\alpha}{}_{\mu\nu,\alpha}\right) \\ &= \frac{1}{2}\left(\eta^{\alpha\beta}h{}_{\beta\nu,\mu\alpha} - h^{\alpha}{}_{\alpha,\mu\nu} + h^{,\alpha}{}_{\mu\alpha,\nu} - h^{,\alpha}{}_{\mu\nu,\alpha}\right) \\ &= \frac{1}{2}\left(h^{,\beta}{}_{\beta\nu,\mu} - h^{\alpha}{}_{\alpha,\mu\nu} + h^{,\alpha}{}_{\mu\alpha,\nu} - h^{,\alpha}{}_{\mu\nu,\alpha}\right) \\ &= \frac{1}{2}\left(-h^{,\alpha}{}_{\mu\nu,\alpha} + h^{,\alpha}{}_{\mu\alpha,\nu} + h^{,\alpha}{}_{\nu\alpha,\mu} - h_{,\mu\nu}\right) \end{aligned} \tag{2.17}$$

where in the last step we rearranged terms and introduced the trace of the perturbation as

$$h \equiv h^{\mu}{}_{\mu}. \tag{2.18}$$

Contracting the Ricci tensor yields the Ricci scalar

$$\begin{aligned} \eta^{\mu\nu}R_{\mu\nu} &\approx \frac{1}{2}\left(-\eta^{\mu\nu}h^{,\alpha}{}_{\mu\nu,\alpha} + \eta^{\mu\nu}h^{,\alpha}{}_{\mu\alpha,\nu} + \eta^{\mu\nu}h^{,\alpha}{}_{\nu\alpha,\mu} - \eta^{\mu\nu}h_{,\mu\nu}\right) \\ &= \frac{1}{2}\left(-h^{\mu}{}_{\mu,\alpha}{}^{,\alpha} + h_{\mu\alpha}{}^{,\mu\alpha} + h_{\nu\alpha}{}^{,\nu\alpha} - h^{,\mu}{}_{,\mu}\right) \\ &= \frac{1}{2}\left(-h^{,\alpha}{}_{,\alpha} + h_{\mu\nu}{}^{,\mu\nu} + h_{\mu\nu}{}^{,\mu\nu} - h^{,\alpha}{}_{,\alpha}\right) \\ &= -\Box h + h_{\mu\nu}{}^{,\mu\nu}, \end{aligned} \tag{2.19}$$

where we have introduced the d'Alembertian operator given by

$$\Box h \equiv h^{,\mu}{}_{,\mu} = \eta^{\mu\nu}\frac{\partial^2 h}{\partial x^{\mu}\partial x^{\nu}}. \tag{2.20}$$

The linearized Einstein tensor is now given by

$$\begin{aligned} G_{\mu\nu} &\approx \frac{1}{2}\left[-h^{,\alpha}{}_{\mu\nu,\alpha} + h^{,\alpha}{}_{\mu\alpha,\nu} + h^{,\alpha}{}_{\nu\alpha,\mu} - h_{,\mu\nu} - \eta_{\mu\nu}\left(-\Box h + h_{\alpha\beta}{}^{,\alpha\beta}\right)\right] \\ &= \frac{1}{2}\left[-\Box h_{\mu\nu} + h^{,\alpha}{}_{\mu\alpha,\nu} + h^{,\alpha}{}_{\nu\alpha,\mu} - h_{,\mu\nu} - \eta_{\mu\nu}\left(-\Box h + h_{\alpha\beta}{}^{,\alpha\beta}\right)\right], \end{aligned} \tag{2.21}$$

and Einstein's field equations are

$$-\Box h_{\mu\nu} + h^{,\alpha}{}_{\mu\alpha,\nu} + h^{,\alpha}{}_{\nu\alpha,\mu} - h_{,\mu\nu} - \eta_{\mu\nu}\left(-\Box h + h_{\alpha\beta}{}^{,\alpha\beta}\right) = 16\pi T_{\mu\nu}. \tag{2.22}$$

In order to simplify the field equations, we introduce a new perturbation given by

$$\psi_{\mu\nu} = h_{\mu\nu} - \frac{1}{2}\eta_{\mu\nu}h. \tag{2.23}$$

We see that the trace of the new perturbation becomes

$$\begin{aligned}\psi \equiv \eta^{\mu\nu}\psi_{\mu\nu} &= \eta^{\mu\nu}h_{\mu\nu} - \frac{1}{2}\eta^{\mu\nu}\eta_{\mu\nu}h \\ &= h - \frac{1}{2}(4)h \\ &= -h,\end{aligned} \tag{2.24}$$

where we have used that the trace of the Minkowski metric is $\eta^{\mu\nu}\eta_{\mu\nu} = 4$. We can then see that the original perturbation can be expressed as

$$h_{\mu\nu} = \psi_{\mu\nu} - \frac{1}{2}\eta_{\mu\nu}\psi. \tag{2.25}$$

Inserting Equation (2.25) into Equation (2.22), we can rewrite the field equations as

$$\begin{aligned}16\pi T_{\mu\nu} &= -\Box\left(\psi_{\mu\nu} - \frac{1}{2}\eta_{\mu\nu}\psi\right) + \psi^{,\alpha}{}_{\mu\alpha,\nu} - \frac{1}{2}\eta_{\mu\alpha}\psi^{,\alpha}{}_{,\nu} + \psi^{,\alpha}{}_{\nu\alpha,\mu} - \frac{1}{2}\eta_{\nu\alpha}\psi^{,\alpha}{}_{,\mu} + \psi_{,\mu\nu} \\ &\qquad - \eta_{\mu\nu}\left(\Box\psi + \psi_{\alpha\beta}{}^{,\alpha\beta} - \frac{1}{2}\eta_{\alpha\beta}\psi^{,\alpha\beta}\right) \\ &= -\Box\psi_{\mu\nu} + \frac{1}{2}\eta_{\mu\nu}\Box\psi + \psi^{,\alpha}{}_{\mu\alpha,\nu} - \frac{1}{2}\psi_{,\mu\nu} + \psi^{,\alpha}{}_{\nu\alpha,\mu} - \frac{1}{2}\psi_{,\mu\nu} + \psi_{,\mu\nu} \\ &\qquad - \eta_{\mu\nu}\left(\Box\psi + \psi_{\alpha\beta}{}^{,\alpha\beta} - \frac{1}{2}\eta_{\alpha\beta}\psi^{,\alpha\beta}\right) \\ &= -\Box\psi_{\mu\nu} + \frac{1}{2}\eta_{\mu\nu}\Box\psi + \psi^{,\alpha}{}_{\mu\alpha,\nu} + \psi^{,\alpha}{}_{\nu\alpha,\mu} - \eta_{\mu\nu}\left(\Box\psi + \psi_{\alpha\beta}{}^{,\alpha\beta} - \frac{1}{2}\Box\psi\right) \\ &= -\Box\psi_{\mu\nu} + \frac{1}{2}\eta_{\mu\nu}\Box\psi + \psi^{,\alpha}{}_{\mu\alpha,\nu} + \psi^{,\alpha}{}_{\nu\alpha,\mu} - \eta_{\mu\nu}\psi_{\alpha\beta}{}^{,\alpha\beta} - \frac{1}{2}\eta_{\mu\nu}\Box\psi,\end{aligned}$$

and obtain

$$-\Box\psi_{\mu\nu} + \psi^{,\alpha}{}_{\mu\alpha,\nu} + \psi^{,\alpha}{}_{\nu\alpha,\mu} - \eta_{\mu\nu}\psi_{\alpha\beta}{}^{,\alpha\beta} = 16\pi T_{\mu\nu}. \tag{2.26}$$

We can now specify a specific gauge to work in, and we choose the de Donder gauge, an analog of the Lorenz gauge, which requires

$$\psi_{\mu\nu}{}^{,\nu} = 0. \tag{2.27}$$

In this specified gauge, Equation (2.26) simplifies and the linearized field equations in the weak field limit reduce to

$$\Box\psi_{\mu\nu} = -\frac{16\pi G}{c^4}T_{\mu\nu}, \tag{2.28}$$

where we have inserted the appropriate powers of G and c to restore physical units. The form of Equation (2.28) is a wave equation for $\psi_{\mu\nu}$, with well known solutions determined by the retarded-time Green's function, which is found by imposing the boundary condition that there are no incoming gravitational waves. Thus, the solution to Equation (2.28) at time t and position $\mathbf{x} = \{x_1, x_2, x_3\}$ is

$$\psi_{\mu\nu}(t, \mathbf{x}) = \frac{4G}{c^4}\int \mathrm{d}^3\mathbf{x}' \frac{T_{\mu\nu}\left(t - \frac{|\mathbf{x}-\mathbf{x}'|}{c}, \mathbf{x}'\right)}{|\mathbf{x} - \mathbf{x}'|}. \tag{2.29}$$

2.1.2 Transverse-Traceless Gauge

We now introduce the gauge symmetry of general relativity in order to ultimately simplify the field equations. General relativity is invariant under coordinate transformations of the form

$$x^\mu \to x'^\mu \tag{2.30}$$

where x'^μ is some arbitrary function of x^μ that is invertible, differentiable, and has a differentiable inverse. Such coordinate transformations yield a metric function in the

new coordinates given by

$$g'_{\mu\nu} = \frac{\partial x^\lambda}{\partial x'^\mu}\frac{\partial x^\rho}{\partial x'^\nu} g_{\lambda\rho}. \tag{2.31}$$

The most general coordinate transform is to modify the coordinate x^μ by some arbitrary infinitesimal vector field,

$$x^\mu \to x'^\mu = x^\mu + \xi^\mu \tag{2.32}$$

where ξ^μ is a function of x^μ and the magnitude of the derivatives, $|\xi_{\mu,\nu}|$, are no larger than $|h_{\mu\nu}|$. Evaluating the metric in these new coordinates, and keeping only terms first order in both $\mathbf{h}$ and $\boldsymbol{\xi}$, we see

$$\begin{aligned} g'_{\mu\nu} &= \left(\delta^\lambda{}_\mu - \xi^\lambda{}_{,\mu}\right)\left(\delta^\rho{}_\nu - \xi^\rho{}_{,\nu}\right)\left(\eta_{\lambda\rho} + h_{\lambda\rho}\right) \\ &\approx \left(\delta^\lambda{}_\mu - \xi^\lambda{}_{,\mu}\right)\left(\eta_{\lambda\nu} + h_{\lambda\nu} - \xi_{\lambda,\nu}\right) \\ &\approx \eta_{\mu\nu} + h_{\mu\nu} - \xi_{\mu,\nu} - \xi_{\nu,\mu}, \end{aligned} \tag{2.33}$$

which means the metric perturbation in the new coordinate system is

$$h'_{\mu\nu} = h_{\mu\nu} - \xi_{\mu,\nu} - \xi_{\nu,\mu}. \tag{2.34}$$

The modified perturbation in the new coordinate system, $\boldsymbol{\psi}'$, is then

$$\begin{aligned} \psi'_{\mu\nu} &= h'_{\mu\nu} - \frac{1}{2}\eta_{\mu\nu}h' \\ &= h_{\mu\nu} - \xi_{\mu,\nu} - \xi_{\nu,\mu} - \frac{1}{2}\eta_{\mu\nu}\left(h - \xi^\alpha{}_{,\alpha} - \xi^\alpha{}_{,\alpha}\right) \\ &= h_{\mu\nu} - \frac{1}{2}\eta_{\mu\nu}h - \xi_{\mu,\nu} - \xi_{\nu,\mu} + \eta_{\mu\nu}\xi^\alpha{}_{,\alpha} \\ &= \psi_{\mu\nu} - \left(\xi_{\mu,\nu} + \xi_{\nu,\mu} - \eta_{\mu\nu}\xi^\alpha{}_{,\alpha}\right). \end{aligned} \tag{2.35}$$

Applying the Lorentz gauge in this new coordinate system, we take the divergence of Equation (2.35)

$$\begin{aligned}\psi'_{\mu\nu}{}^{,\nu} &= \psi_{\mu\nu}{}^{,\nu} - \left(\xi^{,\nu}{}_{\mu,\nu} + \xi^{,\nu}{}_{\nu,\mu} - \eta_{\mu\nu}\xi^{\alpha,\nu}{}_{,\alpha}\right) \\ &= \psi_{\mu\nu}{}^{,\nu} - \left(\Box\xi_\mu + \xi^{,\nu}{}_{\nu,\mu} - \xi^{,\alpha}{}_{\alpha,\mu}\right) \\ &= \psi_{\mu\nu}{}^{,\nu} - \Box\xi_\mu. \end{aligned} \tag{2.36}$$

Equation (2.36) shows that if the the Lorentz gauge condition is satisfied in the original coordinate system it is also satisfied for any general coordinate transformation for which

$$\Box\xi_\mu = 0. \tag{2.37}$$

Our symmetric metric perturbation originally has ten degrees of freedom, just as the general metric tensor does. By choosing the Lorentz gauge, we reduce the degrees of freedom to six. The general coordinate transform given by Equation (2.32) highlights a residual gauge freedom associated with the four functions ξ^μ. As long as the coordinate transform satisfies Equation (2.37), we have the freedom to choose these functions, and as they relate directly to $\psi^{\mu\nu}$ through equation (2.35) this means they can further constrain the metric perturbation. In particular, if we consider the perturbation far from the source, we have the vacuum wave equation given by

$$\Box\psi_{\mu\nu} = 0 \tag{2.38}$$

so that under a coordinate transformation we have

$$\Box\psi'_{\mu\nu} = \Box\psi_{\mu\nu} - \Box\xi_{\mu\nu} \tag{2.39}$$

where

$$\xi_{\mu\nu} = \xi_{\mu,\nu} + \xi_{\nu,\mu} - \eta_{\mu\nu}\xi^\alpha{}_{,\alpha}. \tag{2.40}$$

However, because the d'Alembertian operator commutes with differentiation, Equation (2.37) also means that

$$\Box\xi_{\mu\nu} = 0. \tag{2.41}$$

Thus, using the symmetric metric perturbation that satisfies the Lorentz condition and has six degrees of freedom, we can transform to a new coordinate system by subtracting some $\xi_{\mu\nu}$ term, which depend on the arbitrary functions ξ^{μ} as in Equation 2.35, that will constrain $h'_{\mu\nu}$ in some convenient way without violating the Lorentz constraint and still maintain the vacuum wave equation. To take advantage of this freedom, we will choose ξ_0 such that the trace of metric perturbation is zero

$$h' = 0. \tag{2.42}$$

For this case, we then have

$$\psi'_{\mu\nu} = h'_{\mu\nu}, \tag{2.43}$$

and we can further specify that the spatial components, ξ^i, constrain $h_{0i} = 0$. The Lorentz condition for $\mu = 0$ then requires

$$h'_{oi}{}^{,i} = h'_{00}{}^{,0} + h_{0i}{}^{,i} = 0. \tag{2.44}$$

With $h_{oi} = 0$, we then have that

$$h'_{00}{}^{,0} = 0. \tag{2.45}$$

This indicates that h'_{00} is constant in time, which means that it will not contribute to the time varying part of the gravitational wave. Thus, for the gravitational wave itself, we can treat $h_{00} = 0$ since it will not contribute dynamically to the wave.

The Lorentz gauge condition with the specification of ξ^{μ} such that $h' = 0$ and $h_{0\mu} = 0$ define the so called transverse traceless gauge. This gauge allows us to extract only the dynamic part of the metric perturbation. We summarize the conditions of

the transverse traceless gauge as

$$h^{\alpha}{}_{\alpha} = 0 \tag{2.46}$$

$$h_{0\mu} = 0 \tag{2.47}$$

$$h_{ij}{}^{,i} = 0 \tag{2.48}$$

where the last equation is the Lorentz condition when $h_{o\mu} = 0$. This gauge naturally extracts only the dynamic part of the metric perturbation, and thus is the appropriate gauge to consider when investigating gravitational waves.

2.1.3 Gravitational Waves with Sources

While Equations (2.46)–(2.48) define the transverse-traceless gauge, it is still necessary to determine the actual transverse-traceless components of the metric perturbation. Henceforth, we will denote transverse-traceless as TT, and use a superscript to specify when we are specifically in the TT gauge. We assume that the solution for the original metric perturbation far from the source will be a plane-wave solution of the form

$$h_{\mu\nu} = e_{\mu\nu}\exp(ik_{\lambda}x^{\lambda}), \tag{2.49}$$

where $e_{\mu\nu}$ is a symmetric and constant polarization tensor and k^{λ} is the four-wavevector given by

$$k^{\mu} = \left(\frac{\omega}{c}, k^{i}\right) \tag{2.50}$$

with ω as the angular frequency of the plane wave and k^{i} as the spatial wave vector. For such plane wave solutions, an arbitrary vector can be transformed to be transverse using the projection tensor

$$P_{ij} = \delta_{ij} - n_i n_j \tag{2.51}$$

with

$$n_i = \frac{k_i}{k} \tag{2.52}$$

as the spatial direction of propagation of the plane wave. Then the metric perturbation can be made transverse and traceless by applying the projection tensor as

$$h_{ij}^{\mathrm{TT}} = P^{a}{}_{i} P^{b}{}_{j} h_{ab} - P_{ij} \frac{1}{2} \left(P^{ab} h_{ab} \right) \tag{2.53}$$

where we have used $P^{a}{}_{j} P_{aj} = P_{ij}$ and $P^{a}{}_{a} = 2$.

For galactic CCSN generated gravitational waves, the sources are over $\mathcal{O}(1 \text{ kpc}) \approx \mathcal{O}(10^{16} \text{ km})$ away while the size of the sources, the area behind the shock of the CCSN, is typically no larger than $\mathcal{O}(10^{3} \text{ km})$. The right hand side of Equation (2.28) is integrated over the volume of the source so that $|\mathbf{x}'| \ll |\mathbf{x}|$. We can therefore approximate

$$|\mathbf{x} - \mathbf{x}'| \approx r - n_i x'^{i}, \tag{2.54}$$

where $r = |\mathbf{x}|$ and $n_i = \frac{1}{r} x_i$. Before inserting this approximation, we also note that far from the source the plane-wave approximation for the solution is well satisfied. Then, far from the source we can insert the approximation from Equation (2.54) into Equation (2.28), and we can find the TT components of ψ_{ij} as

$$\psi_{ij}^{\mathrm{TT}} = h_{ij}^{\mathrm{TT}} \approx \frac{4G}{c^4} \frac{1}{r} \left(P^{a}{}_{i} P^{b}{}_{j} - P_{ij} \frac{1}{2} P^{ab} \right) \int \mathrm{d}^3 \mathbf{x}' T_{ab}(t - (r - n_i x'^{i})/c, \mathbf{x}'), \tag{2.55}$$

where we have also used that $\psi_{ij}^{\mathrm{TT}} = h_{ij}^{\mathrm{TT}}$ in the TT gauge.

Note that we have not lost information about $T_{0\nu}$ as we can ultimately relate each component to T_{ij} through the conservation of energy and momentum

$$T^{\mu\nu}{}_{,\nu} = 0. \tag{2.56}$$

In equation 2.56, it is important to emphasize that this is true for the stress-energy tensor of the linearized theory. This means that there are no gravitational corrections to the motion of the source $T^{\mu\nu}$ itself. In other words, Equation (2.56) shows the conservation of energy and momentum in the case of special relativity, where $g_{\mu\nu} =$

$\eta_{\mu\nu}$. To recover energy and momentum conservation in the general sense, i.e., $T^{\mu\nu}{}_{;\nu} = 0$, the nonlinear terms that have been neglected in the derivation of the linearized theory need to be reinserted into the field equations.

We can expand the stress-energy tensor T_{ab} Equation (2.55) as a Taylor series about the point $(t - r/c, \mathbf{x}')$ as

$$T_{ab} = \sum_{m=0}^{\infty} \frac{\partial^m}{\partial t^m} T_{ab}(t - r/c, \mathbf{x}') \frac{(n_i x'^i)^m}{m!}. \tag{2.57}$$

In the limit that the typical velocity of the source, v, is much less than the speed of light c

$$\left| n_i x'^i \frac{\partial^m}{\partial t^m} T_{ab}(t - r/c, \mathbf{x}') \right| \lessapprox \left(\frac{v}{c}\right)^m \left| T_{ab}(t - r/c, \mathbf{x}') \right|, \tag{2.58}$$

and so we can view terms above $m = 0$ as $\mathcal{O}(v/c)^m$-order corrections to $T_{ij}(t - r/c, \mathbf{x}')$. In this slow-motion approximation, the metric perturbation at lowest order thus becomes

$$h_{ij}^{\mathrm{TT}} \approx \frac{4G}{c^4} \frac{1}{r} \left(P^a{}_i P^b{}_j - P_{ij} \frac{1}{2} P^{ab} \right) \int \mathrm{d}^3\mathbf{x}' T_{ab}(t - r/c, \mathbf{x}'). \tag{2.59}$$

We now derive a useful identity using the conservation of energy and momentum in the linearized theory. Consider the differentiation of the quantity $T^{\alpha\beta} x^\mu x^\nu$ with

respect to x^α and x^β,

$$\begin{aligned}
\left(T^{\alpha\beta}x^\mu x^\nu\right)_{,\alpha\beta} &= \left(\left(T^{\alpha\beta}x^\mu x^\nu\right)_{,\alpha}\right)_{,\beta} \\
&= \left(T^{\alpha\beta}{}_{,\alpha}\, x^\mu x^\nu + T^{\alpha\beta}x^\mu{}_{,\alpha}\, x^\nu + T^{\alpha\beta}x^\mu x^\nu{}_{,\alpha}\right)_{,\beta} \\
&= \left(T^{\alpha\beta}\delta^\mu{}_\alpha\, x^\nu + T^{\alpha\beta}x^\mu\delta^\nu{}_\alpha\right)_{,\beta} \\
&= \left(T^{\mu\beta}x^\nu + T^{\nu\beta}x^\mu\right)_{,\beta} \\
&= T^{\mu\beta}{}_{,\beta}\, x^\nu + T^{\mu\beta}x^\nu{}_{,\beta} + T^{\nu\beta}{}_{,\beta}\, x^\mu + T^{\nu\beta}x^\mu{}_{,\beta} \\
&= T^{\mu\beta}\delta^\nu{}_\beta + T^{\nu\beta}\delta^\mu{}_\beta \\
&= 2T^{\mu\nu}.
\end{aligned} \tag{2.60}$$

As this is true for all components of the stress-energy tensor, we can specify to the spatial components and we have

$$T^{ij} = \frac{1}{2}\left[\left(T^{00}x^ix^j\right)_{,00} + 2\left(T^{k0}x^ix^j\right)_{,k0} + \left(T^{kl}x^ix^j\right)_{,kl}\right]. \tag{2.61}$$

Rewriting Equation (2.59) we can obtain

$$h_{ij}^{\mathrm{TT}} \approx \frac{4G}{c^4}\frac{1}{r}\left(P^a{}_iP^b{}_j - P_{ij}\frac{1}{2}P^{ab}\right)\eta_{pa}\eta_{qb}\int \mathrm{d}^3\mathbf{x}'T^{pq}(t - r/c, \mathbf{x}'). \tag{2.62}$$

We can then express the spatial integral of the stress-energy tensor over the source volume, dropping the explicit time and spatial dependencies for convenience, as

$$\begin{aligned}\int \mathrm{d}^3\mathbf{x} T^{pq} &= \frac{1}{2}\left[\int \mathrm{d}^3\mathbf{x}' \left(T^{00}x'^p x'^q\right)_{,00}\right. \\ &\quad \left. + \int \mathrm{d}^3\mathbf{x}' \left(T^{k0}x'^p x'^q\right)_{,k0} + \int \mathrm{d}^3\mathbf{x}' \left(T^{kl}x'^p x'^q\right)_{,kl}\right] \qquad (2.63)\\ &= \frac{1}{2}\left[\int \mathrm{d}^3\mathbf{x}' \left(T^{00}x'^p x'^q\right)_{,00}\right. \\ &\quad \left. + \int \mathrm{d}\mathbf{S}'_k \left(T^{k0}x'^p x'^q\right)_{,0} + \int \mathrm{d}\mathbf{S}'_k \left(T^{kl}x'^p x'^q\right)_{,l}\right] \qquad (2.64)\\ &= \frac{1}{2}\int \mathrm{d}^3\mathbf{x}' \left(T^{00}x'^p x'^q\right)_{,00} \qquad (2.65)\end{aligned}$$

where from Equation (2.63) to (2.64) we used the divergence theorem to convert to surface integrals evaluated at the surface S' of the source (with the k subscript denoting the contraction with the unit vector normal to this surface), and in Equation (2.65) we used the fact that the stress-energy tensor vanishes at the surface of the source to eliminate both of these integrals.

We can now assume that $T^{00} \approx \rho$, with ρ as the rest mass of the source. This approximation is exact if the source is treated as a perfect Newtonian fluid. We then have that the gravitational wave is given by

$$\begin{aligned}h_{ij}^{\mathrm{TT}} &\approx \frac{2G}{c^4}\frac{1}{r}\left(P^a{}_i P^b{}_j - P_{ij}\frac{1}{2}P^{ab}\right)\eta_{pa}\eta_{qb}\int \mathrm{d}^3\mathbf{x}' \left(\rho x'^p x'^q\right)_{,00}\\ &= \frac{2G}{c^4}\frac{1}{r}\left(P^a{}_i P^b{}_j - P_{ij}\frac{1}{2}P^{ab}\right)\int \mathrm{d}^3\mathbf{x}' \left(\rho x'_a x'_b\right)_{,00}\\ &= \frac{2G}{c^4}\frac{1}{r}\left(P^a{}_i P^b{}_j - P_{ij}\frac{1}{2}P^{ab}\right) I_{ab,00}\\ &= \frac{2G}{c^4}\frac{1}{r} I^{\mathrm{TT}}_{ij,00} \qquad (2.66)\end{aligned}$$

where we have introduced the definition of the mass quadrupole moment as

$$I_{ij} = \int \mathrm{d}^3\mathbf{x}' \rho x'_a x'_b \qquad (2.67)$$

and applied the projection operators to get the transverse-traceless components. Using the notation that $\ddot{I} = I_{,00} = \partial_t \partial_t I$, we arrive at the quadrupole formula for gravitational wave emission as

$$h_{ij}^{\mathrm{TT}} = \frac{2G}{c^4}\frac{1}{r}\ddot{I}_{ij}^{\mathrm{TT}}\left(t - \frac{r}{c}\right) \tag{2.68}$$

2.1.4 Gravitational Wave Polarization

In the TT gauge, gravitational waves far from the source are well described as plane waves in the form of Equation (2.49). As a consequence of the TT gauge, our two degrees of freedom for the gravitational wave manifest in the polarization tensor $e_{\mu\nu}$. We can form a basis from this polarization so that any gravitational wave can be described by some linear combination of these basis polarizations.

In terms of the perturbation $\psi_{\mu\nu}$, the Lorentz gauge condition requires

$$\begin{aligned}
0 &= \psi^{\mu\nu}{}_{,\nu} \\
&= \left[e^{\mu\nu}\exp(ik_\lambda x^\lambda) - \frac{1}{2}\eta^{\mu\nu}e^{\alpha}{}_{\alpha}\exp(ik_\lambda x^\lambda)\right]_{,\nu} \\
&= ie^{\mu\nu}k_\lambda \delta^{\lambda}{}_{\nu}\exp(ik_\lambda x^\lambda) - \frac{1}{2}\eta^{\mu\nu}e^{\alpha}{}_{\alpha}k_\lambda\exp(ik_\lambda x^\lambda) \\
&= e^{\mu\nu}k_\nu - \frac{1}{2}e^{\alpha}{}_{\alpha}\eta^{\mu\nu}k_\nu \\
&= k_\nu e^{\mu\nu} - \frac{1}{2}k^\mu e^{\alpha}{}_{\alpha}.
\end{aligned} \tag{2.69}$$

Recall that k^μ is the four-wavevector given by Equation (2.50). If we assume that the infinitesimal coordinate change is of the form

$$\xi^\mu = ic^\mu \exp(ik_\lambda x^\lambda) \tag{2.70}$$

with c^μ as some constant vector, then the condition

$$\begin{aligned}
0 &= \Box\xi^\mu \\
&= \left(ic^\mu \exp(ik_\lambda x^\lambda)\right)^{,\nu}{}_{,\nu} \\
&= \left(-c^\mu k_\lambda \delta^\lambda{}_\nu \exp(ik_\lambda x^\lambda)\right)^{,\nu} \\
&= -ic^\mu k_\nu k_\lambda x^{\lambda,\nu} \exp(ik_\lambda x^\lambda) \\
&= -ic^\mu k_\nu k_\lambda \eta^{\alpha\nu} x^\lambda{}_{,\alpha} \exp(ik_\lambda x^\lambda) \\
&= -ic^\mu k_\nu \eta^{\alpha\nu} k_\lambda \delta^\lambda{}_\alpha \exp(ik_\lambda x^\lambda) \\
&= -ic^\mu k^\alpha k_\alpha \exp(ik_\lambda x^\lambda)
\end{aligned} \tag{2.71}$$

must also hold. For nontrivial solutions, we then have

$$k^\lambda k_\lambda = 0. \tag{2.72}$$

Applying this infinitesimal coordinate change, we also have

$$\begin{aligned}
h'_{\mu\nu} &= h_{\mu\nu} - \xi_{\mu,\nu} - \xi_{\nu,\mu} \\
e'_{\mu\nu}\exp(ik_\lambda x^\lambda) &= e_{\mu\nu}\exp(ik_\lambda x^\lambda) + c_\mu k_\lambda \delta^\lambda{}_\nu \exp(ik_\lambda x^\lambda) + c_\nu k_\lambda \delta^\lambda{}_\mu \exp(ik_\lambda x^\lambda) \\
e'_{\mu\nu} &= e_{\mu\nu} + c_\mu k_\nu + c_\nu k_\mu
\end{aligned} \tag{2.73}$$

for nontrivial solutions.

Now, consider the case of a gravitational wave traveling in the z-direction such that

$$k^1 = k^2 = 0 \tag{2.74}$$

$$k^0 = k^3 \equiv k > 0. \tag{2.75}$$

The TT gauge will enforce Equation (2.47), and so we should also have

$$e'_{00} = e'_{0i} = 0. \tag{2.76}$$

Using Equation (2.73) for the 00 component, we see

$$e'_{00} = e_{00} + 2k_0 c_0, \tag{2.77}$$

and noting that $k_0 = \eta^{0\mu} k_\mu = -k$ we can then solve for c_0 as

$$c_0 = \frac{e_{00}}{2k}. \tag{2.78}$$

In the same way, we can solve for c_i by requiring $e_{0i} = 0$, and we find

$$c_1 = \frac{e_{01}}{k} \tag{2.79}$$

$$c_2 = \frac{e_{02}}{k} \tag{2.80}$$

$$c_3 = \frac{e_{03} + kc_0}{k}. \tag{2.81}$$

As Equation (2.69) is invariant, we can apply it to the infinitesimal coordinate changed system so that

$$\begin{aligned} 0 &= k_\nu e'^{\mu\nu} - \frac{1}{2} k^\mu e'^{\alpha}{}_{\alpha} \\ &= k_\nu \eta^{\alpha\mu} \eta^{\beta\nu} e'_{\alpha\beta} - \frac{1}{2} \eta^{\alpha\mu} k_\alpha \eta^{\sigma\beta} e'_{\sigma\beta} \\ &= k^\beta e'_{\alpha\beta} - \frac{1}{2} k_\alpha \eta^{\sigma\beta} e'_{\sigma\beta} \\ &= k^0 e'_{\alpha 0} + k^3 e'_{\alpha 3} - \frac{1}{2} k_\alpha \left(-e'_{00} + e'_{11} + e'_{22} + e'_{33}\right). \end{aligned} \tag{2.82}$$

Using Equation (2.76), and noting $k^3 = k$, this simplifies to

$$k e'_{\alpha 3} - \frac{1}{2} k_\alpha \left(e'_{11} + e'_{22} + e'_{33}\right) = 0. \tag{2.83}$$

Then, for $\alpha = 0$ this gives

$$\begin{aligned} 0 &= ke'_{30} + \frac{1}{2}k\left(e'_{11} + e'_{22} + e'_{33}\right) \\ 0 &= k\left(e'_{11} + e'_{22} + e'_{33}\right) \\ 0 &= e'_{11} + e'_{22} + e'_{33}. \end{aligned} \tag{2.84}$$

Then, for the spatial components

$$\begin{aligned} 0 &= ke'_{3i} - \frac{1}{2}k_i\left(e'_{11} + e'_{22} + e'_{33}\right) \\ &= ke'_{3i} \\ &= e'_{3i}. \end{aligned} \tag{2.85}$$

This means that Equation (2.84) reduces to

$$e'_{11} + e'_{22} = 0, \tag{2.86}$$

and we this see that

$$e'_{\mu\nu} = \begin{pmatrix} 0 & 0 & 0 & 0 \\ 0 & e'_{11} & e'_{12} & 0 \\ 0 & e'_{12} & -e'_{11} & 0 \\ 0 & 0 & 0 & 0 \end{pmatrix}. \tag{2.87}$$

Using this polarization tensor, we then can define the gravitational wave in the TT gauge as

$$h_{ij}^{\mathrm{TT}} = \begin{pmatrix} h_+ & h_\times & 0 \\ h_\times & -h_+ & 0 \\ 0 & 0 & 0 \end{pmatrix} \tag{2.88}$$

with the gravitational wave strains defined as the polarizations h_+ and $h_\times$.

2.1.5 Gravitational Waves in CCSN

It is often more convenient, when working in spherical polar coordinates, to express quantities in terms of the scalar spherical harmonics $Y^{\ell m}$, which contain all the angular dependence in the ℓ and m superscripts. Note that this means ℓ and m are not components of a tensor. Where convenient for notation, ℓ and m will be used as both super- and subscripts, but they will never be used in this dissertation to denote a tensor component. In this notation, the mass quadrupole moment in the weak field limit can be expressed in terms of the complex conjugate scalar spherical harmonics, Y^*_{2m}, as

$$I_{2m} = \frac{16\sqrt{3}\pi}{15} \int \rho Y^*_{2m} r'^2 \mathrm{d}V' \tag{2.89}$$

with $\mathrm{d}V' = r'^2 \sin\theta \mathrm{d}r' \mathrm{d}\theta \mathrm{d}\varphi$ as the volume element. This notation is convenient so that we can expand the gravitational wave generated by a slow-motion source, far from the source, in terms of multipoles of the form (Thorne, 1980a)

$$h^{\mathrm{TT}}_{ij} = \frac{G}{c^4} \sum_{\ell=2}^{\infty} \sum_{m=-\ell}^{\ell} \frac{1}{r} \left(\frac{\mathrm{d}^\ell}{\mathrm{d}t^\ell} I^{\ell m} \left[t - \frac{r}{c} \right] T^{\mathrm{E2},\ell \mathrm{m}}_{ij} + \frac{\mathrm{d}^\ell}{\mathrm{d}t^\ell} S^{\ell m} \left[t - \frac{r}{c} \right] T^{\mathrm{B2},\ell \mathrm{m}}_{ij} \right), \tag{2.90}$$

where i and j now denote the spherical polar coordinates (r, θ, φ), $I^{\ell m}$ is the mass moment, $S^{\ell m}$ is the mass current, $T^{E2,\ell m}_{ij}$ and $T^{B2,\ell m}_{ij}$ are the transverse-traceless, pure-spin spherical harmonic tensors, $\frac{\mathrm{d}^\ell}{\mathrm{d}t^\ell}$ is the ℓ-th time derivative, and the (ℓm) superscripts denote the degree of the spherical harmonics contained within the definitions of these quantities. Note that we have dropped the TT superscript for all terms on the right hand side. The $E2$ superscript means the tensor spherical harmonic tensor has "electric-type parity" $\pi = (-1)^\ell$, and the $B2$ superscript means that the spherical tensor harmonic has "magnetic-type parity" $\pi = (-1)^{\ell+1}$.

We showed in Section 2.1.3 that the dominant contribution to the gravitational wave in this approximation is the quadrupole mass moment as seen in Equation (2.68). In the weak field limit, Thorne (1980a) quantifies that only contributions from the mass octupole and current quadrupole moments are larger than the intrinsic error

associated with our approximation for the mass quadrupole contribution. Thus, we are motivated to consider only the mass quadrupole moment in Equation (2.90).

The pure-spin tensor spherical harmonics of "electric-type parity", as worked out by Thorne (1980a), are given by

$$T_{ij}^{E_2,\ell m} = \frac{r^2}{2}\sqrt{2\frac{(\ell-2)!}{(\ell+2)!}}\left(2\nabla_i\nabla_j - \gamma_{ij}\nabla^2\right)Y^{\ell m}, \tag{2.91}$$

where $Y^{\ell m}$ are the scalar spherical harmonics and γ_{ij} is the Minkowski metric in spherical polar coordinates. For $\ell = 2$, the constant term becomes

$$\frac{1}{2}\sqrt{2\frac{0!}{4!}} = \frac{1}{4\sqrt{3}}. \tag{2.92}$$

The covariant derivative terms are

$$\nabla_i\nabla_j = \partial_i\partial_j - \Gamma_{ij}^k\partial_k \tag{2.93}$$

and the spherical polar Laplacian is

$$\nabla^2 = \partial_r^2 + \frac{1}{r^2}\left(\partial_\theta^2 + \cot\theta\partial_\theta + \frac{1}{\sin^2\theta}\partial_\varphi^2\right). \tag{2.94}$$

Then, we can determine each component of the spherical harmonic tensor by plugging in each index. For the tensor spherical harmonics to be transverse for a wave traveling in the $\hat{r}$ direction, we must have

$$T_{rj}^{E2,\ell m} = 0. \tag{2.95}$$

For the angular terms, note that the relevant connection coefficients are

$$\Gamma^{\theta}_{\theta\theta} = \Gamma^{\theta}_{\theta\varphi} = \Gamma^{\varphi}_{\theta\theta} = \Gamma^{\varphi}_{\varphi\varphi} = 0 \tag{2.96}$$

$$\Gamma^{\theta}_{\varphi\varphi} = -\sin\theta\cos\theta \tag{2.97}$$

$$\Gamma^{\varphi}_{\theta_{\varphi}} = \cot\theta. \tag{2.98}$$

The $\theta\theta$ term is then

$$\begin{aligned} T^{E2,2m}_{\theta\theta} &= \frac{r^2}{4\sqrt{3}}\left[2\left(\partial^2_\theta - \Gamma^{\theta}_{\theta\theta}\partial_\theta - \Gamma^{\varphi}_{\theta\theta}\partial_\varphi\right) - \gamma_{\theta\theta}\frac{1}{r^2}\left(\partial^2_\theta + \cot\theta\partial_\theta + \frac{1}{\sin^2\theta}\partial^2_\varphi\right)\right]Y^{2m} \\ &= \frac{r^2}{4\sqrt{3}}\left[2\partial^2_\theta - r^2\frac{1}{r^2}\left(\partial^2_\theta + \cot\theta\partial_\theta + \frac{1}{\sin^2\theta}\partial^2_\varphi\right)\right]Y^{2m} \qquad (2.99) \\ &= \frac{r^2}{4\sqrt{3}}\left(\partial^2_\theta - \cot\theta\partial_\theta - \frac{1}{\sin^2\theta}\partial^2_\varphi\right)Y^{2m}. \qquad (2.100) \end{aligned}$$

The symmetric $\theta\varphi$ terms are

$$\begin{aligned} T^{E2,2m}_{\theta\varphi} = T^{E2,2m}_{\varphi\theta} &= \frac{r^2}{4\sqrt{3}}\left[2\left(\partial_\theta\partial_\varphi - \Gamma^{\theta}_{\theta\varphi}\partial_\theta - \Gamma^{\varphi}_{\theta\varphi}\partial_\varphi\right) - \gamma_{\theta\phi}\nabla^2\right]Y^{2m} \qquad (2.101) \\ &= \frac{r^2}{4\sqrt{3}}\left(2\partial_\theta\partial_\varphi - 2\cot\theta\partial_\varphi\right)Y^{2m}. \qquad (2.102) \end{aligned}$$

Finally, the $\varphi\varphi$ term is

$$\begin{aligned} T^{E2,2m}_{\varphi\varphi} &= \frac{r^2}{4\sqrt{3}}\left[2\left(\partial^2_\varphi - \Gamma^{\theta}_{\varphi\varphi}\partial_\theta - \Gamma^{\varphi}_{\varphi\varphi}\partial_\varphi\right) - \gamma_{\varphi\varphi}\frac{1}{r^2}\left(\partial^2_\theta + \cot\theta\partial_\theta + \frac{1}{\sin^2\theta}\partial^2_\varphi\right)\right]Y^{2m} \\ &= \frac{r^2}{4\sqrt{3}}\left[2\partial^2_\varphi + 2\sin\theta\cos\theta\partial_\theta - r^2\sin^2\theta\frac{1}{r^2}\left(\partial^2_\theta + \cot\theta\partial_\theta + \frac{1}{\sin^2\theta}\partial^2_\varphi\right)\right]Y^{2m} \\ &= \frac{r^2}{4\sqrt{3}}\left(2\partial^2_\varphi + 2\sin\theta\cos\theta\partial_\theta - \sin^2\theta\partial^2_\theta - \sin\theta\cos\theta\partial_\theta - \partial^2_\varphi\right)Y^{2m} \\ &= \frac{r^2}{4\sqrt{3}}\left(\partial^2_\varphi + \sin\theta\cos\theta\partial_\theta - \sin^2\theta\partial^2_\theta\right)Y^{2m} \\ &= -\sin^2\theta\frac{r^2}{4\sqrt{3}}\left(\partial^2_\theta - \cot\theta\partial_\theta - \frac{1}{\sin^2\theta}\partial^2_\varphi\right)Y^{2m} \\ &= -\sin^2\theta T^{E2,2m}_{\theta\theta} \qquad (2.103) \end{aligned}$$

Combining Equations (2.100)–(2.103), we can define a new tensor matching the definition of Kotake et al. (2006) as

$$f_{ij}^{2m} \equiv \alpha r^2 \begin{pmatrix} 0 & 0 & 0 \\ 0 & W_{2m} & X_{2m} \\ 0 & X_{2m} & -\sin^2\theta W_{2m} \end{pmatrix} \tag{2.104}$$

with α as a normalization constant and,

$$X_{2m} \equiv 2\partial_\varphi \left(\partial_\theta - \cot\theta\right) Y_{2m}(\theta, \varphi) \tag{2.105}$$

$$W_{2m} \equiv \left(\partial_\theta^2 - \cot\theta\partial_\theta - \frac{1}{\sin^2\theta}\partial_\varphi^2\right) Y_{2m}(\theta, \varphi). \tag{2.106}$$

The quadrupole contribution to the gravitational wave can then be expressed as

$$h_{ij}^{\mathrm{TT}} = \frac{G}{c^4}\frac{1}{r}\sum_{m=-2}^{+2} \frac{d^2}{dt^2} I_{2m}\left(t - \frac{r}{c}\right) f_{ij}^{2m} \tag{2.107}$$

where the mass quadrupole is now expressed by Equation (2.89). The normalization constant α is the first term in Equation (2.91) for $\ell = 2$. This can also be determined by enforcing that

$$\int \mathrm{d}\Omega f_{ab}^{\ell m} f_{cd}^{*\ell' m'} \gamma^{ab}\gamma^{cd} = r^4 \delta^{\ell\ell'}\delta^{mm'} \tag{2.108}$$

for each Latin index running over (θ, φ) and γ_{ab} as the metric of the two-sphere

$$\gamma_{ab} = \begin{pmatrix} r^2 & 0 \\ 0 & r^2\sin^2\theta \end{pmatrix}. \tag{2.109}$$

In either case, the result for $\ell = 2$ is that

$$\alpha = \frac{1}{4\sqrt{3}} \tag{2.110}$$

Each of these terms in Equations (2.105) and (2.106) can be computed explicitly to arrive at the expressions in Appendix A.1 of Yakunin et al. (2015). For completeness, we include the explicit form of each of these terms below:

$$X_{2,2} = i\sqrt{\frac{15}{2\pi}}\sin\theta\cos\theta e^{2i\varphi} \tag{2.111}$$

$$X_{2,1} = i\sqrt{\frac{15}{2\pi}}\sin^2\theta e^{i\varphi} \tag{2.112}$$

$$X_{2,0} = 0 \tag{2.113}$$

$$X_{2,-1} = i\sqrt{\frac{15}{2\pi}}\sin^2\theta e^{-i\varphi} \tag{2.114}$$

$$X_{2,-2} = -i\sqrt{\frac{15}{2\pi}}\sin\theta\cos\theta e^{-2i\varphi} \tag{2.115}$$

$$W_{2,2} = \sqrt{\frac{15}{2\pi}}\frac{1+\cos^2\theta}{2}e^{2i\varphi} \tag{2.116}$$

$$W_{2,1} = \sqrt{\frac{15}{2\pi}}\sin\theta\cos\theta e^{i\varphi} \tag{2.117}$$

$$W_{2,0} = 3\sqrt{\frac{5}{4\pi}}\sin^2\theta \tag{2.118}$$

$$W_{2,-1} = -\sqrt{\frac{15}{2\pi}}\sin\theta\cos\theta e^{-i\varphi} \tag{2.119}$$

$$W_{2,-2} = \sqrt{\frac{15}{2\pi}}\frac{1+\cos^2\theta}{2}e^{-2i\varphi}. \tag{2.120}$$

From these, all f_{ij}^{2m} components can be calculated and we now need only consider the mass quadrupole moment.

In the continuum limit, taking the second time derivative of Equation (2.89) is not problematic. However, in the discretized domain of numerical differentiation, significant noise can be introduced to the calculation. For CCSN, this issue has been demonstrated for gravitational wave calculations in Mezzacappa et al. (2023). To avoid such numerical noise, we can follow the method outlined in Finn and Evans

(1990). Consider the first time derivative of the mass quadrupole

$$\begin{aligned}\frac{\mathrm{d}I_{2m}}{\mathrm{d}t} &= \partial_t \frac{16\sqrt{3}\pi}{15}\int \rho Y^*_{2m} r'^2 \mathrm{d}V \\ &= \frac{16\sqrt{3}\pi}{15}\int Y^*_{2m} r'^2 \partial_t \rho \mathrm{d}V \end{aligned} \tag{2.121}$$

where we can use the fluid continuity equation

$$\partial_t \rho + \nabla_i(\rho v^i) = 0 \tag{2.122}$$

so that

$$\frac{\mathrm{d}I_{2m}}{\mathrm{d}t} = -\frac{16\sqrt{3}\pi}{15}\int Y^*_{2m} r'^2 \nabla_i(\rho v^i)\mathrm{d}V \tag{2.123}$$

and using integration by parts

$$\begin{aligned}\frac{\mathrm{d}I_{2m}}{\mathrm{d}t} &= \frac{16\sqrt{3}\pi}{15}\left[\int \rho v^i \nabla_i \left(Y^*_{2m} r'^2\right) \mathrm{d}V - \int \nabla_i \left(\rho v^i Y^*_{2m} r'^2\right) \mathrm{d}V\right] \\ &= \frac{16\sqrt{3}\pi}{15}\left[\int \rho v^i \nabla_i \left(Y^*_{2m} r'^2\right) \mathrm{d}V \right. \\ &\qquad \left. - \int_0^{2\pi}\int_0^{\pi} Y^*_{2m} \sin\theta \left(r'^4 \rho v^r\right)|^{r=b}_{r=a} \mathrm{d}\theta \mathrm{d}\varphi\right], \end{aligned} \tag{2.124}$$

where we used the divergence theorem for the last term to arrive at Equation (2.124) with $r = a$ and $r = b$ as the inner and outer radial boundaries being considered respectively. We can then write the entire equation explicitly for these radial boundaries, using a and b as subscripts to denote at which boundary r should be evaluated

$$\begin{aligned}\frac{\mathrm{d}I_{2m}}{\mathrm{d}t} = \frac{16\sqrt{3}\pi}{15}\left[\int_0^{2\pi}\mathrm{d}\varphi\int_0^{\pi}\mathrm{d}\theta\int_a^b \mathrm{d}r' r'^3 \left(2\rho v^r Y^*_{2m}\sin\theta + \rho v^\theta \sin\theta \partial_\theta Y^*_{2m} + \rho v^\varphi \partial_\varphi Y^*_{2m}\right)\right. \\ \left. - \int_0^{2\pi}\mathrm{d}\varphi\int_0^{\pi}\mathrm{d}\theta Y^*_{2m}\sin\theta\left(r_b^4 \rho_b v_b^r - r_a^4 \rho_a v_a^r\right)\right]. \end{aligned} \tag{2.125}$$

We now define

$$N_{2m} \equiv \frac{G}{c^4}\frac{\mathrm{d}I_{2m}}{\mathrm{d}t} \tag{2.126}$$

where $\frac{\mathrm{d}I_{2m}}{\mathrm{d}t}$ is given by Equation (2.125). We can then further define

$$A_{2m} \equiv \frac{\mathrm{d}N_{2m}}{\mathrm{d}t^2}, \tag{2.127}$$

so that the gravitational wave is given by

$$h_{ij}^{\mathrm{TT}} = \frac{1}{r}\sum_{m=-2}^{2} A_{2m}\left(t - \frac{r}{c}\right) f_{ij}^{2m}. \tag{2.128}$$

Through the definitions of N_{2m} and A_{2m}, we can now compute the gravitational wave by performing only one numerical derivative, resulting in greater stability for the method. The term A_{2m} is commonly referred to as the amplitude of the gravitational wave, and moving forward we will refer to the gravitational wave h_{ij}^{TT} as the gravitational wave strain. Ultimately, we will compute the two polarizations of the gravitational wave strains as

$$h_{+} = \frac{h_{\theta\theta}}{r^2} \tag{2.129}$$

$$h_{\times} = \frac{h_{\theta\phi}}{r^2 \sin\theta}. \tag{2.130}$$

2.1.6 Gravitational Wave Spectrograms

This section is taken from text in Murphy et al. (2024).

Gravitational wave signals will frequently be converted to frequency space to create spectrograms. We produce spectrograms without detector noise from the gravitational wave strains through the use of the short-time Fourier transform (STFT) given by

$$S(\tau, f) = \int_{-\infty}^{\infty} h_{+}(t) w(t-\tau) e^{-i2\pi f t} dt, \tag{2.131}$$

with w being the analysis window of finite duration that captures the signal power centered around time τ and frequency f. The spectrogram is then given by

$$P(\tau, f) = \|S(\tau, f)\|^2. \tag{2.132}$$

For the spectrograms produced throughout this dissertation, we used a Kaiser windowing function given by

$$w(n) = \frac{I_0\left(\beta\sqrt{1-\left(\frac{2n}{N}-1\right)^2}\right)}{I_0(\beta)}, \tag{2.133}$$

for a window containing $N-1$ points, where I_0 is the zeroth-order modified Bessel function of the first kind. The shape factor, β, is a parameter that changes the equivalent noise bandwidth of the signal between the maximal case ($\beta = 0$) of a rectangular window and the minimal case ($\beta = 40$). Here, noise is introduced through processing the signal with the windowing function, and β is a way to mitigate the effect of this processing noise without completely changing the windowing scheme.

2.2 Perturbative Analysis

For our modal analysis, we linearize the Newtonian hydrodynamic equations following methods in Westernacher-Schneider (2020). We also work in the spherical coordinate basis $\{(\partial_r)^i, (\partial_\theta)^i, (\partial_\phi)^i\}$. For a Newtonian perfect fluid, the equations relating density, ρ, pressure, P, and gravitational potential, Φ, are given by

$$\partial_t \rho + \nabla_i(\rho v^i) = 0, \tag{2.134}$$

$$\partial_t(\rho v_i) + \nabla_j(\rho v^j v_i) + \partial_i P = -\rho \partial_i \Phi, \tag{2.135}$$

$$\nabla^2 \Phi = 4\pi\rho, \tag{2.136}$$

where ∂_μ denotes the partial derivative with respect to the μ component, ∇_i is the spatial covariant derivative, v is the fluid velocity, Latin indices represent spatial components, and repeated indices are summed over. We also use geometrized units, with $G = c = 1$.

We note that the results of Westernacher-Schneider (2020) and Zha et al. (2024) show good agreement between gravitational wave generation in pseudo-Newtonian core collapse supernova simulations and the eigenmodes computed from a purely Newtonian perturbative analysis. A true pseudo-Newtonian modal analysis would involve linearizing some equation of motion for the pseudo-Newtonian potential, instead of Equation (2.136). Considering a definition of the pseudo-Newtonian potential defined by Equation (53) in Rampp and Janka (2002), we can see that introducing this equation would require the linearization of several additional terms and, ultimately, greatly complicate the system of equations needed to describe linear perturbations. The implementation of a pseudo-Newtonian perturbative method may be important to consider, and will be useful in quantifying the accuracy of the Newtonian approach of Westernacher-Schneider (2020), but is beyond the scope of this thesis.

Our final equations are identical to those of Westernacher-Schneider (2020) and Zha et al. (2024). However, to facilitate reproducibility and use by others in any future studies, we wish to account for all assumptions and approximations made to arrive at these equations. To this end, we include in Subsections 2.2.1–2.2.3 a detailed derivation of the Newtonian modal analysis. In Subsection 2.2.4, we describe and justify the boundary conditions we use in our numerical implementation, and in Chapter 3, we outline the computational method we use to find the eigenfrequencies and eigenfunctions of the quasi-normal modes of oscillation of the PNS.

2.2.1 Linearized Equations

We linearize about a spherically-averaged time slice of our three-dimensional simulation data such that thermodynamic variables are replaced by

$$u \to u_0(r) + \delta u, \tag{2.137}$$

where $u_0(r)$ is the spherically-averaged-background (equilibrium) quantity and δu is the corresponding Eulerian perturbation. We note explicitly that because all background quantities are spherically averaged, they only have a radial dependence $\rho_0 = \rho_0(r)$, $P_0 = P_0(r)$, etc., while the perturbations contain, at this point, radial, polar, and azimuthal dependence. We assume that the background is in hydrostatic equilibrium, for which

$$v_0^i = 0. \tag{2.138}$$

Equation (2.135) for the background then becomes

$$\frac{\partial_r P_0}{\rho_0} = -\partial_r \Phi_0. \tag{2.139}$$

For simplicity, moving forward we drop the subscript, 0, for background equilibrium quantities, as well as the explicit radial dependence of all quantities.

Linearizing with respect to the Eulerian perturbations δU, the continuity equation given by Equation (2.134) is then written as

$$\partial_t(\rho + \delta\rho) + \nabla_i \left[(\rho + \delta\rho)(v^i + \delta v^i)\right] = 0, \tag{2.140}$$

which yields

$$\partial_t \delta\rho + \nabla(\rho\delta v^i + \delta\rho v^i + \delta\rho\delta v^i) = -\partial_t \rho - \nabla_i(\rho v^i). \tag{2.141}$$

The terms on the right-hand side sum to zero. They contain only background terms and satisfy Equation (2.134). Additionally, because $v^i = 0$ (the background fluid is assumed to be in hydrostatic equilibrium) and we only keep linear perturbative terms, the second two terms in the covariant derivative above are eliminated. We then have

$$\partial_t \delta\rho + \rho \nabla_i \delta v^i + \delta v^i \nabla_i \rho = 0. \tag{2.142}$$

Recall that for the flat 3-metric, γ_{ij}, the covariant derivative of a generic contravariant vector V^i is given by $\nabla_i V^i = \partial_i V^i + V^i \partial_i \ln\sqrt{\gamma}$, where γ is the determinant of the flat 3-metric and in spherical coordinates $\sqrt{\gamma} = r^2 \sin\theta$. Then,

$$\partial_t \delta\rho + \rho \partial_i \delta v^i + \rho \delta v^i \partial_i \ln\sqrt{\gamma} + \delta v^r \partial_r \rho = 0, \tag{2.143}$$

where we have also used the fact that $\rho = \rho(r)$. Therefore, $\nabla_i \rho = \partial_r \rho$ is the only nonzero derivative term.

We can relate the Eulerian velocity perturbation to the Eulerian fluid element displacement vector ξ^i by

$$\delta v^i = \partial_t \xi^i + v^j \nabla_j \xi^i - \xi^j \nabla_j v^i, \tag{2.144}$$

which reduces to $\delta v^i = \partial_t \xi^i$ when the background velocity is zero. Thus,

$$\partial_t \delta\rho + \rho \partial_i \partial_t \xi^i + \rho \partial_t \xi^i \partial_i \ln\sqrt{\gamma} + \partial_t \xi^r \partial_r \rho = 0. \tag{2.145}$$

Guided by Poisson and Will (2014), as done in Westernacher-Schneider (2020), we integrate this equation in time and set the integration constant to zero to obtain

$$\delta\rho + \rho \partial_i \xi^i + \rho \xi^i \partial_i \ln\sqrt{\gamma} + \xi^r \partial_r \rho = 0. \tag{2.146}$$

The momentum equation given in Equation (2.135) is rewritten by making the same substitutions. The first term is given by

$$\begin{aligned}\partial_t(\rho v_i) &\to \partial_t\left[(\rho+\delta\rho)(v_i+\delta v_i)\right] \\ &= \partial_t(\rho v_i) + \partial_t(\rho\delta v_i + \delta\rho v_i + \delta\rho\delta v_i) \\ &\approx \partial_t(\rho v_i) + \partial_t(\rho\delta v_i) \\ &= \partial_t(\rho v_i) + \partial_t(\rho\gamma_{ij}\delta v^j) \\ &= \partial_t(\rho v_i) + \rho\gamma_{ij}\partial_t\delta v^j + \gamma_{ij}\delta v^j\partial_t\rho. \end{aligned} \tag{2.147}$$

Given that the background fluid is in hydrostatic equilibrium with $v^i = 0$, Equation (2.134) results in $\partial_t\rho = 0$, as well. We then have

$$\partial_t(\rho v_i) \to \partial_t(\rho v_i) + \rho\gamma_{ij}\partial_t\delta v^j. \tag{2.148}$$

The second term in Equation (2.135) becomes

$$\begin{aligned}\nabla_j(\rho v^j v_i) &\to \nabla\left[(\rho+\delta\rho)(v^j+\delta v^j)(v_i+\delta v_i)\right] \\ &= \nabla_j(\rho v^j v_i) + \nabla_j(\rho v^j\delta v_i + \rho\delta v^j v_i + \rho\delta v^j\delta v_i) \\ &\quad + \nabla_j(\delta\rho v^j v_i + \delta\rho v^j\delta v_i + \delta\rho\delta v^j v_i + \delta\rho\delta v^j\delta v_i). \end{aligned} \tag{2.149}$$

Neglecting terms containing higher-order perturbations and using the fact that the background is static, we see that the second and third terms in Equation (2.149) vanish. The second term in Equation (2.135) thus contributes no new terms:

$$\nabla_j(\rho v^j v_i) \to \nabla_j(\rho v^j v_i). \tag{2.150}$$

The final terms in the momentum equation transform straightforwardly to

$$\begin{aligned}\partial_i P &\to \partial_i (P + \delta P) \\ &= \partial_i P + \partial_i \delta P \end{aligned} \tag{2.151}$$

and

$$\begin{aligned}-\rho \partial_i \Phi &\to -(\rho + \delta\rho)\partial_i(\Phi + \delta\Phi) \\ &= -\rho\partial_i\Phi - \delta\rho\partial_i\Phi - \rho\partial_i\delta\Phi - \delta\rho\partial_i\delta\Phi \\ &= -\rho\partial_i\Phi - \delta\rho\partial_i\Phi - \rho\partial_i\delta\Phi, \end{aligned} \tag{2.152}$$

where we have neglected terms higher-order in the perturbations.

Collecting the terms given by Equations (2.148)(2.150),(2.151), and (2.152), the momentum equation becomes

$$\left[\partial_t\ (\rho v_i) + \nabla_j(\rho v^j v_i) + \partial_i P + \rho\partial_i\Phi\right] + \rho\gamma_{ij}\partial_t\delta v^j + \partial_i\delta P = -\delta\rho\partial_i\Phi - \rho\partial_i\delta\Phi. \tag{2.153}$$

The term in square brackets contains only background terms, which satisfy Equation (2.135), and so it vanishes. We are thus left with

$$\rho\gamma_{ij}\partial_t\delta v^j + \partial_i\delta P = -\delta\rho\partial_i\Phi - \rho\partial_i\delta\Phi. \tag{2.154}$$

Expressing the velocity perturbation in terms of the fluid displacement vector, we have

$$\rho\gamma_{ij}\partial_t^2\xi^j + \partial_i\delta P = -\delta\rho\partial_i\Phi - \rho\partial_i\delta\Phi. \tag{2.155}$$

Finally, linearizing the Poisson equation, Equation (2.136), we find

$$\begin{aligned}\nabla^2\delta\Phi &= 4\pi\delta\rho - \nabla^2\Phi + 4\pi\rho \\ &= 4\pi\delta\rho, \end{aligned} \tag{2.156}$$

where the last equality follows because last two terms in the line above satisfy Equation (2.136) and vanish.

We can now specify that our perturbation is purely azimuthal, as has been done in past studies (Westernacher-Schneider, 2020; Morozova et al., 2018; Zha et al., 2024), and we can then split Equation (2.155) into separate radial and azimuthal equations. Using the components of the flat 3-metric in spherical coordinates and recalling that the background terms have only a radial dependence, we can rearrange Equations (2.146), (2.155), and (2.156) to arrive at the following linear system:

$$\delta\rho + \rho\partial_i\xi^i + \rho\xi^i\partial_i \ln\sqrt{\gamma} + \xi^r\partial_r\rho = 0, \tag{2.157}$$

$$\partial_t^2\xi^r + \frac{1}{\rho}\partial_r\delta P + \frac{\delta\rho}{\rho}\partial_r\Phi + \partial_r\delta\Phi = 0, \tag{2.158}$$

$$r^2\partial_t^2\xi^\theta + \frac{1}{\rho}\partial_\theta\delta P + \partial_\theta\delta\Phi = 0, \tag{2.159}$$

$$\nabla^2\delta\Phi - 4\pi\delta\rho = 0. \tag{2.160}$$

2.2.2 Assumption of Hydrostatic Equilibrium

Here, we make the distinction that our simulation data does not include the actual Newtonian potential Φ, but the pseudo-Newtonian effective potential. Since Equations (2.134) and (2.135) are satisfied in both the Newtonian and pseudo-Newtonian frameworks, we eventually intend to use the pseudo-Newtonian quantities for pressure and density. However, we know that Equation (2.136) is not satisfied for the pseudo-Newtonian effective potential of the simulation. For this reason, we will remove direct dependencies on the purely Newtonian potential Φ by using the hydrostatic condition of Equation (2.139) to replace it in terms of the density ρ and pressure P. While Equation (2.139) is not satisfied by the simulation data either, inside the PNS the condition is approximately satisfied.

Consistent with considerations of the energy-averaged neutrino mean free paths in our D15 and D25 models, we define the PNS surface in this analysis as the 10^{11}

g cm^{-3} density contour, with its associated radius as $R_{\rm PNS}$. Figure 2.1 shows how well the hydrostatic condition is satisfied within the PNS at different times, with the earliest time plotted determined by the start time of the HFF, as defined by Murphy et al. (2024).

We see that outside the convective region of D15 at the earliest times, the hydrostatic condition is satisfied to within ∼10%. For D15, the top panel of Figure 2.1 shows that, beyond the surface of the PNS, large deviations from hydrostatic equilibrium are observed, particularly at late times. Thus, within the PNS, to a good approximation we can assume hydrostatic equilibrium and rewrite Equation (2.158) as

$$\partial_t^2 \xi^r + \frac{1}{\rho}\partial_r \delta P - \frac{\delta\rho}{\rho^2}\partial_r P + \partial_r \delta\Phi = 0. \tag{2.161}$$

2.2.3 Linearized System Solutions

The linearized system given by Equations (2.157)–(2.160) can be solved using separation of variables by assuming Anzätze for the variables in the linear system:

$$\delta u = \delta\hat{u}(r) Y_\ell e^{-i\sigma t}, \tag{2.162}$$

$$\xi^r = \eta_r(r) Y_\ell e^{-i\sigma t}, \tag{2.163}$$

$$\xi^\theta = \frac{\eta_\perp(r)}{r^2}\partial_\theta Y_\ell e^{-i\sigma t}, \tag{2.164}$$

with u representing either ρ, P, or Φ, σ as the angular frequency, and Y_ℓ as the axisymmetric spherical harmonics (i.e., $m = 0$). In solving for the Eulerian displacement vector, we introduce the radial component of the amplitude of the displacement as η_r and the azimuthal component of the amplitude of the displacement as $\eta_\perp$. The angular frequency of the perturbation, σ, is related to the linear frequency, f, by $\sigma = 2\pi f$, with f given in units of Hz.

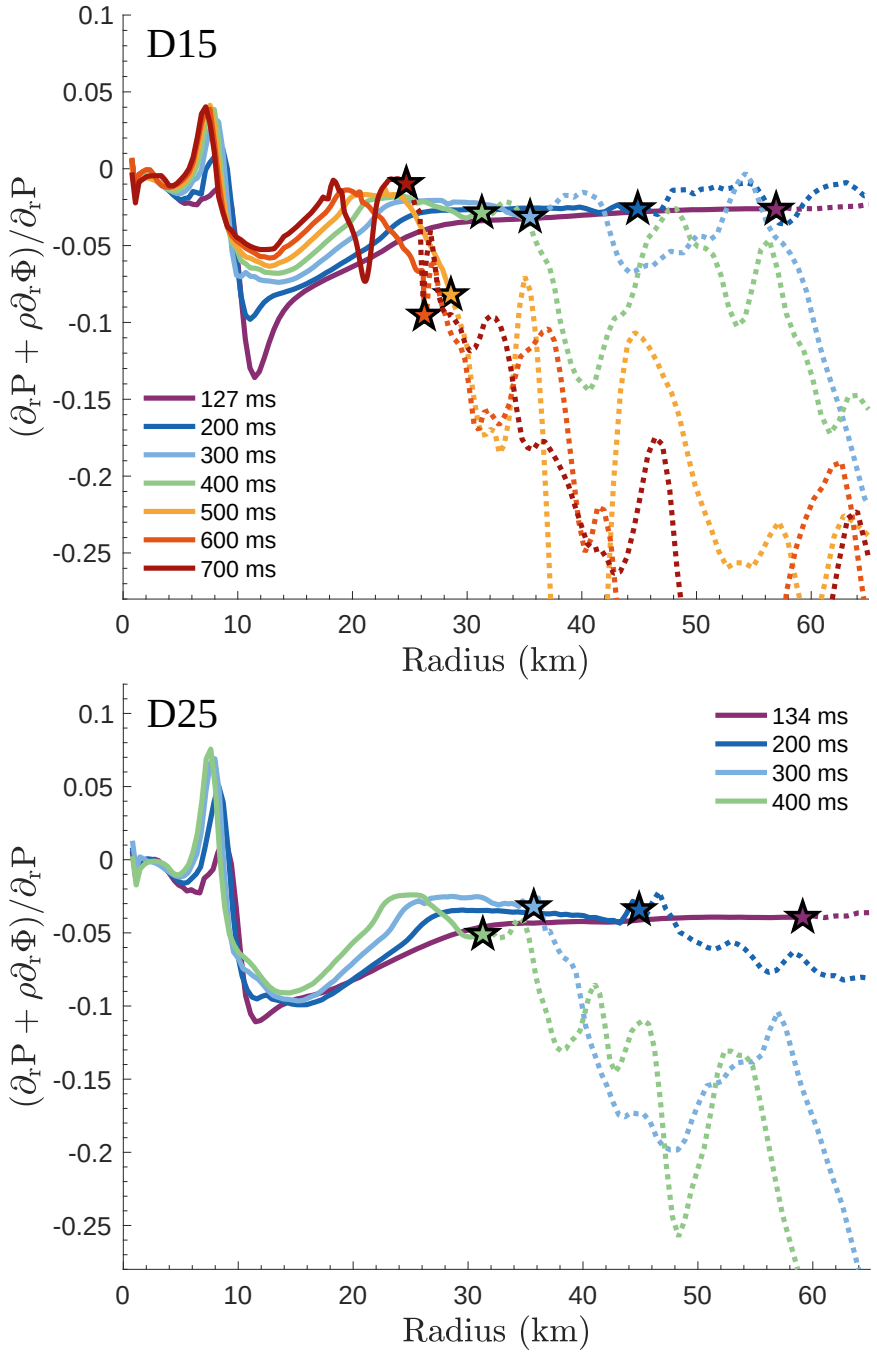


Figure 2.1: Hydrostatic equilibrium deviation for D15 (top) and D25 (bottom). The deviations, where $\partial_r P \neq -\rho\partial_r\Phi$, are plotted at different times differentiated by color. The star symbol indicates the surface of the PNS, defined as the 10^{11} g cm^{-3} density contour. The deviation from hydrostatic equilibrium outside the PNS surface is shown by dotted lines.

We can eliminate the dependence on δP by inserting these Anzäzte into Equation (2.159), to find

$$\begin{aligned} 0 &= r^2\partial_t^2\left(\frac{\eta_\perp}{r^2}\partial_\theta Y_\ell e^{-i\sigma t}\right) + \frac{1}{\rho}\partial_\theta\left(\delta\hat{\rho}Y_\ell e^{-i\sigma t}\right) + \partial_\theta\left(\delta\hat{\Phi}Y_\ell e^{-i\sigma t}\right) \\ &= -\sigma^2\eta_\perp e^{-i\sigma t}\partial_\theta Y_\ell + \frac{\delta\hat{P}}{\rho}e^{-i\sigma t}\partial_\theta Y_\ell + \delta\hat{\Phi}e^{-i\sigma t}\partial_\theta Y_\ell. \end{aligned} \tag{2.165}$$

For nontrivial solutions, the coefficients of $e^{-i\sigma t}\partial_\theta Y_\ell$ must satisfy

$$-\sigma^2\eta_\perp + \frac{1}{\rho}\delta\hat{P} + \delta\hat{\Phi} = 0. \tag{2.166}$$

Rearranging this equation, we thus find $\delta\hat{P}$ is determined by

$$\delta\hat{P} = \rho\left(\sigma^2\eta_\perp - \delta\hat{\Phi}\right). \tag{2.167}$$

As in all other modal analyses of the PNS, we assume the perturbations are adiabatic. Then

$$\frac{\Delta P}{\Delta\rho} = c_s^2, \tag{2.168}$$

where Δ designates a Lagrangian perturbation and c_s^2 is the square of the sound speed. The sound speed is related to the density and pressure by

$$c_s^2 = \frac{\Gamma_1 P}{\rho}, \tag{2.169}$$

with Γ_1 being the local adiabatic index. Lagrangian perturbations can be related to Eulerian perturbations through the Eulerian displacement vector:

$$\Delta u = \delta u + \xi^i\nabla_i u. \tag{2.170}$$

This leads to an additional elimination of the $\delta\hat{\rho}$ dependence. The adiabatic condition becomes

$$\frac{\delta P + \xi^i \partial_i P}{\delta\rho + \xi^i \partial_i \rho} = c_s^2, \tag{2.171}$$

which, due to the spherically-averaged background, reduces to

$$\delta\rho = \frac{1}{c_s^2}\delta P + \frac{1}{c_s^2}\xi^r \partial_r P - \xi^r \partial_r \rho. \tag{2.172}$$

Plugging in our Anzätze for $\delta\rho$, δP, and ξ^r, Equation (2.172) becomes

$$\delta\hat{\rho} Y_\ell e^{-i\sigma t} = \frac{1}{c_s^2}\delta\hat{P} Y_\ell e^{-i\sigma t} + \frac{1}{c_s^2}\eta_r Y_\ell e^{-i\sigma t}\partial_r P - \eta_r Y_\ell e^{-i\sigma t}\partial_r \rho, \tag{2.173}$$

and, for nontrivial solutions, $\delta\hat{\rho}$ must be determined by

$$\delta\hat{\rho} = \frac{1}{c_s^2}\delta\hat{P} + \frac{\eta_r}{c_s^2}\partial_r P - \eta_r \partial_r \rho. \tag{2.174}$$

Using Equation (2.167), and the definition of the sound speed, we then have

$$\begin{aligned}
\delta\hat{\rho} &= \frac{1}{c_s^2}\rho\left(\sigma^2\eta_\perp - \delta\hat{\Phi}\right) + \eta_r \frac{\rho}{\Gamma_1}\frac{\partial_r P}{P} - \eta_r \partial_r \rho \\
&= \rho\left(\frac{\sigma^2}{c_s^2}\eta_\perp - \frac{\delta\hat{\Phi}}{c_s^2} + \frac{\eta_r}{\Gamma_1}\frac{\partial_r P}{P} - \eta_r \frac{\partial_r \rho}{\rho}\right) \\
&= \rho\left(\frac{\sigma^2}{c_s^2}\eta_\perp - \frac{\delta\hat{\Phi}}{c_s^2} - \mathcal{B}\eta_r\right),
\end{aligned} \tag{2.175}$$

where we have introduced the Schwarzschild discriminant, defined as

$$\mathcal{B} = \partial_r \ln\rho - \frac{1}{\Gamma_1}\partial_r \ln P. \tag{2.176}$$

We can now insert our Anzätze into Equations (2.157), (2.158), and (2.160), and use Equations (2.167) and (2.175), to simplify our system of equations. For

Equation (2.157), we find

$$0 = \delta\hat{\rho}Y_\ell e^{-i\sigma t} + \rho\partial_r\left(\eta_r Y_\ell e^{-i\sigma t}\right) + \rho\partial_\theta\left(\frac{\eta_\perp}{r^2}\partial_\theta Y_\ell e^{-i\sigma t}\right) + \rho\eta_r Y_\ell e^{-i\sigma t}\partial_r \ln\sqrt{\gamma} + \rho\frac{\eta_\perp}{r^2}\partial_\theta Y_\ell e^{-i\sigma t}\partial_\theta \ln\sqrt{\gamma} + \eta_r Y_\ell e^{-i\sigma t}\partial_r\rho \tag{2.177}$$

and, evaluating $\partial_i \ln\sqrt{\gamma}$, explicitly

$$0 = \delta\hat{\rho}Y_\ell e^{-i\sigma t} + \rho Y_\ell e^{-i\sigma t}\partial_r\eta_r + \rho\frac{\eta_\perp}{r^2}e^{-i\sigma t}\partial_\theta^2 Y_\ell + \rho\eta_r Y_\ell e^{-i\sigma t}\frac{2}{r} + \rho\frac{\eta_\perp}{r^2}e^{-i\sigma t}\cot\theta\partial_\theta Y_\ell + \eta_r Y_\ell e^{-i\sigma t}\partial_r\rho. \tag{2.178}$$

We can use the identity

$$\partial_\theta^2 Y_\ell + \cot\theta\partial_\theta Y_\ell = -\ell(\ell+1)Y_\ell \tag{2.179}$$

for $\ell \neq 0$ to obtain

$$\begin{aligned} 0 &= \delta\hat{\rho}Y_\ell e^{-i\sigma t} + \rho Y_\ell e^{-i\sigma t}\partial_r\eta_r - \rho\frac{\eta_\perp}{r^2}Y_\ell e^{-i\sigma t}\ell(\ell+1) + \rho\eta_r Y_\ell e^{-i\sigma t}\left(\frac{2}{r} + \frac{\partial_r\rho}{\rho}\right) \\ &= \delta\hat{\rho} + \rho\partial_r\eta_r - \rho\eta_\perp\frac{\ell(\ell+1)}{r^2} + \rho\eta_r\left(\frac{2}{r} + \partial_r\ln\rho\right). \end{aligned} \tag{2.180}$$

Replacing $\delta\hat{\rho}$ with Equation (2.175) we see that

$$\begin{aligned} 0 &= \rho\left(\frac{\sigma^2}{c_s^2}\eta_\perp - \delta\hat{\Phi} - \mathcal{B}\eta_r\right) + \rho\partial_r\eta_r - \rho\eta_\perp\frac{\ell(\ell+1)}{r^2} + \rho\eta_r\left(\frac{2}{r} + \partial_r\ln\rho\right) \\ &= \partial_r\eta_r + \left(\frac{2}{r} + \partial_r\ln\rho - \mathcal{B}\right)\eta_r + \left(\frac{\sigma^2}{c_s^2} - \frac{\ell(\ell+1)}{r^2}\right)\eta_\perp - \frac{1}{c_s^2}\delta\hat{\Phi}. \end{aligned} \tag{2.181}$$

Using the definition of the Schwarzschild discriminant, we then have

$$\partial_r\eta_r + \left(\frac{2}{r} - \frac{1}{\Gamma_1}\partial_r\ln P\right)\eta_r + \left(\frac{\sigma^2}{c_s^2} - \frac{\ell(\ell+1)}{r^2}\right)\eta_\perp - \frac{1}{c_s^2}\delta\hat{\Phi} = 0. \tag{2.182}$$

For Equation (2.161), we find

$$\begin{aligned}
0 &= \partial_t^2 \left(\eta_r Y_\ell e^{-i\sigma t}\right) + \frac{1}{\rho}\partial_r \left(\delta\hat{P} Y_\ell e^{-i\sigma t}\right) - \frac{\partial_r P}{\rho^2}\delta\hat{\rho} Y_\ell e^{-i\sigma t} + \partial_r \left(\delta\hat{\Phi} Y_\ell e^{-i\sigma t}\right) \\
&= -\sigma^2 \eta_r Y_\ell e^{-i\sigma t} + \frac{1}{\rho} Y_\ell e^{-i\sigma t}\partial_r \delta\hat{P} - \frac{\partial_r P}{\rho^2}\delta\hat{\rho} Y_\ell e^{-i\sigma t} + Y_\ell e^{-i\sigma t}\partial_r \delta\hat{\Phi} \\
&= -\sigma^2 \eta_r + \frac{1}{\rho}\partial_r \delta\hat{P} - \frac{\partial_r P}{\rho^2}\delta\hat{\rho} + \partial_r \delta\hat{\Phi}. \qquad (2.183)
\end{aligned}$$

Using Equations (2.167) and (2.175), we can replace $\delta\hat{P}$ and $\delta\hat{\rho}$ so that

$$\begin{aligned}
0 &= -\sigma^2 \eta_r + \frac{1}{\rho}\partial_r \left[\rho\left(\sigma^2 \eta_\perp - \delta\hat{\Phi}\right)\right] - \frac{\partial_r P}{\rho}\left(\frac{\sigma^2}{c_s^2}\eta_\perp - \frac{\delta\hat{\Phi}}{c_s^2} - \mathcal{B}\eta_r\right) + \partial_r \delta\hat{\Phi} \\
&= -\sigma^2 \left(1 - \frac{\mathcal{B}\partial_r P}{\sigma^2 \rho}\right)\eta_r + \sigma^2 \partial_r \eta_\perp + \sigma^2 \left(\partial_r \ln\rho - \frac{\partial_r P}{\rho c_s^2}\right)\eta_\perp - \left(\partial_r \ln\rho - \frac{\partial_r P}{\rho c_s^2}\right)\delta\hat{\Phi}. \qquad (2.184)
\end{aligned}$$

Note that

$$\begin{aligned}
\partial_r \ln\rho - \frac{\partial_r P}{\rho c_s^2} &= \partial_r \ln\rho - \frac{\partial_r P}{\rho}\frac{\rho}{\Gamma_1 P} \\
&= \partial_r \ln\rho - \frac{1}{\Gamma_1}\partial_r \ln P \\
&= \mathcal{B}. \qquad (2.185)
\end{aligned}$$

We can define the gravitational acceleration as $\partial_r P/\rho = \tilde{G}$ and further define the Brunt-Väisälä frequency squared as $\tilde{G}\mathcal{B} = \mathcal{N}^2$. Thus, Equation (2.184) becomes

$$0 = -\sigma^2 \left(1 - \frac{\mathcal{N}^2}{\sigma^2}\right)\eta_r + \sigma^2 \partial_r \eta_\perp + \sigma^2 \mathcal{B}\eta_\perp - \mathcal{B}\delta\hat{\Phi}, \qquad (2.186)$$

and, rearranging terms, we have

$$\partial_r \eta_\perp - \left(1 - \frac{\mathcal{N}^2}{\sigma^2}\right)\eta_r + \mathcal{B}\eta_\perp - \frac{\mathcal{B}}{\sigma^2}\delta\hat{\Phi} = 0. \qquad (2.187)$$

The same procedure for Equation (2.160) yields

$$\begin{aligned} 0 &= \nabla^2 \left(\delta\hat{\Phi} Y_\ell e^{-i\sigma t} \right) - 4\pi \delta\hat{\rho} Y_\ell e^{-i\sigma t} \\ &= \nabla^2 \left(\delta\hat{\Phi} Y_\ell e^{-i\sigma t} \right) - 4\pi\rho \left(\frac{\sigma^2}{c_s^2}\eta_\perp - \frac{\delta\hat{\Phi}}{c_s^2} - \mathcal{B}\eta_r \right) Y_\ell e^{-i\sigma t}. \end{aligned} \tag{2.188}$$

The Laplacian can be evaluated as

$$\begin{aligned} \nabla^2 \left(\delta\hat{\Phi} Y_\ell e^{-i\sigma t} \right) &= \frac{1}{r^2} Y_\ell e^{-i\sigma t} \partial_r r^2 \partial_r \delta\hat{\Phi} + \frac{1}{r^2 \sin\theta} \delta\hat{\Phi} e^{-i\sigma t} \partial_\theta \sin\theta \partial_\theta Y_\ell \\ &= \left(\partial_r^2 \delta\hat{\Phi} + \frac{2}{r}\partial_r \delta\hat{\Phi} \right) Y_\ell e^{-i\sigma t} + \left(\frac{1}{r^2}\partial_\theta^2 Y_\ell + \frac{1}{r^2}\cot\theta \partial_\theta Y_\ell \right) \delta\hat{\Phi} e^{-i\sigma t} \\ &= \left(\partial_r^2 \delta\hat{\Phi} + \frac{2}{r}\partial_r \delta\hat{\Phi} \right) Y_\ell e^{-i\sigma t} - \ell(\ell+1)\frac{\delta\hat{\Phi}}{r^2} Y_\ell e^{-i\sigma t}, \end{aligned} \tag{2.189}$$

where the last step used the identity in Equation 2.179. Substituting Equation (2.189) for the Laplacian term in Equation (2.188), nontrivial solutions require that the coefficients of $Y_\ell e^{-i\sigma t}$ satisfy

$$\partial_r^2 \delta\hat{\Phi} + \frac{2}{r}\partial_r \delta\hat{\Phi} + \left(\frac{4\pi\rho}{c_s^2} - \frac{\ell(\ell+1)}{r^2} \right) \delta\hat{\Phi} + 4\pi\rho\mathcal{B}\eta_r - 4\pi\rho\frac{\sigma^2}{c_s^2}\eta_\perp = 0. \tag{2.190}$$

To keep our ultimate system of equations to first-order ordinary differential equations, we now define

$$F \equiv \partial_r \delta\hat{\Phi}. \tag{2.191}$$

Then, Equation (2.190) becomes

$$\partial_r F + \frac{2}{r}F + \left(\frac{4\pi\rho}{c_s^2} - \frac{\ell(\ell+1)}{r^2} \right) \delta\hat{\Phi} + 4\pi\rho\mathcal{B}\eta_r - 4\pi\rho\frac{\sigma^2}{c_s^2}\eta_\perp = 0. \tag{2.192}$$

We can rearrange Equations (2.182), (2.187), (2.191), and (2.192) to set up a system of ordinary differential equations in r that can be solved to determine the

perturbative quantities. We arrange the system such that

$$\partial_r \vec{u} = \mathbf{A}(\sigma, r, \rho, P, \Gamma_1)\vec{u}, \tag{2.193}$$

where

$$\vec{u} = (\delta\hat{\Phi}, F, \eta_r, \eta_\perp)^T \tag{2.194}$$

and

$$\mathbf{A} = \begin{bmatrix} 0 & 1 & 0 & 0 \\ \left(\frac{\ell(\ell+1)}{r^2} - \frac{4\pi\rho}{c_s^2}\right) & -\frac{2}{r} & -4\pi\rho\mathcal{B} & 4\pi\rho\frac{\sigma^2}{c_s^2} \\ \frac{1}{c_s^2} & 0 & \left(\frac{\partial_r \ln P}{\Gamma_1} - \frac{2}{r}\right) & \left(\frac{\ell(\ell+1)}{r^2} - \frac{\sigma^2}{c_s^2}\right) \\ \frac{\mathcal{B}}{\sigma^2} & 0 & \left(1 - \frac{\mathcal{N}^2}{\sigma^2}\right) & -\mathcal{B} \end{bmatrix}. \tag{2.195}$$

This system of equations assumes that $\ell \neq 0$ and that $\partial_r P/\rho = -\Phi$, as described in the derivation.

2.2.4 Boundary Conditions

We can solve this system by integrating along r and enforcing boundary conditions. The inner boundary conditions are found by imposing regularity conditions at the origin (Hurley et al., 1966), as derived in Westernacher-Schneider (2020) for the Newtonian perturbative equations we are using here. They are:

$$\eta_r(r_0) = A_0 r_0^{\ell-1}, \tag{2.196}$$

$$\eta_\perp(r_0) = \frac{A_0}{\ell} r_0^{\ell}, \tag{2.197}$$

$$\delta\hat{\Phi}(r_0) = C_0 r_0^{\ell}, \tag{2.198}$$

$$\partial_r \delta\hat{\Phi}(r_0) = \ell C_0 r_0^{\ell-1}, \tag{2.199}$$

where r_0 is the inner boundary, A_0 is an arbitrary amplitude taken to be 10^{-5} for our analysis, as in Westernacher-Schneider (2020), and C_0 is found by using a root-finding

method to evaluate

$$\left(\partial_r \delta\hat{\Phi} + \frac{\ell(\ell+1)}{r}\delta\hat{\Phi}\right)\Big|_{R_{\rm PNS}} = 0, \tag{2.200}$$

with $R_{\rm PNS}$ being the radius of the surface of the PNS. Equation (2.200) is equivalent to Equation (A10) of Westernacher-Schneider (2020), and we use it instead of Equation (A12). As noted by Westernacher-Schneider, the rest mass perturbations $\delta\hat{\rho}$ that escape through $R_{\rm PNS}$ are of small amplitude and mainly leak into different harmonics. Therefore, such perturbations can be ignored. We confirm that using Equation (A12) does not yield appreciable differences relative to the results obtained when using Equation (2.200). For the outer boundary condition, we require the Lagrangian pressure perturbation to vanish:

$$\Delta P|_{R_{\rm PNS}} = \left(\rho\sigma^2\eta_\perp - \rho\delta\hat{\Phi} + \eta_r\partial_r P\right)\Big|_{R_{\rm PNS}} = 0, \tag{2.201}$$

corresponding to a free surface. This boundary condition, or the relativistic counterpart, is also used in Morozova et al. (2018); Sotani et al. (2019); Sotani and Takiwaki (2020a); Mori et al. (2023); Wolfe et al. (2023); Zha et al. (2024), with varying definitions of the PNS surface. Figure 2.1 shows that hydrostatic equilibrium below the PNS surface, *i.e.* the 10^{11} g cm^{-3} density contour, is approximately satisfied. We do not implement the vanishing radial perturbation amplitude at the shock as a boundary condition, as done in Torres-Forné et al. (2018, 2019b), given that the region around the shock is far outside of hydrostatic equilibrium. As noted in Chapter 1.5.1, the CHIMERA code enforces spherical symmetry within the first ∼8 km of the origin. Consistent with this treatment, the inner boundary of our modal analysis is set to be just outside the radius of this spherically symmetric region. Thus, the eigenfunctions η_r and $\eta_\perp$ extend below the convective region of the PNS, but not all the way to the origin.

Chapter 3

Computational Development

The main component of the modal analysis code involves solving the system of Equations (2.193). This is accomplished by using a trapezoid integrating method for solving ordinary differential equations. First, create an equally spaced radial grid for the unperturbed background $(r, \rho(r), P(r), \Gamma_1(r))$. Then, consider the integral of Equations (2.193) from the point n to $n+1$

$$\int_n^{n+1} \partial_r \vec{u} \mathrm{d}r = \int_n^{n+1} \mathbf{A}\vec{u} \mathrm{d}r \tag{3.1}$$

$$\vec{u}(r_{n+1}) - \vec{u}(r_n) = \frac{dr}{2} \left(\mathbf{A}(r_n)\vec{u}(r_n) + \mathbf{A}(r_{n+1})\vec{u}(r_{n+1}) \right), \tag{3.2}$$

where we have integrated the left hand side using the fundamental theorem of calculus, and the right hand side has been integrated using the trapezoid rule with a width of dr. Introducing n subscripts to denote quantities at $r = r_n$, we then have

$$\left(\frac{2}{dr}\mathbb{I} - \mathbf{A}_{n+1} \right) \vec{u}_{n+1} = \left(\frac{2}{dr}\mathbb{I} + \mathbf{A}_n \right) \vec{u}_n, \tag{3.3}$$

where $\mathbb{I}$ is the 4×4 identity matrix. Recall that $u(r) = \left(\delta\hat{\Phi}, F, \eta_r, \eta_\perp\right)^T$ from Equation (2.194), so that this system of equations is 4×4. Then,

$$\vec{u}_{n+1} = \left(\frac{2}{dr}\mathbb{I} - \mathbf{A}_{n+1}\right)^{-1}\left(\frac{2}{dr}\mathbb{I} + \mathbf{A}_n\right)\vec{u}_n. \tag{3.4}$$

This means that if we have inner boundary conditions, we can integrate from r_0 to the outer boundary of the system by using Equation (3.4) successively, with each application requiring the inversion of the matrix $(2/dr\mathbb{I} - \mathbf{A}_{n+1})$.

The solutions to Equations (2.193) are the angular frequencies $\sigma = 2\pi f$, where f is the linear frequency in Hz, of the non-radial, quasi-normal modes of oscillation. Each frequency can be found by applying a root solving method to satisfy the boundary condition of Equation (2.201). To bound the root, an array of frequencies can be input into Equation (2.193) and integrated to $R_{\rm PNS}$ by Equation (3.4). After computing Equation (2.201) for each frequency, those frequencies for which the sign of the computation changes can be input into a root finding method to determine the frequency that satisfies Equation (2.201). To accurately integrate out to $R_{\rm PNS}$, the inner boundary conditions of Equations (2.196)–(2.199) must be applied, where C_0 is determined by a root finding method on Equation (2.200). Thus, there is a nested root solve to determine C_0 contained within each frequency root solve.

3.1 Numerical Scheme

The general method to solve Equations (2.193) can now be summarized:

1. Preset some frequency array σ' spanning the range in which we expect to find roots that satisfy Equation (2.201).

    (a) The root finding will not guarantee all roots are found. Therefore, it is important to have frequency resolution within this array fine enough

to capture adjacent eigenfrequencies that may be within ∼10 Hz of each other.

2. Read in spherically-averaged, hydrodynamic and thermodynamic variables for the entire radial grid.
   (a) Compute derivatives of ρ and P using fourth-order finite differencing.
   (b) Interpolate all background quantities onto a uniformly-spaced grid from r_0 to $R_{\rm PNS}$, using cubic splines.
3. For each frequency:
   (a) Preset some array of C_0'.
      i. Ensure sufficient resolution to capture the root.
   (b) Set inner boundary conditions using Equations (2.196) and (2.197).
   (c) Integrate Equation (2.193) to $R_{\rm PNS}$ using Equation (3.4).
   (d) Using values of C_0' that bound Equation (2.200), determine the proper C_0 via the bisection method.
   (e) Use C_0 to set inner boundary conditions using Equations (2.198) and (2.199).
   (f) Integrate Equation (2.193) to the surface of the PNS using Equation (3.4)..
4. Using values of σ' that bound the root of Equation (2.201), employ the bisection method to determine σ.
   (a) Repeat step 3 for the new bounding frequency found at each step of the bisection method.

3.2 Testing Modal Analysis

To test the computational method, we demonstrate the accuracy of the method in determining the quasi-normal oscillation modes of a Newtonian self-gravitating

polytropic star. The structure of such a star can be expressed using the Lane-Emden equation as

$$\frac{1}{\xi^2}\frac{\mathrm{d}}{\mathrm{d}\xi}\left(\xi^2\frac{\mathrm{d}\theta}{\mathrm{d}\xi}\right) = -\theta^n \tag{3.5}$$

where θ and ξ are dimensionless variables defined in terms of the radius r, density ρ, and pressure P of the star as

$$\rho = \rho_c\theta^n \tag{3.6}$$

$$P = P_c\theta^{n+1} \tag{3.7}$$

$$r = \alpha\xi. \tag{3.8}$$

The variable θ is known as the "polytropic temperature," ρ_c is the central density, P_c is the central pressure, and α is a length constant defined as

$$\alpha^2 \equiv \frac{\kappa(n+1)\rho_c^{\frac{1-n}{n}}}{4\pi G}. \tag{3.9}$$

These equations assume a polytropic relation between pressure and density of the form

$$P = \kappa\rho^{1+\frac{1}{n}}, \tag{3.10}$$

where κ and n are real, positive constants and n is known as the polytropic index.

The solutions describing stellar structure through the Lane-Emden equation are well known. For a three-dimensional, spherical self gravitating polytropic star, the exact numerical solution for the dimensionless structure is given by Horedt (2004) in Table 3.1, where $\theta' = \frac{\mathrm{d}\theta}{\mathrm{d}\xi}$. The constant κ is ultimately related to the mass M and radius R of the star as

$$\kappa = -R^{\frac{3-n}{n}}M^{\frac{n-1}{n}}\frac{(4\pi)^{\frac{1}{n}}}{n+1}\left[\left(\xi^2\frac{\mathrm{d}\theta}{\mathrm{d}\xi}\right)\Big|_{\xi=\xi_R}\right]^{\frac{1-n}{n}}\xi_R^{\frac{n-3}{n}}, \tag{3.11}$$

where ξ_R is the value of ξ at the outer radius of the star (i.e., the value in the final

Table 3.1: Dimensionless structure variables for a Newtonian, self-gravitating star with polytropic index $n = 1.5$.

ξ	θ	θ'	θ^{n+1}
0.00000000E+00	1.00000000E+00	0.00000000E+00	1.00000000E+00
1.00000000E-01	9.98334600E-01	-3.32833700E-02	9.95841700E-01
5.00000000E-01	9.59103900E-01	-1.60544900E-01	9.00874100E-01
1.00000000E+00	8.45169800E-01	-2.87255500E-01	6.56689200E-01
3.00000000E+00	1.58857600E-01	-2.84252700E-01	1.00582000E-02
3.60000000E+00	1.10909900E-02	-2.09392700E-01	1.29546700E-05
3.65000000E+00	7.63924200E-04	-2.03719600E-01	1.61296800E-08
3.65375374E+00	0.00000000E+00	-2.03301300E-01	0.00000000E+00

row of Table 3.1). Note that we use geometrized units ($G = c = 1$), so that additional factors of G and c need to be added to make the ultimate expression dimensionless. Then the central density becomes

$$\rho_c = \left[\frac{(n+1)\kappa}{4\pi\alpha^2}\right]^{\frac{n}{n-1}}, \tag{3.12}$$

and the central pressure can be found by plugging ρ_c into Equation (3.10).

As is done by Westernacher-Schneider (2020), we can use this as a background solution for the perturbative analysis derived in Chapter 2.2 to investigate the accuracy of our computational methods. Note that Westernacher-Schneider (2020) use the notation

$$P = \kappa\rho^{\Gamma}, \tag{3.13}$$

so that $n = 1.5$ corresponds to $\Gamma = 5/3$. If we set the stellar mass to 1.4 $M_\odot$ and the radius to 12 km, κ can be determined by Equation (3.11), and the mode frequencies will be $\gtrsim$2 kHz. The numerical solution from Horedt (2004) is rigorous, and used as our fiducial solution to test our accuracy. The dimensionless eigenfrequencies are given by

$$\omega^2 = \frac{\sigma^2}{4\pi\rho_c}, \tag{3.14}$$

and the numerical solution from Horedt (2004) is presented in Table 3.2.

Table 3.2: Quasi-normal oscillation mode frequencies for $n = 1.5$ polytropic star as determined numerically in Horedt (2004).

Mode	ω^2	f [Hz]
${}^2p_6$	6.71	18123
${}^2p_5$	5.00	15644
${}^2p_4$	3.53	13145
${}^2p_3$	2.30	10610
${}^2p_2$	1.31	8007.6
${}^2p_1$	0.572	5291.3
${}^2f$	0.118	2403.3

Presetting the frequency range over which we search determines the resolution of the method. Choosing 100 frequencies equally spaced between 2-20 kHz ensured sufficient resolution for this test problem. The C_0 array range was $\pm 10^{-5}$. Figure 3.1 shows the dimensionless eigenfrequencies calculated from the perturbative analysis method described at the beginning of this chapter, where the background has been interpolated to an equally spaced grid of 2048 cells using cubic splines. These dimensionless eigenfrequencies are compared to those found in Horedt (2004). The horizontal axis represents the radial overtone value of the oscillation mode. The ${}^2f$-mode is a fundamental mode, and each ${}^2p_n$-mode is an n-overtone of the fundamental frequency. The greatest residual, $\frac{|\omega_{\text{Horedt}} - \omega|}{\omega_{\text{Horedt}}} \times 100\%$, is $\sim$2%, showing excellent agreement with the numerical treatment presented in Horedt (2004). This is comparable to the percent residuals reported in Westernacher-Schneider (2020). As our method is based upon a second-order trapezoidal integration method, we should expect close to second-order convergence. In Figure 3.2, the L_2-norm as a function of number of radial cells is plotted as black asterisks. A line showing first-order convergence is plotted in dark-blue, and a line showing second-order convergence is plotted in pale-red. At the resolution achieved at $\sim$256 radial cells, an error term not associated with the integration method begins to dominate. It is suspected that this is particular to the polytropic star, with a sharp, well defined surface at R =12 km. For the contracting PNS within a CCSNe, the surface is less sharply defined, and, as

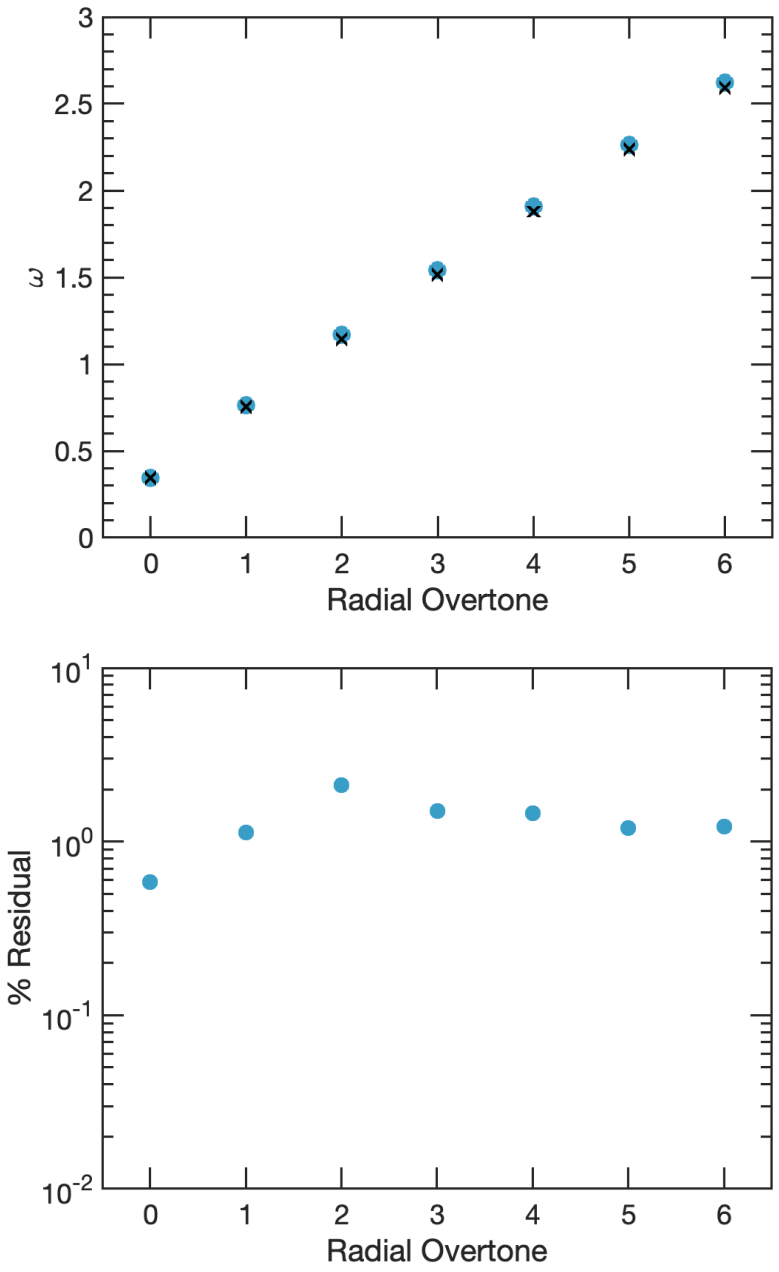


Figure 3.1: Eigenfrequencies and percent residuals for $n = 1.5$ polytropic star. Top: Dimensionless eigenfrequencies for self-gravitating Newtonian polytropic star, as compared to solutions in Horedt (2004). Bottom: Percent residual between our numerical method with 2048 radial cells and Horedt (2004) eigenfrequencies.

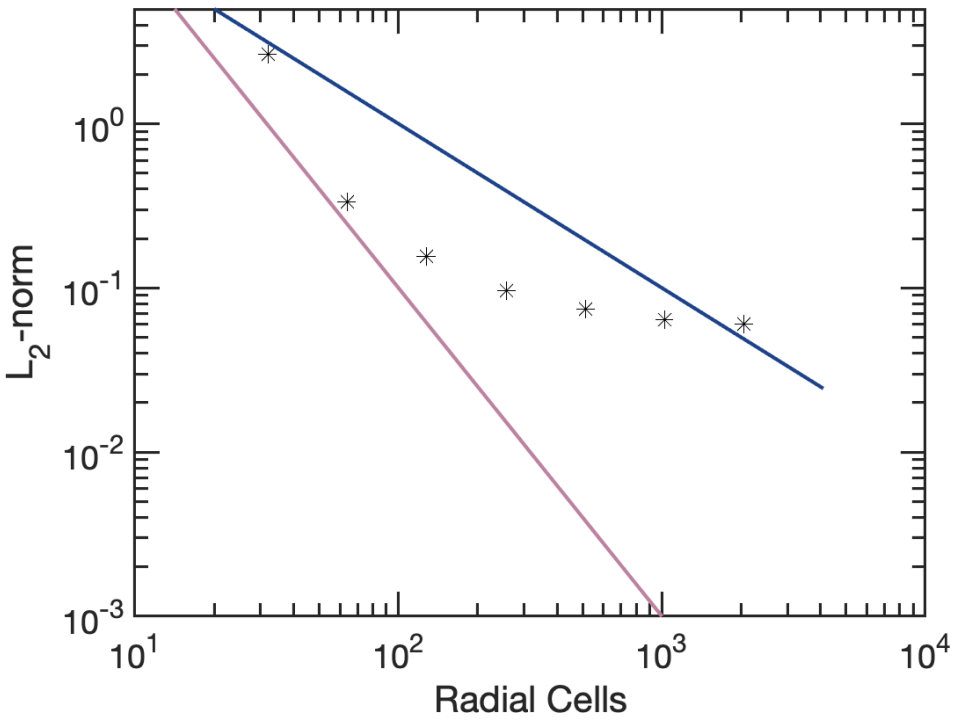


Figure 3.2: L_2-norm as a function of number of radial cells.

pointed out by Westernacher-Schneider (2020), we expect the amplitude of the quasi-normal oscillations to be dampened quickly outside the PNS surface. Nonetheless, this result prompts the consideration of different boundary conditions when applying the perturbative analysis to CHIMERA data in Chapter 4.5.

Chapter 4

Gravitational Wave Analysis for 3D CCSN Simulations

The work described in this section has been submitted to Physical Review D. as "Gravitational Waves as a Probe of Core Collapse Supernova Progenitor Structure." Full citation: Murphy et al. (2025b). The text has been edited, where necessary, to conform to the citation style of this dissertation and to reference sections within this dissertation instead of the original manuscript. Sections from the manuscript that have already been covered in this dissertation have been removed here. In addition to the contents of the submitted paper, Section 4.4 presents the same analysis for model D9.6 and Section 4.5 applies the modal analysis at a different boundary to investigate the effects.

4.1 Models

Using an improved method of spatially decomposing the gravitational wave emission relative to what was reported in Mezzacappa et al. (2023), together with an analysis of the PNS oscillation modes generating the gravitational wave emission, we investigated

the gravitational wave emission from the collapse, and explosion, of the Solar-metallicity 15 $M_\odot$ progenitor from Woosley and Heger (2007) and the zero-metallicity 25 $M_\odot$ progenitor from Heger and Woosley (2010), using three-dimensional core collapse supernova simulations performed with the CHIMERA code Bruenn et al. (2020). These are part of the D-series simulations described in Mezzacappa et al. (2023), with the former denoted as the D15 model and the later as the D25 model. Both models were initially nonrotating. The equation of state used in the D-series combines the EOS from Lattimer and Swesty (1991) with a nuclear incompressibility of $K = 220$ MeV at densities above 10^{11} g cm^{-3}, and the EOS from Baron et al. (1985) for densities below that. A 17-species alpha network computes nuclear burning in the outer regions with temperatures below 6.5 GK Hix and Thielemann (1999).

4.2 Regional Decomposition

The final term in Equation (2.125) is the surface term for the radial boundaries r_a and r_b, which vanishes when the total strain is calculated, where $r_a = 0$ and $r_b = \infty$, with $\rho_b = 0$. However, as has been shown, this term cannot be neglected for calculations where $r_a \neq 0$ and r_b is finite (Eggenberger Andersen et al., 2021a; Mezzacappa et al., 2023; Zha, 2024). If it is neglected, one loses the mathematical equivalence between $\ddot{I}_{2m}$ and $\dot{N}_{2m}$, and computations of the two quantities will diverge. In Mezzacappa et al. (2023), this was known, but the regional decomposition implemented did not show agreement between methods in region 5 specifically, owing to the problems associated with using the shock as a regional boundary.

For this reason, we introduce a modification to the procedure applied in Mezzacappa et al. (2023)—specifically, a modification to the regional breakdown of the gravitational wave sources. Regions 1–4 are identical to our previous work. Region 1 is defined with an inner boundary at the innermost mean radius at which the convective mass flux is 5% of its peak value, and the outer boundary is the outermost mean radius at which the convective mass flux is 5% of its peak value.

Region 2 extends from the outer boundary of region 1 to the mean density contour of 10^{12} g cm^{-3}. Region 3 is bounded below and above by the mean density contours of 10^{12} g cm^{-3} and 10^{11} g cm^{-3}, respectively. Region 4 encompasses the net cooling region from the mean density contour of 10^{11} g cm^{-3} to the mean gain radius, at which net neutrino-heating sets in. Previously, region 5 was defined to extend from the mean gain radius to the maximum shock radius. However, because the contribution to gravitational wave emission outside the shock is minimal (the preshock flow is spherical, given a spherical progenitor), extending region 5 to the edge of the computational domain circumvents challenges associated with using the shock as a regional boundary without compromising the determination of the gravitational wave emission itself. Thus, our new regional decomposition, depicted in Figure 4.1, comprises the same regions 1–4, but region 5 extends from the gain radius to the edge of the computational grid rather than to the shock.

4.3 Models D15 and D25

4.3.1 Regional Decomposition of the Strains

In Figure 4.2, we show the strains for each region, and the total strain, for D15, as determined using the procedure outlined in Chapter 2.1.5 and the regional decomposition described at the beginning of the chapter. In particular, we note the absence of numerical noise in region 5 that was present in Figures 21 and 22 of Mezzacappa et al. (2023). From Figure 4.2, we can determine the dominant region(s) producing strong gravitational wave strains during each epoch of the core collapse supernova. We include both the h_+ and $h_\times$ strains, following the conclusions of Pajkos et al. (2023). For the first 100 ms after bounce, the D15 and D25 models do not produce significant strains, and those are not shown. For the h_+ polarized strains of the D15 model, beginning almost immediately 100 ms after bounce, it is region 4 that initially produces gravitational wave strains followed soon after by

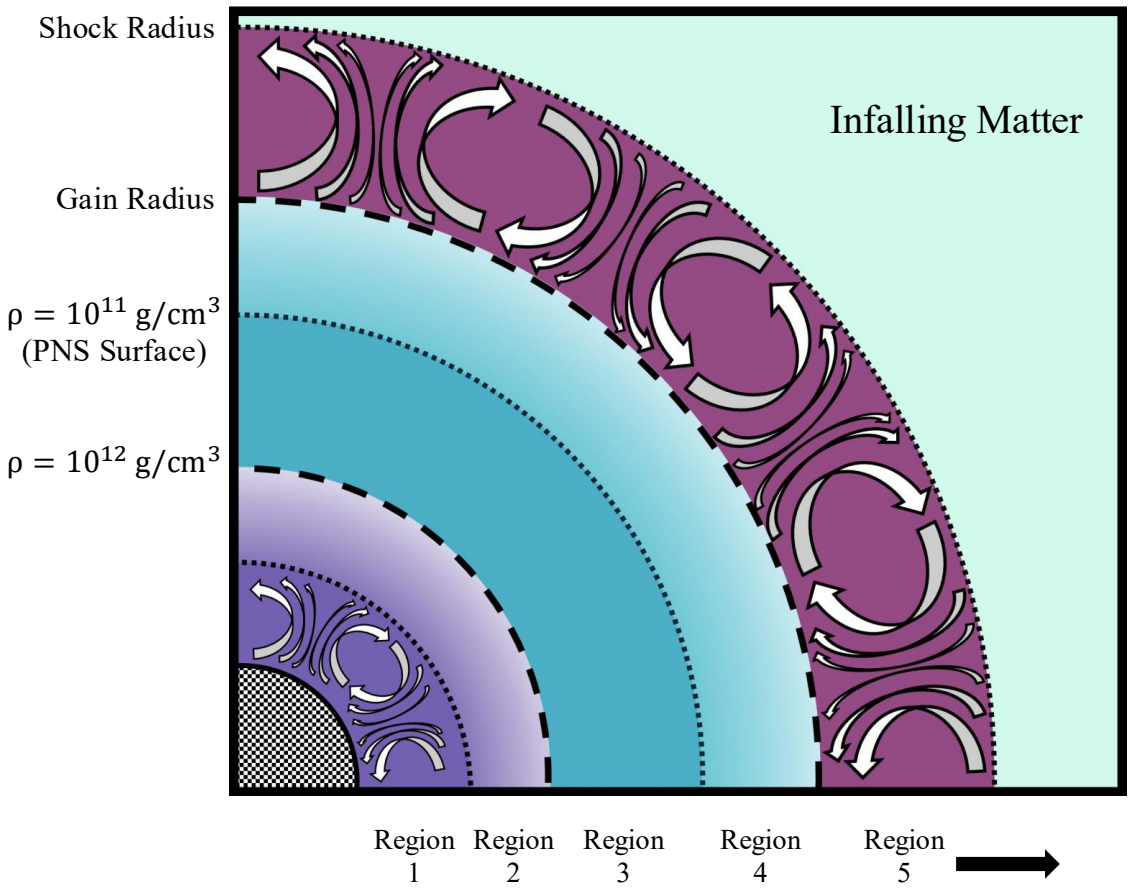


Figure 4.1: Simplified schematic showing regional boundaries, with region 5 extending outside the figure and arrows approximating convective motion.

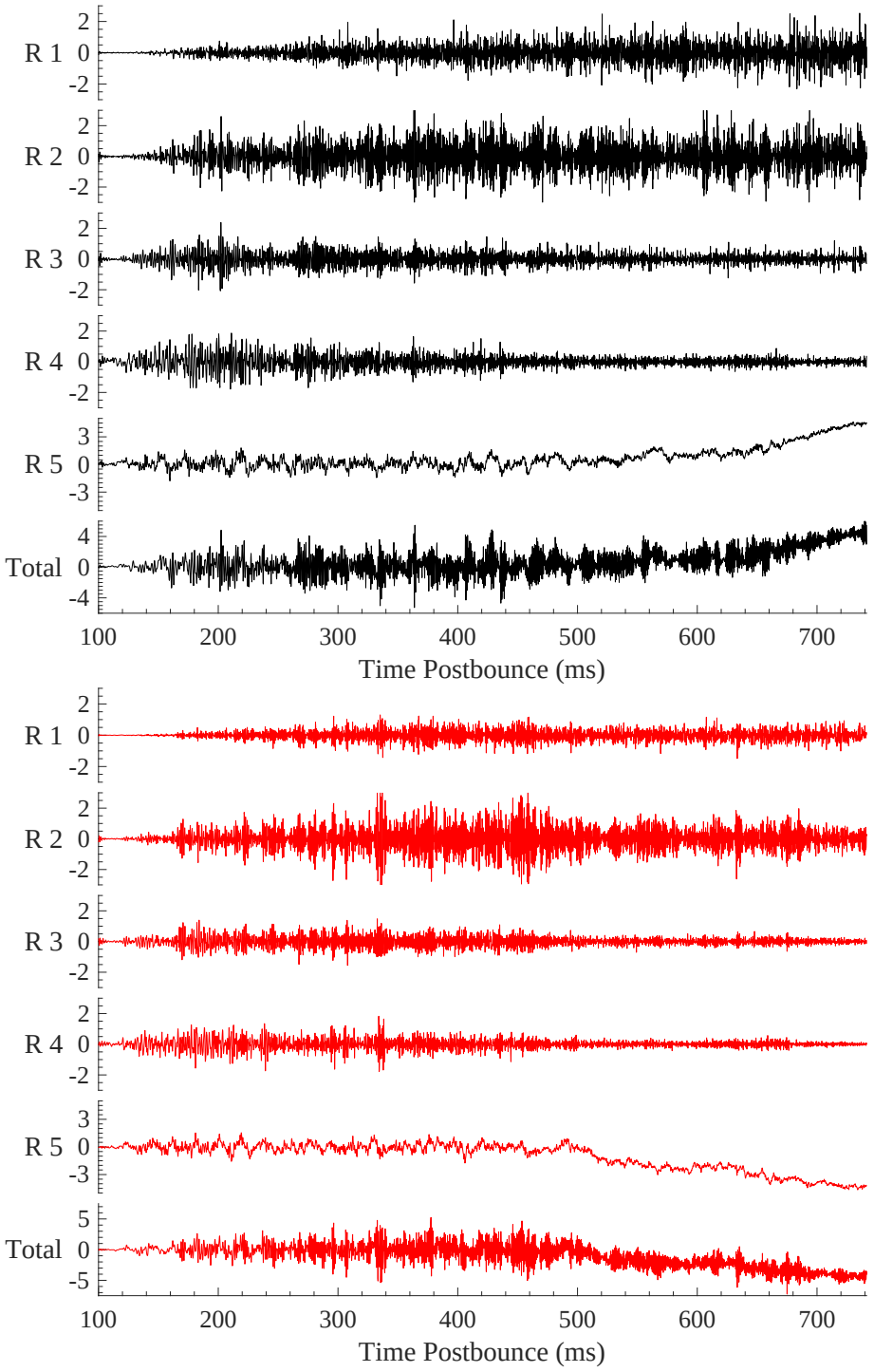


Figure 4.2: Gravitational wave strains by region for D15 with updated boundaries. The vertical axis shows $Dh_{+,\times}$, with $D = 10$ kpc. Top panel shows the strains for the h_+ polarization, bottom panel shows the strains for the $h_\times$ polarization. Note the scales on the vertical axes, as they differ across region and polarization.

region 3, producing strains of a similar amplitude. From 100 to 130 ms, regions 1 and 2 do not show much activity, but 130 ms after bounce they begin to output high-frequency gravitational waves as Ledoux convection sets in (Mezzacappa et al., 2020). The amplitudes of the strains produced in regions 1 and 2 continue to grow, and at 160 ms postbounce the strains of region 2 are roughly the same amplitude as those of regions 3 and 4. Roughly 240 ms after bounce, region 2 has become the region with the largest-amplitude strains. At 300 ms after bounce, region 1 produces strain amplitudes approximately equal to the amplitudes in regions 3 and 4. As the simulation continues, the amplitudes in regions 3 and 4 decrease as accretion onto the PNS subsides after the explosion begins. Regions 1 and 2 maintain their high-amplitude strains for the rest of the simulation, as the Ledoux convection that drives them continues due to the lepton gradients sustained by neutrino diffusion and emission from the PNS. In Figure 4.3, we see that the D25 model shows the same behavior in regional production of gravitational waves with time, although the exact transition times vary between the models. This behavior is clear in both polarizations of the strains.

From these strains, we see that the general evolution of gravitational wave generation for the D-series models 100 ms after bounce proceeds as: (i) region 4 initially produces small amplitude gravitational wave strains, (ii) region 3 produces strains of similar amplitude a few tens of ms later, (iii) Ledoux convection begins and causes gravitational wave strains to be produced in regions 1 and 2, (iv) within 300 ms after bounce region 1 will have strains of the same magnitude as regions 3 and 4, and region 2 will produce the greatest strains, (v) as accretion onto the surface of the PNS slows, the strains produced in regions 3 and 4 decrease, (vi) sustained Ledoux convection keeps the magnitude of the strains produced in regions 1 and 2 fairly constant for the rest of the simulation. Note that, during phases (iii) and (iv), there is a significant contribution to the total strain across regions 1–4. During these phases, ∼200–500 ms for D15 and ∼250–380 ms for D25, we see the greatest total strain in both polarizations. Not included in this analysis is the development

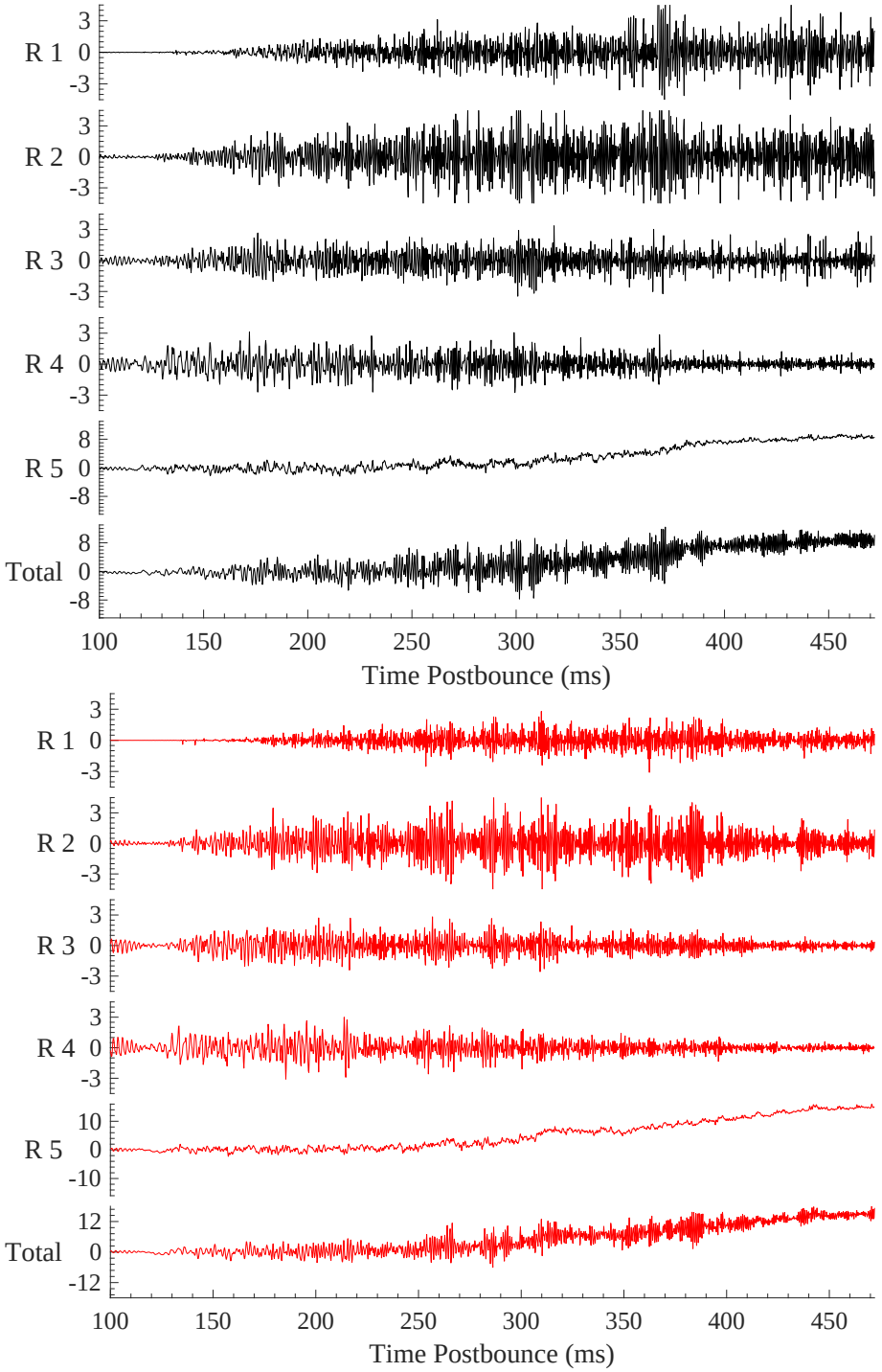


Figure 4.3: Gravitational wave strains by region for D25 with updated boundaries. The vertical axis shows $Dh_{+,\times}$, with $D = 10$ kpc. Top panel shows the strains for the h_+ polarization, bottom panel shows the strains for the $h_\times$ polarization. Note the scales on the vertical axes, as they differ across region and polarization.

of standing-accretion-shock-instability (SASI)–produced gravitational waves, which are below ∼250 Hz, and the gravitational wave memory, which begins to develop at the time of shock revival, with high amplitude, low-frequency, ∼50 Hz and below, gravitational waves.

4.3.2 Fractional Luminosity as a Function of Radius

This evolution of the gravitational wave production in CCSNe is not only seen in the strains. It is also apparent when examining the gravitational wave luminosity. We can compute the total gravitational wave luminosity as a function of time from (Thorne, 1980b)

$$\frac{dE}{dt} = \frac{c^3}{G}\frac{1}{32\pi}\sum_{m=-2}^{+2}\left\langle\left|\frac{dA_{2m}}{dt}\right|^2\right\rangle, \tag{4.1}$$

where the $\langle\rangle$ indicate averaging over several wave cycles and

$$A_{2m} \equiv \frac{dN_{2m}}{dt} = \frac{G}{c^4}\frac{d^2I_{2m}}{dt^2}. \tag{4.2}$$

Due to the nonlinear dependence on A_{2m}, it is not possible to decompose the luminosity into regions, as was done for the strains. However, it is possible to compute Equation (4.1) from the center of the PNS out to a particular radius and compare that to the total gravitational wave luminosity of the entire star. This does not allow for an exact determination of the gravitational wave luminosity within each region of the star, but should allow for an estimate of the fraction of the total luminosity that is emitted within a particular radius, with an obvious correlation then with each region.

Figure 4.4 shows the fractional luminosity as a function of radius and time, for each model, for times after the HFF develops. The procedure for determining the start time of the HFF is described in Murphy et al. (2024) (Section 5.1.5 in this dissertation), and is 127 ms and 134 ms after bounce for D15 and D25, respectively. The radii containing 90% and 95% of the gravitational wave luminosity are plotted

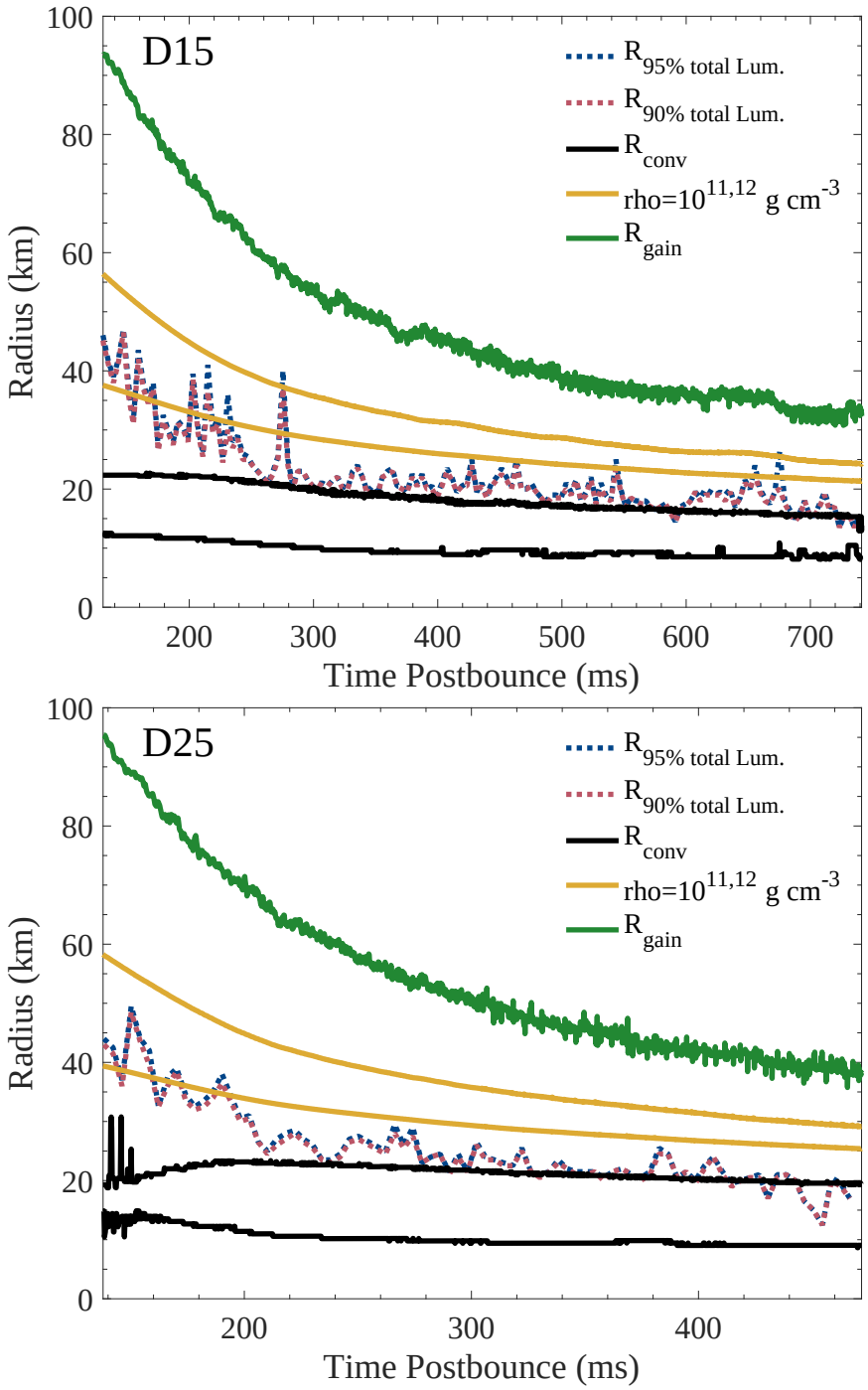


Figure 4.4: Fractional gravitational wave luminosity with respect to time and radius. The regional boundaries corresponding to the definitions in the text are plotted as a function of time in black, yellow, and green. The red dotted line corresponds to the radius at which 90% of the gravitational wave luminosity is contained, and the blue dotted line represents the radius at which 95% of the luminosity is contained.

in red and blue, respectively. The fact that these radii lie on top of each other shows that the majority of the gravitational wave luminosity is well bounded by these radii, and that the radii beyond the red and blue curves do not contribute much to the total gravitational wave luminosity.

In both models, we see that the majority of the gravitational wave luminosity stems from region 3 to the center of the PNS at the onset of the HFF. By 300 ms after bounce for the D15 model and 200 ms after bounce for the D25 model, the majority of the gravitational wave luminosity originates from below region 3. From that time until the end of the simulation, the majority of the gravitational wave luminosity originates from regions 1 and 2. This is consistent with the evolution of the gravitational wave strains in our regional analysis, discussed earlier.

4.3.3 Modal Analysis

The goal of our modal analysis is to find the vibrational modes of the PNS that give rise to its gravitational wave emission. This means that the resulting eigenfunctions for the eigenfrequencies that solve Equation (2.193) need to be consistent with the qualitative behavior we see in the regional strain and fractional luminosity plots of Figures 4.2–4.4. Additionally, the eigenfrequencies should reproduce the qualitative and quantitative behavior, to be discussed, of the spectrograms produced from the gravitationa wave strains. Determining whether a mode reproduces this behavior is nontrivial. To simplify our discussion, we will focus on only the vibrational modes that are close in frequency to the HFF, but we note that the modal analysis produces eigenfrequencies both above and below the HFF.

For our modal analysis, we examine only the quadrupolar, $\ell = 2$ non-radial modes, given that they are the largest contributors to the gravitational wave signal. The PNS modes are labeled according to the Generalized Cowling Nomenclature (GCN) as described in Osaki (1975). The GCN labels each eigenmode by the total number of p-nodes, N_p, and g-nodes, N_g, identified in the phase diagram of $(\eta_r, \eta_\perp)$, and each

mode is uniquely identified by the quantity

$$\tilde{n} \equiv N_p - N_g, \tag{4.3}$$

which monotonically increases with mode frequency. In the phase diagram, a nodal point—*i.e.* a point for which $\eta_r(r) = 0$—is determined to be a p-node if the curve produced by the eigenmode is moving counterclockwise at that point. A g-node is a nodal point where the curve of the eigenmode is moving clockwise at that point. From the definition of $\tilde{n}$, all p-modes have $\tilde{n} > 0$, all g-modes have $\tilde{n} < 0$, an the fundamental f-mode has $\tilde{n} = 0$. The number of nodes for a given eigenmode can change throughout the evolution of the PNS without the label for the mode changing. This is the advantage of the GCN classification. Rodriguez et al. (2023) investigated this method of classification and found it consistently tracked eigenmodes for extended periods of time. Indeed, when plotting the amplitude of the radial eigenfunction, η_r, we confirm that each mode we investigate evolves consistently and is labeled as the same feature across time.

To ensure that no nodal points are missed due to small oscillations, we interpolated the CHIMERA data onto a grid of sufficient resolution to construct the eigenfunctions. For our study, we interpolated to a grid of 8192 radial cells, corresponding to a cell width of $\mathcal{O}(10$ m). For D15, we also determined the number of nodes for a grid of 16,382 cells and found no difference relative to the number obtained with the 8,192 cell grid, as well as no significant changes in the eignefunctions and eigenfrequencies.

The spectrograms for the D-series models presented in Mezzacappa et al. (2023) have been updated using the methods outlined in Section II.C of Murphy et al. (2024) (Section 5.1 of this dissertation). The D25 model uses a window size of 30 ms, while the longer signal of D15 allows us to use a 45 ms window. All other aspects of the windowing scheme are the same as in Murphy et al. (2024) (i.e., $\beta = 6$ and 45 or 30 ms window segments overlapping adjoining segments by $93.\bar{3}\%$ or 90% for models D15 and D25 respectively), meaning that the effective window length is 3 ms for

each model. Figures 4.5 and 4.6 shows the resulting spectrograms overlaid with the eigenfrequencies determined by the procedure outlined in Chapter 2.2, closest to the HFF.

In Figures 4.5 and 4.6, we see that, for each model, the portion of the HFF with the highest power-spectral density is tracked throughout its evolution by different modes predicted by our modal analysis. As the HFF begins to develop, it is the ${}^2g_2$-mode that tracks it best. Between 180–200 ms after bounce the ${}^2g_2$-mode stops tracking the HFF and the ${}^2g_1$ mode takes over as the best tracking mode. Around 400 ms after bounce, the ${}^2f$-mode begins to follow the HFF most closely. We thus identify three modes that track the HFF throughout its evolution: ${}^2g_2$, ${}^2g_1$, and ${}^2f$. In Section 4.5, the eigenfrequencies determined when applying the boundary condition in Equation (2.201) at the 10^{10} g cm^{-3} density contour are plotted on the spectrograms for D15 and they do not track the evolution of the HFF.

Interestingly, we see that the transition from one mode that tracks the HFF to another occurs at an avoided crossing. In the case of D15, we examine these avoided crossings by plotting the amplitude of the radial component of the perturbation in Figure 4.7. We see that, before the first avoided crossing shown on the left side of Figure 4.7, the maximum amplitude of the ${}^2g_2$-mode is significantly larger than the maximum magnitude of the ${}^2g_1$-mode amplitude. At the approximate time of the avoided crossing, 184 ms after bounce, the magnitudes of the maximum amplitudes are approximately equal, as the maximum amplitude has decreased for the ${}^2g_2$-mode and increased for the ${}^2g_1$-mode. This trend continues until the ${}^2g_1$-mode has the larger maximum amplitude. This same pattern is seen in the second avoided crossing shown in the right side of Figure 4.7, as well. Here, the maximum magnitude of the amplitude of the ${}^2g_1$ decreases as the maximum amplitude of the ${}^2f$-mode increases. Note that this avoided crossing lasts a much longer time than in the first case. Avoided crossings indicate times at which the character of the modes tracking the HFF involved swap (Aerts et al., 2010). Thus, these avoided crossings indicate that the character of a mode transitions either to or away from the underlying character of the HFF.

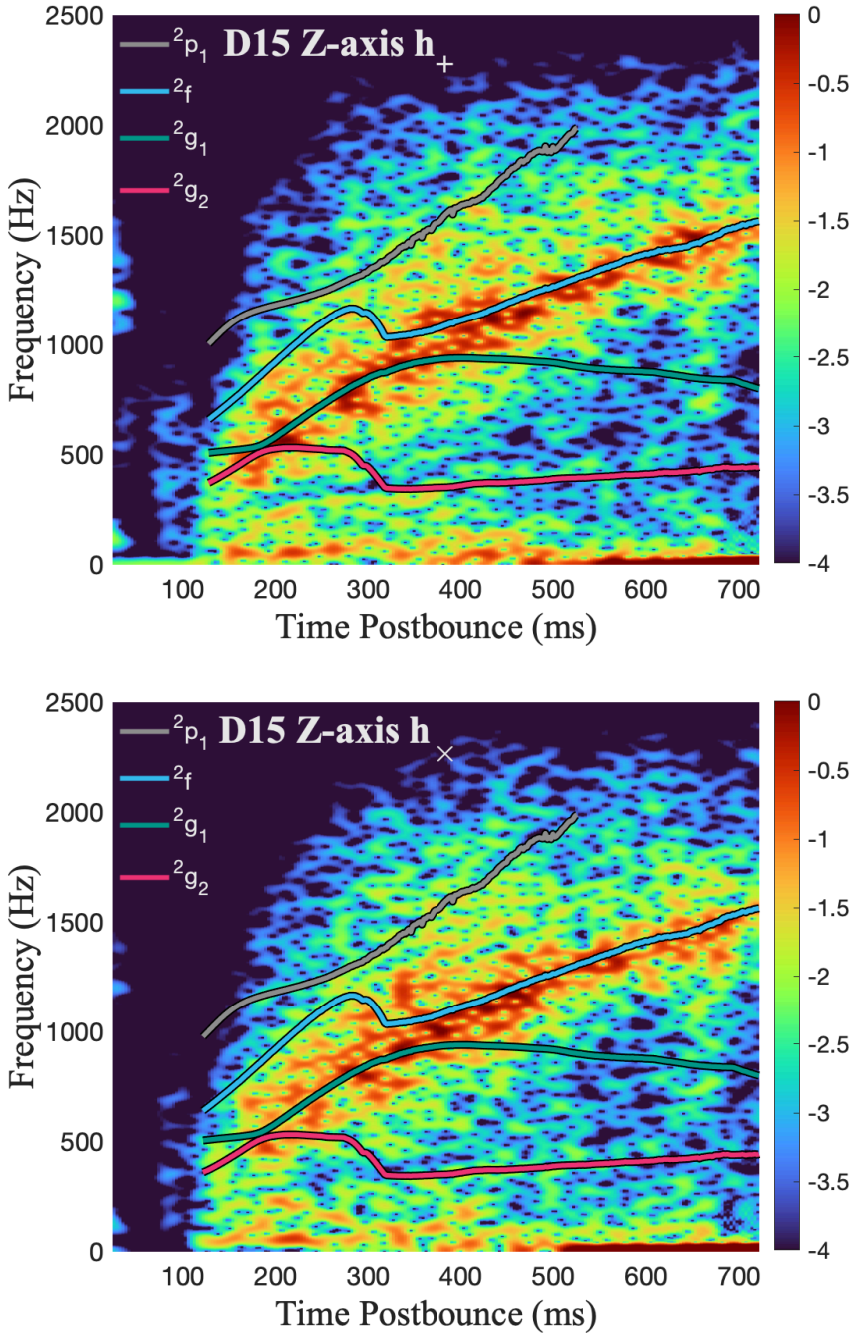


Figure 4.5: Spectrograms and eigenfrequency evolution for model D15. The color axis represents the logarithm of the power spectral density $\log_{10}(\mathrm{P})$. The top panel shows the spectrograms of the h_+ signals, and the bottom panel shows the spectrograms of the $h_\times$ signals. Overlaid on each spectrogram are the eigenfrequencies for each mode that lies close to the HFF, labeled according to the GCN classification as described in the text.

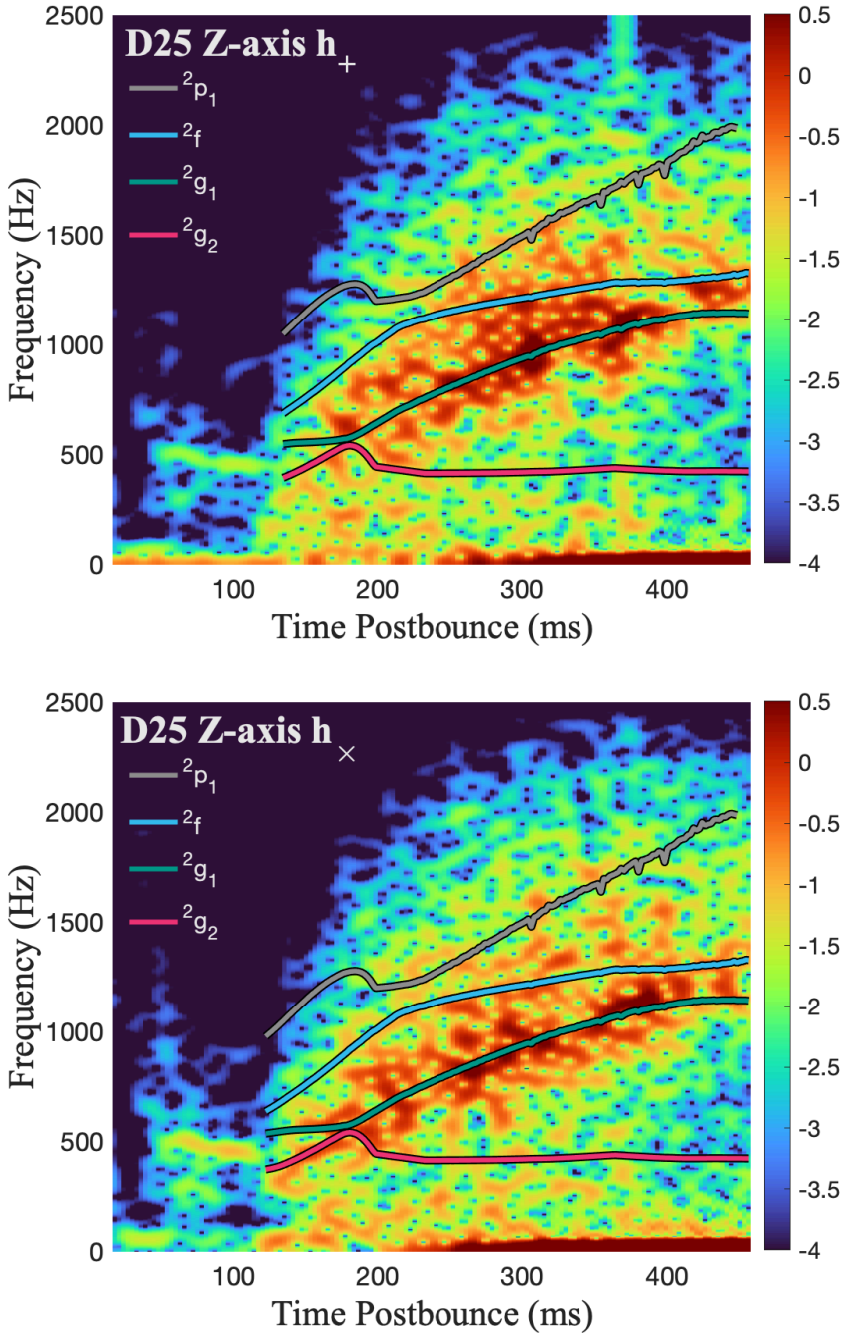


Figure 4.6: Spectrograms and eigenfrequency evolution for model D25. The color axis represents the logarithm of the power spectral density $\log_{10}(\mathrm{P})$. The top panel shows the spectrograms of the h_+ signals, and the bottom panel shows the spectrograms of the $h_\times$ signals. Overlaid on each spectrogram are the eigenfrequencies for each mode that lies close to the HFF, labeled according to the GCN classification as described in the text.

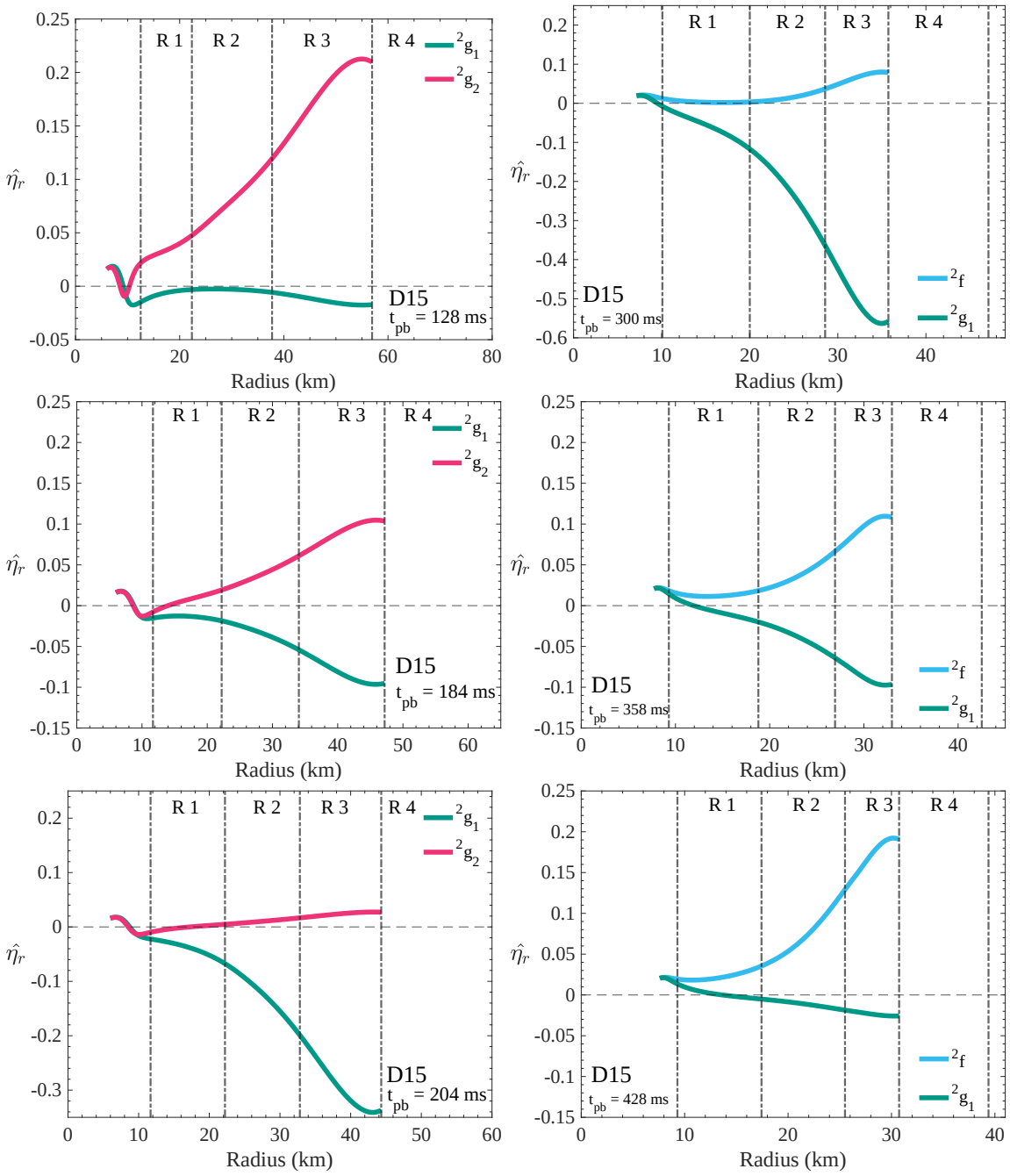


Figure 4.7: Eigenfunction amplitudes around avoided crossing times for D15. Vertical axis shows the amplitude of the radial component of the displacement eigenfunction, η_r, for the $^2g_2$-, $^2g_1$-, and ^2f-modes normalized with respect to the magnitude of the largest amplitude across all modes across all times. The radial boundaries, as defined in the text, are shown as vertical dashed lines. The approximate avoided crossing times are represented by the middle panels.

In order to determine if these modes match the evolution of gravitational wave emission as seen in the simulation data of Figures 4.2–4.6, we investigate the total kinetic energy within a mode, E_{GW}, and the power emitted as gravitational waves, P_{GW}. To compute the total kinetic energy, we first calculate the kinetic energy density of a mode with frequency σ as (Torres-Forné et al., 2018; Morozova et al., 2018)

$$\mathcal{E}(r) = \frac{\sigma^2}{8\pi}\rho\left[\eta_r^2 + \ell(\ell+1)\frac{\eta_\perp^2}{r^2}\right]. \tag{4.4}$$

The total kinetic energy contained within a mode in the Newtonian limit is then given by

$$E_{GW} = 4\pi\int_0^{R_{\rm PNS}} r^2\mathcal{E}dr. \tag{4.5}$$

The total power radiated from each mode as gravitational waves, in the Newtonian limit, is (Thorne, 1969)

$$P_{GW} = \frac{1}{8\pi}\frac{(\ell+1)(\ell+2)}{(\ell-1)l}\left[\frac{4\pi\sigma^{\ell+1}}{(2\ell+1)!!}\int_0^{R_{\rm PNS}}\delta\hat{\rho}r^{l+2}dr\right]^2, \tag{4.6}$$

where $\delta\hat{\rho}$ is defined in Equation (2.175). Just as in the case of gravitational wave luminosity, the nonlinearity with respect to $\delta\hat{\rho}$ makes clear we cannot use Equation (4.6) to calculate the power output regionally. However, we can introduce the gravitational wave production efficiency defined by Torres-Forné et al. (2018) as

$$\eta_{GW} = \frac{P_{GW}}{E_{GW}f}, \tag{4.7}$$

and use the regional energy contained within a mode as

$$\begin{aligned} E_{GW} &= 4\pi\left[\int_{R1} r^2\mathcal{E}dr + \int_{R2} r^2\mathcal{E}dr + \int_{R3} r^2\mathcal{E}dr\right] \\ &= E_1 + E_2 + E_3 \end{aligned} \tag{4.8}$$

to decompose the total power output in gravitational waves as

$$\begin{aligned} P_{GW} &= \eta_{GW} f E_{GW} \\ &= \eta_{GW} f (E_1 + E_2 + E_3) \\ &= P_1 + P_2 + P_3. \end{aligned} \tag{4.9}$$

Figure 4.8 shows the resulting efficiency of gravitational wave production of each mode for each model. With the exception of the ${}^2f$- and ${}^2p_1$-modes at early times, the times where a mode is most efficient correspond directly to the times where they best fit the HFF, for both models. It is unclear why the ${}^2f$-mode is shown to be so efficient at early times when the spectrograms in Figures 4.5 and 4.6 do not show a significant feature at those frequencies, for either model. However, we do note that the ${}^2f$-mode has two nodal points, one p-node and one g-node, during this time of overestimated efficiency. As the magnitude of the amplitude of the radial component of the eigenfunction decreases between these two nodal points, the efficiency of the mode begins to decrease as well. By 300 ms after bounce, the ${}^2f$-mode has no nodal points as shown in the righ side of Figure 4.7. Additionally, in both models a ${}^2p_1$-mode is observed to have a gravitational wave emission efficiency higher than that of both the ${}^2g_1$- and the ${}^2f$-modes until ∼450–460 ms after bounce when the ${}^2f$-mode becomes the highest efficiency mode. We only tracked modes up to 2000 Hz; hence, the artificial termination of the ${}^2p_1$-mode in the plot. We plot the eigenfrequencies of the ${}^2p_1$-mode in Figures 4.5 and 4.6 and see that it does not correspond to any particular feature in the spectrograms. We note that Torres-Forné et al. (2018) see similar behavior, where the ${}^2p_4$-mode is the most efficient emitter of gravitational waves in their model but the ${}^2p_1$ most closely tracks the highest amplitude feature in their spectrogram. At this time we have not investigated what physical mechanism may be responsible for the reduction in efficiency for these modes. As the ${}^2p_1$-mode does not contribute to the HFF, it is not further investigated in this study.

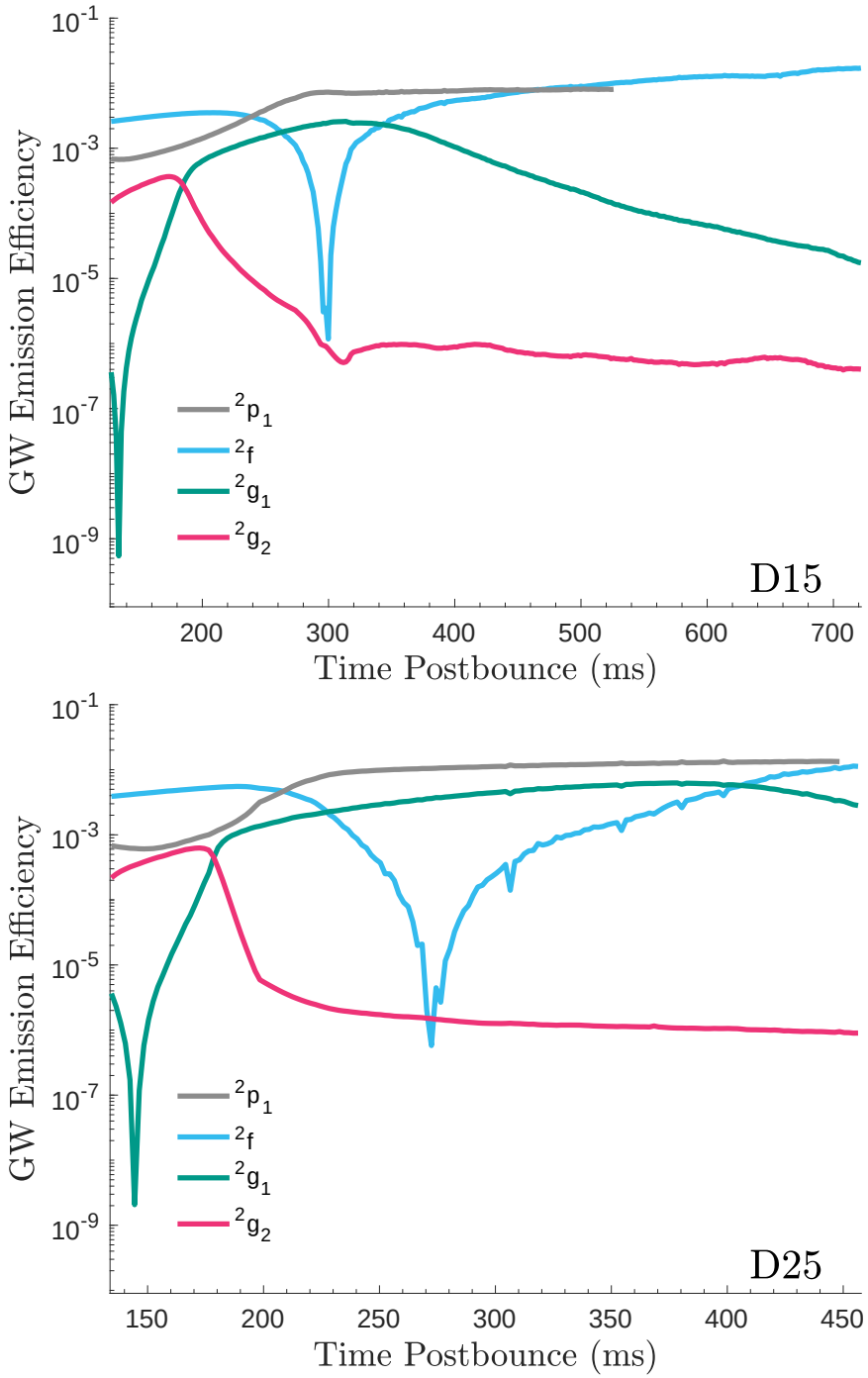


Figure 4.8: PNS oscillation mode gravitational wave production efficiency. The vertical axis shows the efficiency of producing gravitational waves as defined in the text. for both D15 (top) and D25 (bottom), the modes producing gravitational waves most efficiently proceed from ${}^2g_2$ to ${}^2g_1$ to ${}^2f$, coinciding with the modes that match the HFF in Figures 4.5 and 4.6.

For the modes that do match the evolution of the HFF, we compute the approximate regional power emitted as gravitational waves for each region n as

$$P_n = \eta_{GW} f E_n. \tag{4.10}$$

Figure 4.9 shows the power radiated as gravitational waves for each mode by color, and the regions in which the power is radiated are denoted by line type. Note that the vertical axis is on a log scale, to capture the full range of the power radiated as gravitational waves. Before ∼210 ms for the D25 model and before ∼240 ms for the D15 model, the power radiated as gravitational waves is concentrated in region 3, denoted by a solid line, regardless of what mode is emitting the most power at that time. Given that the modal analysis uses the surface of the PNS as the outer boundary, we cannot use it to investigate region 4, but from Figure 4.4, we expect the gravitational wave luminosity to be dominated by region 3 even when the strains are slightly larger in region 4. At ∼240 ms after bounce for the D15 model, and ∼210 ms after bounce for the D25 mode, the dominant power output is from the ${}^2g_1$-mode shown in green, and the majority of the power is emitted in region 2, shown as a dashed line. For the D15 model at ∼350 ms after bounce, the ${}^2g_1$-mode begins to radiate power more strongly from region 1, and at ∼360 ms after bounce, the ${}^2f$-mode, denoted in blue, becomes the dominant emitter of gravitational waves, with the majority of power coming from region 2. The transition of dominant gravitational wave production from region 2 to region 1 for D25 also occurs at ∼330 ms, but when the ${}^2f$-mode becomes dominant at ∼420 ms, region 1 remains the dominant region. At the end of the D15 simulation, the power output of regions 1 and 2 are roughly equal, with region 1 being slightly larger. From Figure 4.7, we see that these transition times correspond approximately to the avoided crossing times as well, again highlighting the fact that these transitions are caused caused by a switch in the character of the modes tracking the HFF.

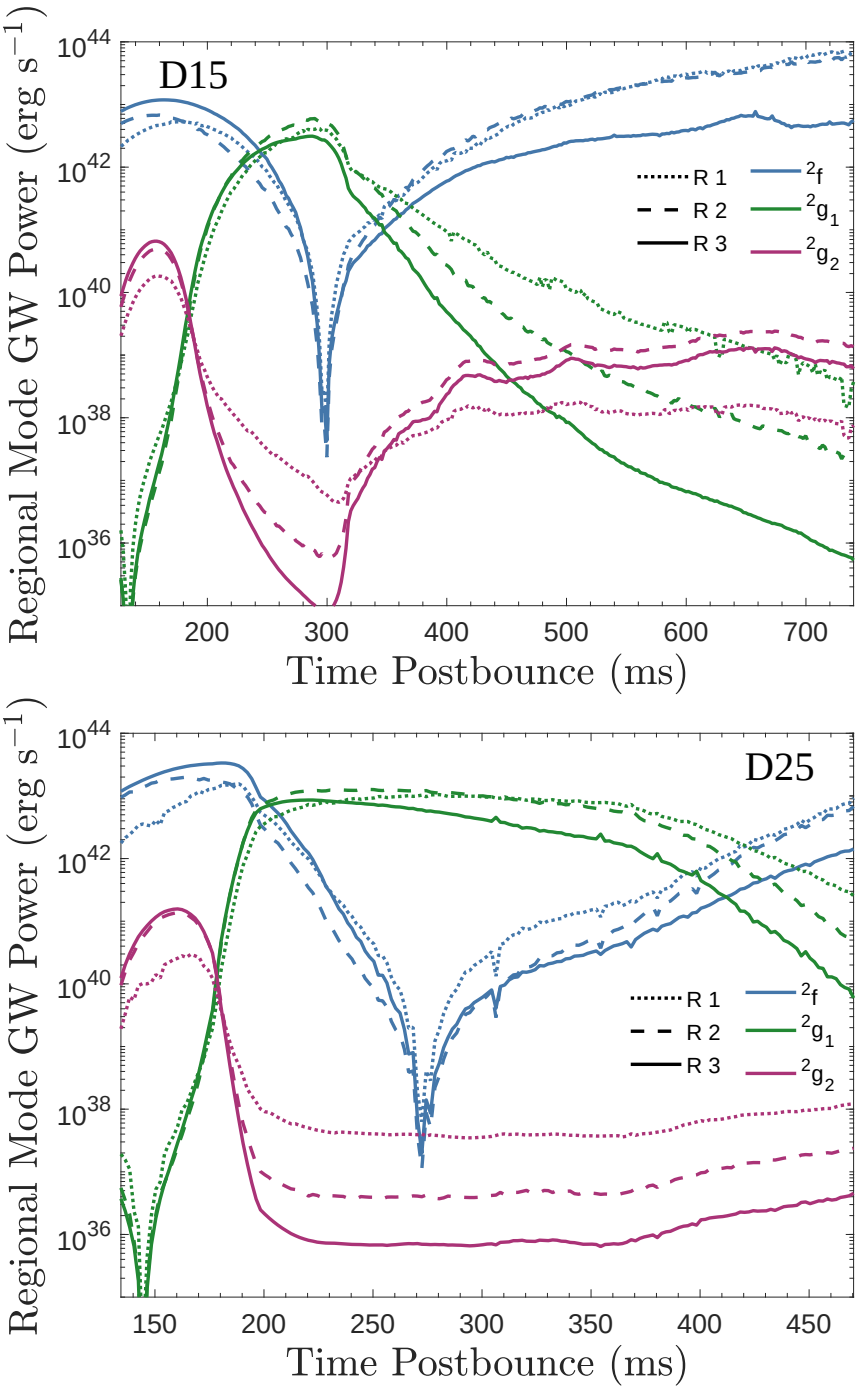


Figure 4.9: PNS oscillation mode power emitted as gravitational waves. The vertical axis shows the power emitted as gravitational waves from Equation (4.10). ^2f-, $^2g_1$-, and $^2g_2$-modes are shown in blue, green, and purple respectively. The region emitting the power is denoted by line type, with regions 1, 2, and 3 denoted by dotted, dashed, and solid lines respectively.

Finally, we examine the individual spectrograms for regions 1–4, given the corresponding strains in Figures 4.2 and 4.3. Figures 4.10 and 4.11 show these spectrograms for model D15 and D25, respectively, produced using the same parameters as in Figures 4.5 and 4.6, overlaid with the eigenfrequencies that lie closest to the HFF from our modal analysis. The evolution of the source of gravitational wave emission is seen in the spectrograms and directly corroborated by the power emitted by each mode in Figure 4.9. In both the D15 and D25 models, gravitational wave emission begins with the highest amplitude strains coming from accretion onto the PNS, in regions 3 and 4, corresponding to low-order ${}^2g$-modes. At these early times, there is no feature in region 1 that is tracked by these modes. Conversely, in the D15 model, after ∼300 ms postbounce, the ${}^2f$-mode is clearly tracked in region 2, and at later times in region 1, as well. During the same period, there is a weaker signal in region 3, and almost no signal in region 4. The D25 model does not evolve long enough for the ${}^2f$-mode to track the HFF, but the ${}^2g_1$-mode does track the HFF in both regions 2 and 3, with the dominant contribution coming from region 2 and with little or no contribution coming from region 3 or 4, respectively, towards the end of the simulation.

4.4 Model D9.6

As outlined in Mezzacappa et al. (2023), the behavior of D9.6 is markedly different than that of D15 and D25. Most of the gravitational energy is emitted within ∼75 ms after bounce, well before the onset of sustained Ledoux convection and the emergence of the HFF, albeit weak in this case. Figure 4.12 shows that 30 ms after bounce, the hydrostatic condition is not significantly violated within the PNS. This is not the case at earlier times, as seen at the edge of the PNS at 20 ms. This means that our analysis will break down for times between 0–30 ms post bounce, and that extending the boundary to another, lower-density contour, or even the shock radius,

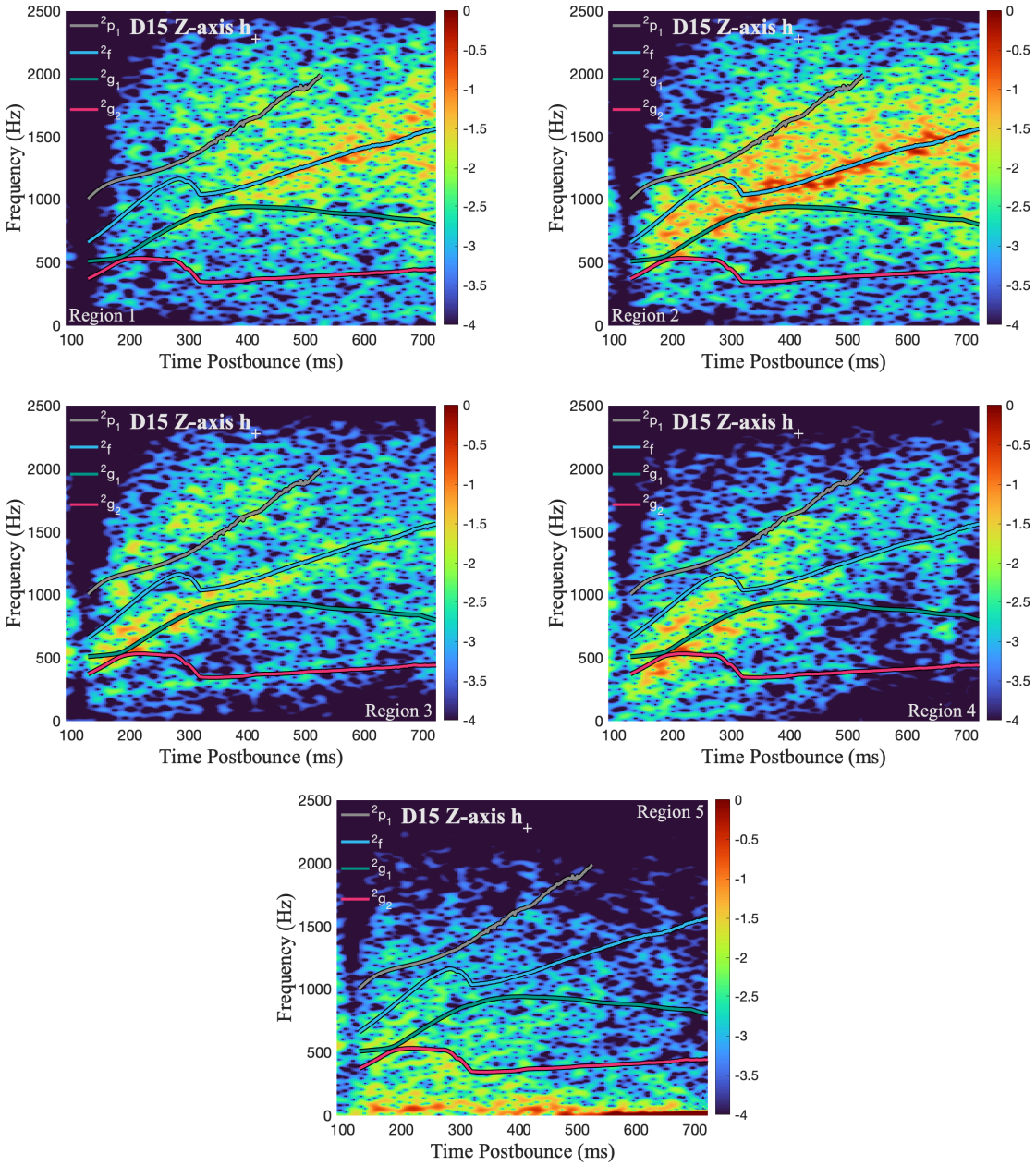


Figure 4.10: Spectrograms by region and overlaid eigenfrequency evolution for D15. Spectrograms correspond to the regional h_+ polarized strains in Figure 4.2. The eigenfrequencies from the modal analysis are overlaid and differentiated by color. Modes are classified according to the GCN classification, as described in the text.

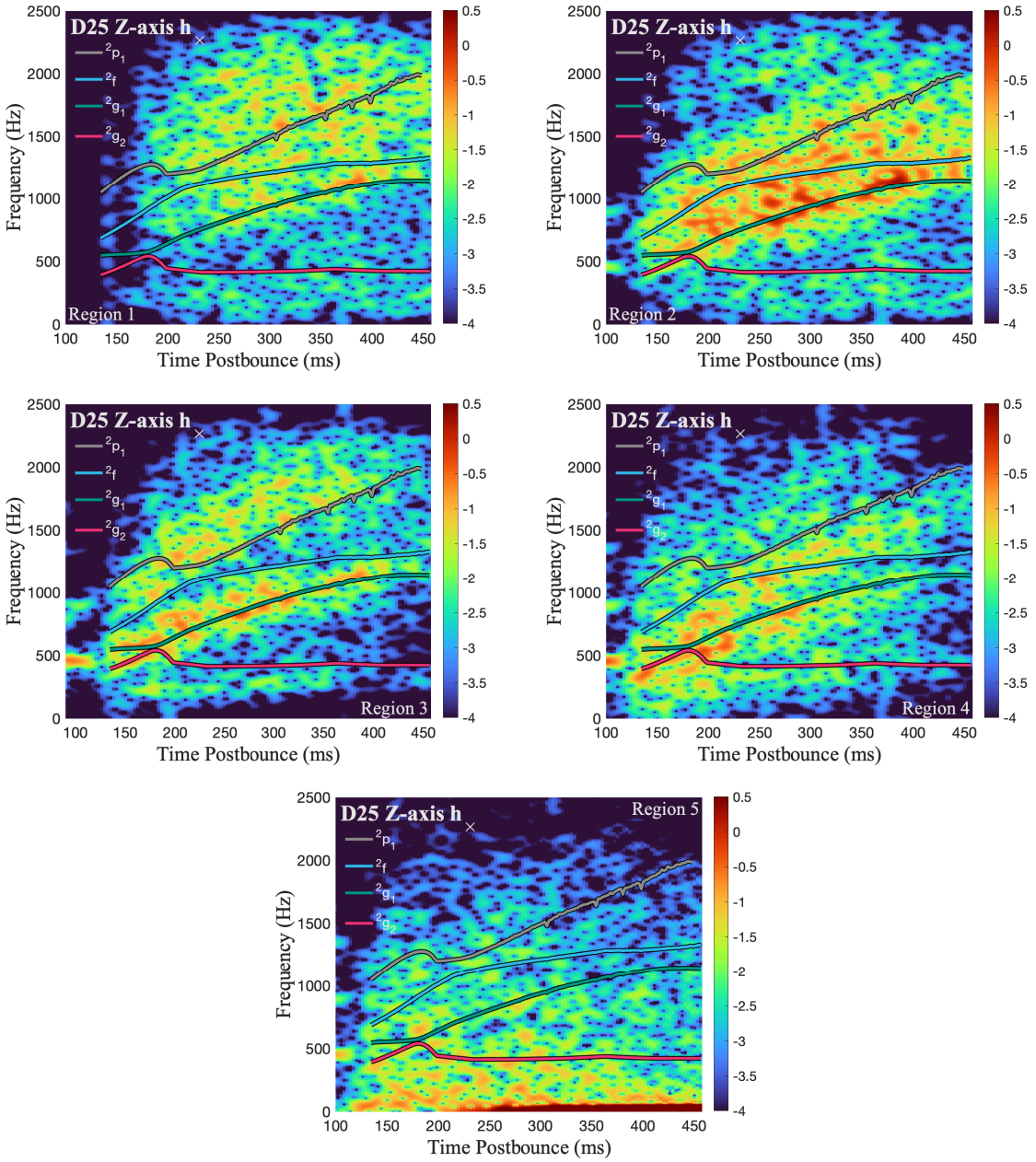


Figure 4.11: Spectrograms by region and overlaid eigenfrequency evolution for D25. Spectrograms correspond to the regional $h_\times$ polarized strains in Figure 4.3. The eigenfrequencies from the modal analysis are overlaid and differentiated by color. Modes are classified according to the GCN classification, as described in the text.

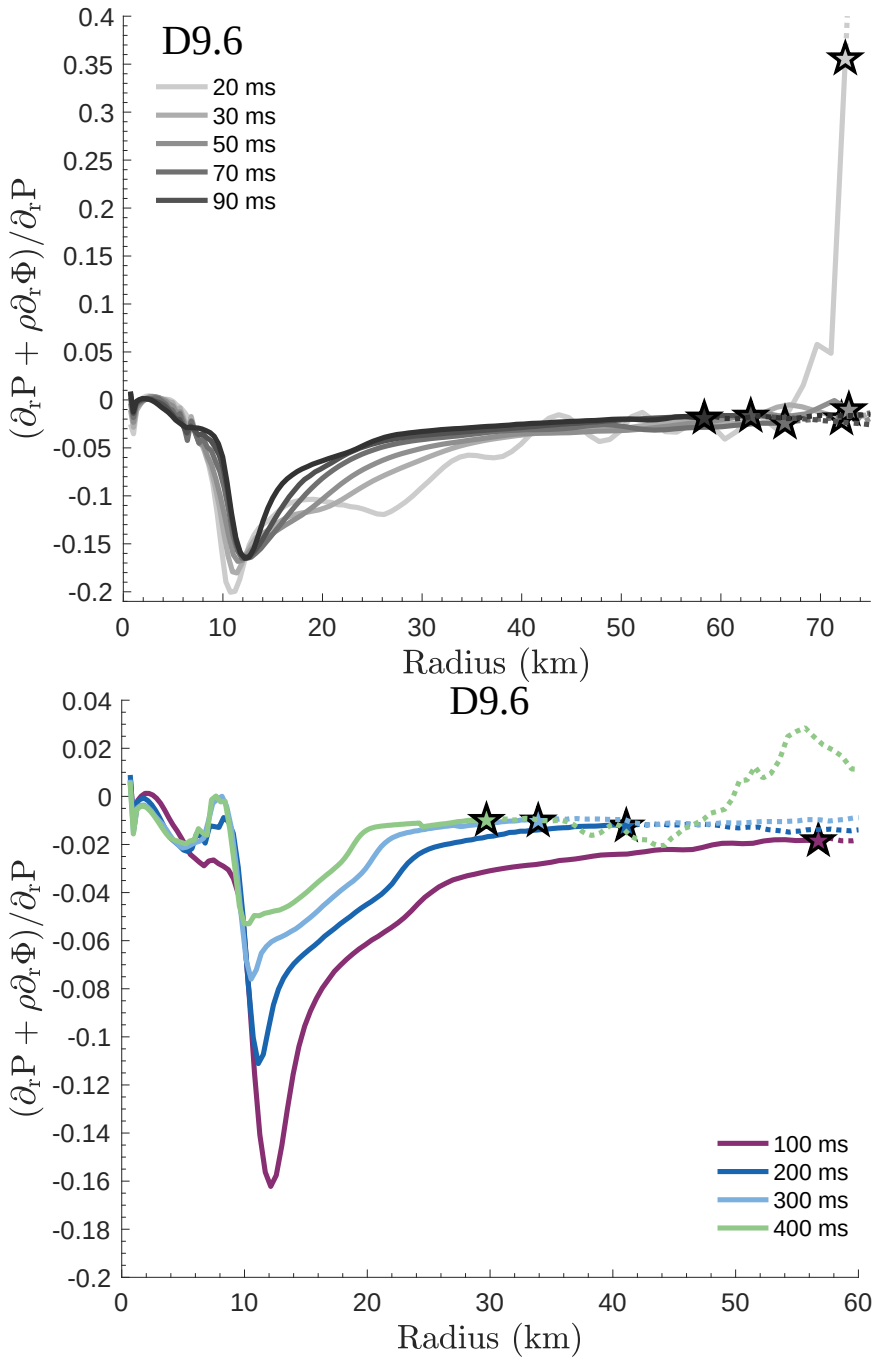


Figure 4.12: Hydrostatic equilibrium deviation for model D9.6. The deviations, where $\partial_r P \neq -\rho\partial_r\Phi$, are plotted at different times differentiated by color. The star symbol indicates the surface of the PNS, defined as the 10^{11} g cm^{-3} density contour. The deviation from hydrostatic equilibrium outside the PNS surface is shown by dotted lines.

will not result in a more accurate analysis. Nonetheless, we present the results of the perturbative analysis from 0–100 ms postbounce in Figure 4.13.

In Figure 4.13, the spectrogram was produced using a shape factor of $\beta = 2$ and 30 ms window segments overlapping adjoining segments by 90%. The most noticeable failing of the perturbative analysis is the lack of any PNS oscillation modes at frequencies above 700 Hz from 0–60 ms postbounce. This is likely the result of these modes existing almost entirely beyond region 3, and thus directly related to the dynamics of the fluid between the surface of the PNS and the shock. We see in Figure 4.14 that the majority of the strain amplitude comes from regions 3 and 4 from 0–50 ms postbounce. Moreover, jumps in amplitude that appear in regions 3 and 4 from 10–50 ms postbounce do not seem to appear in regions 1 and 2 at all. For these reasons, we would not expect the perturbative analysis to capture this behavior. It does seem to capture lower-frequency features, but notably it misses a major feature around 600 Hz from 50–70 ms postbounce. Overall, it seems that the PNS oscillation modes from 0–80 ms postbounce depend strongly on the dynamics immediately behind the shock, which cannot be captured in our analysis. From 80 ms postbounce on, the quasinormal modes begin to track very low spectral power density features that are cut off the color map.

The starting point of the HFF is not clearly defined for D9.6, but examining the time period 100 ms after bounce and beyond will capture approximately the same time period investigated in the D15 and D25 models. Figure 4.15 shows the regional breakdown in the strains using the same regional definitions used in D15 and D25. Unfortunately, beyond 300 ms the regional boundaries introduce too much noise in the h_+ strains to make any specific claims for regions 1–4. Figure 4.16 shows the fractional luminosity for model D9.6 from 100-300 ms postbounce. Unlike in the other models, there is only a short time where the majority of the gravitational wave luminosity is emitted from region 3 and below between 190–200 ms after bounce. Between 100–200 ms after bounce the majority of the gravitational wave luminosity is emitted from region 2 and below. Beyond 200 ms after bounce, the total luminosity

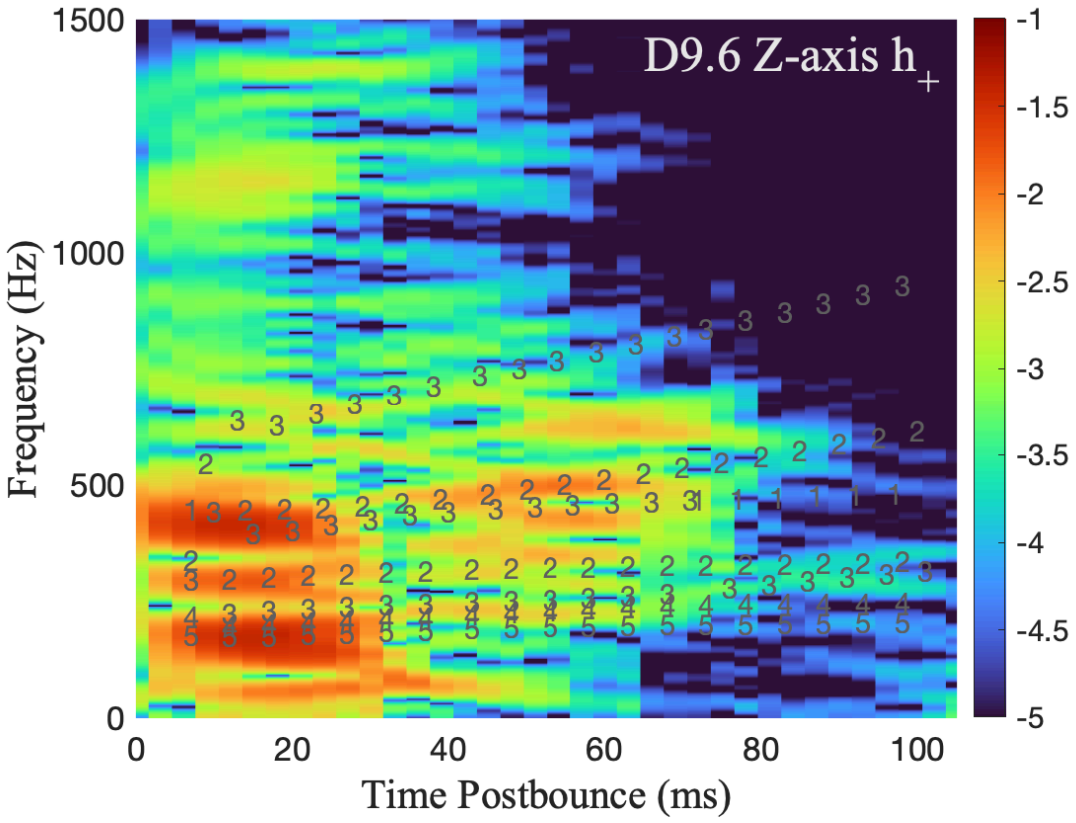


Figure 4.13: Spectrogram for D9.6 with early eigenfrequency evolution overlaid. The spectrogram is made with the same parameters as the D25 model in Figure 4.6. The eigenfrequencies found from the perturbative analysis are overlaid in gray. The number corresponds to the total number of nodes in η_r. We restrict the low frequency modes to those with less than 5 nodes to avoid over crowding the plot.

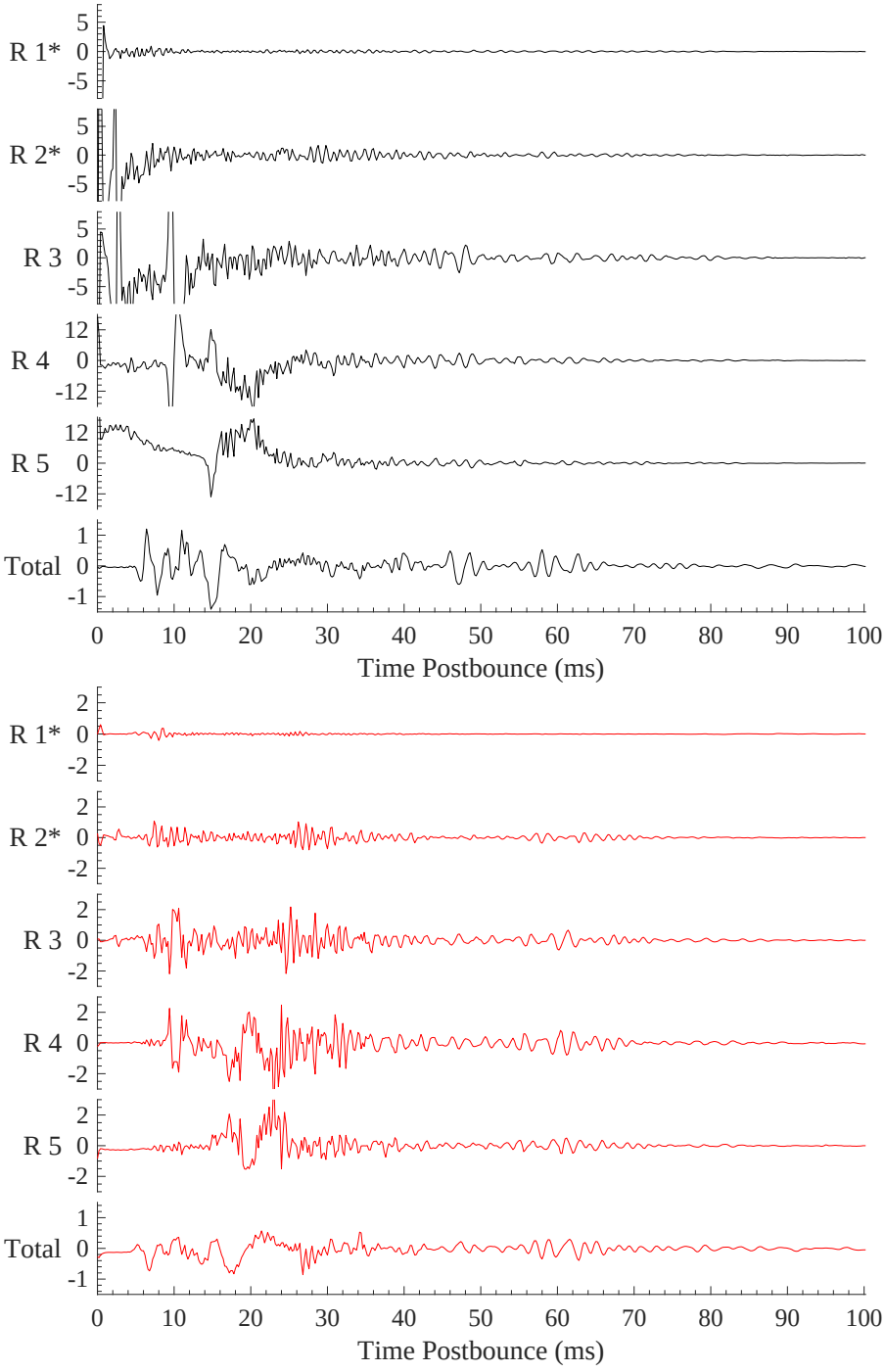


Figure 4.14: Regional strains for D9.6 from 0–100 ms after bounce. The * denotes that regions 1*and 2* are not defined by the convective boundaries of the PNS, which is not well defined during this time. Instead, region 1* is bounded below by the 10^{14} g cm^{-3} density contour and above by the 10^{13} g cm^{-3} density contour. The top of region 1* is the bottom of region 2*.

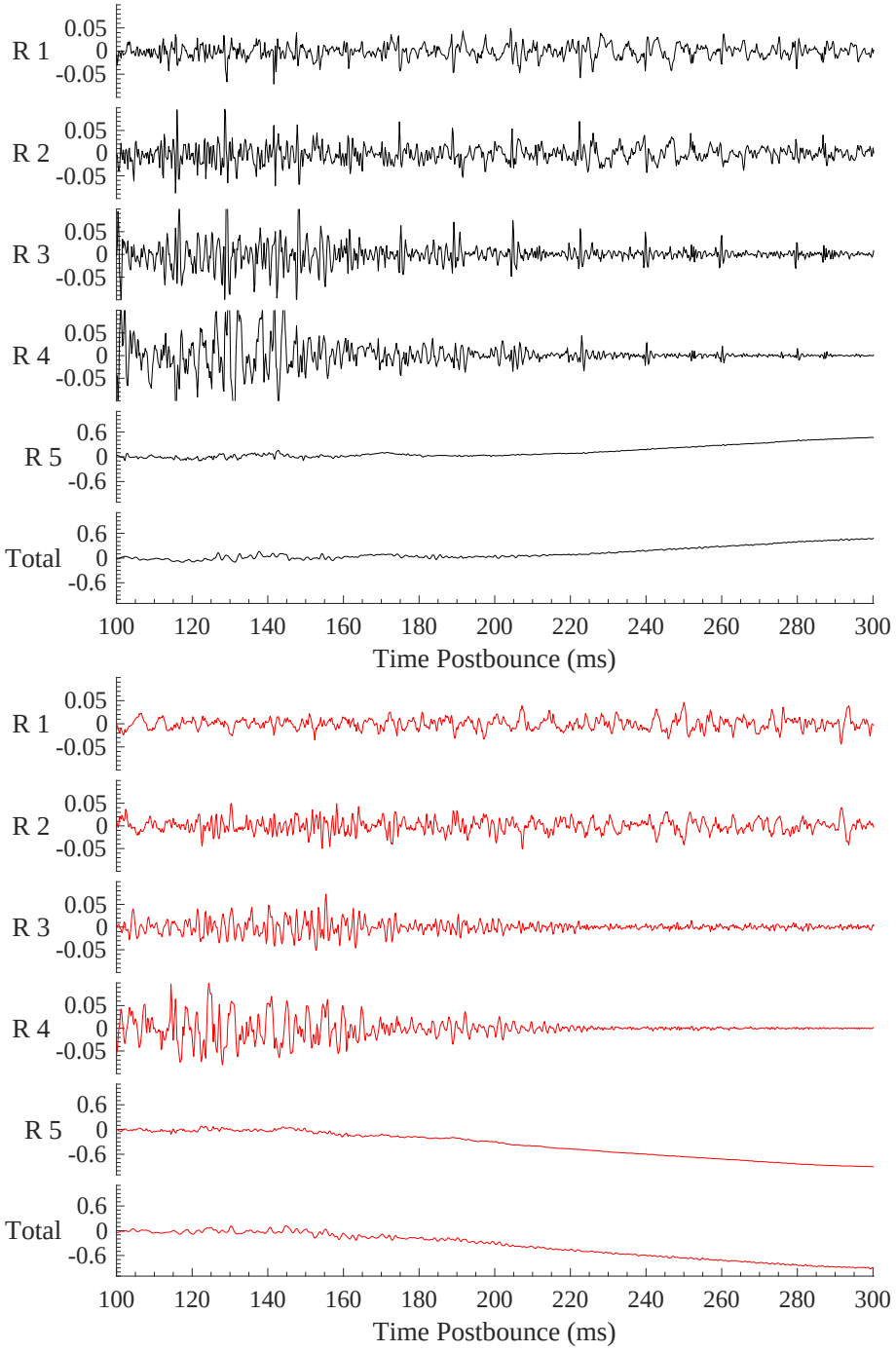


Figure 4.15: Regional strain breakdown for model D9.6.

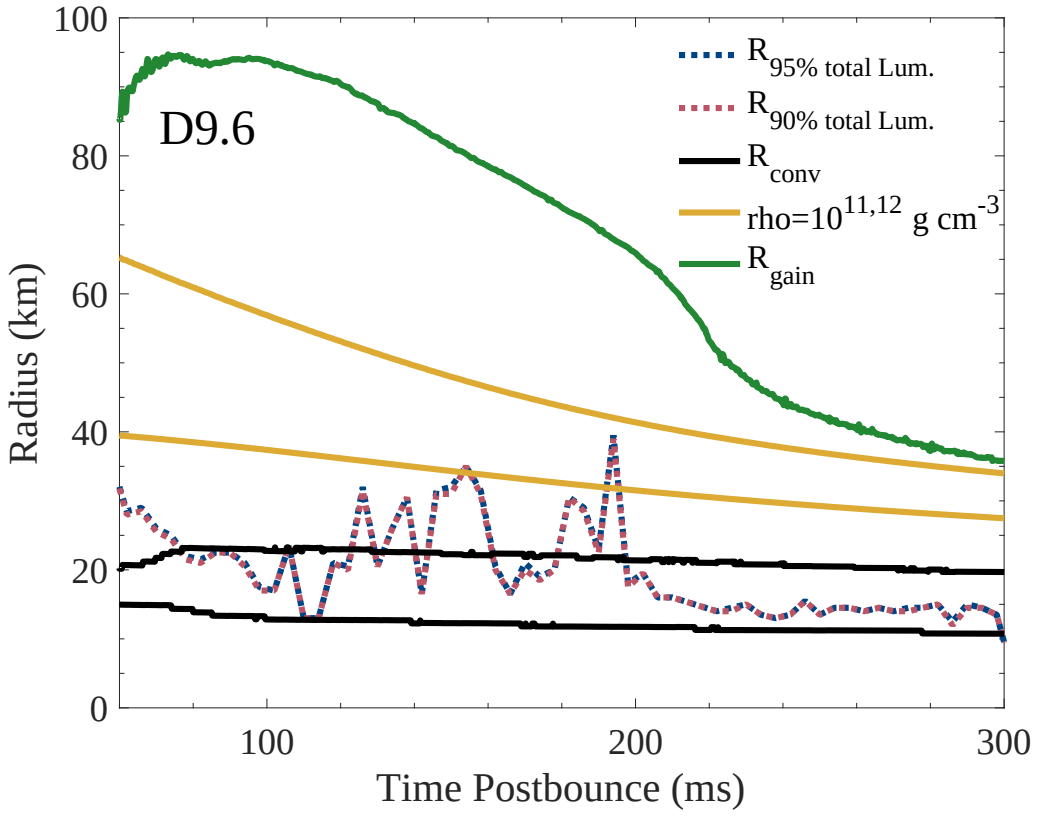


Figure 4.16: Fractional gravitational wave luminosity with respect to time and radius for D9.6.

has decreased by several orders of magnitude when compared to the luminosity before 75 ms postbounce. The weak gravitational waves emitted after this point have the majority of their luminosity being emitted within and below region 1.

In Figure 4.17 we plot the spectrogram for D9.6 with the PNS oscillation mode frequencies identified by our modal analysis overlaid. The spectrogram is produced with the same parameters as for the D25 model (i.e., $\beta = 6$ and 30 ms window segments overlapping adjoining segments by 90%). The same modes describe the HFF as in D15 and D25. While there is significant spectral power density between 1–400 Hz from 100–150 ms postbounce, the ${}^2g_2$-mode sits on top of the strongest feature. The ${}^2g_1$-mode then tracks the HFF from ∼180 ms postbounce to ∼400 ms postbounce. From ∼410 ms postbounce until the end of the simulation, the ${}^2f$-mode tracks the HFF well.

Figure 4.18 shows the gravitational wave emission efficiency by mode in the top panel, and the power radiated as gravitational waves by mode on the bottom panel. As in the D15 and D25 models, the power radiated as gravitational waves is concentrated in region 3 from 100 ms postbounce to ∼190 ms postbounce, with the dominant mode shifting from ${}^2g_2$ to ${}^2g_1$ at ∼170 ms postbounce. From ∼190 ms postbounce to ∼350 ms postbounce gravitational waves are emitted most strongly from region 2 by the ${}^2g_1$-mode. At ∼350 ms postbounce, region 1 begins to dominate the power radiated as gravitational waves in the ${}^2g_1$-mode. Starting at ∼410 ms postbounce, the ${}^2f$-mode becomes the dominate emitter of gravitational waves with regions 1 and 2 approximately equal in the power radiated from them.

4.5 Perturbative Analysis with a Different Boundary

The boundary condition described by Equation (2.201) arises from the association of the PNS surface with a free surface. Westernacher-Schneider (2020) shows that this

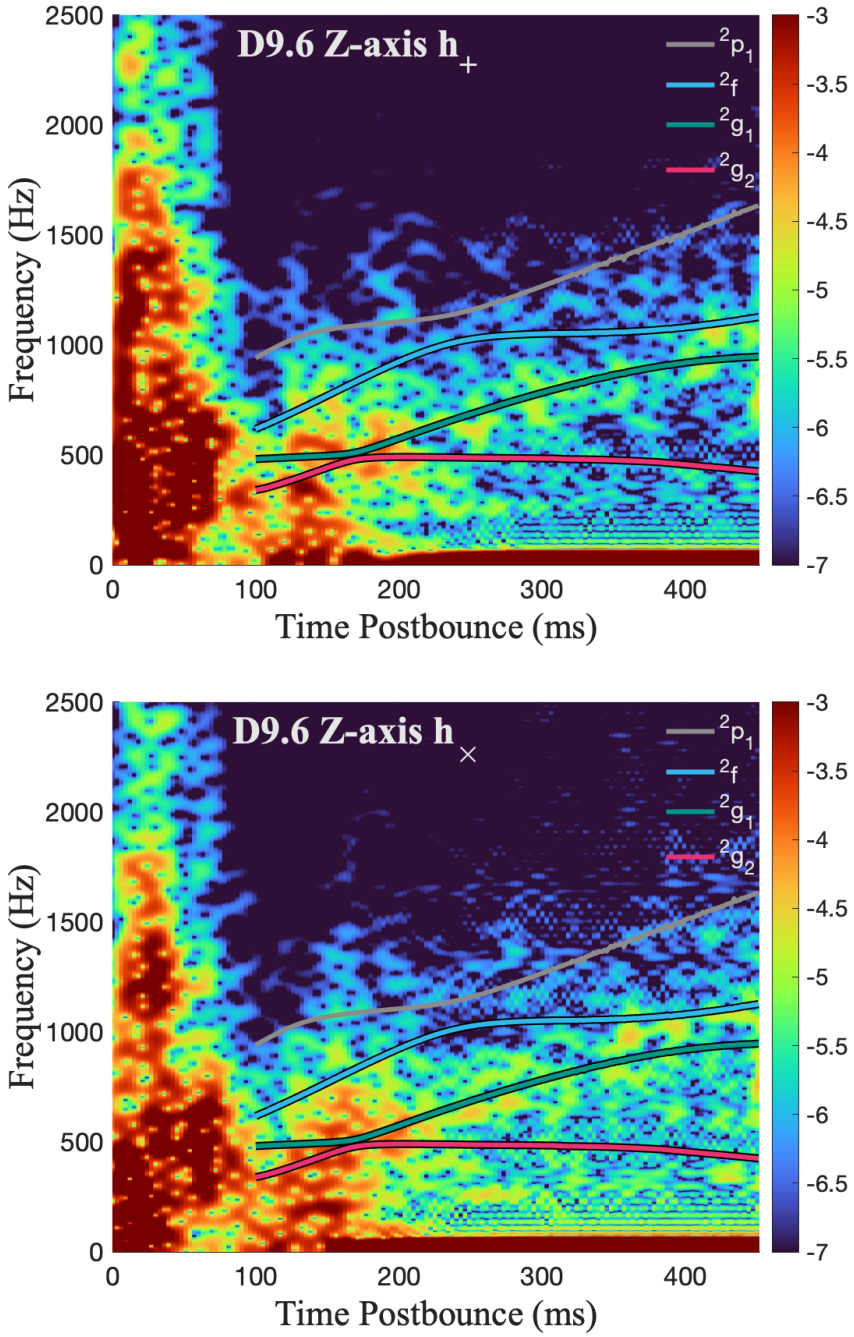


Figure 4.17: Spectrograms and eigenfrequency evolution for model D9.6. The color axis represents the logarithm of the power spectral density $\log_{10}(\mathrm{P})$. The top panel shows the spectrogram of the h_+ signal, and the bottom panel shows the spectrogram of the $h_\times$ signal. Overlaid on each spectrogram are the eigenfrequencies for each mode that lies close to the HFF, labeled according to the GCN classification as described in the text.

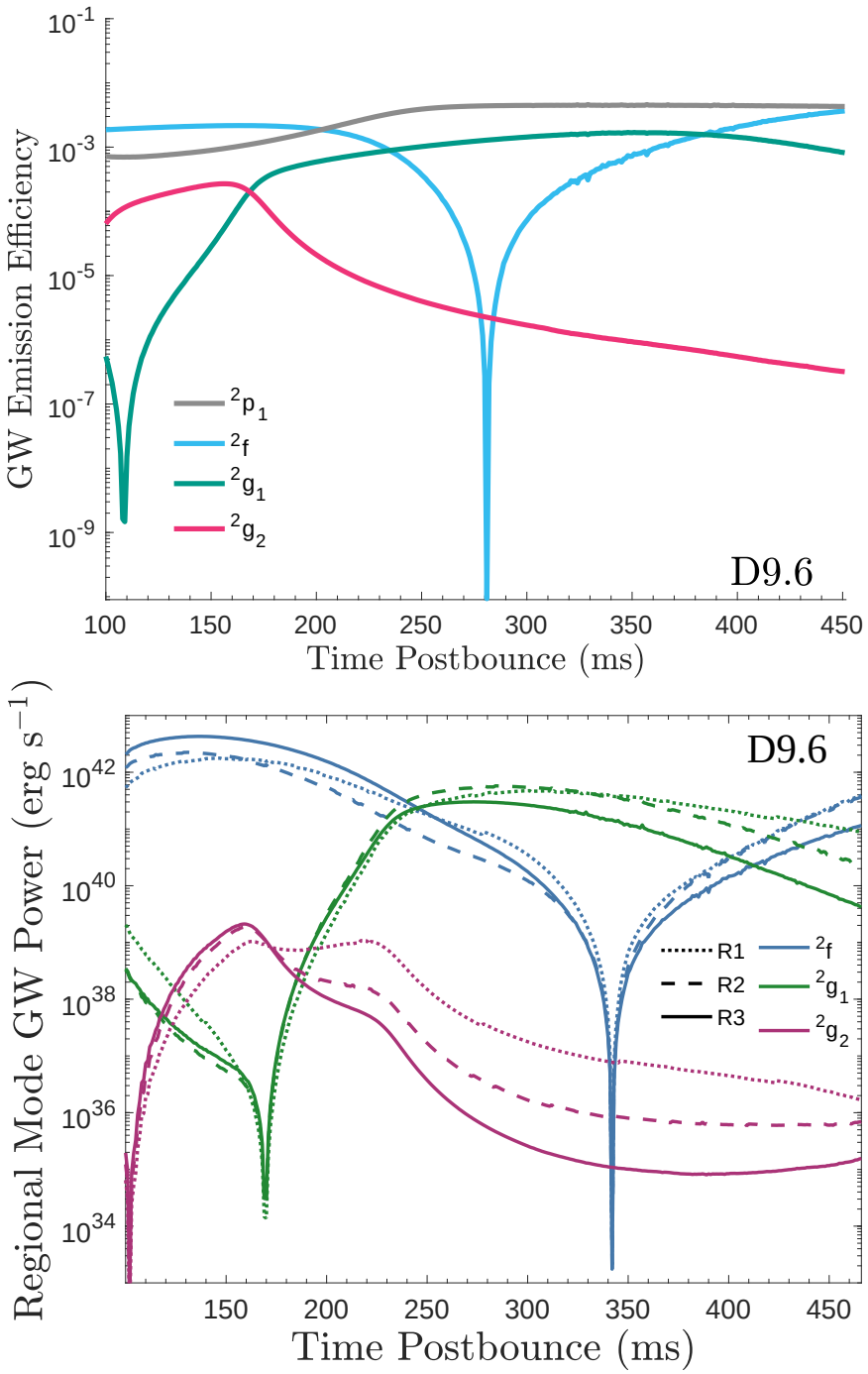


Figure 4.18: Gravitational wave emission efficiency and power output for D9.6. Top panel shows the gravitational wave emission efficiency for D9.6 with different modes denoted by color. Bottom panel shows the gravitational wave power output by each PNS oscillation mode, as denoted by color, from each region, as denoted by line type.

condition can effectively be applied at different density contours, and some studies find better agreement between the eigenfrequencies from their modal analysis and the HFF when the boundary condition is applied at the 10^{10} g cm^{-3} density contour (Torres-Forné et al., 2018, 2019b; Morozova et al., 2018). While it is not directly plotted in Figures 2.1 and 4.12, before ∼300 ms after bounce hydrostatic equilibrium is not violated to any greater degree at the radius of the 10^{10} g cm^{-3} density contour. After ∼300 ms postbounce, this is no longer the case and the PNS surface as we define it is the safer choice of boundary. We justify our choice of boundary based on a physically consistent definition of the PNS, i.e., the flavor- and energy-averaged radius at which neutrinos cease to be transported through diffusion processes. To quantify the effects of moving the boundary, for the D15 model we present the eigenfrequencies found by our modal analysis when we apply the boundary condition at this larger radius in Figure 4.19.

During the time that the hydrostatic boundary condition is less violated (i.e., before ∼300 ms after bounce), the modal analysis finds frequencies that do *not* match well with the HFF. Instead, the HFF seems to be bounded by the ${}^2g_1$- and ${}^2f$-modes, with the ${}^2g_2$-mode not matching with the HFF at all. At late times, the ${}^2f$-mode underestimates the HFF frequency. There are many more avoided crossings in this case, and their interpretation is not straight forward. The ${}^2p_1$-mode is much closer to the HFF from 300–500 ms postbounce as well. Overall, the fit to the HFF is less conclusive in this case, and it does not resolve the minor issues present in the analysis with the boundary at 10^{11} g cm^{-3} (e.g., early ${}^2p_1$-mode still has high efficiency, but does not track any feature in the spectrogram).

4.6 Summary

For the spatial decomposition of the gravitational wave emission, we computed, as in Mezzacappa et al. (2023), the gravitational wave strains from five separate regions: (i) the region of sustained Ledoux convection deep within the PNS, at densities above

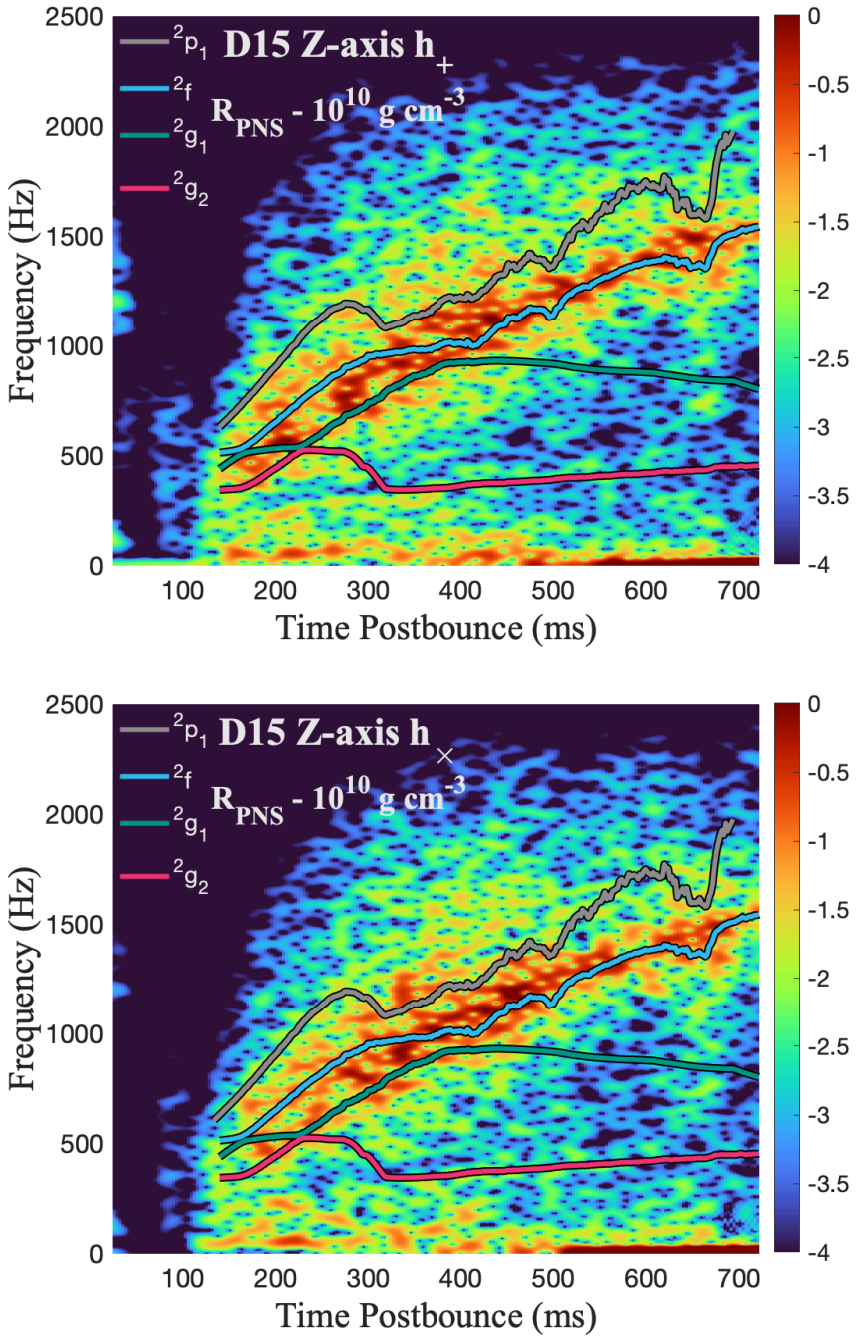


Figure 4.19: Eigenfrequency evolution with the 10^{10} g cm^{-3} density contour as the outer boundary in our modal analysis overlaid on the $h_{+/\times}$-polarized spectrograms for D15.

10^{12} g cm^{-3} (region 1), (ii) the region of convective overshoot (region 2), (iii) the surface layer of the PNS, below a density of 10^{11} g cm^{-3}, which we use to define the PNS surface (region 3), (iv) the net neutrino cooling layer between the PNS surface and the gain radius (region 4), and finally, (v) the region above the gain radius (region 5). For the two models considered here, the general evolution of the gravitational wave strain amplitudes by region is well described as follows: (i) The strains start with small amplitudes in region 4 at ∼100 ms postbounce. (ii) The strain amplitudes rise to similar levels in region 3 by ∼110 ms postbounce. (iii) The strain amplitudes of region 2 become comparable to those of regions 3 and 4 by ∼160 ms postbounce. (iv) Simultaneously, the strains in region 1 also increase but remain slightly below those of regions 2, 3, and 4. (v) The strains in regions 1 and 2 continue to grow while, starting at ∼440 ms postbounce for D15 and ∼300 ms postbounce for D25, the strains in regions 3 and 4 begin to decrease. (vi) The strains in region 1 and 2 become approximately constant, on average, with the highest amplitude strains.

In addition to computing the gravitational wave strains by region and, in particular, following the evolution of the strain amplitudes, we computed the fractional gravitational wave luminosities for our two models, as a function of radius from the center of the PNS. The strains are decomposable by region and can be added to give the total strain. The regional luminosities cannot be added to obtain the total value, but its approximate localization can be accomplished by integrating outward in radius. We find in both of our models that the evolution of the radius within which 90–95% of the luminosity produced is consistent with the evolution of the largest strains, with the 90–95% luminosity contours moving inward with postbounce time from regions 3 and 4 to regions 1 and 2.

The modal analysis, which complements the spatial analysis, as shown in Figures 4.9, 4.10 and 4.11, together providing a more complete picture, affords a third window onto the sources of gravitational emission. We computed a measure of the power emitted as gravitational waves in each region. At the beginning of the HFF, the ${}^2g_2$-mode is the most powerful, neglecting the early evolution of the ${}^2f$-mode, and

region 3 dominates. (Recall that our modal analysis does not extend past region 3.) By ∼180 ms postbounce, the ${}^2g_1$-mode becomes dominant, and regions 2 and 3 radiate gravitational waves with approximately the same power. Over the next ∼30 ms, by ∼210–220 ms postbounce, region 2 becomes the dominant production region of gravitational waves. By ∼360 ms for D15 and ∼420 ms for D25, the ${}^2f$-mode has become the dominant producer of gravitational waves. In the D15 model, the dominant region remains region 2 until region 1 becomes slightly larger at the end of the simulation. For D25, region 1 becomes dominant ∼330 ms and remains dominant for the rest of the simulation.

Thus, all three approaches to sourcing the gravitational wave emission in models D15 and D25 combine to elucidate our understanding of gravitational waves more completely and, moreover, tell a consistent story: Gravitational wave emission is dominated early by the PNS surface layers, as material accretes onto the PNS surface during the development of explosion, and dominated later by the region of sustained Ledoux convection and the region of convective overshoot, deep within the PNS, as explosion develops and accretion onto the PNS surface decreases.

The D9.6 model has quite different characteristics from D15 and D25. The inability of the modal analysis to capture several features from 0–80 ms postbounce points to a clear breakdown in the assumptions of the modal analysis. Since hydrostatic equilibrium is not violated to a much greater degree within the PNS than in the D15 or D25 models, it seems that the poor match is a result of the analysis domain not capturing the full domain of the oscillations. Likely, to accurately capture the motion behind the shock in a modal analysis the perturbative equations will need to allow for a non-stationary background. After ∼100 ms post bounce, the D9.6 model follows the same evolution of modes that track the HFF and the location of the power radiated as gravitational waves as seen in the D15 and D25 case. While the story seen by modal analysis is the same, the context remains different. While the dominant region for gravitational wave power emission is region 2, the strains after 100 ms postbounce are over an order of magnitude lower than those from 0–100

ms postbounce. Thus, the main driver of gravitational wave emission in D9.6 is from outside the PNS, where our modal analysis currently cannot be applied. Even so, the modal analysis does capture the behavior of the HFF well.

4.7 Comparison to Other Work

We focused our modal analysis on the prominent, canonical HFF present in our spectrograms and the spectrograms from other modeling groups. To label our eigenfrequencies, we used the GCN classification scheme. The modes that track the HFF in our two models are the ${}^2g_2$-mode at the onset of the HFF, the ${}^2g_1$-mode beginning at ∼180 ms postbounce, and the ${}^2f$-mode at ∼360 ms postbounce for D15, and at ∼420 ms postbounce for D25. Just as the HFF itself is highly sensitive to progenitor parameters (*e.g.*, the effects of varying mass, demonstrated in Andresen et al. (2017); Vartanyan et al. (2019a)), this sensitivity is also present in the transition times, or avoided crossing times, observed in our two models. This evolution of the HFF from low-order ${}^2g_n$-modes to the ${}^2f$-mode is consistent with the findings from three-dimensional models in Radice et al. (2019) and Nakamura et al. (2022), as well as the findings from two-dimensional models in Sotani and Takiwaki (2020b); Morozova et al. (2018); Zha et al. (2024); Sotani et al. (2024).

Using *indirect* rather than direct methods in the context of three-dimensional models, others have concluded that gravitational wave emission from the PNS is excited primarily from outside Radice et al. (2019); Powell and Müller (2019); Vartanyan et al. (2023). In particular, Radice et al. (2019) calculate the flux of the accreted turbulent kinetic energy at the surface of the PNS and show a trend between it and the total gravitational wave energy emitted, across a range of progenitors from 9–60 $M_\odot$. Powell and Müller (2019) find that this empirical relationship between the turbulent kinetic energy flux onto the PNS and the emitted gravitational wave energy fits the emission from their models, as well, for an ultra-stripped 3.5 $M_\odot$ helium core and an 18 $M_\odot$ progenitor. Additionally, Powell and Müller (2019) also

show that the non-radial kinetic energy within the convective zone of the PNS in their models grows over the same time period that the *total* gravitational wave strain amplitudes are decreasing. With regard to the latter, we *too* see our total strains decrease with time, as we have shown, as the contributions from the surface layers *decrease* and the contributions from the convective and convective-overshoot layers are more or less sustained over the later periods of our runs. Therefore, a decrease in the *total* strain does *not* imply that the primary excitation mechanism of gravitational wave emission from the PNS is accretion onto it *at all times*. A similar analysis was conducted by Vartanyan et al. (2023), who correlated turbulent accretion onto the PNS with periods of maximum strain. Again, as we have shown here, we *expect* the period of maximum strain to correspond to the period in which *all* regions we have defined here contribute significantly to gravitational wave emission—i.e., when we have significant surface emission, excited by accretion onto the PNS, *and* significant emission from the convective and convective-overshoot layers, excited by sustained Ledoux convection. The total strain does not, and cannot, tell us how the strain is *partitioned* over the regions of the PNS. Therefore, it cannot tell us that the strains in the convective and convective-overshoot regions remain large after the total strain has dropped off as accretion-induced strains drop off. Our results, based on *direct* methods, show that the origin of the high-frequency gravitational wave emission in core collapse supernovae, which stems from the PNS, is generally more complex than has been assessed by other methods, and time-dependent.

Finally, in the modal analysis by Zha et al. (2024), based on two-dimensional axisymmetric CCSN simulation data, they find that the same eigenmodes we have identified here as best fitting the HFF in our spectrograms also fit the HFF in their spectrograms, namely the ${}^2g_2$-, ${}^2g_1$-, and ${}^2f$-modes, with early times after bounce matched by ${}^2g_n$-modes with more nodes, up to $n = 4$. They emphasize that the eigenfunctions that best match the HFF are *global*—i.e., that the amplitudes of the eigenfunctions are significant throughout the PNS. This global nature is also noted in the perturbative analysis of axisymmetric models in Eggenberger Andersen et al.

(2021a). Our results show the same global character, as seen directly in the amplitudes of the eigenfunctions plotted in Figure 4.7, which are appreciably nonzero throughout the PNS. However, it is clear there exist times when the power output across these regions differs by at least an order of magnitude, especially beyond 300 ms postbounce, between regions 1 or 2 and region 3 as shown by Figure 4.9. That is, while global in nature, the dominant contributions to gravitational wave emission can still be sourced.

Chapter 5

Gravitational Wave Analysis of Two-Dimensional CCSN Simulations

While three-dimensional models are necessary to obtain the greatest physical fidelity, their computational costs currently prohibit their use to investigate the large parameter space of both progenitor effects and physics implementation. To this end, we utilize two-dimension CCSN simulations that include all the same physics as in the D-series, but in an axisymmetric model that removes the azimuthal dimension of the problem. The trade off is the ability to study several CCSN models at once at the expense of a forced symmetry that will not always be present.

This chapter investigates two sets of two-dimensional CHIMERA CCSN simulations and analyzes the production of gravitational waves in each case. The first set of seven models are collectively called the CHIMERA E-series, and each model uses the same non-rotating, Solar metallicity, 15 $M_{\odot}$ progenitor of Woosley and Heger (2007). The nuclear equation of state (EOS) implemented in each model is different, and the explosion dynamics are described in Landfield (2018). The second set of models is known as the CHIMERA F-series, and consists of two models that are started from

progenitors that are nearly identical in all observable properties, but differ in internal structure. The models both use the SFHo nuclear EOS, described in more detail in Section 5.1. The explosion dynamics of the CHIMERA F-series are described in Bruenn et al. (2023).

5.1 Dependence of the Reconstructed Core Collapse Supernova Gravitational Wave High-Frequency Feature on the Nuclear Equation of State in Real Interferometric Data

The work described in this section has been published in Physical Review D. as "Dependence of the Reconstructed Core-Collapse Supernova Gravitational Wave High-Frequency Feature on the Nuclear Equation of State, in Real Interferometric Data." Full citation: Murphy et al. (2024). The text has been edited, where necessary, to conform to the citation style of this dissertation and to reference sections within this dissertation instead of the original manuscript. Sections from the manuscript that have already been covered in this dissertation have been removed here. Section IV in the original manuscript contains results obtained by collaborators at the Laser Interferometer Gravitational Wave Observatory and was written by Alejandro Casallas-Lagos. As I did not contribute directly to those results, I do not include that section in this dissertation.

5.1.1 Introduction

As gravitational-wave–based astronomy continues to mature with the detections of compact binary mergers Abbott et al. (2024, 2023), anticipation is growing for the advancements that will result from the detection of gravitational waves (GWs) from the next Galactic core-collapse supernova (CCSN). While LIGO-Virgo-KAGRA

(LVK) GW interferometers Aasi et al. (2015); Acernese et al. (2015); Aso et al. (2013) work to increase the ability to detect these events, it is the role of CCSN simulations to provide insight on what such detections can reveal about the Universe. This thesis examines theoretical GW signals produced by CCSN simulations that utilized different nuclear equations of state (EOS) and uses current detection capabilities and analysis techniques to demonstrate the ability to resolve differences in GW signals due to different EOS. Our research builds on findings from Casallas-Lagos et al. (2023) and Lin et al. (2023), employing real LIGO interferometric noise from the second half of the O3b observing run Abbott et al. (2023). This noise is analyzed to identify, reconstruct, and characterize the High Frequency Feature (HFF), observed in all CCSN GW signal predictions based on the two- and three-dimensional numerical simulations performed to date.

From the moment of bounce onward, each stage of a CCSN will generate GWs, as described in Abdikamalov et al. (2022) and Mezzacappa and Zanolin (2024). The present study focuses on the high-frequency GW signal arising from accretion onto the PNS, as well as sustained Ledoux convection due to lepton gradients deep within the PNS. These lepton gradients become large enough to cause Ledoux convection in the PNS around 100 ms postbounce and are sustained for on the order of seconds as neutrinos continue to diffuse out of the PNS. During this time, the PNS contracts. This contraction causes the frequency of the GWs produced by Ledoux convection to increase with time until the PNS reaches a stable radius, at which point the GW frequency remains constant while Ledoux convection continues. We call this feature the High Frequency Feature (HFF), using nomenclature introduced in Casallas-Lagos et al. (2023). Based on analysis of the quasi-normal modes of oscillation of the PNS, previous studies have concluded that the HFF corresponds to the frequency evolution of either a g-mode oscillation (Marek et al., 2009; Cerdá-Durán et al., 2013; Kuroda et al., 2017; Müeller et al., 2013; Kawahara et al., 2018) or a combination of g-mode and f-mode oscillations (Sotani and Takiwaki, 2016; Morozova et al., 2018; Torres-Forné et al., 2018, 2019a; Radice et al., 2019; Sotani and Takiwaki, 2020b; Sotani

et al., 2021; Zha et al., 2024). The classification of these modes may connect to the PNS properties, but such analysis is beyond the scope of this chapter.

In CCSN simulations, the EOS not only connects the state and thermodynamic variables, but also regulates the radius and contraction of the PNS. An EOS is called 'stiff' if it has more resistance to compression and thus yields a larger neutron star radius, and 'soft' if it is more easily compressed, yielding a smaller neutron star radius. Different EOS result in different dynamical evolution of the PNS and influence gravitational wave generation from bounce and for several seconds afterwards as the PNS evolves. A clear goal of gravitational wave analysis, therefore, is to quantify the differences in gravitational wave signals that arise from different EOS. In addition to the HFF, prominent gravitational wave features often studied in connection to the EOS in CCSN simulations are the Standing Accretion Shock Instability (SASI) (Marek et al., 2009; Kuroda et al., 2016a, 2017; Kotake et al., 2017; Powell et al., 2021; Kuroda et al., 2022), which generates gravitational waves at lower frequencies, and the gravitational wave burst and subsequent ring down caused by core bounce for models with rotation (Dimmelmeier et al., 2008; Yasutake et al., 2007; Eggenberger Andersen et al., 2021b; Richers et al., 2017; Afle and Brown, 2021a; Mitra et al., 2024).

Early connections between gravitational wave signals in CCSNe and the EOS were noted in Seidel et al. (1988). Using an EOS that parameterized the stiffness of the EOS in spherically symetric simulations, they found that stiffer parameterizations led to slightly more efficient gravitational wave production. Marek et al. (2009) investigated the gravitational wave and neutrino emissions in two-dimensional CCSN numerical simulations using a 15 $M_{\odot}$ progenitor, comparing stiff and soft EOS. They observed that PNS formed under the soft EOS, being more compact, generated gravitational waves of higher amplitude than those produced under the stiff EOS, after 100 ms post-bounce. Additionally, they noted that (i) the peak frequency of the waveform spectrum for the HFF was above 300 Hz, (ii) the peak frequency for the SASI was below 200 Hz, with (iii) both frequencies being elevated in the case of the softer EOS.

Eggenberger Andersen et al. (2021b) used EOS models based on a Skyrme-type force to investigate the sensitivity of the effective nucleon mass and isoscalar incompressibility modulus on the gravitational wave signal in two-dimensional CCSN simulations. They found that the peak of the gravitational wave frequency spectrum $f_{\rm peak}$ increases with effective nucleon mass parameter, while no variations seemed to occur in the gravitational wave signal from variation of the isoscalar incompressibility modulus parameter. This effect persisted in simulations with central angular speeds of 1 rad $\rm s^{-1}$, though the gravitational wave amplitudes decreased, and the effect was not discernible at central angular speeds of 2 rad $\rm s^{-1}$. Additionally, this study produced second-order polynomial fits to the HFF and reported different coefficients across the nucleon effective mass parameter.

Morozova et al. (2018) compared calculated PNS oscillation frequencies directly with gravitational wave signals produced from two-dimensional CCSN simulations of 10, 13, and 19 $M_\odot$ progenitors. Quantitative differences were reported for gravitational wave amplitudes, gravitational wave energy emitted, and for the frequencies of PNS quasi–normal-mode oscillations across the three EOS they considered and for each progenitor mass. At later times, the f-mode oscillations matched well with the peak frequency evolution of the gravitational wave signal, and a quadratic polynomial fit using the f-mode oscillation frequencies resulted in distinct coefficients for each EOS.

Camelio et al. (2017) investigated the oscillation modes of the PNS using three different EOS, and found that the time it took the PNS to reach the maximum (minimum) oscillation frequency of the f-(g-)mode varied by as much as 0.5 seconds. Using data from one-, two-, and three-dimensional CCSNe simulation data, Sotani and Takiwaki (2020b) computed PNS oscillation frequencies and found only minor differences in their evolution using the DD2 and TGTF EOS. By analyzing the f-mode PNS oscillations together with spacetime oscillations, w-modes, Sotani (2019) determined the different mass and radius evolution of the PNS for a CCSN model using a 15 $M_\odot$ progenitor and both the SFHx and TM1 EOS, in the absence of noise.

Universal relations describing the gravitational wave peak frequency evolution as either an f- or g-mode were investigated in Torres-Forné et al. (2019a); Sotani et al. (2021); Wolfe et al. (2023). Bizouard et al. (2021); Bruel et al. (2023) investigated parameter estimation using universal relations in Gaussian simulated noise. In each study, different EOS were considered, but the focus was the accuracy of the parameterization independent of the EOS. A similar modal analysis and universal relation study for the data presented here could be performed but is beyond the scope of this chapter.

Yasutake et al. (2007) studied gravitational wave signals from CCSN simulations using a phenomenological EOS that allowed for a first-order quantum chromodynamics (QCD) phase transition. In the absence of rotation, they saw a 10% increase in gravitational wave amplitude immediately after bounce when compared to the same EOS without a phase transition. Zha et al. (2020) combined the STOS EOS with the MIT bag-model EOS to study similar QCD phase transitions in CCSNe. They found that the core experienced a secondary collapse at the QCD phase transition that resulted in gravitational wave amplitudes 30 times stronger than typical signals from purely hadronic EOS.

For failed CCSNe, Pan et al. (2018) investigated the gravitational wave signals from black-hole–producing two-dimensional CCSN simulations starting from a 40 $M_\odot$ progenitor, using four different EOS. They noted visible differences in the characteristic strain evolution $h_{\rm char}$, and they also noted that black-hole–formation times varied from 450 ms to 1300 ms across the EOS used. In the context of pulsational pair instability supernovae, Powell et al. (2021) investigated gravitational wave signals in Gaussian noise for current and future detectors for 85 and 100 $M_\odot$progenitors, using the LS220, SFHo, and SFHx EOS. They find that the HFF increases slowest for SFHx and fastest for LS220.

Jakobus et al. (2023) examined the gravitational wave signals from two-dimensional general relativistic CCSN simulations starting from 35 $M_\odot$and 85 $M_\odot$progenitors, using the SFHx EOS as well as a chiral mean field EOS with a smooth crossover to

quark matter. The CMF EOS causes the HFF to increase slightly faster than the SFHx EOS, for both progenitors. They also identified a low-frequency feature that decreases in frequency with time. In the SFHx models, this feature only appeared in the 85 $M_{\odot}$progenitor, but it was of much higher frequency and decreased more slowly than in the CMF EOS models. This feature emanated from deep within the core of the PNS, allowing for its use as a probe to study nuclear matter beyond nuclear saturation density.

Beyond the effects of EOS, the progenitor properties can affect the HFF as well. Rotation of the progenitor tends to have a stabilizing effect on the radius of the PNS, leading to a slower contraction time. This would tend to decrease the slope of the HFF as seen, *e.g.*, in Andresen et al. (2019); Pajkos et al. (2019, 2021); Pan et al. (2021); Takiwaki et al. (2021). The mass of the progenitor will affect the amplitude of the GW strains, as well as the slope of the HFF (Andresen et al., 2017; Vartanyan et al., 2019b; Mezzacappa et al., 2023), though a systematic study is necessary to quantify the effect more precisely. Additionally, Wang and Pan (2024) and Jardine et al. (2022) show that the internal structure of the progenitor and the presence of strong magnetic fields can affect the HFF slope, respectively. In this study, we choose to study the effects of the EOS on the HFF in isolation of all progenitor parameters. In essence, we are assessing the maximum amount of information that could be gathered about the EOS, at least in our approach, in the event of a Galactic core collapse supernova gravitational wave detection, assuming that all of the other parameters affecting the HFF slope are known.

Previously, Casallas-Lagos et al. (2023) formulated a machine learning (ML) approach using real LIGO interferometric noise to estimate the slope of the HFF peak over time across different two- and three-dimensional CCSN models incorporating distinct EOS. The results indicated that the HFF slope is influenced by factors such as the progenitor mass, rotation, metalicity, and EOS. In scenarios with non-rotating progenitors and consistent EOS across CCSN simulations, the HFF slope without noise ranged from 3406, 1907, to 1288 Hz s^{-1} for progenitors of 15, 20, and 35 $M_{\odot}$,

respectively, demonstrating variability in HFF slopes up to 63% for a mass change of 57%. For a 15 $M_{\odot}$ progenitor rotating at 0.5 rad s^{-1}, the HFF slope found was 2246 Hz s^{-1}, reflecting a 34% reduction from its non-rotating counterpart of the same mass. These signals were introduced into real interferometric LIGO noise through a cWB event production analysis, in standard configuration, for different Galactic distances 1, 5, and 10 kpc. The ML algorithm managed to predict the slope with an error under 10% for nearly all models except three. Moreover, the orientation of the source was found to have a minimal impact on the slope estimation of the HFF, despite variations in the intensity of CCSN GW signals with orientation, as discussed in Müller (2020); Morozova et al. (2018). Differences in HFF slope due to orientation angle with the GW source were under 5%. The study confirmed the reliable estimation of the HFF slope in real interferometric noise and highlighted several physical parameters that influence this estimation.

This thesis continues the development of the HFF as a tool to gain physical insight from Galactic-CCSN-produced gravitational wave signals and, in particular, examines the effects of the EOS on it. We extract GW signals from two-dimensional, axisymmetric CCSN simulations Landfield (2018); Landfield et al. (2024) performed with the Chimera code Bruenn et al. (2020). Five models were considered that employed five distinct EOS in the CCSN simulations: DD2, FSUGold, IUFSU, SFHo, and SFHx. These EOS were chosen for their compatibility with current experimental and observational constraints, as discussed in Tews et al. (2017). We note, these EOS do not cover the full range of permissible EOS. Discussions on the explosion characteristics of the two-dimensional simulations can be found in Landfield (2018). These GW signals are first analyzed in the absence of noise to determine the intrinsic differences in HFF slope due to differing EOS in the models considered and signal processing settings. Using these intrinsic slope values, we then investigate our ability to resolve different EOS through the detection of GWs and analysis of the HFF using real interferometric LIGO data in a Coherent-Waveburst (cWB)-event production analysis Klimenko et al. (2016). Our results spans Galactic distances of 1, 5, and 10

kpc in an equatorial orientation, but varying orientations are achievable by adjusting the term $1/r$ equivalently to a multiplication by the cosine of the orientation angle θ, as detailed in Creighton and Anderson (2011).

5.1.2 Chimera E-series Simulations

The two-dimensional simulations used in this section are from the E-series examination of nuclear EOS effects Landfield (2018); Landfield et al. (2024). The simulations are referred to by the EOS label such that the simulation implementing the DD2 EOS will be referred to as E-DD2. The initial conditions for each simulation are that of the 15 $M_\odot$ pre-supernova progenitor of Woosley and Heger (2007), which is a non-rotating progenitor of Solar metallicity. The same 15 $M_\odot$ progenitor is used in the three-dimensional simulation in Mezzacappa et al. (2023) from which we compare two- and three-dimensional results. For the two-dimensional simulations, there are 720 adaptive radial zones and 240 angular zones of fixed angle. The radial zones redistribute with time to sufficiently resolve the shock and the PNS surface.

5.1.3 Included Equations of State

Each of the EOS used in the E-series uses a relativistic mean field (RMF) approximation to model nuclear interactions. They differ in the method of parameterization of the RMF, and in how the values for those parameters are determined. Each of these EOS extend nuclear statistical equilibrium (NSE) models, applicable from low densities up to a few tenths of nuclear saturation density, to RMF-based models to capture the high-density behavior of the EOS. In NSE, the ensemble of nuclei and non-uniform nuclear matter are represented via a statistical model as described in Hempel and Schaffner-Bielich (2010). Nuclei are treated as Maxwell-Boltzmann particles, and the nucleons are treated with RMF models. This representation includes several thousand nuclei with binding energies either taken from experimental measurements or theoretical nuclear structure calculations. Where

nuclear structure calculations are used, they are calculated using the same RMF parameterization as the one applied to nucleons, if available.

The DD2 EOS uses a density-dependent (DD) RMF for nuclear interactions (Typel et al., 2010) that come from describing the meson scalar and vector self energies with density-dependent forms. The "2" differentiates it from the original DD EOS (Typel, 2005). The DD EOS used theoretical nucleon masses instead of experimental values as is done for the DD2 EOS.

The FSUGold EOS implements a RMF treatment with additional ω- and ρ-meson couplings in the Lagrangian (Todd-Rutel and Piekarewicz, 2005). This results in softening the EOS of symmetric nuclear matter and modifies the density dependence of the symmetry energy.

The IUFSU EOS builds upon the FSUGold EOS with more recent experimental and observational data (Fattoyev et al., 2010). This introduces two new empirical parameters that affect the EOS at different densities. At intermediate densities, the EOS is softened by reducing the neutron skin thickness of ^{208}Pb. At high densities, the EOS is stiffened by increasing the maximum neutron star mass relative to FSU predictions.

SFHo and SFHx are EOS that use a RMF parameterization that was uniquely fitted using observational neutron star radius determinations Steiner et al. (2013). Each EOS is based on the parameterization of Steiner et al. (2005), with parameters varied such that saturation properties agree with predictions from nuclear masses, giant monopole resonances, and so that the maximum neutron star mass is larger than 1.93 $M_{\odot}$. Additionally, the ordinary model, SFHo, uses the most probable neutron star mass-radius curve from Steiner et al. (2010) to further constrain the parameters of the RMF, while the extreme model, SFHx, attempts to minimize the radius of low-mass neutron stars in its parameterization. As a result of this, the logarithmic derivative of the symmetry energy for SFHx is in the lower part of the acceptable range, 20-120 MeV.

In addition to these five EOS, the E-series also includes a simulation that used the Lattimer-Swesty EOS Lattimer and Swesty (1991) with a nuclear incompressibiliy of $K = 220$ MeV combined with the BCK EOS Baron et al. (1985) at densities below 10^{11} g cm^{-3}, referred to collectively as LSBCK. This EOS was not investigated in terms of resolvability because it is no longer within the allowable region of EOS, as shown in Tews et al. (2017). However, this is the same EOS that was used for the three-dimensional simulations in Mezzacappa et al. (2023). This allows for a separate, but necessary, analysis of the effect of dimensionality on HFF properties, in Section 5.1.6.

5.1.4 Slope Estimation Without Noise

For the spectrograms in this section, the gravitational wave signal was sampled at 5000 Hz. For the windowing function, we chose a shape factor of $\beta = 6$, which approximates a Hann windowing scheme, with 45 millisecond window segments overlapping adjoining segments by 93.$\bar{3}$%. This resulted in spectrograms that were visually well resolved in both the time and frequency domains.

Using the gravitational wave extraction method described in Section 2.1 we obtain the gravitational wave strains plotted in Figure 5.1 for a detection distance of $D = 10$ kpc. Spectrograms of those strains are plotted in Figure 5.2, where the color axis shows the logarithm of the power spectrum, $\log_{10}(P)$. We see evidence of all the gravitational wave features expected from CCSNe, with the exception of the core-bounce signal due to rotation because these models are non-rotating. We see the effects of prompt convection from 10–60 ms in each simulation. The quiescent period is shown from 60–100 ms by the region where the power spectral density drops below the cutoff value on the colormap, indicating weak gravitational wave emission. The HFF starts at some point after 100 ms in the 200–400 Hz range and increases to 1 kHz before 600 ms. Below the HFF, we see the effects of neutrino-driven convection and the SASI, though this is not the focus of this thesis. In each model, at the onset

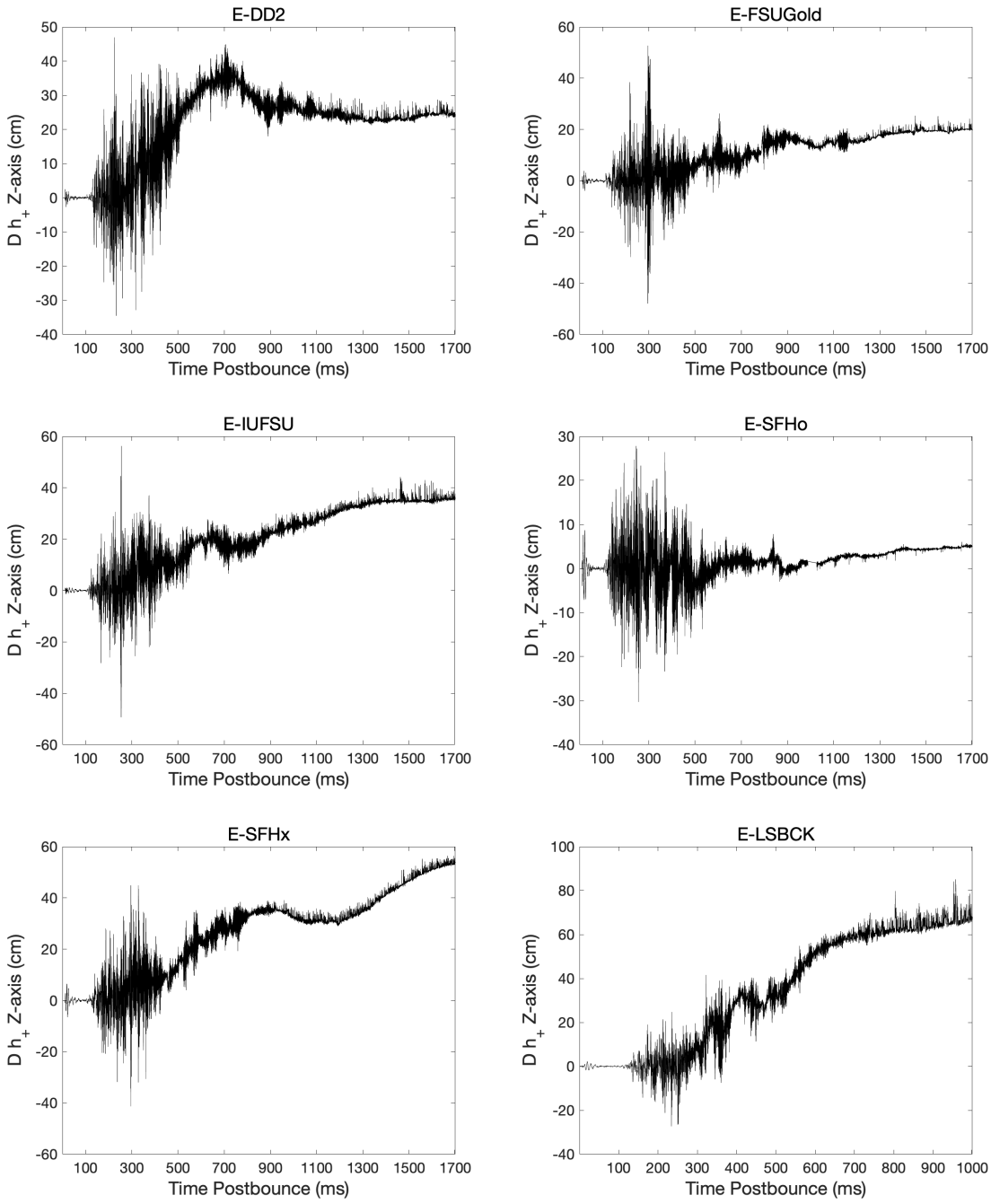


Figure 5.1: Strains for each E-series model computed along the z-axis at the source. The small-amplitude, high-frequency signal at late times, superimposed on the low-frequency signals, and the associated noise seen in our spectrograms, are the result of dynamic spatial regridding and of no physical consequence. The noise is smallest in E-SFHo and largest in E-LSBCK.

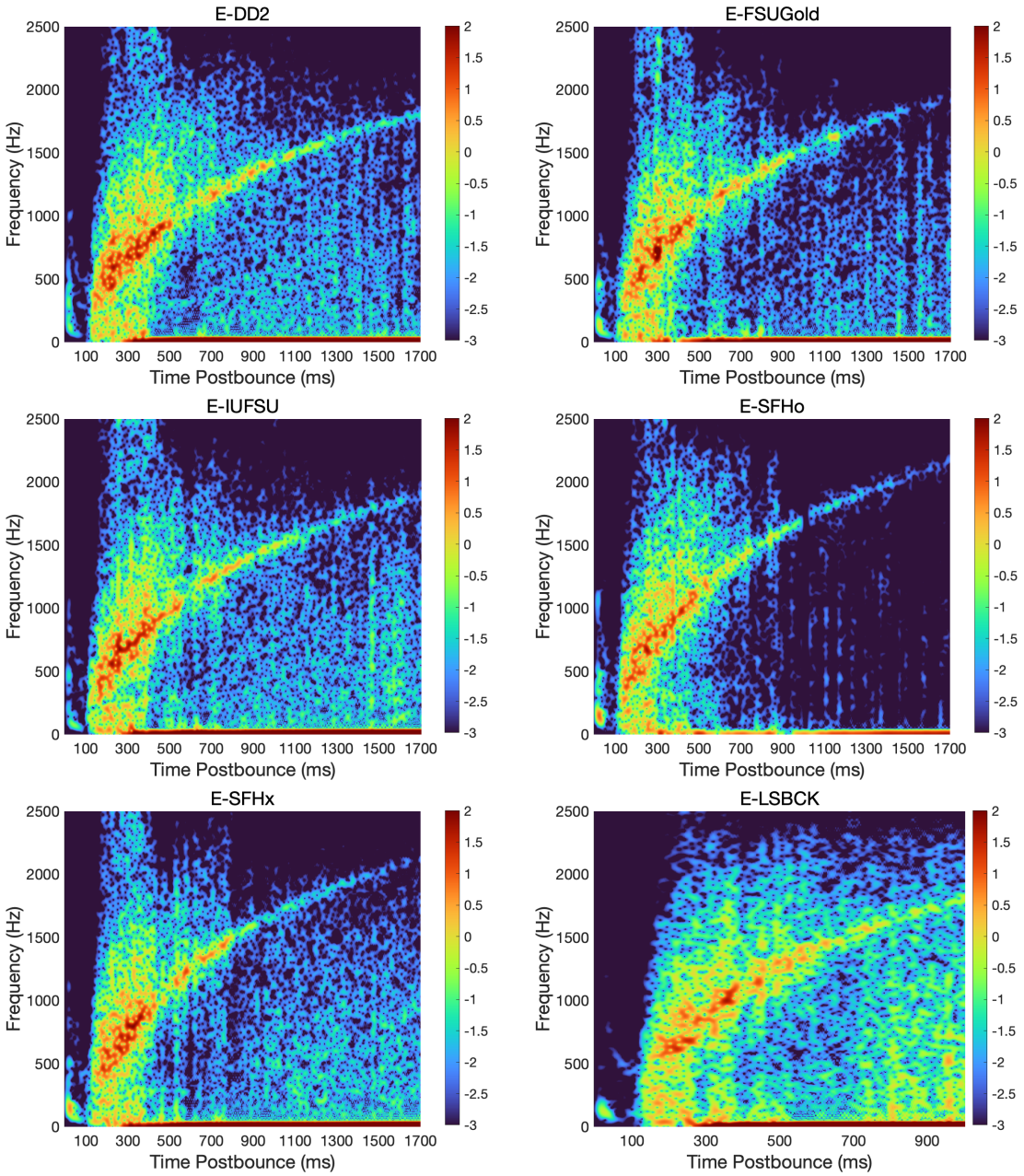


Figure 5.2: Spectrograms for each E-series model, with the color axis showing the logarithm of the power spectrum, $\log_{10}(P)$.

of explosion, there is a feature with high power spectral density at frequencies below $\sim$ 50 Hz, corresponding to gravitational wave memory developing at the onset of explosion. For each model, the HFF persists into late times in the simulation and has not yet plateaued. This is consistent with a PNS that has not yet reached its final radius.

5.1.5 Fit to HFF

As depicted in Figure 5.2, the late-stage behavior of the HFF deviates from linearity. However, as demonstrated in the likelihood maps of Figure 6 in Section IV of Murphy et al. (2024), the likelihood of detecting signals above 1 kHz is low given the present sensitivity of the LIGO interferometers. Hence, our focus, following the approach of Casallas-Lagos et al. (2023), is on the signal beneath 1 kHz where the HFF shows a roughly linear relationship with time. Additional justification for considering the HFF as linear under 1 kHz is provided in Section 5.1.7.

A key factor in determining the slope of the HFF is the choice of the start time of the HFF. As indicated in Casallas-Lagos et al. (2023), this choice influences the estimation of the HFF slope, and points to the need to establish a criterion to uniformly define the initial HFF time. Though the stochastic features on the spectrogram are weaker than the HFF, they are not negligible. As a result, the power spectral densities in Figure 5.2 show signals above the threshold on the color axis in the quiescent period. Including points from this region where the maximum power spectral density rapidly oscillates between frequency bins can strongly impact our estimation of the linear time dependence of the HFF. Therefore, it is crucial to carefully determine the point at which the HFF signal surpasses these signals in strength.

We define this point as the start of the HFF signal, t_{HFF}. If part of the region of the spectrogram in the quiescent period is included in the HFF signal, it can affect the measured slope of the HFF by up to 10%. In order to compare slope

values consistently, we defined $t_{\rm HFF}$ such that it avoids this region of the spectrogram without excluding the beginning of the HFF, across all models. To define $t_{\rm HFF}$, we first determine the maximum power spectral density for a single frequency bin above 50 Hz across the entire time domain. This avoids including the high power spectral densities for low frequencies that are related to the gravitational wave memory and not related to the HFF. See Richardson et al. (2024) for a discussion of the contributions to the CCSN gravitational wave signal below 50 Hz. We then locate the time at which a single frequency bin above 250 Hz – *i.e.* the upper limit for SASI based gravitational wave signals – exceeds 1% of the maximum power spectral density we determined. This frequency bin was chosen by inspection of previous signals to ensure we capture only the HFF signal at early times. Table 5.1 shows the starting frequencies of the HFF at $t_{\rm HFF}$, which are all well above the 250 Hz threshold. This provides a clear demarcation between the noisy signal of the quiescent period and the HFF, as is shown by the gray, dashed line depicting $t_{\rm HFF}$ in Figure 5.3.

Once the start time of the HFF is determined in the noiseless case, we perform a least-squares regression on the frequency bins of maximum power spectral density for

Table 5.1: HFF first-order polynomial approximation coefficients: $f(t) = \alpha t + \beta$.

EOS	α [Hz s^{-1}]	β [Hz]	$t_{\rm HFF}$ [ms]	MAPE [%]
DD2	1451	403.9	125.8	5.655
FSUGold	1802	420.7	138.4	6.198
IUFSU	1631	375.8	118.9	5.906
SFHo	2218	359.3	122.3	8.135
SFHx	2010	410.4	135.4	4.666
LSBCK-2D	2713	394.7	128.5	7.646
LSBCK-3D	2727	359.3	130.1	6.074

Second column gives the first-order time dependence of the HFF, *i.e.* linear slope α. Third column gives the starting frequency of the HFF at $t_{\rm HFF}$, β. Fourth column is the start time of the HFF, $t_{\rm HFF}$, as defined in the text. Fifth column represents the maximum absolute percent error (MAPE) of the actual maximum frequencies A_t and the predicted frequencies F_t for n fitted points, $MAPE = 100\frac{1}{n}\sum_{t=1}^{n}|\frac{A_t - F_t}{A_t}|$.

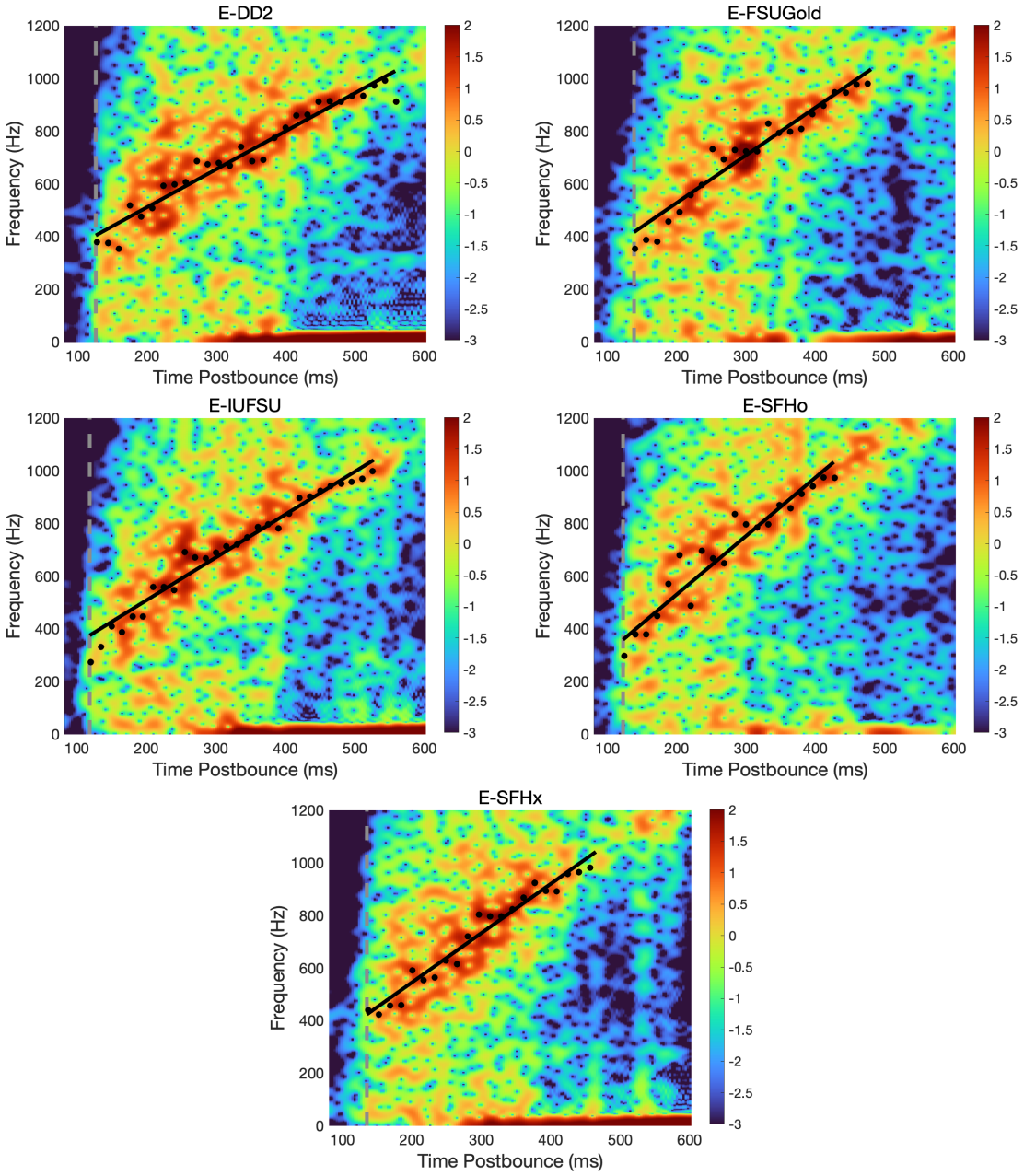


Figure 5.3: Linear-best-fit lines for maximum power spectral density output. The solid, black line is the first-order approximation, $f = \alpha t + \beta$, of the HFF, as described in the text. The gray, dashed lines represent the starting time of the HFF, t_{HFF}.

each time bin of the spectrogram, shown in black circles in Figure 5.3. This regression determines an approximation of the HFF of the form $f(t) = \alpha t + \beta$, with α as the linear coefficient and β as the starting frequency of the HFF. We note that our regression starts at $t = t_{\mathrm{HFF}}$ and not $t = 0$, which would correspond to the time of bounce. The interpretation of β is thus the starting frequency of the HFF, $\beta = f(t_{\mathrm{HFF}})$. Figure 5.4 shows the spectrograms for each model with the linear approximation of the HFF shown as a black line.

Table 5.1 shows the slope of the HFF, starting frequency of the HFF, start time of the HFF (t_{HFF}), and maximum absolute percent error (MAPE) of the linear approximation of the observed peak frequencies. There is a clear difference in the slope of the HFF for each of these models. The slope of the HFF could thus be used to further constrain the allowable EOS for the densities and temperatures present during CCSN events. How tightly this coefficient could constrain the allowable EOS will be discussed in section 5.1.8.

5.1.6 Dimensionality Comparison

The artificiality of axisymmetry in these two-dimensional models amplifies modes aligned with the symmetry axis, and the inverted turbulent cascade favors the formation of large eddies in post-shock neutrino-driven convection. As a consequence, larger gravitational wave strains are produced (Mezzacappa et al., 2020; O'Connor and Couch, 2018). Therefore, it is necessary to demonstrate the impact of axisymmetry on the HFF and its detection. Thus, we also conducted an analysis for a single EOS used in Chimera simulations in both two and three dimensions. While the three-dimensional simulation was not carried out to late times, the HFF exceeds the 1 kHz threshold within the first few hundred milliseconds.

In Figure 5.5, the spectrograms for the two- and three-dimensional simulations using the LSBCK EOS are shown. The beginning of the HFF was defined with t_{HFF}

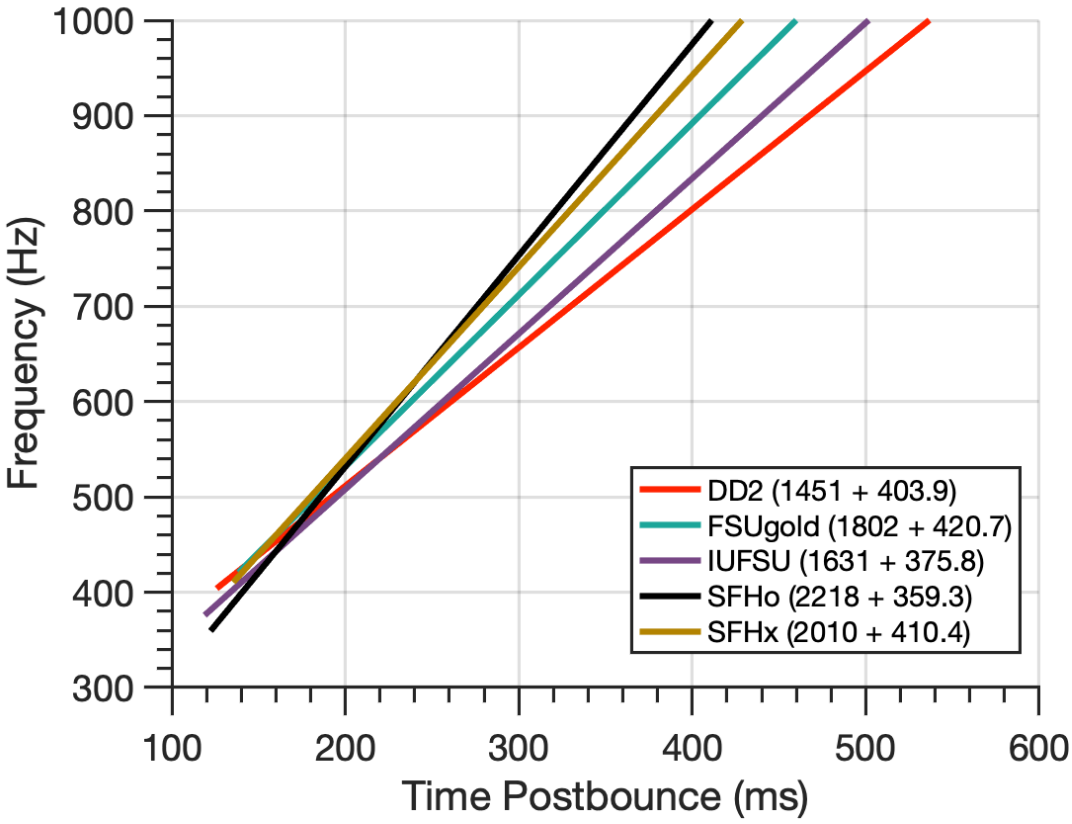


Figure 5.4: First-order HFF approximations without noise, across E-series models. ***N.B., This figure has been reproduced with the exact same data from Murphy et al. (2024) to better fit within this dissertation.***

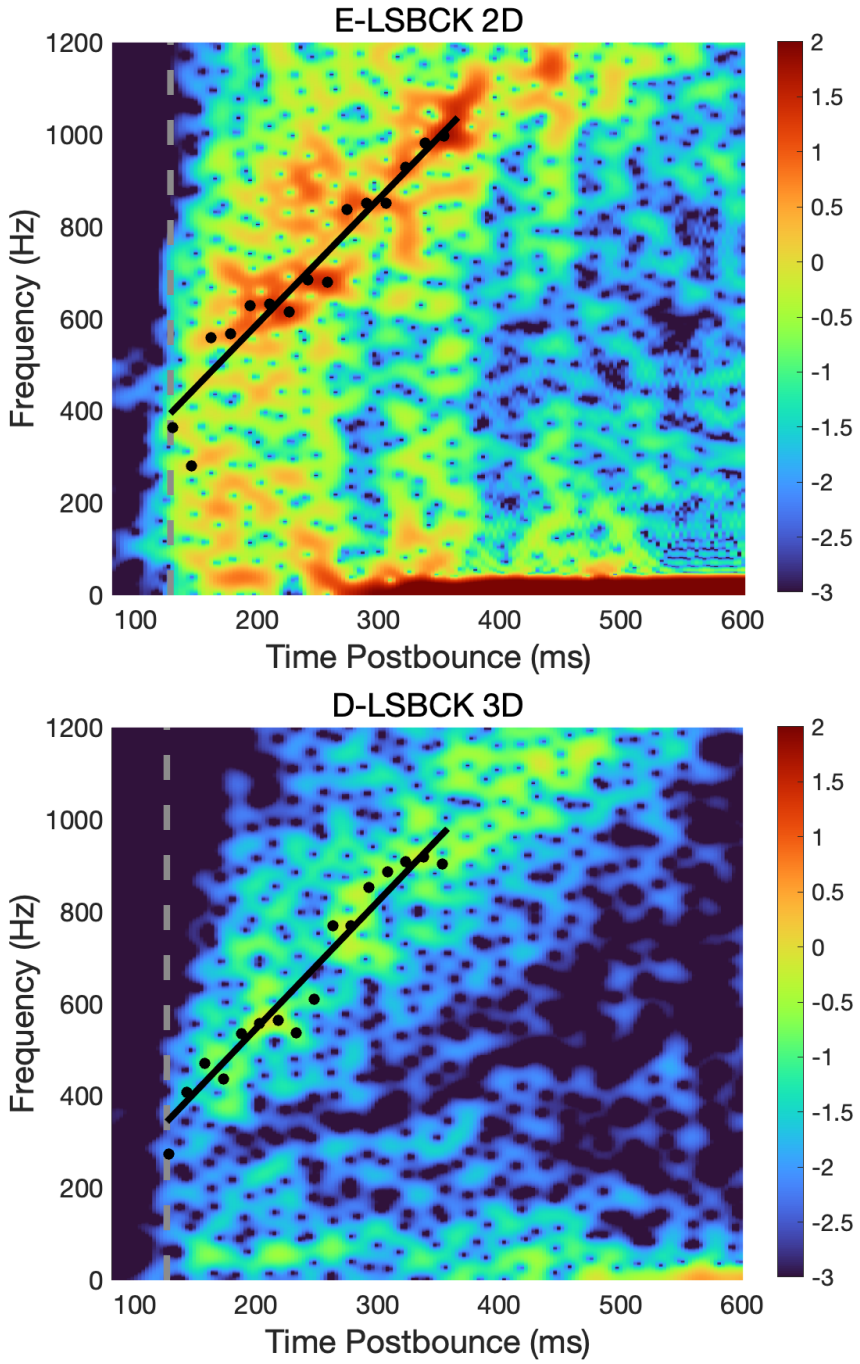


Figure 5.5: Spectrograms for two-dimensional (top) and three-dimensional (bottom) CCSN simulations using the LSBCK EOS with first-order HFF approximation. Spectrograms were produced using the same parameters used in Figure 5.3, the black line shows the first-order approximation of the HFF, and the gray, dashed line represents t_{HFF} as defined previously.

and the HFF polynomial fit was computed as described in Section 5.1.5. The two-dimensional spectrogram shows an HFF polynomial approximation with a slope of 2713 Hz s^{-1}, starting HFF frequency of 395 Hz, and t_{HFF} of 0.1285 s. The three-dimensional spectrogram shows an HFF polynomial approximation with a slope of 2727 Hz s^{-1}, starting HFF frequency of 359 Hz, and t_{HFF} of 0.1301 s. These results are promising, showing that between two- and three-dimensional simulations the effect on the measurable properties of the HFF seem minimal. It also shows the consistency of the definition of t_{HFF}, differing only by 1.6 ms. However, the color axis on each spectrogram does show significant differences in the strength of the signal. The mean power spectral density across the spectrogram for the two-dimensional gravitational wave signal is ~ 8.4 times larger than the mean power spectral density across the spectrogram for the three-dimensional gravitational wave signal. This means that the properties of the HFF should be consistent between two- and three-dimensional simulations in the noiseless case, but that real CCSN events may be weaker than the signals that give the results we present in the following section.

5.1.7 Curvature of the HFF

As mentioned in Section 5.1.4, a natural extension to this analysis would be to examine the curvature of the HFF. Section IV B in Murphy et al. (2024) shows that the current detection probability of the HFF above 1 kHz is low, and this was part of our justification for examining only the first-order time dependence of the HFF. Here, we show that approximating the HFF time dependence to second-order time results in different estimates of curvature for the HFF signal below 1 kHz, and the curvature for the signal up to 2 kHz.

The procedure for defining the starting time of the signal is the same as described in Section 5.1.5. Instead of performing a first-order regression, we now allow our regression to include terms up to second order in time. In Figure 5.6, the light, gray, dotted curve uses the coefficients determined for the HFF signal below 1 kHz. The

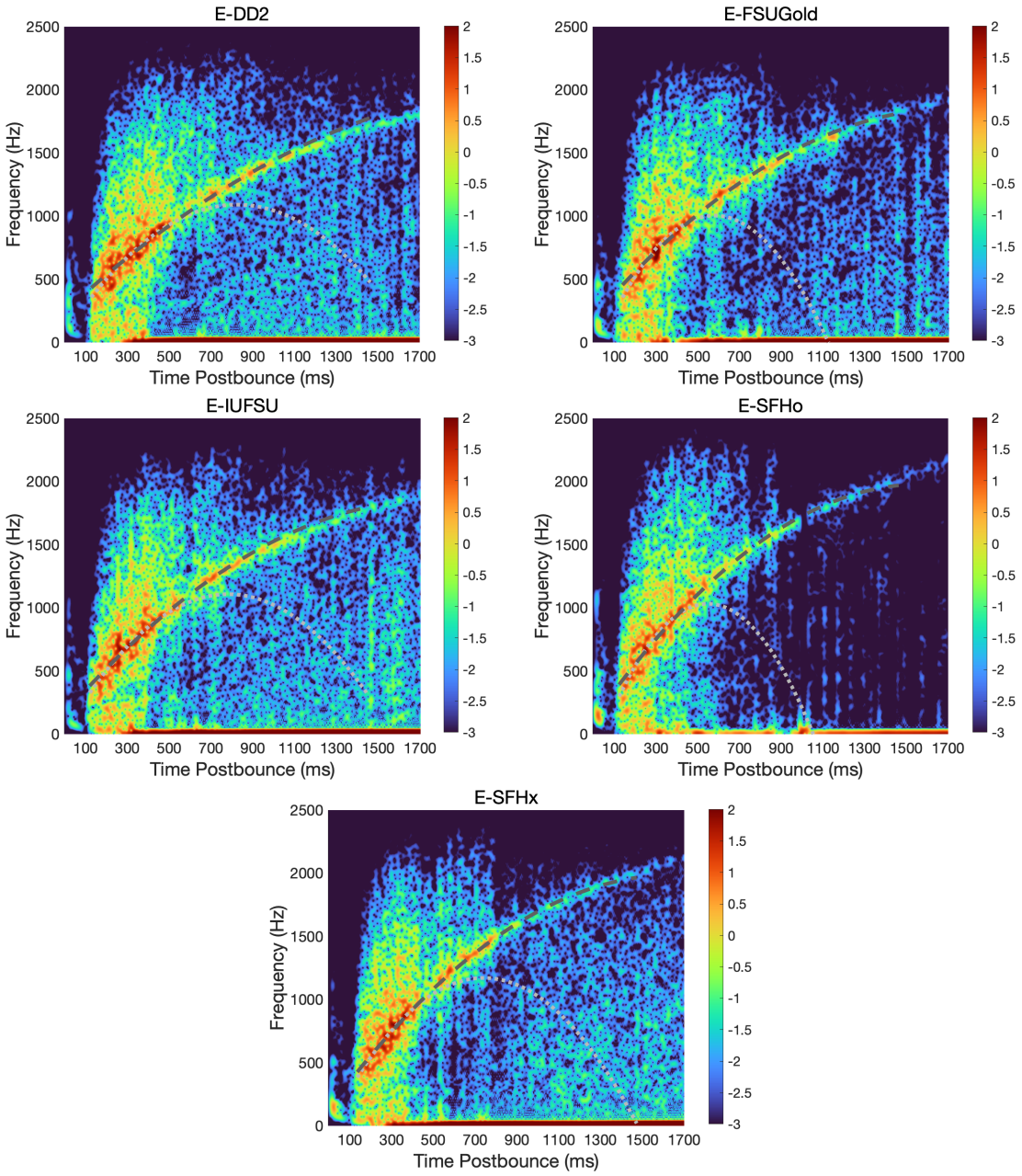


Figure 5.6: Quadratic-best-fit lines for maximum power spectral density output. The color axis shows the logarithm of the power spectrum, $\log_{10}(P)$. The light gray curve is determined using the coefficients of the second-order regression of the HFF signal below 1 kHz, while the dark gray line uses the coefficients determined from the regression of the HFF signal below 2 kHz.

dark, gray, dashed curve uses coefficients determined for the HFF signal below 2 kHz. Table 5.2 shows the coefficients for each approximation.

We see that the curve using the < 1 kHz HFF coefficients overestimates the curvature when compared to the curve that uses the < 2 kHz coefficients. Further, the first-order coefficients reported in Table 5.2 for the < 2 kHz HFF differ from the first-order coefficients for the linear approximation given in Table 5.1 by $< 3.3\%$ for all models except E-IUFSU, which differs by 8%. This shows that our measurement of the first-order time dependence of the HFF in the absence of noise below 1 kHz is in agreement with the first order time dependence of the HFF below 2 kHz when time dependence up to second order is included in our regression model.

5.1.8 Discussion

Table 5.3 shows the results from Section IV in Murphy et al. (2024) for the E-series GW signals at distances of 1, 5, and 10 kpc. In each case, a mean slope $\hat{\bar{s}}$ is found using the DNN, and the RMSE and MAPE values relate the HFF approximation using $\hat{\bar{s}}$ to the value of the slope without noise s. Table 5.4 reports the same results for the HFF starting frequency, denoted as β in Section 5.1.5.

Table 5.2: Coefficients for the second-order approximation in time of the HFF below 1 kHz and below 2 kHz.

EOS	HFF Below 1 kHz			HFF Below 2 kHz		
	γ [Hz s^{-2}]	α [Hz s^{-1}]	β [Hz]	γ [Hz s^{-2}]	α [Hz s^{-1}]	β [Hz]
DD2	-1504	2100	357.4	-321.5	1436	433.0
FSUGold	-3354	2951	355.8	-541.3	1743	454.9
IUFSU	-1776	2355	326.9	-524.9	1762	382.3
SFHo	-4047	3448	297.6	-745.7	2177	391.6
SFHx	-2148	2601	383.6	-673.3	2052	426.0

Each column represents a coefficient in the approximation of the HFF time dependence of the form $f(t) = \gamma t^2 + \alpha t + \beta$.

Table 5.3: HFF slope estimation results in real interferometric noise for distances of 1 kpc, 5 kpc, and 10 kpc.

EOS	s [Hz s^{-1}]	$\hat{\bar{s}}$ [Hz s^{-1}]	STD [Hz s^{-1}]	RMSE [Hz s^{-1}]	MAPE [%]
		1 kpc			
DD2	1398	1402	103.54	301.72	5.6
FSUGold	1665	1610	126.93	228.84	1.2
IUFSU	1502	1566	100.66	229.11	3.1
SFHo	2131	2092	52.63	249.39	0.5
SFHx	2000	2003	60.43	159.30	0.6
		5 kpc			
DD2	1398	1742	293.13	223.11	21
FSUGold	1665	2002	258.56	332.91	15
IUFSU	1502	1812	201.69	154.25	17
SFHo	2131	2501	313.45	256.74	18
SFHx	2000	2311	298.12	106.10	12
		10 kpc			
DD2	1398	2377	765.30	635.93	32
FSUGold	1665	2544	678.70	468.19	27
IUFSU	1502	2404	555.41	526.20	24
SFHo	2131	2670	401.92	486.82	21
SFHx	2000	2687	368.12	416.60	20

The slope estimation without noise is reported for each E-series signal in the second column. Then, for each detection distance, the mean estimated slope $\hat{\bar{s}}$ is reported with its corresponding standard deviation. The root-mean-square error is given by $RMSE = \sqrt{(\sum_i (s_i - \bar{s}_i)/n)}$, as a measure between the approximation using the slope without noise and the approximation using the mean slope from the DNN. Likewise, the MAPE uses the same formula shown in Table 5.1, but the error is calculated between the approximation using the slope determined without noise and the approximation using the mean slope from the deep neural network (DNN) described in Section IV of Murphy et al. (2024).

Table 5.4: HFF starting frequency estimation results, in real interferometric noise, for distances of 1 kpc, 5 kpc, and 10 kpc.

EOS	$\bar{\beta}$ [Hz]	STD [Hz]	RMSE [Hz]	MAPE [%]
	1 kpc			
DD2	419	5.21	11.23	4.32
FSUGold	429	8.51	13.47	6.05
IUFSU	378	9.01	14.04	6.67
SFHo	364	8.39	12.57	6.01
SFHx	408	5.87	11.74	4.94
	5 kpc			
DD2	531	12.94	13.54	10.18
FSUGold	550	18.92	27.14	15.73
IUFSU	505	20.04	29.37	16.34
SFHo	481	19.49	27.01	15.24
SFHx	523	15.50	25.21	11.36
	10 kpc			
DD2	649	27.39	31.30	23.62
FSUGold	714	31.32	34.01	30.98
IUFSU	708	33.51	36.37	33.75
SFHo	698	30.21	33.23	33.13
SFHx	660	29.94	32.12	26.17

$\bar{\beta}$ is the mean HFF starting frequency obtained from the DNN, and it is reported with its corresponding standard deviation for each Galactic distance. The RMSE and MAPE are computed using the same formulas described in Table 5.3 and Table 5.1, respectively. These quantities are computed with respect to their values as determined without noise.

Figure 5.7 shows the linear estimation of the HFF for the E-series GW signals with the $\pm 1\sigma$ results shaded for each model for each Galactic detection distance. This shading encompasses the standard deviations in both HFF slope and HFF starting frequency. As seen in Table 5.4, the mean HFF starting frequency varies with detection distance. This is reflected in Figure 5.7, as each plot has a different HFF starting frequency on the frequency axis.

From Figure 5.4, it is clear that in the absence of noise the slope of the HFF of gravitational waves generated from CCSN simulation is distinguishable for each EOS used. Our analysis in the absence of noise shows a variation on the order of 50% in the HFF slope for the E-DD2 simulation versus the E-SFHo simulation. These represent the lowest and highest slope values of the HFF, respectively. The smallest variation is between E-SFHo and E-SFHx, varying by 10% in HFF slope. This highlights the level of accuracy that is needed to detect these differences. When noise is introduced, a slope error estimation of up to 50% has the possibility to discern differences in EOS slopes in the extreme cases. Likewise, a slope error estimation below 10% has reached the necessary level of accuracy to differentiate the smallest differences in slope we observe in the noiseless case.

Using the methods established in Casallas-Lagos et al. (2023), we show the capability of using the slope of the HFF to investigate CCSNe. We note that the definition of the beginning of the HFF signal is less relevant when the signal is injected with real LIGO noise because, in this case, strains below noise levels cannot be distinguished. Thus, the HFF signal starts, in the detections with real noise, where the strain overcomes the noise threshold of the detector. The mean HFF starting frequency reported in Table 5.4 is then a result of the range of starting frequencies that may be detected depending on when the signal overcomes the noise threshold.

Figure 5.7 shows the estimation errors for both HFF slope and HFF starting frequency for 1, 5, and 10 kpc. At 1 kpc, there are regions with no overlap in estimation error between each E-series model. We see the emergence of two groupings: the steep-sloped E-SFHo and E-SFHx models and the more-shallow-sloped E-DD2

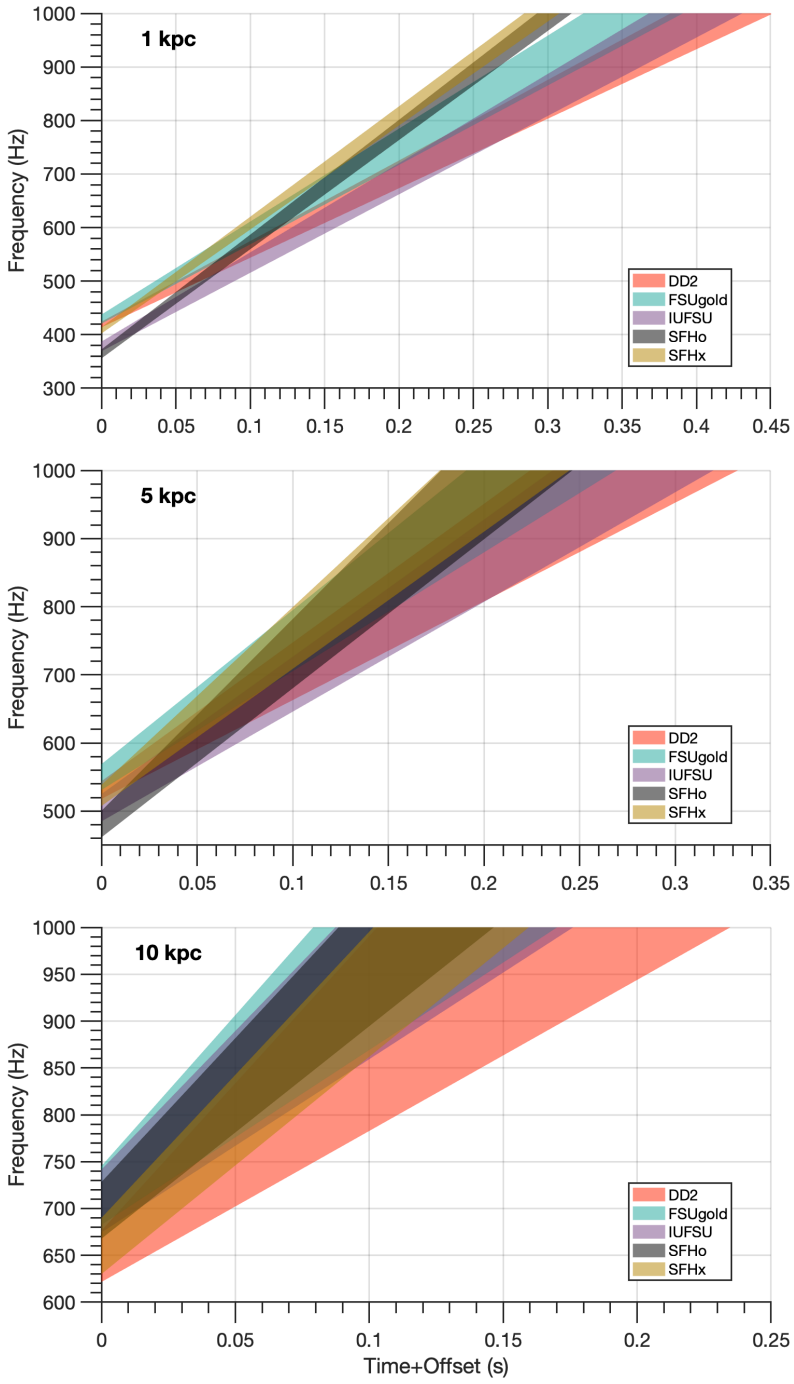


Figure 5.7: HFF slopes estimated by our DNN model including the range of variability of the HFF starting frequency across E-series models for detection distances of 1 kpc, 5 kpc, and 10 kpc.

N.B., This figure has been reproduced with the exact same data from Murphy et al. (2024) to better fit within this dissertation.

and E-IUFSU models. The estimation error of E-FSUGold crosses both groupings, having a high HFF starting frequency but more shallow slope. Having low estimation error in the HFF starting frequency allows for clear distinctions between models with similar slopes. E-SFHo and SFHx are similar in slope, but well resolved and separated in HFF starting frequency. The same is true for E-IUFSU and E-DD2. The minimum slope resolvability is between E-SFHo and E-SFHx, which differ by 4.4% and have HFF starting frequencies differing by 12%. The minimum HFF starting frequency resolvability is between E-DD2 and E-FSUGold, which differ by 2.4% and have HFF slopes differing by 15%. In other words, for EOS models with larger differences in HFF starting frequency we can resolve smaller differences in HFF slope. Conversely, for EOS models with roughly similar HFF starting frequencies we require a greater separation in HFF slope in order to resolve them.

At 5 kpc, the HFF starting frequency is notably higher across all models. This is due to the weaker signal strength at the beginning of the HFF when compared to the increased noise, so the HFF is detected at a later time in the signal. We thus lose the clear period of resolvability at early signal times, as seen in the 1 kpc detection. Nonetheless, E-SFHx and E-SFHo remain largely distinguishable from E-DD2 and E-IUFSU, though distinguishing within these groups is more difficult. E-FSUGold remains distinguishable at early times, but not at later times.

At 10 kpc, as the the reconstruction of the earlier HFF signal is further affected by the noise, the HFF starting frequency continues to rise. The resolvability between the groups, seen at 1 and 5 kpc, is lost. However, the upper bounds of E-FSUGOld and lower bounds of E-DD2 in both HFF starting frequency and slope are still resolvable. With the expected improvements in sensitivity in future runs, when interferometers will reach design sensitivity and when the number of interferometers will increase, we expect the uncertainty in the starting frequency to decrease, as well as the uncertainty in the slope. For this reason the results presented here should be thought of as conservative.

These results are consistent with the noise data from the LIGO O3 run conducted in 2019 through 2020. The LIGO O4 run is currently underway, with improved sensitivity, but O4 noise data is not yet available. With the improved sensitivity of future detectors, we expect the ability to measure the slope of the HFF below 1 kHz to improve as well. In our models, SNR is decreased with distance to the event due to the inverse relationship of gravitational wave signal amplitude with distance. This means that improved SNR for future detectors will effectively shift our results to larger distances by the same factor. In the case of the order-of-magnitude improvements to detection sensitivity currently projected for the Einstein Telescope (Maggiore et al., 2020) and Cosmic Explorer (Reitze et al., 2019), our 1 kpc results would be, conservatively, representative of 10 kpc detections.

As noted in Section 5.1.6, the strain amplitudes of gravitational wave signals from two-dimensional CCSN simulations are overestimated in comparison to those from three-dimensional CCSN simulations. This means that the gravitational wave signals considered in this study are likely stronger than the expected gravitational wave signal from a Galactic CCSN. We noted that the power spectral density is ~ 8.4 times higher for the two-dimensional model than for the three-dimensional model, with all other model parameters being identical. Due to the inverse linear relationship with signal strength and distance, this means we can approximate the two-dimensional results as three-dimensional results that are ~ 8.4 times closer than the signals analyzed in Figure 5.7.

5.1.9 Conclusion

This thesis shows the capability of using HFF slope measurements to distinguish between the possible EOS at play in CCSN events within 1 kpc for current-generation detectors. The improved sensitivity of future detectors will improve our ability to distinguish between different EOS, for distances at least an order of magnitude larger. We also expect further benefits from customized tuning of cWB for PE purposes,

as shown in Lin et al. (2023). These improved sensitivities will also allow for an estimation of the nonlinear time dependence of the HFF, given the signal above 1 kHz will become detectable. We leave a study of this phase of the evolution of the HFF to future work.

In this study, we investigated the effects on the HFF of varying the EOS in isolation, without varying progenitor parameters. Not only do parameters like rotation rate (Andresen et al., 2019; Pajkos et al., 2019, 2021; Pan et al., 2021; Takiwaki et al., 2021) and mass (Andresen et al., 2017; Vartanyan et al., 2019b; Mezzacappa et al., 2023) affect the slope of the HFF, but parameters varied simultaneously affect the slope in more complex ways. As seen in Wang and Pan (2024), varying the internal structure at the same time as rotation rate leads to HFF slopes that are decreased less than when there is no internal structure variation. Similarly, Jardine et al. (2022) show that the presence of strong magnetic fields may also counteract the effect of rotation on the slope of the HFF.

Future studies investigating the combined effects of varying intrinsic properties of the progenitor and the EOS are necessary in order to develop a complete understanding of what can be learned about the EOS from the detection of the HFF in the next Galactic CCSN. The study conducted here can be viewed as providing limits on what we can hope to learn.

5.2 Gravitational Waves as a Probe of Core Collapse Supernova Progenitor Structure

The work described in this section has been submitted to Physical Review D. as "Gravitational Waves as a Probe of Core Collapse Supernova Progenitor Structure." Full citation: Murphy et al. (2025a). The text has been edited, where necessary, to conform to the citation style of this dissertation and to reference sections within this

dissertation instead of the original manuscript. Sections from the manuscript that have already been covered in this dissertation have been removed here.

5.2.1 Introduction

As we anticipate the next Galactic core collapse supernova (CCSN), it is necessary to continue investigations into the effects progenitor properties have on the CCSN-generated gravitational wave signal. Already, studies have shown intrinsic differences in gravitational wave signal from progenitors with differing mass Andresen et al. (2017); Vartanyan et al. (2019b); Mezzacappa et al. (2023); Vartanyan et al. (2023), rotation rate Andresen et al. (2019); Pajkos et al. (2019); Powell and Müller (2020); Pan et al. (2021); Takiwaki et al. (2021); Zha and O'Connor (2022); Wang and Pan (2024), and magnetic field strengths Jardine et al. (2022); Bugli et al. (2023); Powell et al. (2023); Powell and Müller (2024). Beyond these physical effects on the gravitational wave signal, our understanding of fundamental physics also influences the signal generated in CCSN simulations as seen in simulations that implement differing nuclear equations of state Marek et al. (2009); Morozova et al. (2018); Pan et al. (2018); Powell et al. (2021); Eggenberger Andersen et al. (2021b), differing neutrino properties Mori et al. (2025); Ehring et al. (2024), and include quantum phase transitions Yasutake et al. (2007); Zha et al. (2020); Kuroda et al. (2022); Zha and O'Connor (2022). Understanding these effects is not only theoretically important to build our understanding of the gravitational wave production, but they also allow for the possibility of extracting progenitor parameters Warren et al. (2020); Afle and Brown (2021b); Pajkos et al. (2021), proto-neutron star (PNS) evolution parameters Bizouard et al. (2021); Powell and Müller (2022); Bruel et al. (2023); Wolfe et al. (2023); Sasaoka et al. (2024), and constraining fundamental physics theories, *e.g.* the nuclear equation of state Jakobus et al. (2023); Murphy et al. (2024), through a gravitational wave detection. In this study, we aim to both improve our understanding of gravitational wave production in CCSNe and to explore the

use of a gravitational wave detection as a means to investigate stellar structure by presenting the gravitational wave signals of two progenitors with nearly identical mass but differing internal structures. The explosion dynamics of these 15.78 $M_\odot$ and 15.79 $M_\odot$ progenitors are described in Bruenn et al. (2023).

At every phase of the CCSN, gravitational waves carry information imprinted by the dynamics of the explosion, which in turn depends, in part, on the internal structure of the progenitor star. In previous studies, varying the compactness parameter of the progenitor accounts for the bulk internal structural differences between progenitor models. The compactness parameter for the inner core with mass M is defined by O'Connor and Ott (2011) at the time of core bounce as

$$\xi_M \equiv \frac{M/M_\odot}{R(M)/1000 \text{ km}}, \tag{5.1}$$

and it has been shown to quantitatively affect the gravitational wave signal produced in CCSN simulations. Warren et al. (2020) used one-dimensional CCSN simulations to show a positive correlation between the compactness of progenitors that failed to explode and the rate of change, *i.e.* slope with respect to time, of the peak frequency of the gravitational wave emission. The peak gravitational wave emission frequency is approximated through a combination of PNS modal analysis following Morozova et al. (2018) and the peak frequency evolution assuming a $g-$mode type oscillation as derived by Müeller et al. (2013). Using two-dimensional CCSN simulations, Pajkos et al. (2021) corroborated this positive correlation with direct determinations of the slope of the peak frequency evolution from gravitational wave calculations. For rotating CCSNe, they showed the feasibility of determining the compactness of the progenitor core using this peak frequency slope and the bounce signal. Wang and Pan (2024) saw the same positive correlation between compactness parameter and peak frequency evolution for two-dimensional CCSN simulations with progenitors of differing internal structure arising from binary accretion during stellar evolution.

Our study contributes to the growing body of gravitational waveforms generated from CCSN simulations, and investigates the gravitational wave production in detail not only from two progenitors with varying compactness parameters, *i.e.* varying internal structures, but also from progenitors that are nearly identical in every other respect. This allows us to show, in a limited case, the effects of varying internal structure in isolation of other progenitor parameters. The general differences we observe can be attributed in part to the compactness parameter, as in the studies cited above, but we will also endeavor to connect specific gravitational wave features to the unique dynamics described in the CCSN simulations of Bruenn et al. (2023).

5.2.2 Core-Collapse Supernova Models

We examine the gravitational wave emission from two-dimensional simulations of collapse, and explosion, of two progenitors of nearly equal mass, using the CHIMERA simulation code Bruenn et al. (2020). The zero age main sequence masses of the progenitors are 15.78 $M_\odot$ and 15.79 $M_\odot$, and the models were evolved to precollapse by Sukhbold et al. (2018) and updated as described in Section 2 of Bruenn et al. (2023). The explosion dynamics of each model are described in detail in Section 5 of Bruenn et al. (2023). Of particular importance to our study are Figure 4 showing the compactness of each model, Figure 5 showing the shock radius (top) and mass accretion rate at the shock location (bottom), Figure 8 showing the PNS mass and radius evolution, and Figure 16 showing the neutrino accretion and core luminosities.

Here, we briefly overview the key differences that were observed in the dynamics of each model from collapse through explosion. The 15.78 $M_\odot$ progenitor undergoes a fourth carbon shell burning phase 0.1 yr before collapse at the same time as the first oxygen shell ignition. This slows the contraction of the core and results in a silicon core mass that is smaller than that of the 15.79 $M_\odot$ progenitor at the time of collapse. The 15.79 $M_\odot$ progenitor undergoes its fourth carbon shell burning stage roughly 8 hr before collapse. The end result is that the 15.78 $M_\odot$ progenitor has a

sharp drop in its density profile that is not present in the 15.79 $M_\odot$ progenitor, as shown in Bruenn et al. (2023) Figure 4. These differing density profiles lead to the 15.78 $M_\odot$ progenitor being less compact, $\xi_{2.5} = 0.136$, than the 15.79 $M_\odot$ progenitor, $\xi_{2.5} = 0.206$, where ξ_M is given by Equation (5.1).

Using the multiphysics CHIMERA code, these precollapse progenitors were evolved through explosion as part of the CHIMERA F-series simulations. We will denote them by their respective masses as F15.78 and F15.79. The CHIMERA code simulates CCSNe using Newtonian self-gravity with a monopole correction for general relativistic effects, multigroup flux-limited diffusion four-species neutrino transport in the ray-by-ray approximation, Newtonian hydrodynamics, and a nuclear reaction network. Neutrino emission and absorption interactions included are electron capture on protons and nuclei, electron—positron annihilation and nucleon—nucleon bremsstrahlung and the corresponding inverse weak reactions. The neutrino scattering processes included are isoenergetic scattering on nuclei, and neutrino—electron and neutrino—nucleon scattering. The nuclear reaction network includes a 14 species α-chain network, with three inert species (protons, neutrons, and ^{56}Fe) added actively but not reactively, as described in Bruenn et al. (2023). The nuclear equation of state (EOS) implemented for regions in nuclear statistical equilibrium is the SFHo EOS of Steiner et al. (2013) incorporated using WeakLib Landfield (2018). For each model, simulations are axisymmetric with 720 non-uniform radial cells and 240 fixed angular cells of width 0.75°. The radial extent of each model comprised the inner 3.56 $M_\odot$, reaching out to the helium shell. This corresponds to an outer radius of 61,250 km for the less compact F15.78 model and 48,960 km for the F15.79 model. The radial dimension is refined at different length scales throughout the simulation, to capture features in both the PNS and around the shock.

Each model collapses, halts collapse, and bounces back with a shock wave generated from the repulsive strong nuclear force accounted for by the SFHo EOS. The shock wave generated loses energy as it moves outwards through the supersonically infalling matter and eventually stalls, as expected from neutrino-driven CCSN theory

Müller (2020); Burrows and Vartanyan (2021); Mezzacappa (2023); Janka (2025). Due to the sharper density gradient in F15.78, the shock is revived 120 ms after bounce due to a drop in the ram pressure ahead of the shock while significant neutrino luminosity from accretion onto the PNS surface is still occurring. Conversely, the shock of the F15.79 model is revived approximately 220 ms after bounce after neutrinos and antineutrinos have deposited energy behind the shock, slowly building up pressure behind it until the shock overcomes the ram pressure ahead of it. Shock revival is captured in Figure 5.a of Bruenn et al. (2023), and explosion energy is shown in Figure 7.b. The late revival of the shock for F15.79 results in a more energetic explosion.

As the shock is revived, the explosion dynamics of each model continue to diverge. We highlight that, in particular, the mass accretion onto the PNS drops at the onset of explosion for the F15.78 model in comparison to the F15.79 model, as seen in Figure 5.c in Bruenn et al. (2023). This, in addition to the already less massive silicon core at the onset of collapse, results in the F15.78 model evolving a less massive PNS than the F15.79 model. Figure 8 of Bruenn et al. (2023) shows the radial and mass evolution of the PNS for both models.

5.2.3 Gravitational Wave Extraction

In previous studies Mezzacappa et al. (2020, 2023); Murphy et al. (2025b), in addition to the total gravitational wave strain, the computational domain was decomposed into five regions within which the gravitational wave strains could be computed. These regions were, in order, the convective region of the proto-neutron star (PNS), the convective overshoot layer of the PNS, the surface layer of the PNS defined from the 10^{12} to the 10^{11} g cm^{-3} density contours, the net cooling layer behind the shock, and the net heating layer behind the shock (Murphy et al. (2025b) extended this last region out to the grid boundary instead of the shock radius). For the 3D models considered in those studies, each of these regions was well defined. In the 2D models we consider here, this is not the case. In particular, the edges of the PNS convective

region are not well defined, and the gain radius is oscillatory for long periods of the simulation. Thus, for this study, we implement a subset of the five regions presented in Mezzacappa et al. (2020, 2023); Murphy et al. (2025b), with regions denoted by roman numerals in Figure 5.8. Region I is now the central region of the PNS comprising the spherically symmetric inner core as well as the convective and convective overshoot layers. Region II is the region about the surface of the PNS, including both the regions below the PNS surface, down to the 10^{12} g cm^{-3} density contour, and the net cooling layer above the PNS surface, out to the 10^{10} g cm^{-3} density contour, which captures the lower boundary of the gain radius. Region III now includes everything above the net cooling layer, to the outer boundary of the computational grid. This allows us to make determinations about the gravitational wave generations deep within the PNS (region I), around the surface of the PNS (region II), and outside of the PNS (region III).

In addition to the gravitational wave signal from the matter motion, we also present the gravitational waveforms from the anisotropic emission of neutrinos. We extract the waveforms following the methods discussed in Richardson et al. (2025), using

$$h_{+/\times}(t,\theta,\phi,\nu) = \frac{2}{D}\int_0^t dt' L_E^\nu(t')\alpha_{+/\times}(t',\theta,\phi), \tag{5.2}$$

where L_E^ν is the global, integrated energy luminosity of neutrinos, and $\alpha_{+/\times}$ is the anisotropy parameter.

5.2.4 Total Gravitational Wave Strain

At late times during the CCSN simulation, refinement of the radial grid around the shock happens frequently as it moves through the computational domain. For the calculation of gravitational wave strains, this can result in the appearance of sudden, massive, "numerical" changes in velocity at cell interfaces. From one time step to the next, the fluid moves with a physical velocity between cells. However, as the grid refines, the boundaries of these cells can change on the order of kilometers

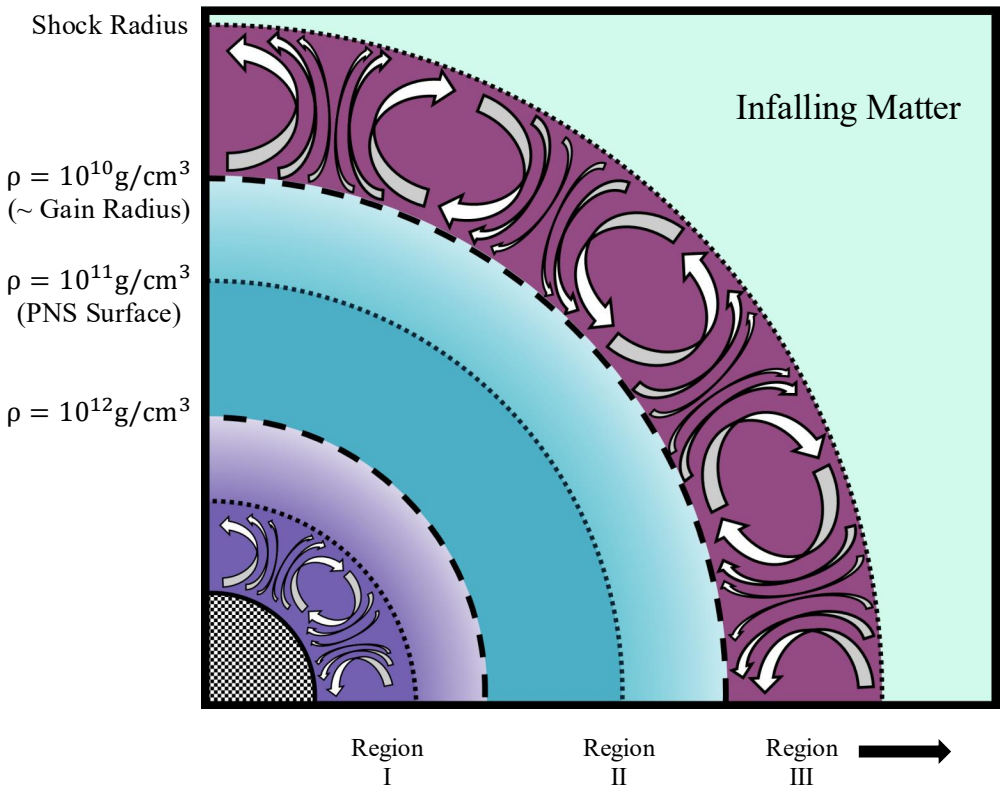


Figure 5.8: Depiction of new regions I–III for two-dimensional CCSN models. The boundaries of each region are defined by density contours, denoted as black dashed lines with values shown on the vertical axis. Dotted lines depict boundaries used in previous three-dimensional studies.

between time steps. This can cause the gravitational wave computation to compute large, non-physical velocity derivatives for boundaries that moved. Since this effect is localized around the shock, it does not affect the overall strain computation, only the contribution from the cells around the shock. This causes non-physical "combs" to appear in the gravitational wave strains, and they appear only in region III, which contains the shock. Region III, at late times, is dominated by the evolution toward the gravitational wave memory, which exists in the 10s of Hz range of the gravitational wave signal. As the high-frequency "combs" are non-physical, we implement a low-pass filter attenuated at 100 Hz on the signal from region III. This filtering retains the physical, low-frequency component of the gravitational wave strains that comes from outside the PNS in region III, and it also retains the physical high-frequency component of the gravitational wave strains that comes from regions I and II, as shown in Mezzacappa et al. (2023) and Murphy et al. (2025b).

Figure 5.9 shows the gravitational wave strains multiplied by a distance of 10 kpc, computed as described in Section 5.2.3, for each model. Several distinct features can be seen. The magnitude of the strain for F15.79 is notably larger than that of F15.78, with maximum strain magnitudes of $\sim$60 cm and $\sim$30 cm, respectively. Additionally, the gravitational wave memory that begins to develop for F15.79 is almost twice as large as the memory for F15.78. The memory ramp up—i.e. the slope of the strain as it approaches a constant memory value—is also visibly greater for F15.79 than for F15.78.

We present spectrograms of the gravitational wave signal for each model in Figure 5.10, using the methods described in Section 2.1.6. Our Kaiser windowing scheme has a leakage parameter of 0.85, a time window of 45 ms, and an overlap percentage for each time window of 93.3%. The color axis for each spectrogram shows the base-10 logarithm of the power spectral density. The F15.78 spectrogram not only has a weaker overall signal, shown by the lower (i.e. less red) power spectral density compared to F15.79, but it also shows a narrower band structure at high frequencies. This reflects the fewer and less energetic accretion events onto the PNS in the F15.78

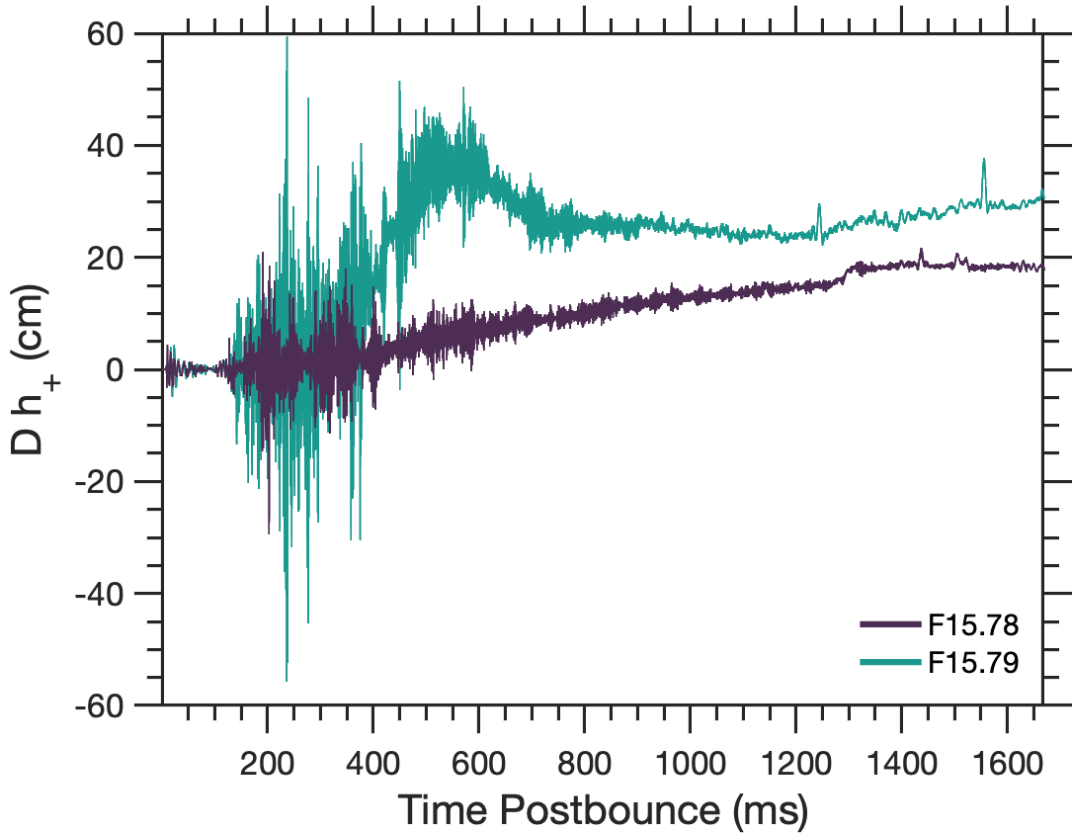


Figure 5.9: h_+-polarized strains multiplied by a distance of 10 kpc for F15.78 (purple) and F15.79 (teal).

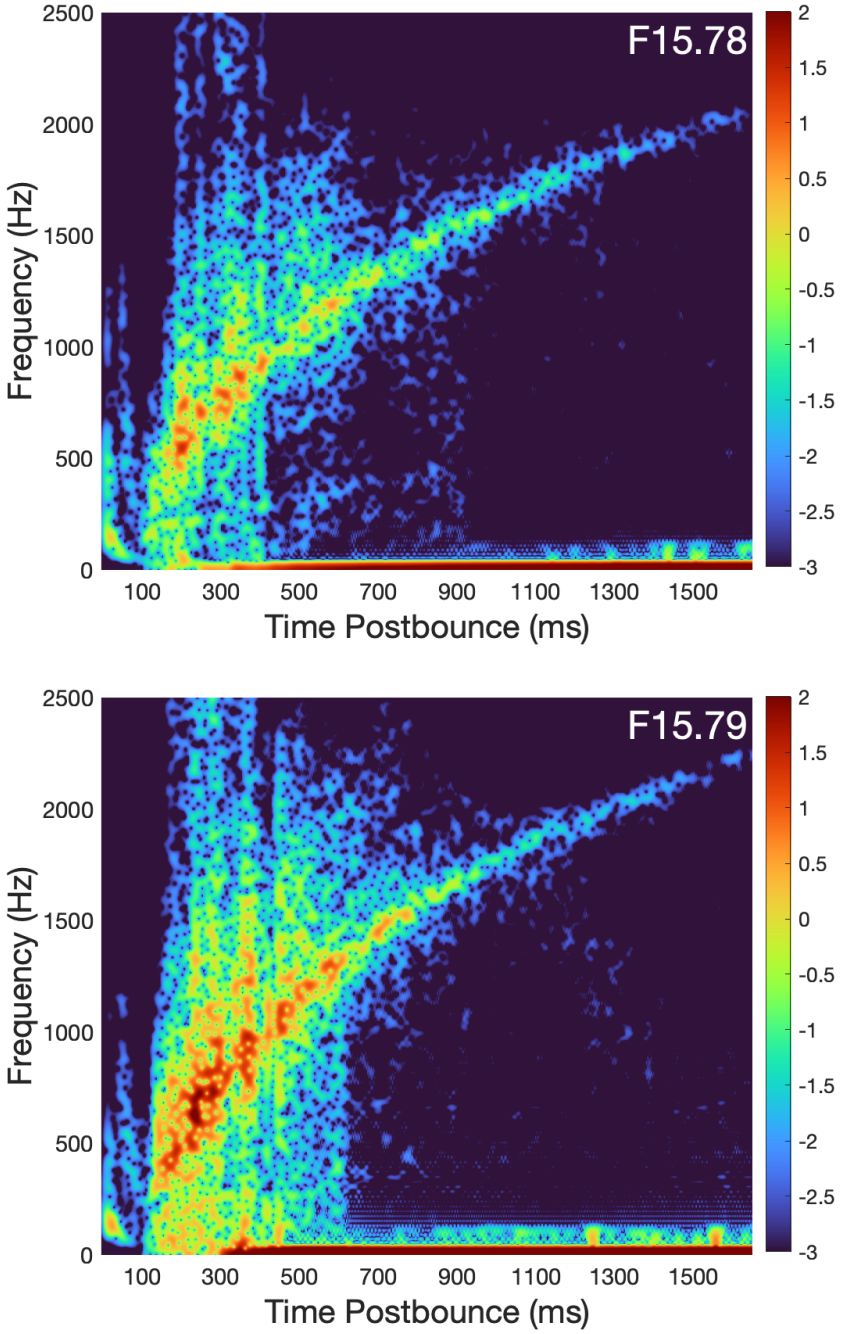


Figure 5.10: Spectrograms for F15.78 and F15.79.
The color axis depicts the logarithm of the power spectral density, $\log_{10}(P)$.

model, which is in accordance with Figure 5.c of Bruenn et al. (2023). Likewise, the low-frequency component associated with turbulent neutrino-driven convection and SASI motion is also noticeably weaker for F15.78. This is due to the relatively prompt shock revival that does not allow for extensive neutrino heating, contrasted in the F15.79 model where this feature lasts ∼100 ms longer and persists after the onset of explosion.

Following the procedure of Murphy et al. (2024), presented in Section 5.1, we also determine the linear approximation of the peak frequency evolution in the absence of detector noise, shown in Figure 5.11. In Murphy et al. (2024) and Casallas-Lagos et al. (2023), the peak frequency evolution is termed the High Frequency Feature (HFF). The linear approximation of the HFF is found by determining the frequencies with maximum power spectral density in each time window from the beginning of the feature, $t_{\rm HFF}$, to the time at which the maximal spectral density frequency reaches 1000 Hz. For details on the definition of $t_{\rm HFF}$ (termed $t_{\rm HFF}$ in the reference) and the reason for our cutoff at 1000 Hz see Murphy et al. (2024). The coefficients, starting time for the HFF, and maximum actual percent error (MAPE) of the linear approximation are given in Table 5.5. We find that the slope for F15.78 is 1789 Hz s^{-1} and the slope for F15.79 is 2263 Hz s^{-1}. As the PNS quasi-normal oscillation

Table 5.5: F-series linear approximation coefficients for the HFF.

	α [Hz s^{-1}]	β [Hz]	$t_{\rm HFF}$ [ms]	MAPE [%]
F15.78	1789	433.6	125.0	6.958
F15.79	2263	394.9	132.5	6.778

HFF approximated as $f(t) = \alpha t + \beta$. Second column gives the linear slope α of the HFF. Third column gives the starting frequency of the HFF, β. Fourth column is the start time of the HFF, $t_{\rm HFF}$. Fifth column represents the maximum absolute percent error (MAPE) between the actual maximum frequencies A_t and the frequencies predicted from the linear approximation F_t for n fitted points: $\text{MAPE} \equiv 100\frac{1}{n}\sum_{t=1}^{n}|\frac{A_t - F_t}{A_t}|$.

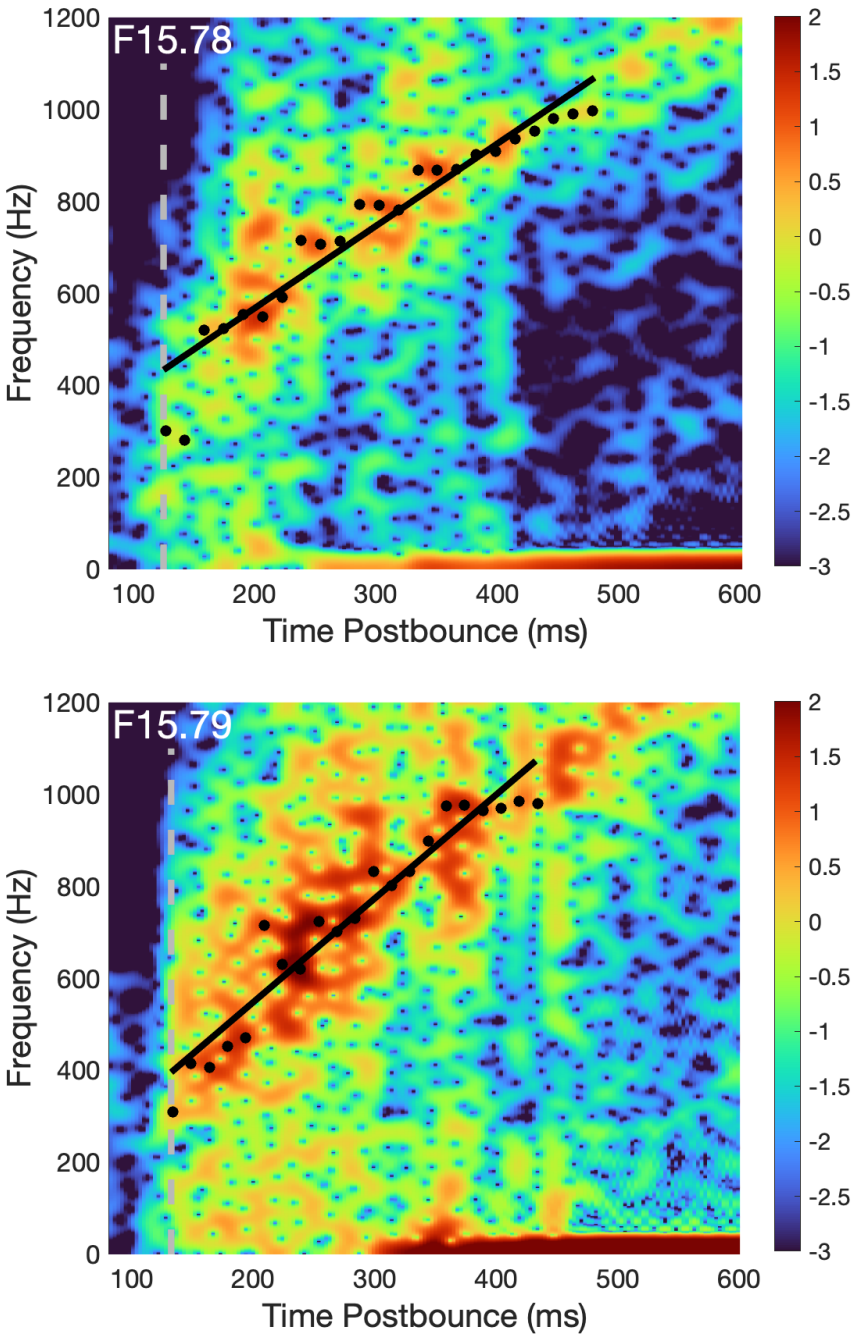


Figure 5.11: F-series spectrograms overlaid with the linear approximation of the HFF. The gray dashed line denotes the start time of the HFF.

modes generate gravitational waves, the radius of the PNS contracts and causes the oscillation frequency to rise. The higher slope of the HFF for F15.79 thus agrees with the the greater contraction rate of the PNS that is seen in Figure 8 of Bruenn et al. (2023).

The gravitational wave luminosity is presented in Figure 5.12, and the cumulative gravitational wave energy is shown in Figure 5.13. As in Mezzacappa et al. (2023), the right panel of Figure 5.12 also includes the gravitational wave luminosity averaged over seven cycles to eliminate high-frequency noise in the emission. This allows for easier distinguishability between the signals, but also lowers the luminosities as well as the emitted energies, the latter of which are indicated with dotted lines in Figure 5.13. We see that the gravitational wave luminosity is greater in F15.78 for the first few 10s of ms after bounce compared to F15.79, but at ∼135 ms postbounce F15.79 begins to produce greater gravitational wave luminosities. This is matched by the evolution of the gravitational wave energy, shown in Figure 5.13, where the total energy emitted as gravitational waves in F15.79 surpasses that of F15.78 at ∼140 ms. The bulk of the gravitational wave emission has finished by the end of each simulation.

5.2.5 Regional Decomposition

Decomposing the strains from each model into regions I–III reveals further differences in the gravitational wave production as the simulations evolve. Figure 5.14 shows the gravitational wave strain multiplied by a distance of 10 kpc, for each region. In region I, the strain is produced deep within the PNS, from the Ledoux convection and convective overshoot regions. Region II contains the strain produced in the surface layers of the PNS, including the cooling region above the surface of the PNS. The strain produced in region III is generated from the net heating region behind the shock, and beyond. The low-pass filter is applied at 933 ms and 624 ms postbounce for F15.78 and F15.79, respectively.

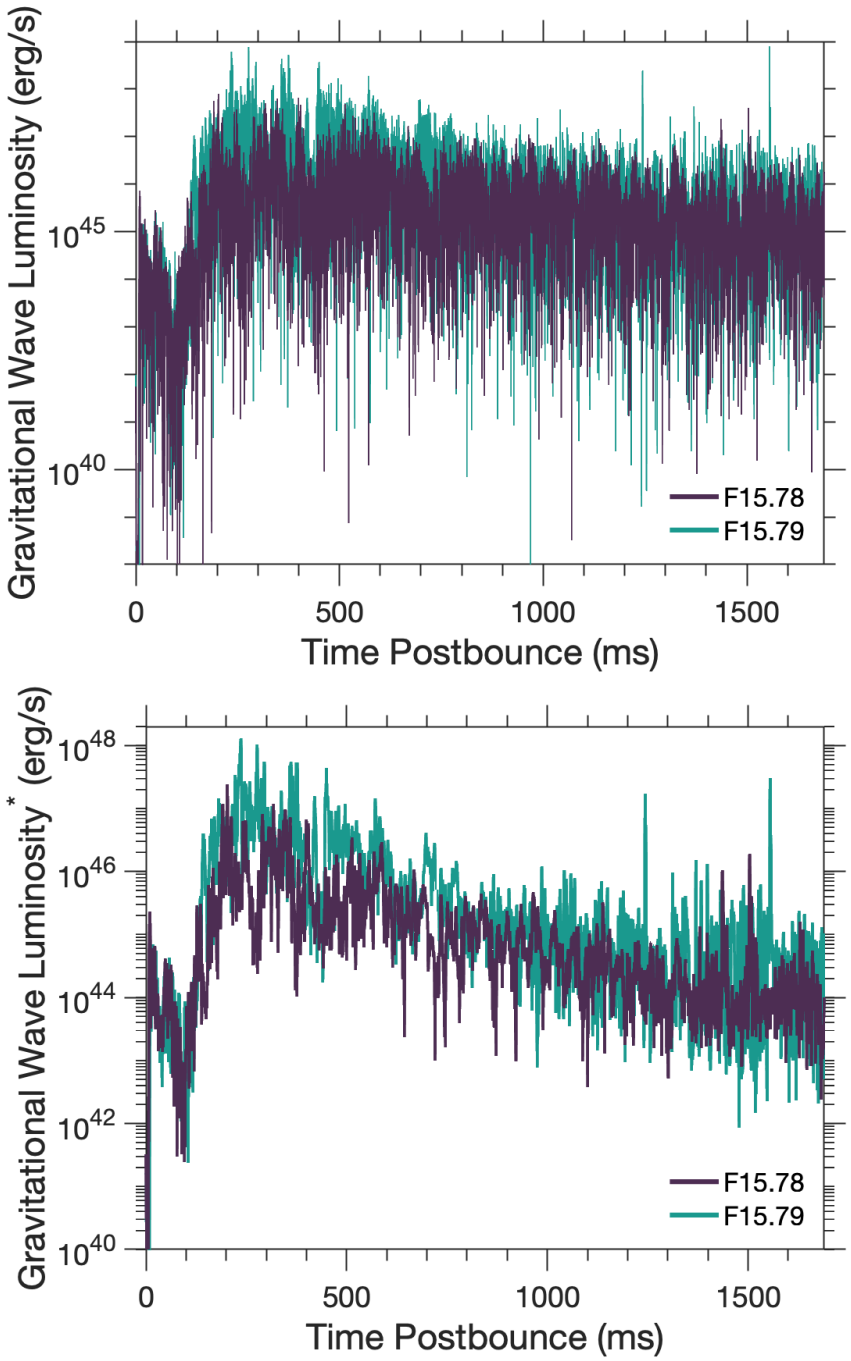


Figure 5.12: Gravitational wave luminosity for F15.78 (purple) and F15.79 (teal). Top: Gravitational wave luminosity computed at every time cycle. Bottom: Gravitational wave luminosity computed by averaging over seven time cycles.

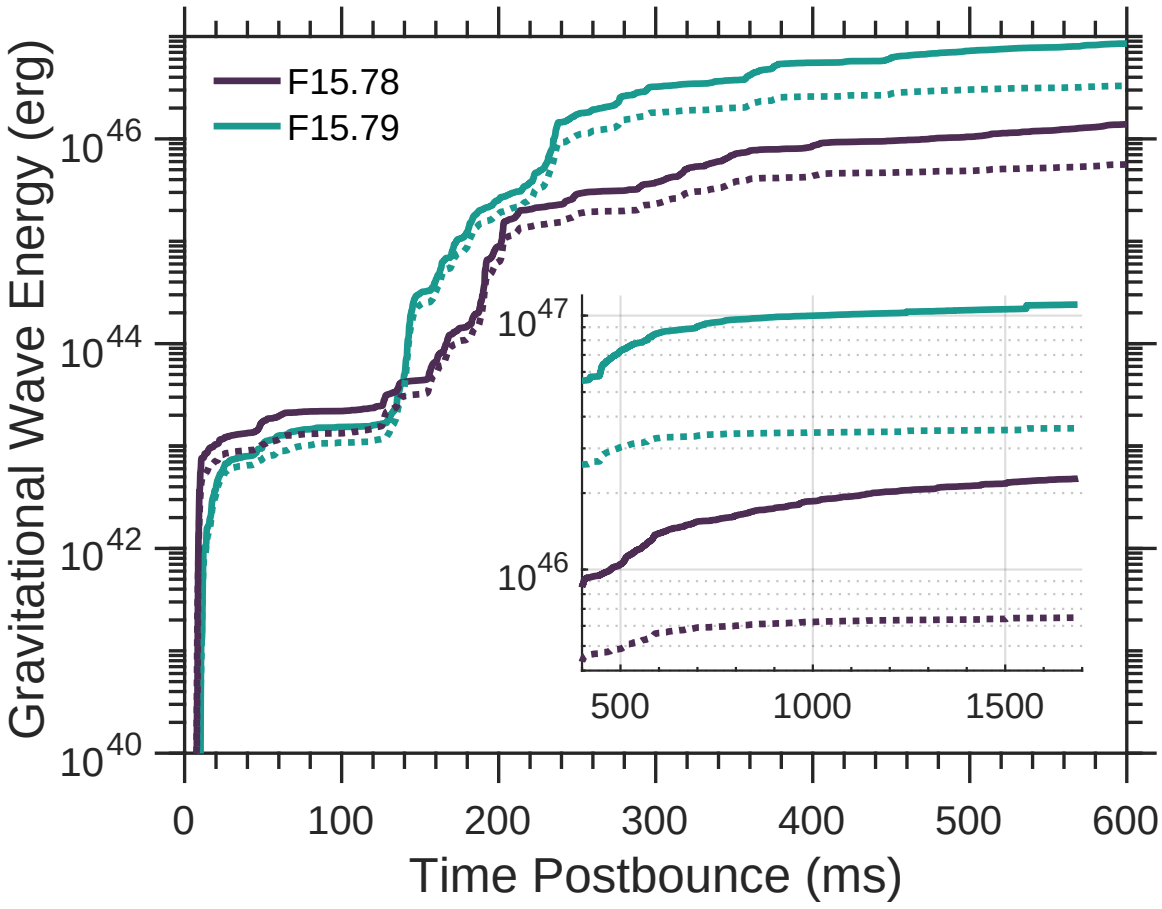


Figure 5.13: Total gravitational wave energy for F15.78 (purple) and F15.79 (teal). Dotted lines show cumulative energy from the seven cycle average. Inset shows the gravitational wave energy for late times.

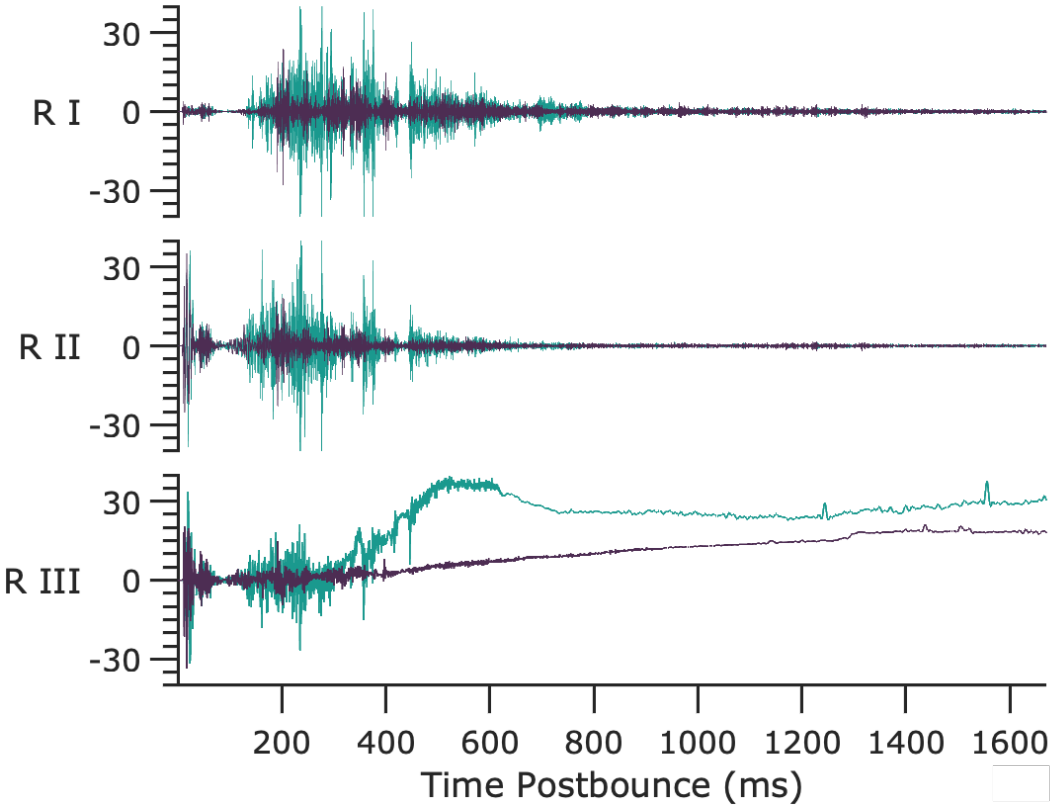


Figure 5.14: Gravitational wave strains produced in regions I, II, and III, for F15.78 (purple) and F15.79 (teal).

5.2.6 Prompt Convection

Within $\sim$ 10 ms, both models experience prompt convection driven by lepton and/or entropy gradients deep within the PNS, whose impact settles within $\sim$75 ms as judged by the gravitational wave strains. Figures 5.15 and 5.16 show the onset and dissipation of prompt convection and prompt-convection–induced turbulence in each model by plotting the electron fraction for the inner 50 km of the star. The contour (pink) in each case denotes the outer boundary of region I. For both models, the electron-fraction gradients are clearly visible, as is the mixing of higher electron fraction matter and lower electron fraction matter as a result of the convection. The convective motion in the F15.78 model appears to be more vigorous, which causes larger gravitational wave strains in region I, as seen in Figure 5.17. In the bottom panel of Figures 5.15 and 5.16 we plot the Ledoux criterion given by (Bruenn and Mezzacappa, 1994)

$$\left(\frac{\partial \ln\rho}{\partial \ln Y_e}\right)_{s,P}\left(\frac{\mathrm{d}\ \ln Y_e}{\mathrm{d}r}\right)+\left(\frac{\partial \ln\rho}{\partial \ln S}\right)_{Y_e,P}\left(\frac{\mathrm{d}\ \ln S}{\mathrm{d}r}\right)>0, \tag{5.3}$$

where the positive inequality indicates the condition for convective instabilities (*i.e.*, negative values are connectively stable), and ρ, Y_e, S, and P are the spherically averaged density, electron fraction, entropy per baryon, and pressure, respectively. The dark blue curves in the bottom panels of Figures 5.15 and 5.16 show the Ledoux criterion at the starting times of prompt convection, and both show sharp positive peaks at small radii. This indicates an instantaneous instability to convection that will take tens of milliseconds to dissipate. We see the peak is larger for F15.78, leading to more vigorous convection than in the F15.79 case. Several such events occur for each model, but the final instantaneous convective instabilities settle within $\sim$100 ms after bounce, as shown by the orange curves in the bottom panels of Figures 5.15 and 5.16. Figure 5.17 shows a decrease in gravitational wave strain for both models on this same time scale.

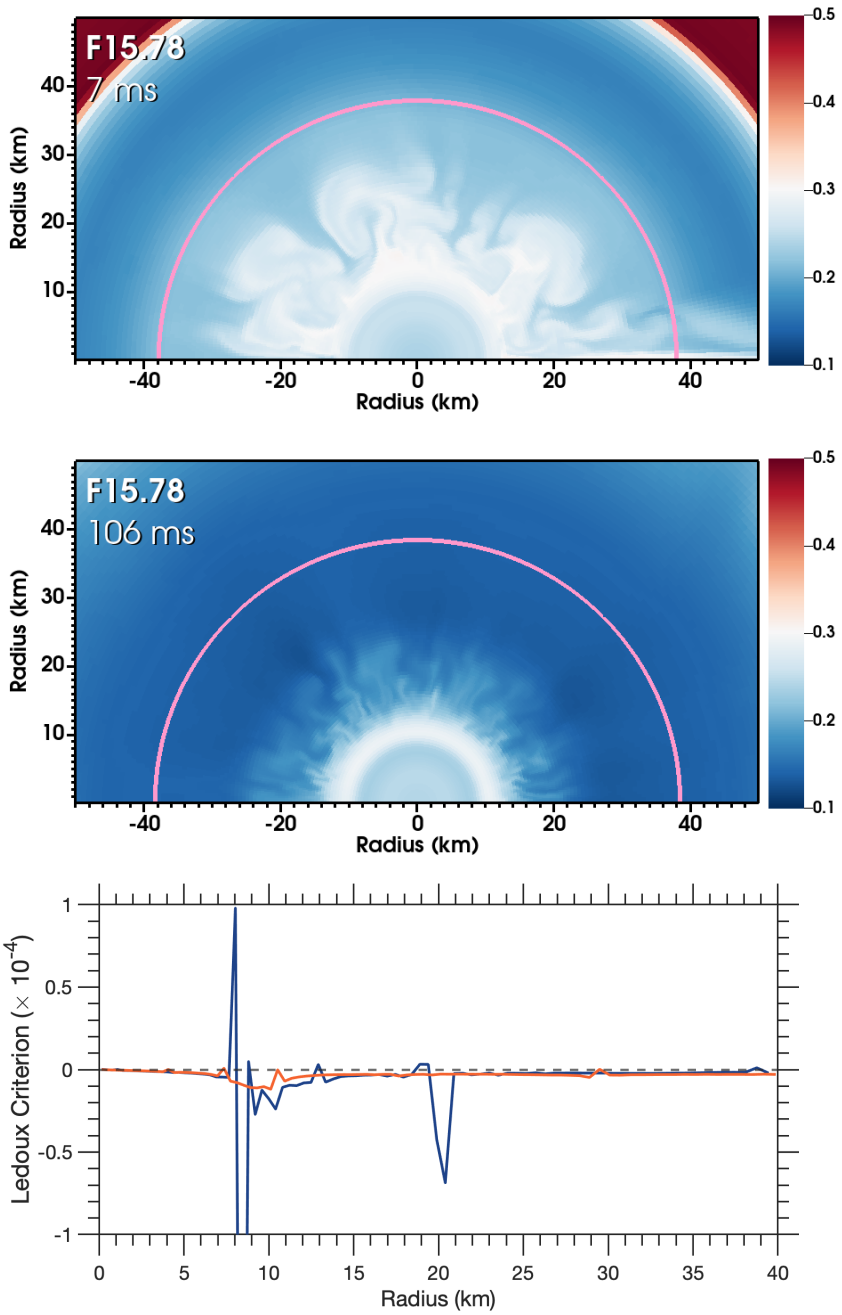


Figure 5.15: Electron fraction and Ledoux criterion for F15.78 shortly after bounce. Plots of electron fraction within the inner 50 km of the star for F15.78 at 7 ms (top) and 106 ms (middle) postbounce, displaying the onset and dissipation of prompt convection and prompt-convection–induced turbulence. Color axis represents electron fraction. The contour (pink) corresponds to the outer boundary of region I. The bottom panel shows the Ledoux criterion, as defined in the text, as a function of radius at 7 ms (dark blue) and 106 ms (orange) postbounce.

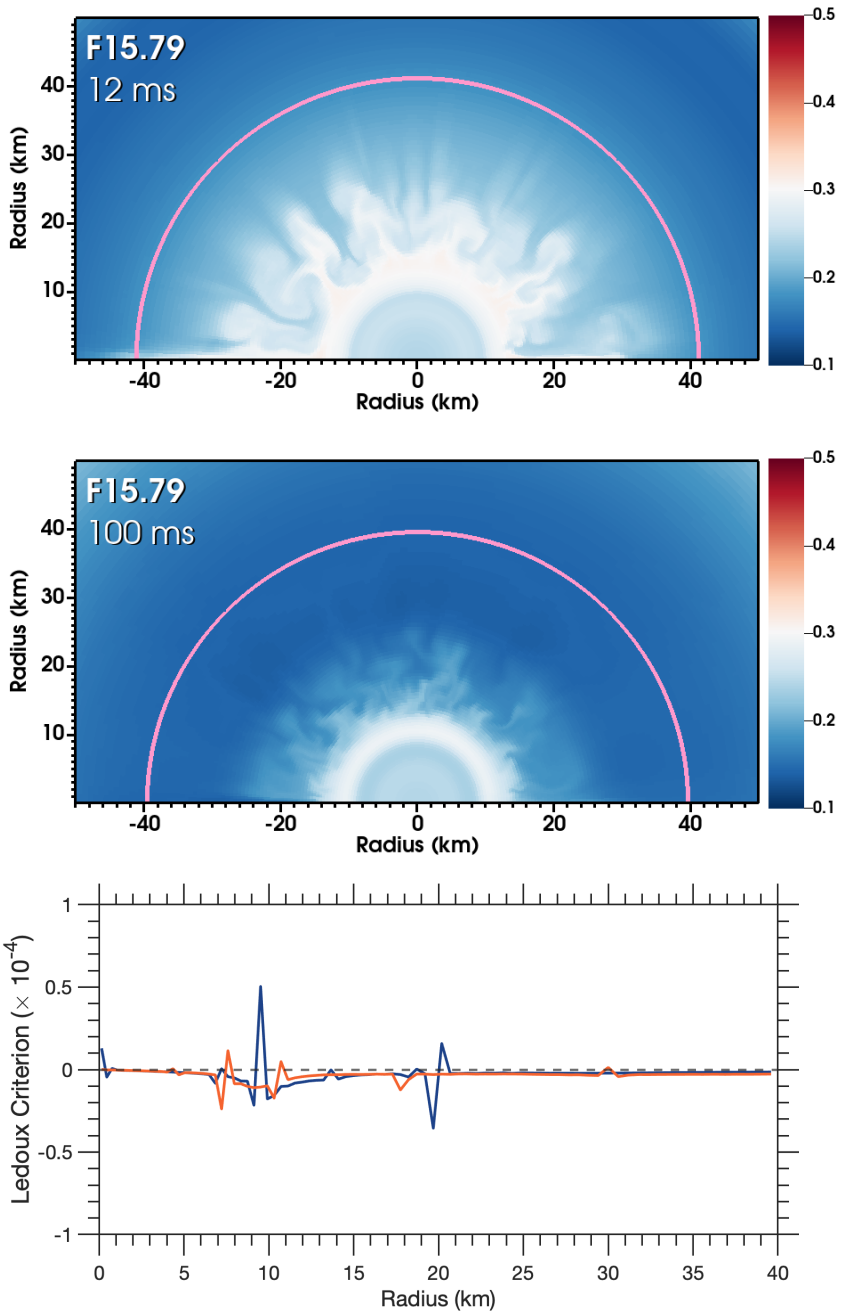


Figure 5.16: Electron fraction and Ledoux criterion for F15.79 shortly after bounce. Plots of electron fraction within the inner 50 km of the star for F15.79 at 12 ms (top) and 100 ms (middle) postbounce, displaying the onset and dissipation of prompt convection and prompt-convection–induced turbulence. Color axis represents electron fraction. The contour (pink) corresponds to the outer boundary of region I. The bottom panel shows the Ledoux criterion, as defined in the text, as a function of radius at 12 ms (dark blue) and 100 ms (orange) postbounce.

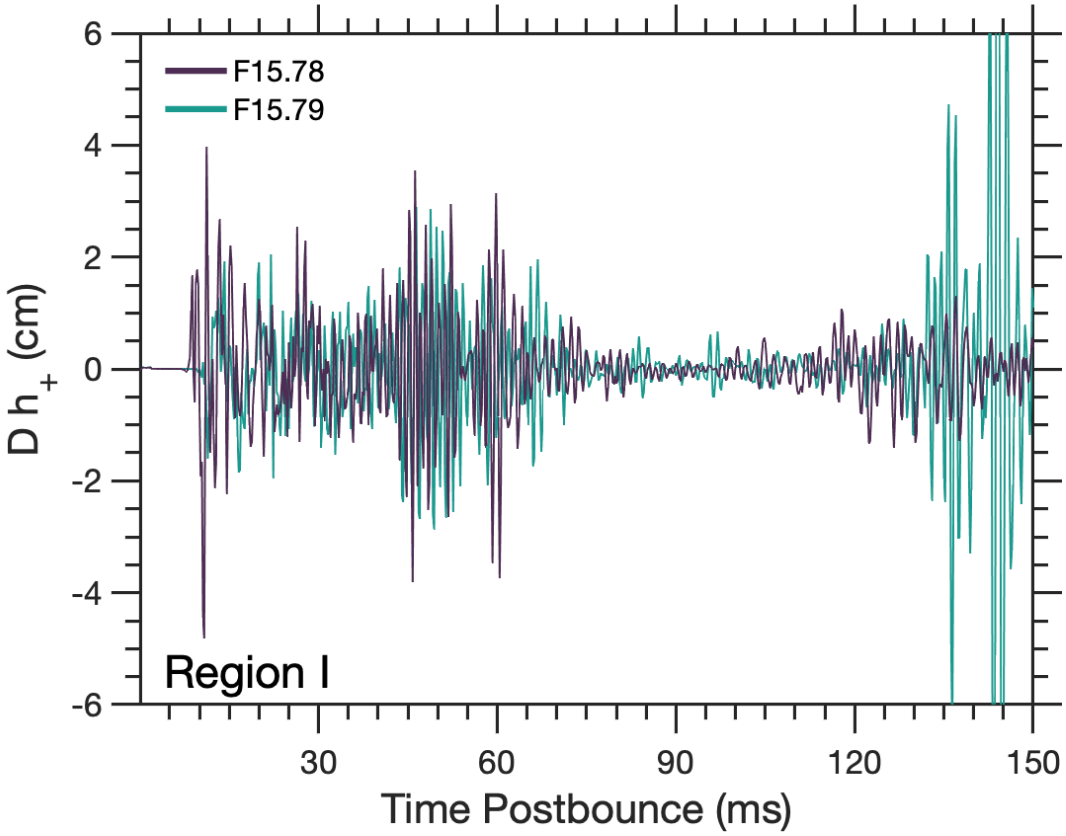


Figure 5.17: Gravitational wave strains produced in region I, multiplied by a distance of 10 kpc, during the first 150 ms after core bounce for F15.78 (purple) and F15.79 (teal).

5.2.7 Neutrino-Driven Convection and the SASI

After the quiescent phase, which lasts ∼100 ms and during which time the gravitational wave emission is low, the phase of accretion-induced, high-frequency gravitational wave emission begins. During the period over which the magnitude of the gravitational wave strain is maximum, from ∼150–650 ms for both models, we see from Figure 5.14 that significant contributions to the total gravitational wave strain come from each region. Figures 5.18 and 5.19 depict the specific entropy for the inner 200 km of the star at three different times, for F15.78 and F15.79, respectively. In these figures, the lower-entropy accretion funnels are distinct, as are the high-entropy plumes. The top panels, at 190 ms postbounce and 244 ms postbounce, respectively, correspond to the times at which we see in Figure 5.9 the maximum gravitational wave strains. At these postbounce times, accretion funnels penetrate nearly to the outer boundary of region I in the PNS, denoted by the contour (pink) in each panel. They excite oscillations in both regions I and II, as seen in Figure 5.14. The postbounce times also match the times at which the neutrino luminosities are maximum in each model, as seen in Figure 16 of Bruenn et al. (2023). The neutrino luminosities are fed by accretion onto the PNS. The middle panels of Figures 5.18 and 5.19, at 398 and 446 ms postbounce, respectively, depict the last significant accretion events in each model. The postbounce time in each case corresponds to the last large-amplitude strain in the gravitational wave strains produced in region II, as seen in Figure 5.14. Finally, the bottom panels in Figures 5.18 and 5.19, at 756 and 664 ms postbounce, respectively, depict the times when accretion funnels no longer make any contact with the PNS. The contours (purple) denote the outer boundaries of region II. These times correspond to the times at which the strains in region II have dropped significantly, as seen in Figure 5.14. These times also correspond to the sharp decline in neutrino accretion luminosity for each model, as shown in Figure 16 of Bruenn et al. (2023).

Figure 5.20 shows the gravitational wave strains beginning at 600 ms postbounce for regions I and II. We see that the gravitational wave strains in region II are now

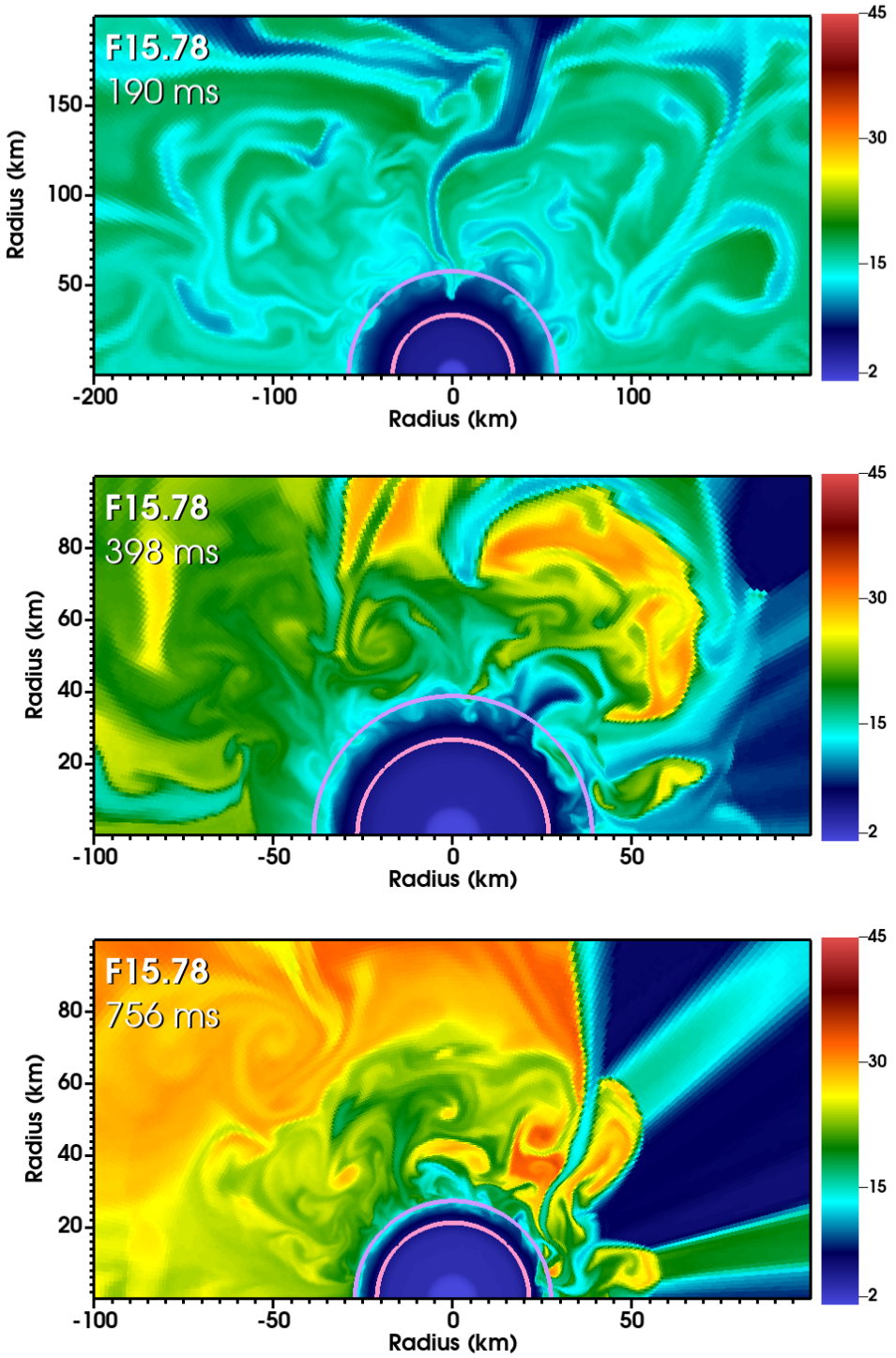


Figure 5.18: Specific entropy within the inner 200 km of the F15.78 model at 190 ms (top), 398 ms (middle), and 756 ms (bottom) postbounce.

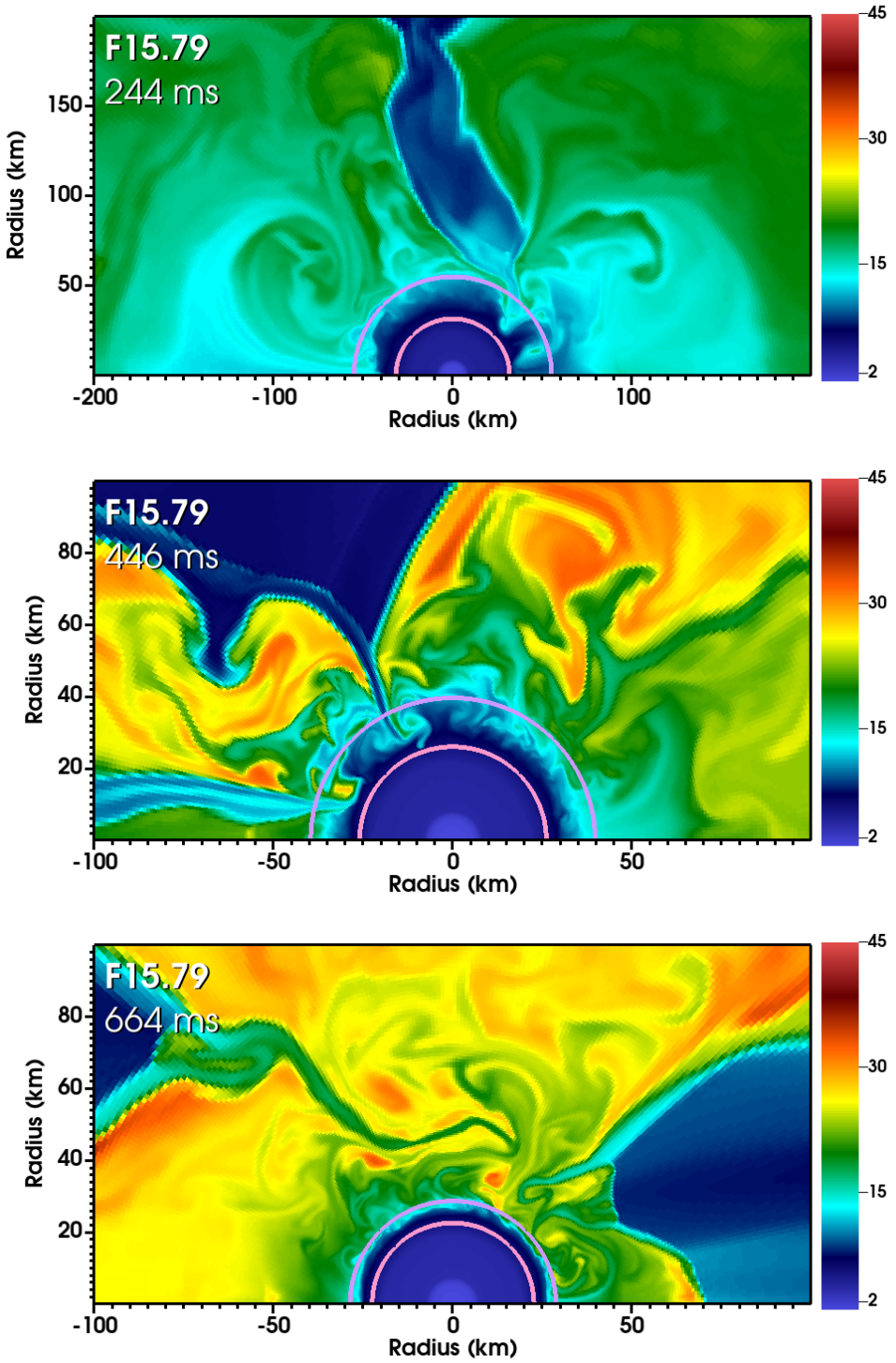


Figure 5.19: Specific entropy within the inner 200 km of the F15.79 model at 244 ms (top), 446 ms (middle), and 664 ms (bottom) postbounce.

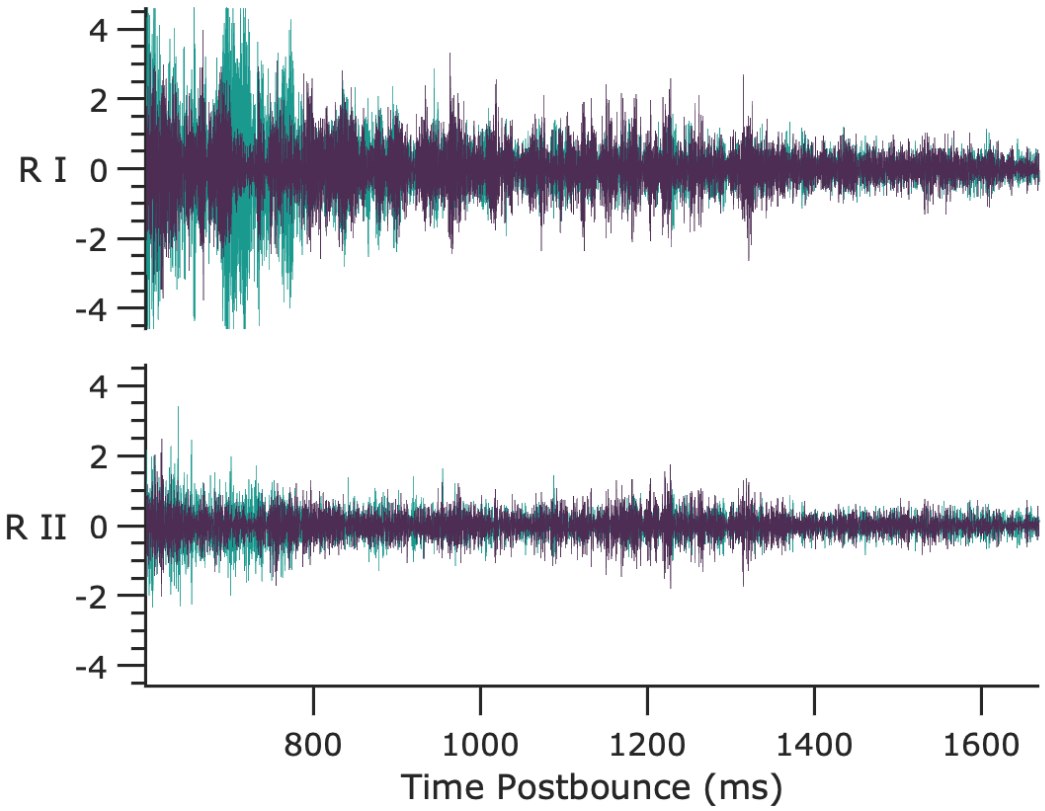


Figure 5.20: Gravitational wave strains produced in regions I and II, multiplied by a distance of 10 kpc, starting at 600 ms postbounce for F15.78 (purple) and F15.79 (teal).

smaller than those in region I, for both models. Interestingly, the gravitational wave strain from F15.78 becomes larger in region I at ∼800 ms post bounce. Given that this is shortly after the end of accretion-assisted gravitational wave production in F15.79, this indicates that sustained Ledoux convection in F15.79, sustained by the diffusion of neutrinos out of the PNS and, consequently, the sustained lepton-fraction gradients, is weaker than that of F15.78, similar to our conclusion earlier regarding prompt convection.

5.2.8 Linear Memory

The gravitational wave memory is the sum of contributions from gravitational wave emitted due to matter motion and the anisotropic emission of neutrinos. We first make connections directly to the matter strains shown in Figure 5.9 in order to highlight these differences in isolation. We present in Figures 5.21 and 5.22 snapshots of the entropy for each model across different times. For both models, after the shock is revived the prolate shock expansion causes a low frequency increase in gravitational wave strain seen as a "tail" in Figure 5.9. The stronger explosion in the F15.79 model results in a larger increase in the strain, as seen in bilateral entropy plumes signifying matter moving outward at 422 and 500 ms after bounce for each model, respectively. Interestingly, in the F15.78 model we observe a plume generated perpendicular to the axis of explosion between 600–800 ms after bounce, shown at 734 ms after bounce in Figure 5.22. This additional plume decreases the quadrupole moment of the explosion, and we see this effect decreasing the overall gravitational wave strains as well. No such feature develops in F15.78. Near the end of the simulation, we see that both models exhibit strong plumes moving outward along a single direction, with F15.79 having the stronger explosion feature. This causes the overall gravitational wave memory affect from the matter to be larger for the F15.79 model.

In Figure 5.23, we present the neutrino component of the gravitational wave signal, for both models. We plot the contribution to the gravitational wave strain from each

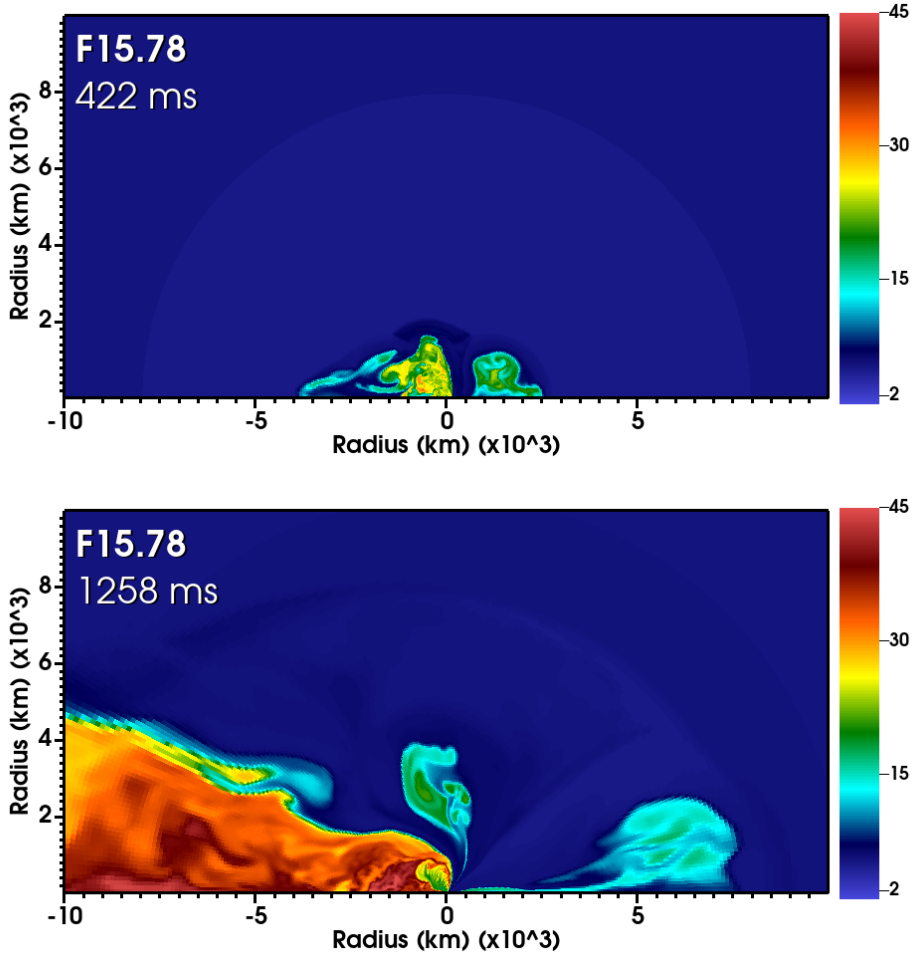


Figure 5.21: F15.78 specific entropy at 442 ms and 1258 ms for $r <= 10{,}000$ km. Displays key hydrodynamic features that contribute to the evolution of the memory resulting from the matter outflows.

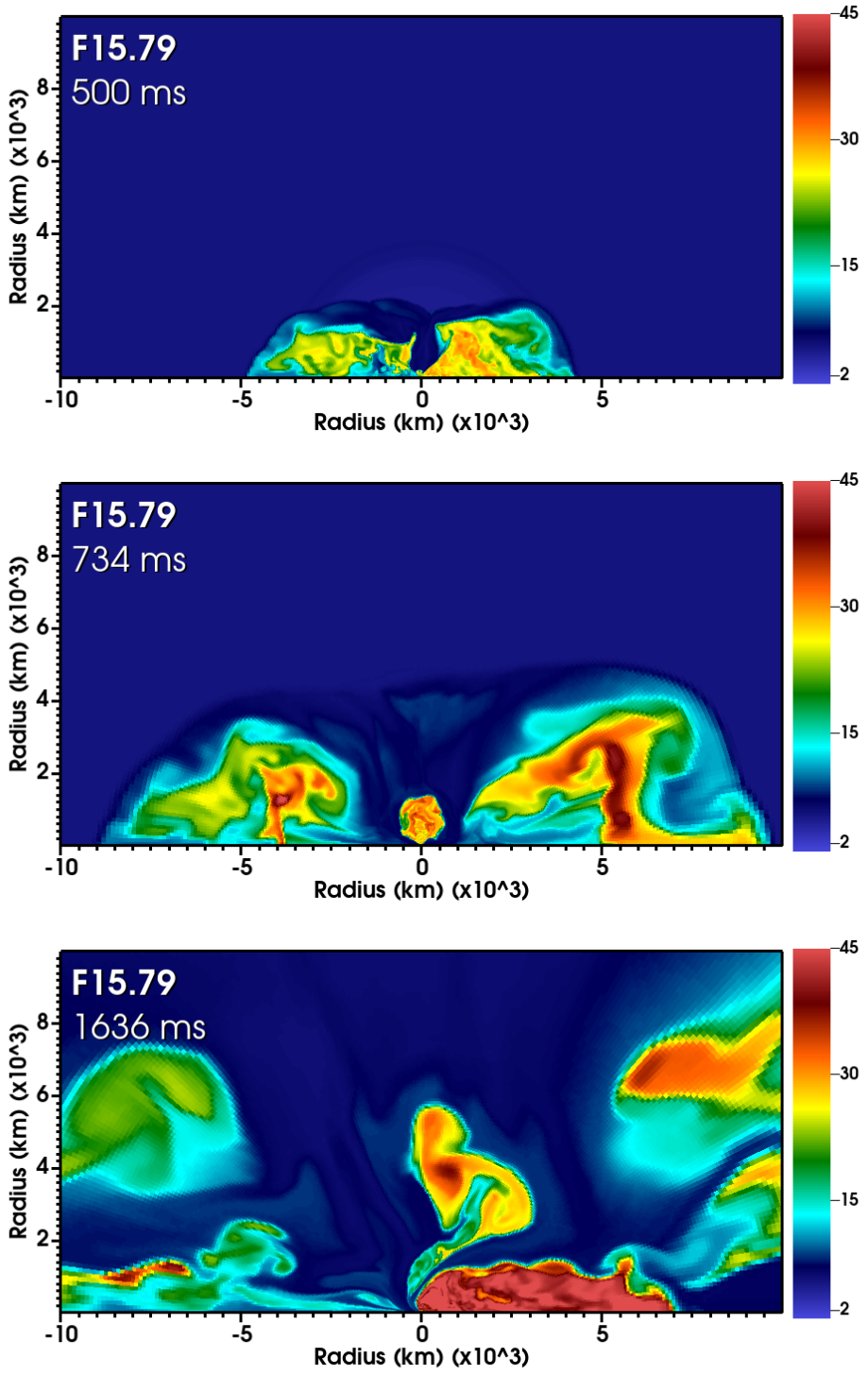


Figure 5.22: F15.79 specific entropy at 500, 734, and 1636 ms for $r <= 10{,}000$ km. Displays key hydrodynamic features that contribute to the evolution of the memory resulting from the matter outflows.

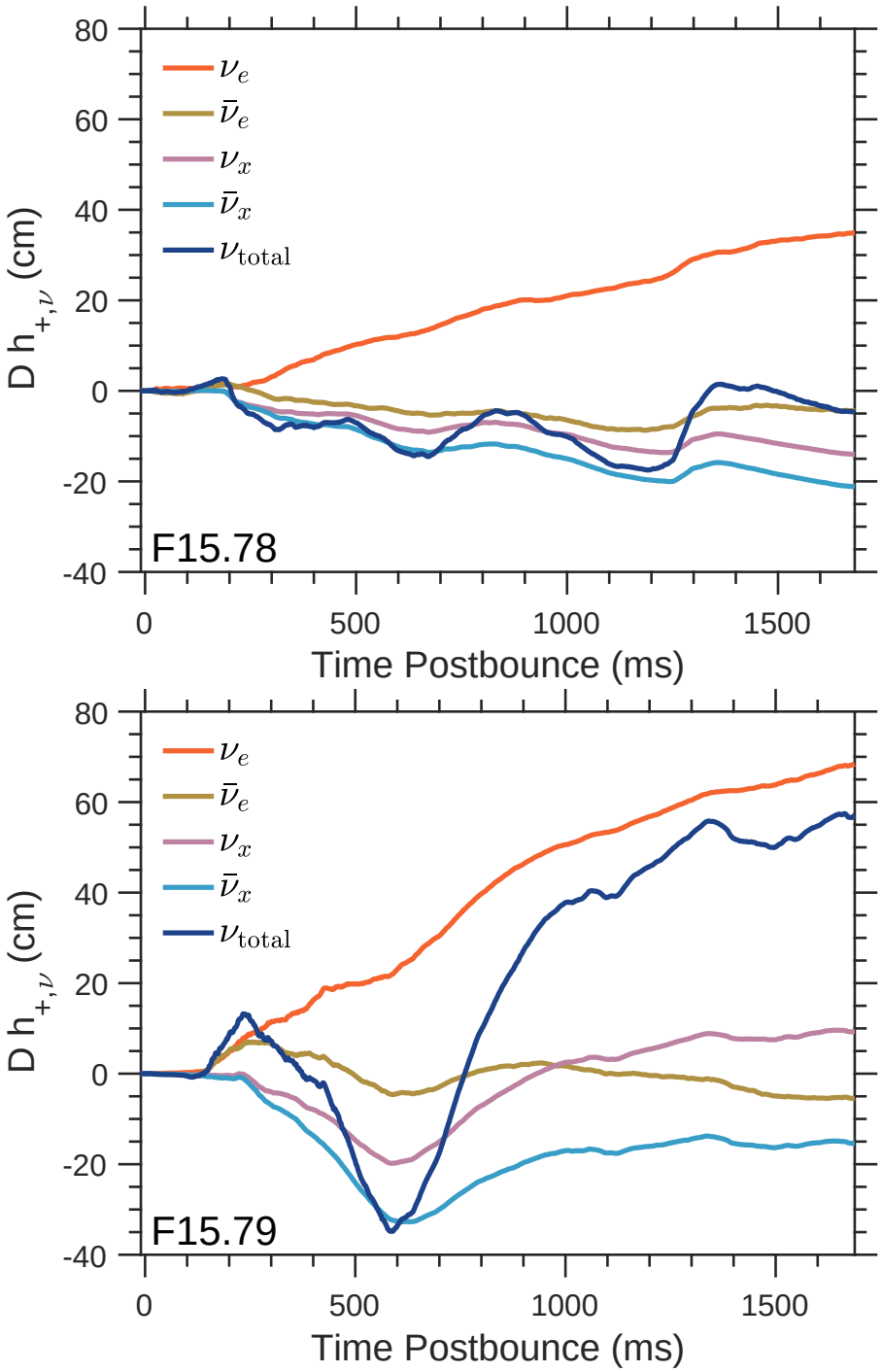


Figure 5.23: Gravitational wave strain from the anisotropic emission of neutrinos. Strains multiplied by a distance of 10 kpc, and strains from different neutrino species are distinguished by color: electron neutrinos (orange), anti-electron neutrinos (yellow), heavy neutrinos ($\mu + \tau$ neutrinos; purple), anti-heavy neutrinos (light blue), and the total neutrino-produced gravitational wave strain (dark blue).

neutrino specie, as well as the total. The detected gravitational wave strain would of course be the sum of the contributions from matter motion and neutrino emission, shown in Figure 5.24. Comparing this figure with Figure 5.9, we see that the addition of the contribution from neutrino emission has two significant effects: (1) There is a significant change in the amplitude of the gravitational wave memory. (2) A low-frequency modulation is introduced in the evolution to the memory. However, because the frequency modulation is so low, the spectrograms remain identical to those shown in Figures 5.10 for the matter contribution only.

5.2.9 Summary, Discussion, and Conclusion

We computed the gravitational wave strains produced from the core collapse supernovae of two progenitor stars with nearly identical mass but of differing internal structure. The differing explosion dynamics of these two models, as outlined in Bruenn et al. (2023), resulted in distinct gravitational wave strains, as seen in Figure 5.9. Significantly larger amplitudes associated with accretion-induced, high-frequency gravitational wave emission and with low-frequency emission from explosion and anisotropic neutrino emission are observed in model F15.79. This is accompanied by a larger gravitational wave luminosity and a larger total emitted gravitational wave energy.

By decomposing the gravitational wave strain production into three regions, we showed that the period of maximum gravitational wave strain corresponds to the time during which all regions are contributing significantly. This overlaps with the accretion period onto the PNS, and we depict accretion funnels penetrating nearly to the outer boundary of region I in Figures 5.18 and 5.19. By $\sim$700 ms, accretion onto the PNS ends for both models, and the high-frequency gravitational wave strain is produced largely within region I, as shown in Figure 5.20. That is, accretion-induced, high-frequency gravitational wave emission has given way to sustained-Ledoux-convection–induced, high-frequency gravitational wave emission.

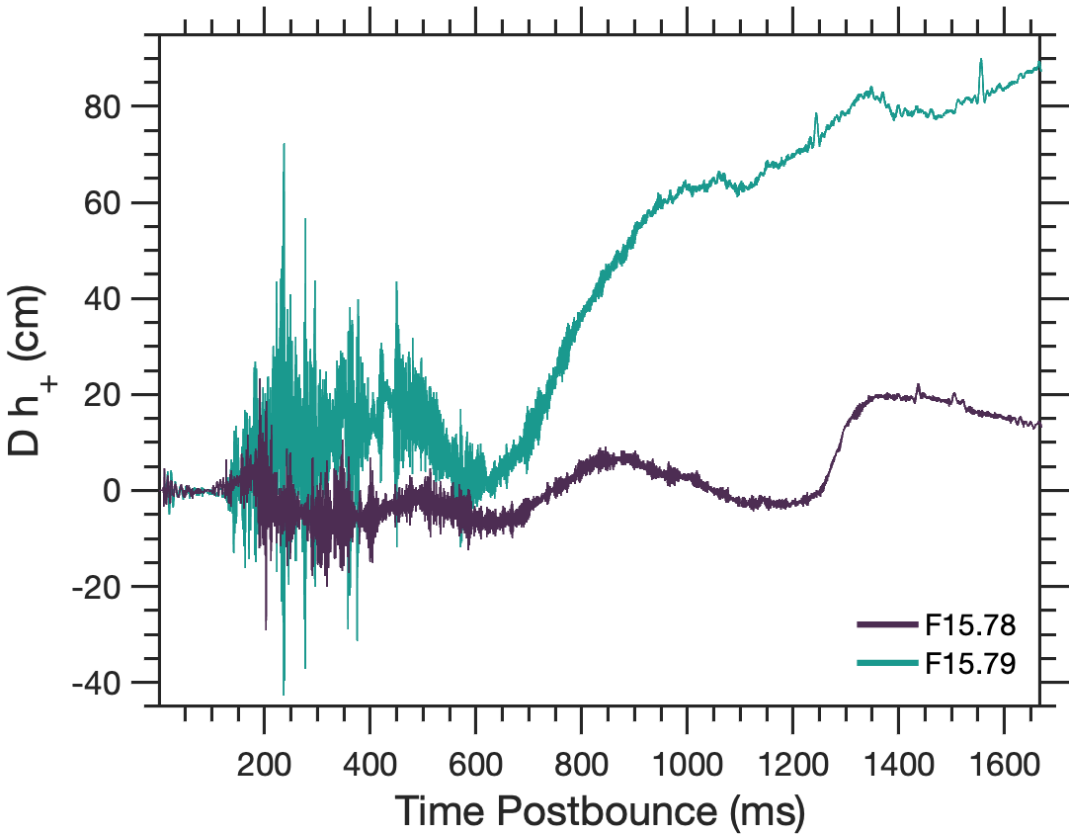


Figure 5.24: Total h_+-polarized gravitational wave strain from both the anisotropic emission of neutrinos and matter motion, multiplied by a distance of 10 kpc for F15.78 (purple) and F15.79 (teal). The observer of the explosion is aligned along the z-axis of the simulation.

Our data agrees with the positive correlation found between compactness parameter and peak frequency evolution found in Warren et al. (2020) and Pajkos et al. (2021). Figure 5.11 shows that the more compact model, F15.79, has a peak frequency that increases more rapidly, as determined by the larger slope of the HFF, than for the less compact model. Table 5.1 shows that the difference in slope of the HFF between models is ∼20%, with a difference in starting frequency of ∼10%. As in Murphy et al. (2024), we quantify this variation in the absence of any other progenitor differences (e.g., differences in rotation rate). Wang and Pan (2024) show the effects of varying progenitor rotation rate in tandem with compactness parameter. They present models where progenitors with relatively higher compactness parameters have a smaller HFF slope than a less compact counterpart that is rotating less rapidly.

It is now well established that the gravitational wave emission in two-dimensional and three-dimensional CCSN simulations differ considerably in both amplitude and sourcing (e.g., see Andresen et al. (2017); O'Connor and Couch (2018); Mezzacappa et al. (2020)). In particular, two-dimensional simulations point to accretion onto the PNS as the dominant excitation mechanism for gravitational wave production, and that is the case in our study as well. However, three-dimensional CCSN simulations have shown that excitation from deep within the core of the PNS, from convection, can be comparable to the excitation from outside the PNS during the accretion phase, and dominant after it Andresen et al. (2017); Mezzacappa et al. (2023); Murphy et al. (2025b). In two dimensions, the greater compactness of the F15.79 progenitor led to accretion-induced gravitational wave emission of significantly larger amplitude and duration. Three-dimensional simulations, counterparts to the two-dimensional simulations presented here, would have to be performed to ascertain the differences. On the other hand, the contraction rate of the PNS, and thus the slope of the HFF, seems less affected by the dimensionality of the simulation Sotani and Takiwaki (2020b).

Chapter 6

Conclusions and Outlook

In this dissertation, I presented a comprehensive analysis of gravitational wave generation in CCSNe using the state-of-the-art CHIMERA simulation code. I extracted gravitational wave strains from two- and three-dimensional CHIMERA simulations using Equations (2.125)–(2.130), and constructed the pipeline to create spectrograms from gravitational wave strains using the methods in Section 2.1.6. I modified the region 5 boundary defined in Mezzacappa et al. (2023) to extend to the edge of the computational grid, as shown in Figure 4.1, so that the strain calculation could be performed including the surface term in Equation (2.125) for each region. Combining this regional decomposition of the strains with the modal analysis of the PNS, as described in Section 2.2 and Chapter 3, I showed the source and character of the high frequency component of the gravitational wave signal changes with time. The signal begins as a low-order ${}^2g$-mode, excited by accretion onto the surface of the PNS, and migrates deeper into the convective and convective-overshoot regions of the PNS over the course of the CCSN simulation, eventually becoming an ${}^2f$-mode. I then demonstrated that this high frequency component of the signal is sensitive to the nuclear EOS, and, in principle, differences in nuclear EOS are detectable with current generation gravitational wave detectors. Finally, I presented the gravitational wave

signals for progenitors with differing internal structures, showing that these differences are imprinted on the gravitational wave signal.

6.1 Future Modal Analyses

The modal analysis derived in Section 2.2, while effective and capable of explaining the character of the high-frequency component of the gravitational wave signal, is not yet fully mature. This is seen, for example, in the incongruous power output predicted for the early time ${}^2f$- and ${}^2p_1$-modes by the modal analysis that is not present in the spectrograms. An analysis that fully agrees with the spectrograms, which are produced without any assumptions on the matter motions of the PNS, would reduce the predicted power output by these modes to agree with the spectrograms. The most immediate improvement to be made would be to account for perturbations along the ϕ direction by including ξ^ϕ terms in Equations (2.157)–(2.160), and introducing the linearized equation for the ξ^ϕ perturbation. This would mean the Anzätze in Equations (2.162)–(2.164) would now depend on the full spherical harmonics $Y_{\ell m}$, which would change the identities used to arrive at the final form of Equations (2.193). The new system of equations would include five, coupled ordinary differential equations to describe the perturbations, including two separate evolution equations for η_θ and η_ϕ instead of the current evolution equation for the composite variable$\eta_\perp$. While this would make the system more difficult to solve, additional computational costs may be mitigated by using the already optimized ordinary differential equation solver ODEPACK (Hindmarsh, 2019). For the current system, the trapezoidal integration method proved to be much faster than ODEPACK without appreciable loss of accuracy.

Another possibility to improve the modal analysis would be to relax the assumption of hydrostatic equilibrium. In Tseneklidou et al. (2025), a perturbative method is introduced that allows for a non-static background (i.e., $v_o \neq 0$ as we required in hydrostatic equilibrium). This makes it possible to account for

accretion onto the PNS in the background, instead of treating it as a perturbation. Eventually, it will be necessary to account for a non-spherical background, e.g. reading in CHIMERA data directly as the background without spherically averaging the quantities. Together, these advancements may be enough to properly model the ${}^2f$- and ${}^2p_1$-modes at the early times when they are not present in the spectrogram. If none of these advancements properly lower the gravitational wave production efficiency of these modes at early times, the final consideration for improvement would be re-derive the linearized perturbation equations without any assumption of hydrostatic equilibrium on the background solution.

6.2 Discussion and Future Outlook

The sophistication of current CCSN simulation codes now allows for sophisticated predictions for the multimessenger signals from CCSNe. As the high frequency component of the gravitational wave signal is directly connected to the oscillation frequency of the PNS and its contraction, a gravitational wave detection would allow for an unprecedented view of the first few seconds of life for a neutron star or black hole. One clear goal of CCSN simulation is to determine precisely how the high frequency gravitational wave signal evolution relates to PNS evolution. Fortunately, asteroseismology provides insight into how different oscillation modes relate to the physical properties of a star.

For ${}^2g$-modes, the restoring force of the oscillation is buoyancy, and the frequency of oscillation is proportional to the surface gravity at radius R

$$f \propto \frac{GM}{R^2}. \tag{6.1}$$

For the fundamental ${}^2f$-mode, the restoring force of the oscillation is pressure driven, and the frequency of the oscillation is proportional to the mean density over the whole

region that is oscillating

$$f \propto \sqrt{\frac{GM}{R^3}}. \tag{6.2}$$

Several studies have already used this knowledge to investigate so-called "universal relations" connecting gravitational wave frequency to the surface gravity or mean density (Müeller et al., 2013; Cerdá-Durán et al., 2013; Pan et al., 2018; Torres-Forné et al., 2019a; Powell and Müller, 2019, 2020; Sotani et al., 2021; Mori et al., 2023; Sotani et al., 2024). Then, with the application of a particular universal relation, either the surface gravity or mean density of the PNS can be tracked as a function of time by determining the high frequency component of the gravitational wave signal as a function of time (Bizouard et al., 2021; Powell and Müller, 2022; Bruel et al., 2023).

The modal analysis presented here indicates the PNS evolution may be complicated enough to warrant the consideration of both types of universal relations, as first done in Torres-Forné et al. (2019a). This would involve an initial relation based on the surface gravity of the PNS for the first part of the signal, corresponding to the time in which the low-order ${}^2g$-modes dominate in gravitational wave production, and a relation based on the mean density for the later time signal dominated by the ${}^2f$-mode oscillation of the PNS. While determining which part of the signal corresponds to which universal relation is more complicated in a real detection, such an analysis would allow for the determination of the mass and radius individually, instead of only their relation to each other.

Regardless of our ability to extract the PNS mass and radius evolution directly from the HFF, the evolution of the HFF itself is sensitive to many different parameters. In this dissertation, two such parameters were considered in isolation: nuclear EOS and stellar structure. Moreover, the differences between these parameters are discernible through measurements of the slope of the HFF. While differences in HFF slope are apparent between the E-series models that utilized different nuclear EOS, the precise mechanism causing this differences is not immediately clear. As an example,

consider the incompressibility parameter, K, that can be used as a measure of how "stiff" a nuclear EOS is, with higher incompressibility corresponding to a "stiffer" EOS. The stiffest nuclear EOS considered in Section 5.1 is for model E-SFHo, which has the greatest HFF slope. However, the second stiffest nuclear EOS is for E-DD2, which has the lowest HFF slope. Future investigations focused on the nuclear physics of each EOS will help determine which differences in EOS parameters contribute to the changes that are tracked in the HFF.

It is clear that other factors affect the PNS contraction rate, and thus slope of the HFF, as well. In general, rotating progenitors stabilize the core to contraction and slow PNS contraction (Andresen et al., 2019; Powell and Müller, 2020; Pajkos et al., 2021; Takiwaki et al., 2021). Varying multiple parameters simultaneously complicates the analysis of the HFF still further (Wang and Pan, 2024; Jardine et al., 2022). Indeed, within this dissertation three models using the SFHo nuclear EOS were presented: E-SFHo, F15.78, and F15.79. The E-series model has a lower progenitor mass, 15 $M_\odot$ than the F-series models. E-SFHo has a compactness of $\xi_{2.5} = 0.148$, which is in between the compactness of the F15.78 and F15.79 models, $\xi_{2.5} = 0.136$ and $\xi_{2.5} = 0.206$ respectively. However, the slope of the HFF for E-SFHo is 2218 Hz s^{-1}, only $\sim$2% lower than the slope of F15.79 (2263 Hz s^{-1}) and $\sim$19% larger than the slope of F15.78 (1789 Hz s^{-1}). Already, varying both mass and compactness simultaneously presents challenges in interpretation. The compactness seems to have a much larger effect on the PNS contraction rate than the progenitor mass, but making a definitive conclusion on the sensitivity to compactness variations is not possible with only three models.

This dissertation presents one comparison between models where the HFF was not greatly affected by the dimensionality of models using the same nuclear EOS, but more work remains to be done to confirm this with other models. Sotani and Takiwaki (2020b) provide two- and three-dimensional models using two additional nuclear EOS, the DD2 EOS and TGTF EOS (Togashi et al., 2017). For the DD2 EOS, they find results similar to what was reported for the LSBCK EOS in Section

5.1.6. The differences in PNS contraction rate for the TGTF EOS are small, but observable. Without the gravitational wave data, it is not evident if this difference is large enough to greatly affect the HFF. Ideally, the effects of each parameter affecting the HFF slope (e.g., progenitor mass, rotation, compactness, magnetic field strength, etc.) should be assessed in three-dimensions. Realistically, some investigation should quantify the impact of dimensionality on each parameter.

While current CCSN simulations have reached a high level of fidelity and modern HPC architectures have made three-dimensional simulations possible, the theory of CCSN is far from complete and quantifiable predictions from CCSN simulations are only just beginning. Already, the next generation of high-fidelity CCSNe simulations are in development across the globe, and the next generation of gravitational wave detectors are being designed for increased sensitivity. Together, these advancements, along with the ever increasing capabilities of HPC, promise to make the next galactic core collapse supernova among the most illuminating events in human history.

Bibliography

Aasi, J. et al. (2015). Advanced LIGO. *Classical and Quantum Gravity*, 32(7):074001. 112

Abbott, B. P., Abbott, R., Abbott, T. D., Abernathy, M. R., Acernese, F., Ackley, K., Adams, C., Adams, T., Addesso, P., Adhikari, R. X., and et al. (2016). Observation of Gravitational Waves from a Binary Black Hole Merger. *Phys. Rev. Lett.*, 116(6):061102. 15

Abbott, R. et al. (2023). Gwtc-3: Compact binary coalescences observed by ligo and virgo during the second part of the third observing run. *Phys. Rev. X*, 13:041039. 111

Abbott, R. et al. (2023). Open Data from the Third Observing Run of LIGO, Virgo, KAGRA, and GEO. *Ap.J. Suppl.*, 267(2):29. 112

Abbott, R. et al. (2024). Gwtc-2.1: Deep extended catalog of compact binary coalescences observed by ligo and virgo during the first half of the third observing run. *Phys. Rev. D*, 109:022001. 111

Abdikamalov, E., Pagliaroli, G., and Radice, D. (2022). Gravitational Waves from Core-Collapse Supernovae. In Bambi, C., Katsanevas, S., and Kokkotas, K. D., editors, *Handbook of Gravitational Wave Astronomy*, page 21. Springer, Singapore. 15, 112

Acernese, F. et al. (2015). Advanced Virgo: a second-generation interferometric gravitational wave detector. *Classical and Quantum Gravity*, 32(2):024001. 112

Adams, S. M., Kochanek, C. S., Beacom, J. F., Vagins, M. R., and Stanek, K. Z. (2013). Observing the Next Galactic Supernova. *Ap.J.*, 778(2):164. 14

Aerts, C., Christensen-Dalsgaard, J., and Kurtz, D. W. (2010). *Asteroseismology*. Springer Dordrecht. 82

Afle, C. and Brown, D. A. (2021a). Inferring physical properties of stellar collapse by third-generation gravitational-wave detectors. *Phys. Rev. D*, 103(2):023005. 113

Afle, C. and Brown, D. A. (2021b). Inferring physical properties of stellar collapse by third-generation gravitational-wave detectors. *Phys. Rev. D*, 103(2):023005. 139

Andresen, H., Glas, R., and Janka, H. T. (2021). Gravitational-wave signals from 3D supernova simulations with different neutrino-transport methods. *Mon. Not. R. Ast. Soc.*, 503(3):3552–3567. 17

Andresen, H., Müller, B., Müller, E., and Janka, H.-T. (2017). Gravitational wave signals from 3d neutrino hydrodynamics simulations of core-collapse supernovae. *Mon. Not. R. Ast. Soc.*, 468(2):2032–2051. 16, 18, 107, 116, 138, 139, 169

Andresen, H., Müller, E., Janka, H.-T., Summa, A., Gill, K., and Zanolin, M. (2019). Gravitational waves from 3d core-collapse supernova models: The impact of moderate progenitor rotation. *Mon. Not. R. Ast. Soc.*, 486(2):2238–2253. 16, 116, 138, 139, 174

Aso, Y., Michimura, Y., Somiya, K., Ando, M., Miyakawa, O., Sekiguchi, T., Tatsumi, D., and Yamamoto, H. (2013). Interferometer design of the KAGRA gravitational wave detector. *Phys. Rev. D*, 88(4):043007. 112

Baade, W. and Zwicky, F. (1934a). Cosmic Rays from Super-novae. *Proceedings of the National Academy of Science*, 20(5):259–263. 3

Baade, W. and Zwicky, F. (1934b). On Super-novae. *Proceedings of the National Academy of Science*, 20(5):254–259. 3

Baade, W. and Zwicky, F. (1934c). Remarks on Super-Novae and Cosmic Rays. *Physical Review*, 46(1):76–77. 3

Baron, E., Cooperstein, J., and Kahana, S. (1985). Type-II supernovae in 12-solar-mass and 15-solar-mass stars The equation of state and general relativity. *Phys. Rev. Lett.*, 55:126–129. 72, 120

Bethe, H. A. and Wilson, J. R. (1985). Revival of a stalled supernova shock by neutrino heating. *Ap.J.*, 295:14–23. 5

Bionta, R. M., Blewitt, G., Bratton, C. B., Casper, D., and Ciocio, A. (1987). Observation of a neutrino burst in coincidence with supernova 1987A in the Large Magellanic Cloud. *Phys. Rev. Lett.*, 58:1494–1496. 15

Bizouard, M.-A., Maturana-Russel, P., Torres-Forné, A., Obergaulinger, M., Cerdá-Durán, P., Christensen, N., Font, J. A., and Meyer, R. (2021). Inference of protoneutron star properties from gravitational-wave data in core-collapse supernovae. *Phys. Rev. D*, 103(6):063006. 18, 115, 139, 173

Blondin, J. M. and Mezzacappa, A. (2006). The Spherical Accretion Shock Instability in the Linear Regime. *Ap.J.*, 642(1):401–409. 7

Blondin, J. M., Mezzacappa, A., and DeMarino, C. (2003). Stability of Standing Accretion Shocks, with an Eye toward Core-Collapse Supernovae. *Ap.J.*, 584(2):971–980. 7

Bollig, R., Yadav, N., Kresse, D., Janka, H.-T., Müller, B., and Heger, A. (2021). Self-consistent 3D Supernova Models From -7 Minutes to +7 s: A 1-bethe Explosion of a 19 $M_\odot$ Progenitor. *Ap.J.*, 915(1):28. 11

Bruel, T., Bizouard, M.-A., Obergaulinger, M., Maturana-Russel, P., Torres-Forné, A., Cerdá-Durán, P., Christensen, N., Font, J. A., and Meyer, R. (2023). Inference of protoneutron star properties in core-collapse supernovae from a gravitational-wave detector network. *Phys. Rev. D*, 107(8):083029. 18, 115, 139, 173

Bruenn, S. W. (1985). Stellar core collapse - Numerical model and infall epoch. *Ap.J. Suppl.*, 58:771–841. 13

Bruenn, S. W. (1985). Stellar core collapse - Numerical model and infall epoch. *Ap.J. Suppl.*, 58:771–841. 13

Bruenn, S. W., Blondin, J. M., Hix, W. R., Lentz, E. J., Messer, O. E. B., Mezzacappa, A., Endeve, E., Harris, J. A., Marronetti, P., Budiardja, R. D., and et al. (2020). Chimera: A massively parallel code for core-collapse supernova simulations. *Ap.J. Suppl.*, 248(1):11. 1, 12, 72, 117, 141

Bruenn, S. W. and Mezzacappa, A. (1994). Prompt Convection in Core Collapse Supernovae. *Ap.J.*, 433:L45–L48. 155

Bruenn, S. W., Sieverding, A., Lentz, E. J., Sukhbold, T., Hix, W. R., Huk, L. N., Harris, J. A., Messer, O. E. B., and Mezzacappa, A. (2023). Comparison of the Core-collapse Evolution of Two Nearly Equal-mass Progenitors. *Ap.J.*, 947(1):35. 111, 140, 141, 142, 143, 149, 151, 159, 167

Bugli, M., Guilet, J., Foglizzo, T., and Obergaulinger, M. (2023). Three-dimensional core-collapse supernovae with complex magnetic structures - II. Rotational instabilities and multimessenger signatures. *Mon. Not. R. Ast. Soc.*, 520(4):5622–5634. 139

Bugli, M., Guilet, J., and Obergaulinger, M. (2021). Three-dimensional core-collapse supernovae with complex magnetic structures - I. Explosion dynamics. *Mon. Not. R. Ast. Soc.*, 507(1):443–454. 9

Buras, R., Rampp, M., Janka, H.-T., and Kifonidis, K. (2006). Two-dimensional hydrodynamic core-collapse supernova simulations with spectral neutrino transport. I. Numerical method and results for a 15 $M_\odot$ star. *Astron. Astrophys.*, 447:1049–1092. 10, 13

Burbidge, E. M., Burbidge, G. R., Fowler, W. A., and Hoyle, F. (1957). Synthesis of the Elements in Stars. *Rev. Mod. Phys.*, 29(4):547–650. 3

Burrows, A., Hayes, J., and Fryxell, B. A. (1995). On the Nature of Core-Collapse Supernova Explosions. *Ap.J.*, 450:830. 6

Burrows, A. and Lattimer, J. M. (1988). Convection, Type II supernovae, and the early evolution of neutron stars. *Phys. Rep.*, 163(1):51–62. 6

Burrows, A., Radice, D., and Vartanyan, D. (2019). Three-dimensional supernova explosion simulations of 9-, 10-, 11-, 12-, and 13-$M_\odot$ stars. *Mon. Not. R. Astron. Soc*, 485(3):3153–3168. 11

Burrows, A., Radice, D., Vartanyan, D., Nagakura, H., Skinner, M. A., and Dolence, J. C. (2020). The overarching framework of core-collapse supernova explosions as revealed by 3D FORNAX simulations. *Mon. Not. R. Ast. Soc.*, 491(2):2715–2735. 11

Burrows, A. and Vartanyan, D. (2021). Core-collapse supernova explosion theory. *Nature*, 589(7840):29–39. 9, 143

Camelio, G., Lovato, A., Gualtieri, L., Benhar, O., Pons, J. A., and Ferrari, V. (2017). Evolution of a proto-neutron star with a nuclear many-body equation of state: Neutrino luminosity and gravitational wave frequencies. *Phys. Rev. D*, 96(4):043015. 114

Casallas-Lagos, A., Antelis, J. M., Moreno, C., Zanolin, M., Mezzacappa, A., and Szczepańczyk, M. J. (2023). Characterizing the temporal evolution of the high-frequency gravitational wave emission for a core collapse supernova with laser

interferometric data: A neural network approach. *Phys. Rev. D*, 108(8):084027. 112, 116, 123, 134, 149

Cerdá-Durán, P., DeBrye, N., Aloy, M. A., Font, J. A., and Obergaulinger, M. (2013). Gravitational Wave Signatures in Black Hole Forming Core Collapse. *Ap.J.*, 779(2):L18. 112, 173

Clark, D. H. and Stephenson, F. R. (1977). *The historical supernovae*. Pergamon Press, Oxford. 2, 14

Coffin, S. C., Williams, B. J., and Katsuda, S. (2022). A Third-epoch Proper Motion Study of the Forward Shock in Kepler's Supernova Remnant. *Ap.J.*, 926(1):84. 2

Colella, P. and Woodward, P. (1984). The Piecewise Parabolic Method (PPM) for Gas-Dynamical Simulations. *Journ. Comp. Phys.*, 54:174–201. 12

Colgate, S. A., Grasberger, W. H., and White, R. H. (1961). The Dynamics of Supernova Explosions. *AJ*, 66:280. 4

Colgate, S. A. and White, R. H. (1966). The Hydrodynamic Behavior of Supernovae Explosions. *Ap.J.*, 143:626. 4

Couch, S. M. (2013). On the Impact of Three Dimensions in Simulations of Neutrino-Driven Core-collapse Supernova Explosions. *Ap.J.*, 775:35. 7

Creighton, J. D. E. and Anderson, W. G. (2011). *Gravitational-wave physics and astronomy: An introduction to theory, experiment and data analysis*. Weinheim, Germany : Wiley-VCH. 118

Díaz-Rodríguez, M., Murphy, J. W., Williams, B. F., Dalcanton, J. J., and Dolphin, A. E. (2021). Progenitor mass distribution for 22 historic core-collapse supernovae. *Mon. Not. R. Ast. Soc.*, 506(1):781–790. 2

Dimmelmeier, H., Font, J. A., and Müller, E. (2002). Relativistic simulations of rotational core collapse I. Methods, initial models, and code tests. *Astron. Astrophys.*, 388:917–935. 9

Dimmelmeier, H., Ott, C. D., Marek, A., and Janka, H.-T. (2008). Gravitational wave burst signal from core collapse of rotating stars. *Phys. Rev. D*, 78(6):064056. 16, 113

Dolence, J. C., Burrows, A., and Zhang, W. (2015). Two-dimensional Core-collapse Supernova Models with Multi-dimensional Transport. *Ap.J.*, 800:10. 7

Dubey, A., Reid, L. B., and Fisher, R. (2008). Introduction to FLASH 3.0, with application to supersonic turbulence. *Physica Scripta Volume T*, 132:014046. 12

Eggenberger Andersen, O., Zha, S., da Silva Schneider, A., Betranhandy, A., Couch, S. M., and O'Connor, E. P. (2021a). Equation-of-state Dependence of Gravitational Waves in Core-collapse Supernovae. *Ap.J.*, 923(2):201. 72, 108

Eggenberger Andersen, O., Zha, S., da Silva Schneider, A., Betranhandy, A., Couch, S. M., and O'Connor, E. P. (2021b). Equation-of-state Dependence of Gravitational Waves in Core-collapse Supernovae. *Ap.J.*, 923(2):201. 113, 139

Ehring, J., Abbar, S., Janka, H. T., Raffelt, G., Nakamura, K., and Kotake, K. (2024). Gravitational-Wave Signatures of Nonstandard Neutrino Properties in Collapsing Stellar Cores. *arXiv e-prints*, page arXiv:2412.02750. 139

Epstein, R. I. (1979). Lepton-driven convection in supernovae. *Mon. Not. R. Ast. Soc.*, 188:305–325. 6

Fattoyev, F. J., Horowitz, C. J., Piekarewicz, J., and Shen, G. (2010). Relativistic effective interaction for nuclei, giant resonances, and neutron stars. *Phys. Rev. C*, 82(5):055803. 119

Finn, L. S. and Evans, C. R. (1990). Determing gravitational radiation from Newtonian self-gravitating systems. *Ap.J.*, 351:588–600. 43

Foglizzo, T., Galletti, P., Scheck, L., and Janka, H.-T. (2007). Instability of a Stalled Accretion Shock: Evidence for the Advective-Acoustic Cycle. *Ap.J.*, 654:1006–1021. 7

Fryxell, B., Müller, E., and Arnett, D. (1989). *Hydrodynamics and nuclaer burning*. Max-Planck-Inst. für Physik und Astrophysik. 10

Fryxell, B., Olson, K., Ricker, P., Timmes, F. X., Zingale, M., Lamb, D. Q., MacNeice, P., Rosner, R., Truran, J. W., and Tufo, H. (2000). FLASH: An Adaptive Mesh Hydrodynamics Code for Modeling Astrophysical Thermonuclear Flashes. *Ap.J. Suppl.*, 131:273–334. 12

Glas, R., Just, O., Janka, H. T., and Obergaulinger, M. (2019). Three-dimensional Core-collapse Supernova Simulations with Multidimensional Neutrino Transport Compared to the Ray-by-ray-plus Approximation. *Ap.J.*, 873(1):45. 7

Green, D. A. (2002). Historical supernovae and their remnants. *Highlights of Astronomy*, 12:350–353. 2, 14

Hanke, F., Marek, A., Mueller, B., and Janka, H.-T. (2012). Is Strong SASI Activity the Key to Successful Neutrino-Driven Supernova Explosions? *Ap.J.*, 755:138. 7

Hanke, F., Müller, B., Wongwathanarat, A., Marek, A., and Janka, H.-T. (2013). SASI Activity in Three-dimensional Neutrino-hydrodynamics Simulations of Supernova Cores. *Ap.J.*, 770:66. 10

Hayes, J. C., Norman, M. L., Fiedler, R. A., Bordner, J. O., Li, P. S., Clark, S. E., ud-Doula, A., and Mac Low, M.-M. (2006). Simulating Radiating and Magnetized Flows in Multiple Dimensions with ZEUS-MP. *Ap.J. Suppl.*, 165:188–228. 11

Heger, A. and Woosley, S. E. (2010). Nucleosynthesis and Evolution of Massive Metal-free Stars. *Ap.J.*, 724:341–373. 72

Hempel, M. and Schaffner-Bielich, J. (2010). A statistical model for a complete supernova equation of state. *Nucl. Phys. A*, 837:210–254. 118

Herant, M., Benz, W., Hix, W. R., Fryer, C. L., and Colgate, S. A. (1994). Inside the Supernova: A Powerful Convective Engine. *Ap.J.*, 435:339. 6

Hindmarsh, A. C. (2019). ODEPACK: Ordinary differential equation solver library. Astrophysics Source Code Library, record ascl:1905.021. 171

Hirata, K., Kajita, T., Koshiba, M., Nakahata, M., and Oyama, Y. (1987). Observation of a neutrino burst from the supernova SN1987A. *Phys. Rev. Lett.*, 58:1490–1493. 15

Hix, W. R. and Meyer, B. S. (2006). Thermonuclear Kinetics in Astrophysics. *Nucl. Phys. A*, 777:188–207. 13

Hix, W. R. and Thielemann, F. K. (1999). Computational methods for nucleosynthesis and nuclear energy generation. *J. Comp. Appl. Math*, 109(1):321–351. 72

Horedt, G. P. (2004). *Polytropes - Applications in Astrophysics and Related Fields*, volume 306. Springer Dordrecht. xiii, 65, 66, 67, 68

Hurley, M., Roberts, P. H., and Wright, K. (1966). The Oscillations of Gas Spheres. *Ap.J.*, 143:535. 60

Jakobus, P., Müller, B., Heger, A., Zha, S., Powell, J., Motornenko, A., Steinheimer, J., and Stöcker, H. (2023). Gravitational Waves from a Core g Mode in Supernovae as Probes of the High-Density Equation of State. *Phys. Rev. Lett.*, 131(19):191201. 115, 139

Janka, H. T. (2025). Long-Term Multidimensional Models of Core-Collapse Supernovae: Progress and Challenges. *arXiv e-prints*, page arXiv:2502.14836. 9, 143

Janka, H. T., Buras, R., Kitaura Joyanes, F. S., Marek, A., Rampp, M., and Scheck, L. (2005). Neutrino-driven supernovae: An accretion instability in a nuclear physics controlled environment. *Nucl. Phys. A*, 758:19–26. 7

Janka, H. T. and Mueller, E. (1996). Neutrino heating, convection, and the mechanism of Type-II supernova explosions. *Astron. Astrophys.*, 306:167. 7

Janka, H.-T. and Müller, E. (1995). Neutrino-driven Type-II supernova explosions and the role of convection. *Phys. Rep.*, 256:135–156. 7

Jardine, R., Powell, J., and Müller, B. (2022). Gravitational wave signals from 2D core-collapse supernova models with rotation and magnetic fields. *Mon. Not. R. Ast. Soc.*, 510(4):5535–5552. 116, 138, 139, 174

Kawahara, H., Kuroda, T., Takiwaki, T., Hayama, K., and Kotake, K. (2018). A Linear and Quadratic Time-Frequency Analysis of Gravitational Waves from Core-collapse Supernovae. *Ap.J.*, 867(2):126. 112

Klimenko, S., Vedovato, G., Drago, M., Salemi, F., Tiwari, V., Prodi, G. A., Lazzaro, C., Ackley, K., Tiwari, S., Da Silva, C. F., and Mitselmakher, G. (2016). Method for detection and reconstruction of gravitational wave transients with networks of advanced detectors. *Phys. Rev. D*, 93(4):042004. 117

Kotake, K., Kuroda, T., and Hayama, K. (2017). Multimessenger Predictions from 3D General-Relativistic Core-Collapse Supernovae Models. In Marcowith, A., Renaud, M., Dubner, G., Ray, A., and Bykov, A., editors, *Supernova 1987A:30 years later - Cosmic Rays and Nuclei from Supernovae and their Aftermaths*, volume 331, pages 329–338. 113

Kotake, K., Sato, K., and Takahashi, K. (2006). Explosion mechanism, neutrino burst and gravitational wave in core-collapse supernovae. *Rep. Prog. Phys.*, 69:971–1143. 20, 42

Kuroda, T., Arcones, A., Takiwaki, T., and Kotake, K. (2020). Magnetorotational Explosion of a Massive Star Supported by Neutrino Heating in General Relativistic Three-dimensional Simulations. *Ap.J.*, 896(2):102. 12

Kuroda, T., Fischer, T., Takiwaki, T., and Kotake, K. (2022). Core-collapse Supernova Simulations and the Formation of Neutron Stars, Hybrid Stars, and Black Holes. *Ap.J.*, 924(1):38. 113, 139

Kuroda, T., Kotake, K., Hayama, K., and Takiwaki, T. (2017). Correlated Signatures of Gravitational-wave and Neutrino Emission in Three-dimensional General-relativistic Core-collapse Supernova Simulations. *Ap.J.*, 851(1):62. 16, 112, 113

Kuroda, T., Kotake, K., and Takiwaki, T. (2012). Fully General Relativistic Simulations of Core-collapse Supernovae with an Approximate Neutrino Transport. *Ap.J.*, 755:11. 12

Kuroda, T., Kotake, K., and Takiwaki, T. (2016a). A New Gravitational-wave Signature from Standing Accretion Shock Instability in Supernovae. *Ap.J.*, 829(1):L14. 16, 113

Kuroda, T., Takiwaki, T., and Kotake, K. (2016b). A New Multi-energy Neutrino Radiation-Hydrodynamics Code in Full General Relativity and Its Application to the Gravitational Collapse of Massive Stars. *Ap.J. Suppl.*, 222:20. 12

Landfield, R. E. (2018). *Sensitivity of Neutrino-Driven Core-Collapse Supernova Models to the Microphysical Equation of State*. PhD thesis, Univeristy of Tennessee Knoxville. 110, 117, 118, 142

Landfield, R. E., Lentz, E. J., Hix, W. R., Mezzacappa, A., Endeve, E., Messer, O. E. B., Bruenn, S. W., and Harris, J. A. (2024). Sensitivity of Neutrino-driven Core-collapse Supernova Models to the Nuclear Equation of State. *Ap.J.*, in prep. 117, 118

Lattimer, J. M. and Swesty, F. D. (1991). A generalized equation of state for hot, dense matter. *Nucl. Phys. A*, 535:331–376. 72, 120

Lentz, E. J., Bruenn, S. W., Hix, W. R., Mezzacappa, A., Messer, O. E. B., Endeve, E., Blondin, J. M., Harris, J. A., Marronetti, P., and Yakunin, K. N. (2015). Three-dimensional core-collapse supernova simulated using a 15 $M_\odot$ progenitor. *Ap.J.*, 807:L31. 14

Li, W., Chornock, R., Leaman, J., Filippenko, A. V., Poznanski, D., Wang, X., Ganeshalingam, M., and Mannucci, F. (2011). Nearby supernova rates from the Lick Observatory Supernova Search - III. The rate-size relation, and the rates as a function of galaxy Hubble type and colour. *Mon. Not. Roy. Ast. Soc.*, 412:1473–1507. 14

Liebendörfer, M., Mezzacappa, A., Thielemann, F.-K., Messer, O. E., Hix, W. R., and Bruenn, S. W. (2001). Probing the gravitational well: No supernova explosion in spherical symmetry with general relativistic Boltzmann neutrino transport. *Phys. Rev. D*, 63(10):103004. 5

Liebendörfer, M., Whitehouse, S. C., and Fischer, T. (2009). The Isotropic Diffusion Source Approximation for Supernova Neutrino Transport. *Ap.J.*, 698:1174–1190. 11

Lin, Z., Rijal, A., Lunardini, C., Morales, M. D., and Zanolin, M. (2023). Characterizing a supernova's standing accretion shock instability with neutrinos and gravitational waves. *Phys. Rev. D*, 107(8):083017. 112, 138

Maggiore, M., Van Den Broeck, C., Bartolo, N., Belgacem, E., Bertacca, D., Bizouard, M. A., Branchesi, M., Clesse, S., Foffa, S., García-Bellido, J., Grimm, S., Harms, J., Hinderer, T., Matarrese, S., Palomba, C., Peloso, M., Ricciardone, A., and Sakellariadou, M. (2020). Science case for the Einstein telescope. *J. Cosmol. Astropart. Phys*, 2020(3):050. 137

Marek, A., Dimmelmeier, H., Janka, H.-T., Müller, E., and Buras, R. (2006). Exploring the relativistic regime with Newtonian hydrodynamics: an improved effective gravitational potential for supernova simulations. *Astron. Astrophys.*, 445:273–289. 10

Marek, A., Janka, H.-T., and Müller, E. (2009). Equation-of-state dependent features in shock-oscillation modulated neutrino and gravitational-wave signals from supernovae. *Astron. Astrophys.*, 496:475–494. 112, 113, 139

Melson, T., Janka, H.-T., Bollig, R., Hanke, F., Marek, A., and Müller, B. (2015a). Neutrino-driven Explosion of a 20 Solar-mass Star in Three Dimensions Enabled by Strange-quark Contributions to Neutrino-Nucleon Scattering. *Ap.J.*, 808:L42. 11

Melson, T., Janka, H.-T., and Marek, A. (2015b). Neutrino-driven Supernova of a Low-mass Iron-core Progenitor Boosted by Three-dimensional Turbulent Convection. *Ap.J.*, 801:L24. 11

Mezzacappa, A. (2005). ASCERTAINING THE CORE COLLAPSE SUPERNOVA MECHANISM: The State of the Art and the Road Ahead. *Annual Review of Nuclear and Particle Science*, 55(1):467–515. 5

Mezzacappa, A. (2023). Toward Realistic Models of Core Collapse Supernovae: A Brief Review. In Bisikalo, D., Wiebe, D., and Boily, C., editors, *The Predictive Power of Computational Astrophysics as a Discover Tool*, volume 362 of *IAU Symposium*, pages 215–227. 143

Mezzacappa, A., Calder, A. C., Bruenn, S. W., Blondin, J. M., Guidry, M. W., Strayer, M. R., and Umar, A. S. (1998). An Investigation of Neutrino-driven Convection and the Core Collapse Supernova Mechanism Using Multigroup Neutrino Transport. *Ap.J.*, 495(2):911–926. 7

Mezzacappa, A., Marronetti, P., Landfield, R. E., Lentz, E. J., Murphy, R. D., Raphael Hix, W., Harris, J. A., Bruenn, S. W., Blondin, J. M., Bronson Messer, O. E., Casanova, J., and Kronzer, L. L. (2023). Core collapse supernova gravitational wave emission for progenitors of 9.6, 15, and 25M⊙. *Phys. Rev. D*, 107(4):043008. v, vi, 14, 16, 18, 43, 71, 72, 73, 81, 91, 103, 116, 118, 120, 138, 139, 143, 144, 146, 151, 169, 170

Mezzacappa, A., Marronetti, P., Landfield, R. E., Lentz, E. J., Yakunin, K. N., Bruenn, S. W., Hix, W. R., Messer, O. E. B., Endeve, E., Blondin, J. M., and Harris, J. A. (2020). Gravitational-wave signal of a core-collapse supernova explosion of a 15 $M_\odot$ star. *Phys. Rev. D*, 102(2):023027. 16, 18, 19, 76, 126, 143, 144, 169

Mezzacappa, A. and Zanolin, M. (2024). Gravitational Waves from Neutrino-Driven Core Collapse Supernovae: Predictions, Detection, and Parameter Estimation. *arXiv e-prints*, page arXiv:2401.11635. 15, 112

Mitra, A., Orel, D., Abylkairov, Y. S., Shukirgaliyev, B., and Abdikamalov, E. (2024). Probing nuclear physics with supernova gravitational waves and machine learning. *Mon. Not. R. Ast. Soc.*, 529(4):3582–3592. 113

Mori, K., Takiwaki, T., Kotake, K., and Horiuchi, S. (2025). Three-dimensional core-collapse supernova models with phenomenological treatment of neutrino flavor conversions. *PASJ*, 77(2):L9–L15. 139

Mori, M., Suwa, Y., and Takiwaki, T. (2023). Long-term gravitational wave asteroseismology of supernovae: From core collapse to 20 seconds postbounce. *Phys. Rev. D*, 107(8):083015. 61, 173

Morozova, V., Radice, D., Burrows, A., and Vartanyan, D. (2018). The Gravitational Wave Signal from Core-collapse Supernovae. *Ap.J.*, 861(1):10. 52, 61, 86, 103, 107, 112, 114, 117, 139, 140

Müeller, B., Janka, H.-T., and Marek, A. (2013). A new multi-dimensional general relativistic neutrino hydrodynamics code of core-collapse supernovae. iii. gravitational wave signals from supernova explosion models. *Ap.J.*, 766:43. 112, 140, 173

Müller, B. (2015). The dynamics of neutrino-driven supernova explosions after shock revival in 2D and 3D. *Mon. Not. Roy. Ast. Soc.*, 453:287–310. 8, 10

Müller, B. (2016). The Status of Multi-Dimensional Core-Collapse Supernova Models. *Proc. Astron. Soc. Aust.*, 33:e048. 5

Müller, B. (2020). Hydrodynamics of core-collapse supernovae and their progenitors. *Living Reviews in Computational Astrophysics*, 6(1):3. 117, 143

Müller, B., Gay, D. W., Heger, A., Tauris, T. M., and Sim, S. A. (2018). Multidimensional simulations of ultrastripped supernovae to shock breakout. *Mon. Not. R. Ast. Soc.*, 479(3):3675–3689. 10

Müller, B. and Janka, H.-T. (2015). Non-radial instabilities and progenitor asphericities in core-collapse supernovae. *Mon. Not. Roy. Ast. Soc.*, 448:2141–2174. 9

Müller, B., Janka, H.-T., and Marek, A. (2012). A New Multi-Dimensional General Relativistic Neutrino Hydrodynamics Code for Core-Collapse Supernovae II. Relativistic Explosion Models of Core-Collapse Supernovae. *Ap.J.*, 756:84. 8

Müller, B., Melson, T., Heger, A., and Janka, H.-T. (2017). Supernova simulations from a 3D progenitor model - Impact of perturbations and evolution of explosion properties. *Mon. Not. Roy. Ast. Soc.*, 472:491–513. 10

Müller, B., Tauris, T. M., Heger, A., Banerjee, P., Qian, Y.-Z., Powell, J., Chan, C., Gay, D. W., and Langer, N. (2019). Three-dimensional simulations of neutrino-driven core-collapse supernovae from low-mass single and binary star progenitors. *Mon. Not. Roy. Ast. Soc.*, 484(3):3307–3324. 10

Müller, B. and Varma, V. (2020). A 3D simulation of a neutrino-driven supernova explosion aided by convection and magnetic fields. *Mon. Not. R. Ast. Soc.*, 498(1):L109–L113. 10

Müller, B., Viallet, M., Heger, A., and Janka, H.-T. (2016). The Last Minutes of Oxygen Shell Burning in a Massive Star. *Ap.J.*, in press. 11

Murphey, C. T., Hogan, J. W., Fields, B. D., and Narayan, G. (2021). Witnessing history: sky distribution, detectability, and rates of naked-eye Milky Way supernovae. *Mon. Not. R. Ast. Soc.*, 507(1):927–943. 2, 14

Murphy, R. D., Brinkman, E., Richardson, C., Semenak, E., Mezzacappa, A., Marronetti, P., Lentz, E. J., and Bruenn, S. (2025a). Gravitational Waves as a Probe of Core Collapse Supernova Progenitor Structure. *arXiv e-prints*, in prep. v, vi, 138

Murphy, R. D., Casallas-Lagos, A., Mezzacappa, A., Zanolin, M., Landfield, R. E., Lentz, E. J., Marronetti, P., Antelis, J. M., and Moreno, C. (2024). Dependence of the reconstructed core-collapse supernova gravitational wave high-frequency feature on the nuclear equation of state in real interferometric data. *Phys. Rev. D*, 110(8):083006. v, vi, 45, 53, 78, 81, 111, 123, 127, 129, 131, 132, 135, 139, 149, 169

Murphy, R. D., Mezzacappa, A., Lentz, E. J., and Marronetti, P. (2025b). Core collapse supernova gravitational wave sourcing and characterization based on three-dimensional models. *Phys. Rev. D.* v, vi, 20, 71, 143, 144, 146, 169

Nakamura, K., Takiwaki, T., and Kotake, K. (2019). Long-term simulations of multi-dimensional core-collapse supernovae: Implications for neutron star kicks. *PASJ*, 71(5):98. 11

Nakamura, K., Takiwaki, T., and Kotake, K. (2022). Three-dimensional simulation of a core-collapse supernova for a binary star progenitor of SN 1987A. *Mon. Not. R. Ast. Soc.*, 514(3):3941–3952. 12, 18, 107

Nakamura, K., Takiwaki, T., Matsumoto, J., and Kotake, K. (2025). Three-dimensional magnetohydrodynamic simulations of core-collapse supernovae - I. Hydrodynamic evolution and protoneutron star properties. *Mon. Not. R. Ast. Soc.*, 536(1):280–294. 12

Obergaulinger, M. and Aloy, M. Á. (2022). Magnetorotational core collapse of possible gamma-ray burst progenitors - IV. A wider range of progenitors. *Mon. Not. R. Ast. Soc.*, 512(2):2489–2507. 9

O'Connor, E. and Couch, S. (2015). Two Dimensional Core-Collapse Supernova Explosions Aided by General Relativity with Multidimensional Neutrino Transport. *Ap.J.*, submitted. 8

O'Connor, E. and Couch, S. (2018). Exploring Fundamentally Three-dimensional Phenomena in High-fidelity Simulations of Core-collapse Supernovae. *Ap.J.*, 865:81. 18, 126, 169

O'Connor, E. and Ott, C. D. (2011). Black Hole Formation in Failing Core-Collapse Supernovae. *Ap.J.*, 730:70. 140

Omand, C. M. B., Sarin, N., and Temim, T. (2025). SN 1054 as a pulsar-driven supernova: implications for the crab pulsar and remnant evolution. *Mon. Not. R. Ast. Soc.*, 536(1):408–421. 2

Osaki, Y. (1975). Nonradial oscillations of a 10 solar mass star in the main-sequence stage. *PASJ*, 27(2):237–258. 80

Ott, C. D., Abdikamalov, E., Mösta, P., Haas, R., Drasco, S., O'Connor, E. P., Reisswig, C., Meakin, C. A., and Schnetter, E. (2013). General-relativistic Simulations of Three-dimensional Core-collapse Supernovae. *Ap.J.*, 768:115. 12

Ott, C. D., Abdikamalov, E., O'Connor, E., Reisswig, C., Haas, R., Kalmus, P., Drasco, S., Burrows, A., and Schnetter, E. (2012). Correlated gravitational wave and neutrino signals from general-relativistic rapidly rotating iron core collapse. *Phys. Rev. D*, 86(2):024026. 12

Ott, C. D., Roberts, L. F., da Silva Schneider, A., Fedrow, J. M., Haas, R., and Schnetter, E. (2018). The Progenitor Dependence of Core-collapse Supernovae from Three-dimensional Simulations with Progenitor Models of 12-40 $M_\odot$. *Ap.J.*, 855:L3. 12

Pajkos, M. A., Couch, S. M., Pan, K.-C., and O'Connor, E. P. (2019). Features of Accretion-phase Gravitational-wave Emission from Two-dimensional Rotating Core-collapse Supernovae. *Ap.J.*, 878(1):13. 116, 138, 139

Pajkos, M. A., VanCamp, S. J., Pan, K.-C., Vartanyan, D., Deppe, N., and Couch, S. M. (2023). Characterizing the Directionality of Gravitational Wave Emission from Matter Motions within Core-collapse Supernovae. *Ap.J.*, 959(1):21. 73

Pajkos, M. A., Warren, M. L., Couch, S. M., OConnor, E. P., and Pan, K.-C. (2021). Determining the Structure of Rotating Massive Stellar Cores with Gravitational Waves. *Ap.J.*, 914(2):80. 16, 116, 138, 139, 140, 169, 174

Pan, K.-C., Liebendörfer, M., Couch, S. M., and Thielemann, F.-K. (2018). Equation of State Dependent Dynamics and Multi-messenger Signals from Stellar-mass Black Hole Formation. *Ap.J.*, 857(1):13. 115, 139, 173

Pan, K.-C., Liebendörfer, M., Couch, S. M., and Thielemann, F.-K. (2021). Stellar Mass Black Hole Formation and Multimessenger Signals from Three-dimensional

Rotating Core-collapse Supernova Simulations. *Ap.J.*, 914(2):140. 12, 17, 116, 138, 139

Poisson, E. and Will, C. M. (2014). *Gravity: Newtonian, Post-Newtonian, Relativistic*. Cambridge University Press. 49

Powell, J. and Müller, B. (2019). Gravitational wave emission from 3D explosion models of core-collapse supernovae with low and normal explosion energies. *Mon. Not. R. Ast. Soc.*, 487(1):1178–1190. 10, 16, 17, 107, 173

Powell, J. and Müller, B. (2020). Three-dimensional core-collapse supernova simulations of massive and rotating progenitors. *Mon. Not. R. Ast. Soc.*, 494(4):4665–4675. 10, 16, 139, 173, 174

Powell, J. and Müller, B. (2022). Inferring astrophysical parameters of core-collapse supernovae from their gravitational-wave emission. *Phys. Rev. D*, 105(6):063018. 18, 139, 173

Powell, J. and Müller, B. (2024). The gravitational-wave emission from the explosion of a 15 solar mass star with rotation and magnetic fields. *Mon. Not. R. Ast. Soc.*, 532(4):4326–4339. 10, 17, 139

Powell, J., Müller, B., Aguilera-Dena, D. R., and Langer, N. (2023). Three dimensional magnetorotational core-collapse supernova explosions of a 39 solar mass progenitor star. *Mon. Not. R. Ast. Soc.*, 522(4):6070–6086. 9, 139

Powell, J., Müller, B., and Heger, A. (2021). The final core collapse of pulsational pair instability supernovae. *Mon. Not. R. Ast. Soc.*, 503(2):2108–2122. 16, 113, 115, 139

Radice, D., Morozova, V., Burrows, A., Vartanyan, D., and Nagakura, H. (2019). Characterizing the Gravitational Wave Signal from Core-collapse Supernovae. *Ap.J.*, 876(1):L9. 11, 16, 18, 107, 112

Rampp, M. and Janka, H. T. (2002). Radiation hydrodynamics with neutrinos. Variable Eddington factor method for core-collapse supernova simulations. *Astron. Astrophys.*, 396:361–392. 10, 47

Reitze, D., Adhikari, R. X., Ballmer, S., Barish, B., Barsotti, L., Billingsley, G., Brown, D. A., Chen, Y., Coyne, D., Eisenstein, R., Evans, M., Fritschel, P., Hall, E. D., Lazzarini, A., Lovelace, G., Read, J., Sathyaprakash, B. S., Shoemaker, D., Smith, J., Torrie, C., Vitale, S., Weiss, R., Wipf, C., and Zucker, M. (2019). Cosmic Explorer: The U.S. Contribution to Gravitational-Wave Astronomy beyond LIGO. In *Bulletin of the American Astronomical Society*, volume 51, page 35. 137

Richardson, C. J., Andresen, H., Mezzacappa, A., Zanolin, M., Benjamin, M. G., Marronetti, P., Lentz, E. J., and Szczepańczyk, M. J. (2024). Detecting Gravitational Wave Memory in the Next Galactic Core-Collapse Supernova. *Phys. Rev. Lett.*, 133(23):231401. 17, 124

Richardson, C. J., Mezzacappa, A., Murphy, R. D., Andresen, H., Schluterman, K., Zanolin, M., Lentz, E. J., and Marronetti, P. (2025). Low-Frequency Gravitational Waves in Three-Dimensional Core-Collapse Supernova Models. *Phys. Rev. D*, in prep. 144

Richardson, C. J., Zanolin, M., Andresen, H., Szczepańczyk, M. J., Gill, K., and Wongwathanarat, A. (2022). Modeling core-collapse supernovae gravitational-wave memory in laser interferometric data. *Phys. Rev. D*, 105(10):103008. 17

Richers, S., Ott, C. D., Abdikamalov, E., O'Connor, E., and Sullivan, C. (2017). Equation of state effects on gravitational waves from rotating core collapse. *Phys. Rev. D*, 95(6):063019. 16, 113

Ritter, A., Parker, Q. A., Lykou, F., Zijlstra, A. A., Guerrero, M. A., and Le Dû, P. (2021). The Remnant and Origin of the Historical Supernova 1181 AD. *Ap.J.*, 918(2):L33. 2

Roberts, L. F., Ott, C. D., Haas, R., O'Connor, E. P., Diener, P., and Schnetter, E. (2016). General-Relativistic Three-Dimensional Multi-group Neutrino Radiation-Hydrodynamics Simulations of Core-Collapse Supernovae. *Ap.J.*, 831:98. 12

Rodriguez, M. C., Ranea-Sandoval, I. F., Chirenti, C., and Radice, D. (2023). Three approaches for the classification of protoneutron star oscillation modes. *Mon. Not. R. Ast. Soc.*, 523(2):2236–2246. 81

Sandoval, M. A., Hix, W. R., Messer, O. E. B., Lentz, E. J., and Harris, J. A. (2021). Three-dimensional Core-collapse Supernova Simulations with 160 Isotopic Species Evolved to Shock Breakout. *Ap.J.*, 921(2):113. 15

Sasaoka, S., Sakai, Y., Dominguez, D., Somiya, K., Sakai, K., Oohara, K.-i., Meyer-Conde, M., and Takahashi, H. (2024). Parameter estimation of protoneutron stars from gravitational wave signals using the Hilbert-Huang transform. *Phys. Rev. D*, 110(10):104020. 139

Seidel, E., Myra, E. S., and Moore, T. (1988). Gravitational radiation from type-II supernovae: The effect of the high-density equation of state. *Phys. Rev. D*, 38(8):2349–2356. 113

Skinner, M. A., Burrows, A., and Dolence, J. C. (2016). Should One Use the Ray-by-Ray Approximation in Core-collapse Supernova Simulations? *Ap.J.*, 831:81. 7

Skinner, M. A., Dolence, J. C., Burrows, A., Radice, D., and Vartanyan, D. (2019). FORNAX: A Flexible Code for Multiphysics Astrophysical Simulations. *Ap.J. Suppl.*, 241:7. 11

Smartt, S. J. (2009). Progenitors of Core-Collapse Supernovae. *Ann. Rev. Astron. Astrophys.*, 47:63–106. 14

Sotani, H. (2019). Gravitational waves from protoneutron stars and nuclear equation of state. *Astronomische Nachrichten*, 340(217):217–220. 114

Sotani, H., Kuroda, T., Takiwaki, T., and Kotake, K. (2019). Dependence of the outer boundary condition on protoneutron star asteroseismology with gravitational-wave signatures. *Phys. Rev. D*, 99(12):123024. 61

Sotani, H., Müller, B., and Takiwaki, T. (2024). Universality in supernova gravitational waves with protoneutron star properties. *Phys. Rev. D*, 109(12):123021. 107, 173

Sotani, H. and Takiwaki, T. (2016). Gravitational wave asteroseismology with protoneutron stars. *Phys. Rev. D*, 94(4):044043. 112

Sotani, H. and Takiwaki, T. (2020a). Accuracy of the relativistic Cowling approximation in protoneutron star asteroseismology. *Phys. Rev. D*, 102(6):063025. 61

Sotani, H. and Takiwaki, T. (2020b). Dimension dependence of numerical simulations on gravitational waves from protoneutron stars. *Phys. Rev. D*, 102(2):023028. 107, 112, 114, 169, 174

Sotani, H., Takiwaki, T., and Togashi, H. (2021). Universal relation for supernova gravitational waves. *Phys. Rev. D*, 104(12):123009. 112, 115, 173

Srivastava, V., Ballmer, S., Brown, D. A., Afle, C., Burrows, A., Radice, D., and Vartanyan, D. (2019). Detection prospects of core-collapse supernovae with supernova-optimized third-generation gravitational-wave detectors. *Phys. Rev. D*, 100(4):043026. 15

Steiner, A. W., Hempel, M., and Fischer, T. (2013). Core-collapse Supernova Equations of State Based on Neutron Star Observations. *Ap.J.*, 774(1):17. 119, 142

Steiner, A. W., Lattimer, J. M., and Brown, E. F. (2010). The Equation of State from Observed Masses and Radii of Neutron Stars. *Ap.J.*, 722:33–54. 119

Steiner, A. W., Prakash, M., Lattimer, J. M., and Ellis, P. J. (2005). Isospin asymmetry in nuclei and neutron stars. *Phys. Rep.*, 411:325–375. 119

Stephenson, F. R. and Green, D. A. (2009). A Catalogue of "Guest Stars" Recorded in East Asian History from Earliest Times to A.D. 1600. *Journal for the History of Astronomy*, 40:31–54. 2

Stockinger, G., Janka, H. T., Kresse, D., Melson, T., Ertl, T., Gabler, M., Gessner, A., Wongwathanarat, A., Tolstov, A., Leung, S. C., Nomoto, K., and Heger, A. (2020). Three-dimensional models of core-collapse supernovae from low-mass progenitors with implications for Crab. *Mon. Not. R. Ast. Soc.*, 496(2):2039–2084. 10

Sukhbold, T., Woosley, S. E., and Heger, A. (2018). A High-resolution Study of Presupernova Core Structure. *Ap.J.*, 860(2):93. 141

Summa, A., Janka, H.-T., Melson, T., and Marek, A. (2018). Rotation-supported neutrino-driven supernova explosions in three dimensions and the critical luminosity condition. *Ap.J.*, 852(1):28. 11

Takiwaki, T., Kotake, K., and Foglizzo, T. (2021). Insights into non-axisymmetric instabilities in three-dimensional rotating supernova models with neutrino and gravitational-wave signatures. *Mon. Not. R. Ast. Soc.*, 508(1):966–985. 16, 116, 138, 139, 174

Takiwaki, T., Kotake, K., and Suwa, Y. (2012). Three-dimensional Hydrodynamic Core-collapse Supernova Simulations for an 11.2 $M_\odot$ Star with Spectral Neutrino Transport. *Ap.J.*, 749:98. 11

Takiwaki, T., Kotake, K., and Suwa, Y. (2014). A Comparison of Two- and Three-dimensional Neutrino-hydrodynamics Simulations of Core-collapse Supernovae. *Ap.J.*, 786:83. 11, 12

Takiwaki, T., Kotake, K., and Suwa, Y. (2016). Three-dimensional simulations of rapidly rotating core-collapse supernovae: finding a neutrino-powered explosion

aided by non-axisymmetric flows. *Mon. Not. Roy. Ast. Soc.*, 461:L112–L116. 11, 12

Tews, I., Lattimer, J. M., Ohnishi, A., and Kolomeitsev, E. E. (2017). Symmetry Parameter Constraints from a Lower Bound on Neutron-matter Energy. *Ap.J.*, 848(2):105. 117, 120

Thorne, K. S. (1969). Nonradial Pulsation of General-Relativistic Stellar Models.IV. The Weakfield Limit. *Ap.J.*, 158:997. 86

Thorne, K. S. (1980a). Multipole expansions of gravitational radiation. *Reviews of Modern Physics*, 52(2):299–340. 39, 40

Thorne, K. S. (1980b). Multipole expansions of gravitational radiation. *Reviews of Modern Physics*, 52(2):299–340. 78

Todd-Rutel, B. G. and Piekarewicz, J. (2005). Neutron-Rich Nuclei and Neutron Stars: A New Accurately Calibrated Interaction for the Study of Neutron-Rich Matter. *Phys. Rev. Lett.*, 95:122501. 119

Togashi, H., Nakazato, K., Takehara, Y., Yamamuro, S., Suzuki, H., and Takano, M. (2017). Nuclear equation of state for core-collapse supernova simulations with realistic nuclear forces. *Nucl. Phys. A*, 961:78–105. 174

Torres-Forné, A., Cerdá-Durán, P., Obergaulinger, M., Müller, B., and Font, J. A. (2019a). Universal Relations for Gravitational-Wave Asteroseismology of Protoneutron Stars. *Phys. Rev. Lett.*, 123(5):051102. 112, 115, 173

Torres-Forné, A., Cerdá-Durán, P., Passamonti, A., and Font, J. A. (2018). Towards asteroseismology of core-collapse supernovae with gravitational-wave observations - I. Cowling approximation. *Mon. Not. R. Ast. Soc.*, 474(4):5272–5286. 61, 86, 87, 103, 112

Torres-Forné, A., Cerdá-Durán, P., Passamonti, A., Obergaulinger, M., and Font, J. A. (2019b). Towards asteroseismology of core-collapse supernovae with gravitational wave observations - II. Inclusion of space-time perturbations. *Mon. Not. R. Ast. Soc.*, 482(3):3967–3988. 61, 103

Travaglio, C. and Hix, W. R. (2013). Nucleosynthesis in thermonuclear supernovae. *Frontiers of Physics*, 8:199–216. 13

Tseneklidou, D., Luna, R., Cerdá-Durán, P., and Torres-Forné, A. (2025). Proto-neutron star oscillations including accretion flows. *arXiv e-prints*, page arXiv:2503.16317. 171

Typel, S. (2005). Relativistic model for nuclear matter and atomic nuclei with momentum-dependent self-energies. *Phys. Rev. C*, 71(6):064301. 119

Typel, S., Röpke, G., Klähn, T., Blaschke, D., and Wolter, H. H. (2010). Composition and thermodynamics of nuclear matter with light clusters. *Phys. Rev. C*, 81(1):015803. 119

Varma, V., Müller, B., and Schneider, F. R. N. (2023). 3D simulations of strongly magnetized non-rotating supernovae: explosion dynamics and remnant properties. *Mon. Not. R. Ast. Soc.*, 518(3):3622–3636. 10

Vartanyan, D. and Burrows, A. (2020). Gravitational Waves from Neutrino Emission Asymmetries in Core-collapse Supernovae. *Ap.J.*, 901(2):108. 17

Vartanyan, D., Burrows, A., and Radice, D. (2019a). Temporal and angular variations of 3D core-collapse supernova emissions and their physical correlations. *Mon. Not. R. Ast. Soc.*, 489(2):2227–2246. 107

Vartanyan, D., Burrows, A., and Radice, D. (2019b). Temporal and angular variations of 3D core-collapse supernova emissions and their physical correlations. *Mon. Not. R. Ast. Soc.*, 489(2):2227–2246. 116, 138, 139

Vartanyan, D., Burrows, A., Radice, D., Skinner, M. A., and Dolence, J. (2019c). A successful 3D core-collapse supernova explosion model. *Mon. Not. Roy. Ast. Soc.*, 482:351–369. 11

Vartanyan, D., Burrows, A., Wang, T., Coleman, M. S. B., and White, C. J. (2023). Gravitational-wave signature of core-collapse supernovae. *Phys. Rev. D*, 107(10):103015. 17, 107, 108, 139

Vartanyan, D., Coleman, M. S. B., and Burrows, A. (2022). The collapse and three-dimensional explosion of three-dimensional massive-star supernova progenitor models. *Mon. Not. R. Ast. Soc.*, 510(4):4689–4705. 11

Wang, H.-S. and Pan, K.-C. (2024). The Influence of Stellar Rotation in Binary Systems on Core-collapse Supernova Progenitors and Multimessenger Signals. *Ap.J.*, 964(1):23. 116, 138, 139, 140, 169, 174

Wang, T. and Burrows, A. (2024). Supernova Explosions of the Lowest-mass Massive Star Progenitors. *Ap.J.*, 969(2):74. 11

Warren, M. L., Couch, S. M., O'Connor, E. P., and Morozova, V. (2020). Constraining Properties of the Next Nearby Core-collapse Supernova with Multimessenger Signals. *Ap.J.*, 898(2):139. 139, 140, 169

Westernacher-Schneider, J. R. (2020). Consistent perturbative modeling of pseudo-Newtonian core-collapse supernova simulations. *Phys. Rev. D*, 101(8):083021. 46, 47, 49, 52, 60, 61, 66, 67, 70, 100

Wilson, J. R. and Mayle, R. W. (1988). Convection in core collapse supernovae. *Phys. Rep.*, 163(1):63–77. 6

Wolfe, N. E., Fröhlich, C., Miller, J. M., Torres-Forné, A., and Cerdá-Durán, P. (2023). Gravitational Wave Eigenfrequencies from Neutrino-driven Core-collapse Supernovae. *Ap.J.*, 954(2):161. 61, 115, 139

Wongwathanarat, A., Hammer, N. J., and Müller, E. (2010). An axis-free overset grid in spherical polar coordinates for simulating 3D self-gravitating flows. *Astron. Astrophys.*, 514:A48. 10

Woosley, S. E. and Bloom, J. S. (2006). The Supernova Gamma-Ray Burst Connection. *ARA&A*, 44(1):507–556. 9

Woosley, S. E. and Heger, A. (2007). Nucleosynthesis and remnants in massive stars of solar metallicity. *Phys. Rep.*, 442:269–283. 72, 110, 118

Yadav, N., Müller, B., Janka, H. T., Melson, T., and Heger, A. (2020). Large-scale Mixing in a Violent Oxygen-Neon Shell Merger Prior to a Core-collapse Supernova. *Ap.J.*, 890(2):94. 11

Yakunin, K. N., Mezzacappa, A., Marronetti, P., Yoshida, S., Bruenn, S. W., Hix, W. R., Lentz, E. J., Messer, O. E. B., Harris, J. A., Endeve, E., Blondin, J. M., and Lingerfelt, E. J. (2015). Gravitational wave signatures of *ab initio* two-dimensional core collapse supernova explosion models for 12–25 $M_\odot$ stars. *Phys. Rev. D*, 92:084040. 43

Yamada, S., Nagakura, H., Akaho, R., Harada, A., Furusawa, S., Iwakami, W., Okawa, H., Matsufuru, H., and Sumiyoshi, K. (2024). Physical mechanism of core-collapse supernovae that neutrinos drive. *Proceedings of the Japan Academy, Series B*, 100(3):190–233. 9

Yasutake, N., Kotake, K., Hashimoto, M.-A., and Yamada, S. (2007). Effects of QCD phase transition on gravitational radiation from two-dimensional collapse and bounce of massive stars. *Phys. Rev. D*, 75(8):084012. 113, 115, 139

Zha, S. (2024). Proper way to spatially decompose the gravitational-wave origin in stellar collapse simulations. *Phys. Rev. D*, 110(8):083034. 72

Zha, S., Eggenberger Andersen, O., and O'Connor, E. P. (2024). Unveiling the nature of gravitational-wave emission in core-collapse supernovae with perturbative analysis. *Phys. Rev. D*, 109(8):083023. 47, 52, 61, 107, 108, 113

Zha, S. and O'Connor, E. (2022). Impact of rotation on the multimessenger signatures of a hadron-quark phase transition in core-collapse supernovae. *Phys. Rev. D*, 106(12):123037. 139

Zha, S., O'Connor, E. P., Chu, M.-c., Lin, L.-M., and Couch, S. M. (2020). Gravitational-wave Signature of a First-order Quantum Chromodynamics Phase Transition in Core-Collapse Supernovae. *Phys. Rev. Lett.*, 125(5):051102. 115, 139

Vita

Robert Daniel Murphy grew up in Murfreesboro, TN where he attended Siegel High School and first fell in love with physics for its ability to describe *everything* in the Universe. This love of physics was nurtured and expanded upon as he attended Middle Tennessee State University, where received a Bachelor of Arts degree in Philosophy and a Bachelor of Science degree in Physics. He then pursued a graduate education at The University of Tennessee, Knoxville and joined the theoretical astrophysics research group with collaborators at Oak Ridge National Laboratory to study core collapse supernovae (CCSNe). This research led to an appreciation of high performance computing as a powerful tool for conducting science. He received his Master of Science degree after working on neutrino transport within CCSNe. He then devoted his Ph.D. research to studying gravitational wave generation within CCSNe, with the goal of enhancing the ability to extract knowledge of the underlying physics involved in these events using gravitational wave detections. In August 2025, he hopes to graduate with his Doctorate of Philosophy in Physics from The University of Tennessee with an Interdisciplinary Graduate Minor in Computational Science.